VICERRECTORÍA DE INVESTIGACIÓN Y POSTGRADO
DIRECCIÓN DE POSTGRADOS Y POSTÍTULOS

FACULTAD DE CIENCIAS
DEPARTAMENTO DE FÍSICA Y ASTRONOMÍA

THE IMPACT OF THE DYNAMICAL STATE OF CLUSTERS ON THE PHYSICAL AND STRUCTURAL PROPERTIES OF GALAXIES

Tesis presentada para optar al Grado Académico de Magíster en Astronomía.

AUTOR: SIMÓN IGNACIO VÉLIZ ASTUDILLO

LA SERENA, CHILE, MAYO 2024

CONSTANCIA

Don . . . .

HACE CONSTAR:

Que el trabajo correspondiente a la presente Tesis de Magíster, titulada “The impact of the dynamical state of clusters on the physical and structural properties of galaxies”, ha sido realizada por Don Simón Ignacio Véliz Astudillo, bajo mi dirección.

Para que conste y en cumplimiento de las normativas vigentes de la Universidad de la Serena, Chile, firmo el presente documento en La Serena, Chile, Mayo de 2024.

TESIS PARA OPTAR AL GRADO DE MAGÍSTER EN ASTRONOMÍA

TÍTULO : THE IMPACT OF THE DYNAMICAL STATE OF CLUSTERS ON THE PHYSICAL AND STRUCTURAL PROPERTIES OF GALAXIES
PRESENTADA POR : SIMÓN IGNACIO VÉLIZ ASTUDILLO
DIRECTOR DE TESIS : JOSÉ LUIS NILO CASTELLÓN & ELEÁZAR RODRIGO CARRASCO

TRIBUNAL CALIFICADOR

El tribunal de tesis, conformado por:

PRESIDENTE :
MIEMBROS DEL TRIBUNAL: *
*
*
*
*

ACUERDAN OTORGARLE LA CALIFICACIÓN DE:

La Serena, Chile, **Mayo de 2024**

“(...) How often have I said to you that when you have eliminated the impossible, whatever remains, however improbable, must be the truth?” - Sir Arthur Conan Doyle

AGRADECIMIENTOS

La culminación de mi trabajo de tesis representa estos años de trabajo, aprendizaje, y experiencias compartidas. Esta instancia no solo refleja mi esfuerzo personal, sino también el invaluable apoyo de quienes me han acompañado en este viaje académico y personal.

En este sentido, me gustaría comenzar expresando mi gratitud a José Luis Nilo y Rodrigo Carrasco, mis directores. En este período de tiempo han sido los responsables de mi crecimiento académico, y cada uno a su estilo, realmente han sido una guía profesional y han estimulado mi deseo de continuar desarrollándome en el área de la investigación.

Sin embargo, la vida como estudiante de postgrado -afortunadamente- no solo abarca el ámbito académico. Indudablemente las horas de ping-pong fueron un pilar de mi estabilidad emocional en estos años. En este sentido, me gustaría agradecer a todos aquellos que han estado presente en esos y otros tantos momentos (mención especial a la *sala de la esquizofrenia*).

Finalmente, agradezco a mi familia por su apoyo incondicional; a mi madre, Marcela Astudillo; mi hermana, Paloma Véliz; mi padre, Renso Véliz; mi tía, Marina Astudillo; y mi primo, Camilo Gómez. Han sido los pilares de mi vida, de no ser por ustedes no podría haber llegado hasta aquí. Pero, quiero hacer una especial mención a mi pareja, Mary Verdugo. Literalmente has vivido junto a mí todo este período en donde he pasado buenos y malos momentos, y has sido mi soporte principal para poder concretar esto, con toda la carga mental que eso conlleva. Mi más genuino agradecimiento por todo tu amor y comprensión.

Resumen

En el contexto del modelo cosmológico ΛCDM (del inglés, Λ *Cold Dark Matter*), los cúmulos de galaxias masivos se forman de manera jerárquica por medio de fusiones y acreciones suaves. El modelo predice que numerosos cúmulos de galaxias pueden estar en alguna etapa de fusión en cualquier época. Estos procesos son los más energéticos del Universo después del Big Bang, liberando energías del orden del orden de 10^{64} erg/s, lo cual los hace laboratorios únicos para estudiar la evolución de las galaxias. Bajo estas condiciones, las galaxias podrían experimentar procesos extremos que alteren sus propiedades estructurales y físicas. En este estudio, evaluamos el estado dinámico de 87 cúmulos de galaxias masivos ($M_{500} > 1.5 \times 10^{14} M_{\odot}$) en el rango de *redshift* de $0.10 < z < 0.35$ usando datos ópticos del LS DR10 (del inglés, *Legacy Survey Data Release 10*) en conjunto con datos en rayos-X del archivo de Chandra y XMM-Newton, separándolos en relajados, intermedios y perturbados. También, clasificamos las galaxias en tipos morfológicos por medio de parámetros estructurales, los cuales fueron calculados utilizando métodos paramétricos y no paramétricos. Además, determinamos las propiedades físicas de estas estructuras empleando métodos de ajustes de sus distribuciones espectrales de energía.

Hemos encontrado que si bien casi no se observan diferencias en los valores medianos de las propiedades físicas y estructurales de las galaxias entre cúmulos relajados y perturbados, el estado dinámico sí afecta significativamente sus distribuciones. Más aún, nuestros resultados sugieren que el efecto de la dinámica de los cúmulos en sus galaxias miembro es diferencial, donde las galaxias de baja masa y pertenecientes a la secuencia roja de estos sistemas son más susceptibles a sufrir cambios físicos y estructurales. Por otro lado, al estudiar relaciones fundamentales de los cúmulos de galaxias, notamos que la secuencia roja; la relación masa-tamaño; y la relación entre la morfología, la tasa de formación estelar y el ambiente local en

donde se encuentran las galaxias (caracterizado por la densidad local y la distancia al centro de los cúmulos) no presentan diferencias estadísticamente significativas entre cúmulos relajados y perturbados.

Finalmente, considerando que en nuestro trabajo inicialmente clasificamos los estados dinámicos como relajados, intermedios y perturbados, se observa que los cúmulos intermedios no siempre representan un nivel evolutivo entre los sistemas relajados y perturbados. En realidad, estos pueden constituir estructuras con dinámicas más complejas, lo que requiere una interpretación cautelosa para evitar malos entendidos acerca de sus estados dinámicos.

Abstract

In the context of the Λ Cold Dark Matter cosmological model, massive galaxy clusters form hierarchically by merging and smooth accretion. The model predicts that numerous clusters of galaxies may be in some stage of merging in any epoch. These processes are the most powerful in the Universe after the Big Bang, releasing energies of the order of 10^{64} erg/s, making them unique laboratories to studying galaxy evolution. Under such conditions, galaxies may undergo extreme processes that alter their structural and physical properties. In this study, we evaluate the dynamical state of 87 massive galaxy clusters ($M_{500} > 1.5 \times 10^{14} M_{\odot}$) in the redshift range of $0.10 < z < 0.35$ using optical data from Legacy Surveys Data Release 10 in conjunction with X-ray data from the Chandra and XMM-Newton archives. Additionally, we classify galaxies into morphological types using structural parameters, calculated through parametric and non-parametric methods. Furthermore, we determine the physical properties of these structures using spectral energy distribution (SED) fitting methods.

We found that while there are almost no differences in the median values of the physical and structural properties of galaxies between relaxed and disturbed clusters, the dynamical state significantly affects their distributions. Moreover, our results suggest that the effect of cluster dynamics on their member galaxies is differential, where low-mass and red sequence galaxies of these systems are more susceptible to experiencing physical and structural changes. On the other hand, when studying fundamental relations of galaxy clusters, we note that the red sequence; the mass-size relation; and the morphology/star formation rate-local density relation, do not show statistically significant differences between relaxed and disturbed clusters.

Finally, considering that in this work the dynamical states were initially classified as relaxed, intermediate, and disturbed, it is observed that intermediate clusters do not always represent

an evolutionary level between relaxed and disturbed systems. Indeed, these may constitute structures with more complex dynamics, which requires careful interpretation to avoid misunderstandings about their dynamical states.

Contents

1 Introduction **1**

1.1 Galaxies 1

1.2 Clusters of galaxies 4

1.3 Interaction of galaxy clusters 9

1.4 Thesis goals 12

2 Data **14**

2.1 Optical images and catalogs 14

2.2 X-ray images and catalogs 15

2.3 Cluster catalog and photometric redshifts 17

2.4 Spectroscopic redshift catalogs 19

2.5 Sample selection 21

3 Analysis **23**

3.1 Cluster membership 23

3.2 BCG selection 25

3.3 Cluster properties 27

3.3.1 Fundamental properties 28

3.3.2 Spectroscopic members and velocity dispersion 28

3.4 Cluster dynamical states 28

3.4.1 Dynamical state proxies 28

3.4.2 Weighted boolean sum 34

3.5 Structural properties of galaxies 38

3.5.1 Non-parametric approach 45

3.5.2 Parametric approach 50
3.5.3 Morphological classification of galaxies 54
3.6 Physical properties of galaxies 57
3.6.1 Normalized colors 57
3.6.2 Stellar mass and specific star formation rate 57
3.7 Quality cuts 59

4 Results 62
4.1 Photometric redshifts quality 62
4.2 Characterization of galaxy clusters 63
4.3 Galaxy properties 65
4.3.1 Overall results 66
4.3.2 Mass dependence 69
4.3.3 Morphology dependence 74
4.4 Fundamental relations of galaxy clusters 78
4.4.1 Color magnitude diagram 78
4.4.2 Mass-size relation 87
4.4.3 Morphology/SFR vs local environment 91

5 Discussion 94
5.1 Photometric redshifts and cluster membership 94
5.2 Dynamical state of galaxy clusters 95
5.2.1 BCG selection method 95
5.2.2 Dynamical parameters 97
5.2.3 Classification of dynamical states 97
5.3 Structural parameters of galaxies 99
5.4 Physical parameters of galaxies 103
5.5 Galaxy properties on different environments 105
5.6 Fundamental relations of galaxy clusters 107

6 Summary, conclusions and outlook **110**

A Additional data of galaxy clusters **149**

A.1 Galaxy cluster properties 149

A.2 Red galaxies and hot gas distributions 152

List of Figures

1.1 Hubble Tuning Fork (Hubble, 1936). 2

1.2 Morphology-density relation (Dressler, 1980). 7

1.3 The Bullet cluster: An exmple of a highly disturbed cluster (Clowe et al., 2006). 10

2.1 Example of the X-ray images processed by Yuan and Han (2020). 16

2.2 Richness (λ) and mass (M_{500}) distributions of the full sample. 22

3.1 Completeness and contamination fraction using the probabilistic method to assign cluster membership. 25

3.2 Double gaussian fits applied to the color distribution of clusters. 26

3.3 Normalized color-magnitude diagrams with red sequence fits. 27

3.4 Pairgrid with the correlations of the six dynamical state proxies used in this thesis. 35

3.5 Parameter space of the first two principal components (PC 1 and PC 2) obtained from the six dynamic parameters. 36

3.6 Distribution of the weighted Boolean sum for the whole galaxy clusters sample. 38

3.7 SExtractor segmentation map example. 40

3.8 Photometric calibration example 43

3.9 Selected stars used to reconstruct the ePSF in the Abell 3038 cluster 45

3.10 Example output from `statmorph` for a bulge-dominated galaxy. 46

3.11 Example output from `statmorph` for a disk-dominated galaxy. 47

3.12 Example output from `GALFITM` for a bulge-dominated galaxy. 52

3.13 Example output from `GALFITM` for a disk-dominated galaxy. 53

3.14 Principal component analysis of the morphological parameters G and M_{20}. 56

3.15 Set of filters used to create the model magnitude libraries in `Le Phare`. 59

3.16 Boxplots of the χ^2_ν and χ^2 parameters obtained with `GALFITM` and `Le Phare`, respectively. . . 60
3.17 Number of galaxies in each quality cut. 61

4.1 Comparison between $z_{\rm spec}$ and $z_{\rm phot}$. 62
4.2 Radar charts with the six dynamical parameters for all galaxy clusters. 64
4.3 Peculiar velocity distribution of six example galaxy clusters. 65
4.4 Initial stellar mass distributions for the three types of dynamical states of galaxy clusters. . . 66
4.5 Distribution of structural parameters for all galaxies. 67
4.6 Distribution of physical parameters for all galaxies. 68
4.7 Distribution of structural parameters for low-mass galaxies. 70
4.8 Distribution of structural parameters for high-mass galaxies. 71
4.9 Distribution of physical parameters for low-mass galaxies. 71
4.10 Distribution of physical parameters for high-mass galaxies. 72
4.11 Distribution of structural parameters for bulge-dominated galaxies. 75
4.12 Distribution of structural parameters for disk-dominated galaxies. 76
4.13 Distribution of physical parameters for bulge-dominated galaxies. 76
4.14 Distribution of physical parameters for disk-dominated galaxies. 77
4.15 Normalized and stacked color-magnitude diagramas, separating the sample into relaxed, intermediate and disturbed clusters. 79
4.16 Distribution of structural parameters for Red Sequence galaxies. 81
4.17 Distribution of structural parameters for Green Valley galaxies. 82
4.18 Distribution of structural parameters for Blue Cloud galaxies. 83
4.19 Distribution of physical parameters for Red Sequence galaxies. 83
4.20 Distribution of physical parameters for Green Valley galaxies. 84
4.21 Distribution of physical parameters for Blue Cloud galaxies. 84
4.22 Mass-size relations separating galaxies by morphological type. 88
4.23 Mass-size relations separating galaxies by quenching state. 88
4.24 Mass-size relation using Sersic index as control parameters 90
4.25 Mass-size relation using sSFR as a control parameter. 91

4.26 Morphology/SFR-density relation. 92
4.27 Morphology/SFR-clustercentric distance relation. 93

5.1 Completeness-contamination plane for the probabilistic cluster membership method, comparing with previous works. 95
5.2 Example of clusters with BCGs that have contamination. 96
5.3 Radar charts with the medians of the six dynamical parameters for the three subsamples. . . 98
5.4 Median values of the dynamical state proxies with 1σ regions. 99
5.5 Galaxies with unreliable `statmorph` measurements. 101
5.6 Comparison of the morphological classification carried out using GMOS and DECam in the Abell 3827 galaxy cluster. 102
5.7 Comparison of structural parameters between different photometric bands. 103
5.8 Uncertainties for stellar mass and specific star formation rate. 104
5.9 Summary of the results of applying the Kolmogorov-Smirnov test to all the cluster populations studied in this thesis, comparing relaxed clusters with disturbed ones. 106

A.1 Contours of the X-ray surface brightness and red sequence galaxies distributions. 152
A.2 Contours of the X-ray surface brightness and red sequence galaxies distributions. 153
A.3 Contours of the X-ray surface brightness and red sequence galaxies distributions. 154

List of Tables

2.1 Dynamical parameters for the first 10 clusters extracted from Yuan et al. (2022). 17
2.2 Clusters of galaxies identified from the DES×unWISE data extracted from Wen and Han (2022). 19
2.3 Galaxy clusters with spectroscopic redshifts available in the literature and databases. 20

3.1 Normalized statistical weight of the dynamical parameters associated to the first principal component. 37

LIST OF TABLES

3.2 `SExtractor` parameters used to obtain the photometric catalogs and segmentation maps. . . 39

3.3 Output parameters given by `SExtractor` 41

3.4 Parameters used to create the SED libraries. 58

4.1 Comparison of the photometric redshift quality obtained by Wen and Han (2021) using the *kNN* method and those obtained through SED fitting with the `Le Phare` code. 63

4.2 Median values (M) and standard deviations (σ) of the structural and physical parameters in the three environments studied for all galaxies. 68

4.3 Results of the Kolmogorov-Smirnov hypothesis tests applied to the physical and morphological parameters for all galaxies in the sample. 68

4.4 Abundances of galaxies for all the sample. 69

4.5 Median values (M) and standard deviations (σ) of the morphological and physical parameters in the three studied environments. Here, we separate between high and low mass galaxies. . . 72

4.6 Results of the Kolmogorov-Smirnov hypothesis tests applied to the physical and morphological parameters for galaxies separated into high and low mass. 73

4.7 Abundances of galaxies for low-mass and high-mass populations. 73

4.8 Median values (M) and standard deviations (σ) of the morphological and physical parameters in the three studied environments. Here, we separate between bulge-dominated and disk-dominated galaxies. 77

4.9 Results of the Kolmogorov-Smirnov hypothesis tests applied to the physical and morphological parameters for galaxies separated into bulge-dominated and disk-dominated. 78

4.10 Results of the t-tests applied to the parameters of robust linear regressions applied to red galaxies in the three types of clusters. 79

4.11 Median values (M) and standard deviations (σ) of the structural and physical parameters in the three studied environments. Here, we separate between Red Sequence, Green Valley and Blue Cloud galaxies. 85

4.12 Results of the Kolmogorov-Smirnov hypothesis tests applied to the physical and morphological parameters for galaxies separated into Red Sequence, Green Valley and Blue Cloud. 86

4.13 Abundances of galaxies for color-magnitude diagram populations. 87

4.14 Results of the t-tests applied to the slopes of the linear regressions for the three types of clusters in the mass-size plane. 89

A.1 Full cluster catalog 149

A.2 Continuation of Table A.1 150

Chapter 1

Introduction

1.1 Galaxies

Edwin Hubble ushered in the era of extragalactic astronomy with his seminal work, “The Realm of Nebulae” (Hubble, 1936). In this publication, he succinctly presented his findings and conclusions from years of prior research, confirming the nature of galaxies as isolated systems similar to our Milky Way. Furthermore, through spectroscopic and photometric observations of Cepheid variable stars, he derived their radial velocities from the redshift of spectral lines and determined distances using the period-luminosity relationship. With these data, he inferred that the universe is undergoing expansion.

Hubble’s groundbreaking discoveries marked a paradigm shift in our understanding of the cosmos. Since then, extragalactic astronomy has undergone significant development, leading to a consensus that galaxies represent overdensities of dark and baryonic matter, capable of converting cold molecular gas into stellar mass (Huertas-Company et al., 2016). The baryonic component of galaxies extends beyond stars to include dust and gas, which reside primarily in the interstellar medium (Schneider, 2015).

These celestial objects exhibit diverse morphologies. Hubble keenly observed this characteristic, leading to the creation of the first morphological classification system for galaxies, commonly known as the Hubble Tuning Fork (see Figure 1.1). In this system, he proposed an evolutionary sequence starting with elliptical galaxies (E), which vary in ellipticity and are denoted from E7 to E0 in decreasing order of elongation. Following in the sequence are lenticular galaxies (S0), which feature a well-defined disk. Hubble suggested that S0 galaxies represent an intermediate stage between Es and the continuing sequence of spiral galaxies (S). The latter are easily recognizable by their prominent spiral arms. On the basis of this characteristic, spirals are classified according to the degree of tightness of their spiral arms, denoted as a, b, or c in decreasing order of tightness. Additionally, if these galaxies possess bars, they are designated as SB. Finally, there is the irregular morphological type (Irr), which does not share characteristics with any of the aforementioned types.

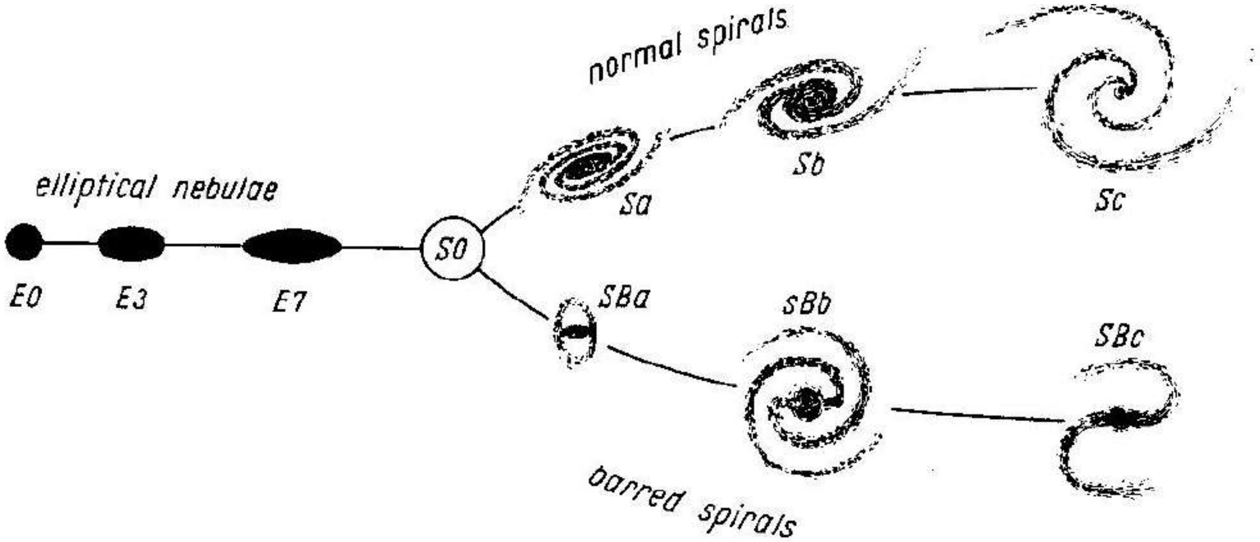

Figure 1.1: Evolutive sequence of *nebulae* proposed by Edwin Hubble, also known as Hubble Tuning Fork. Irregular galaxies are not found in this sequence because they are highly peculiar, and Hubble argues that almost all of them require individual consideration and cannot be classified within this system (Hubble, 1936).

Proposed almost a century ago, this classification system endures in current usage due to its simplicity and versatility. It has also served as the foundation for other systems developed and utilized in the literature (e.g., de Vaucouleurs et al., 1991; Fasano et al., 2012). However, it has been demonstrated that Hubble's proposed linear evolutionary sequence is indeed incorrect. Instead, the hierarchical structure formation paradigm is widely accepted within the scientific community (e.g., White and Rees, 1978; White and Frenk, 1991; Cole et al., 1994). In this scenario, based on the standard Lambda Cold Dark Matter cosmological model (ΛCDM, Blumenthal et al., 1984), the nonlinear evolution of small perturbations in the initial dark matter density field results in the formation of dark matter halos. Subsequently, due to the gravitational attraction of these halos, pre-galactic baryonic matter concentrates towards their deep potential wells (Benson, 2010).

During the formation process of the galactic structure, they are affected by tidal torques from the large-scale surroundings (Barnes and Efstathiou, 1987). The resulting angular momentum allows the formation of initial disks, which can merge with others, forming larger structures. In the case of galaxies with spiral arms, it has been suggested that these are manifestations of spiral-shaped density waves (Lin and Shu, 1964, 1966). Furthermore, based on this model, it is proposed that the formation of elliptical galaxies arises from the merger of two or more progenitor galaxies of similar size (Barnes, 1989), and even mergers with smaller galaxies (minor mergers, Bournaud et al., 2007).

In addition to the morphological variations exhibited by galaxies, they also manifest differences in their physical properties, which can be derived from photometric and spectroscopic observations. Generally, in the literature, binary classification has been favored for various physical properties, especially when extragalactic objects are at significant distances. For instance, classifications exist for color (red or blue), star formation rate (quiescent or star-forming), mass (low-mass and high-mass), metallicity (metal-poor or metal-rich), and age (old or young). Extensive evidence in the literature demonstrates a connection between structural properties (morphology) and the physical properties of galaxies (e.g., Roberts and Haynes, 1994; Van den Bergh, 1998; Blanton and Moustakas, 2009; Wijesinghe et al., 2010). There is a tendency for elliptical and lenticular galaxies (also referred to as early-type galaxies) to be redder, older, metal rich, quiescent, and more massive. In contrast, spiral and irregular galaxies (also known as late-type) tend to be bluer, younger, metal poor, star-forming, and less massive.

By the mid-20th century, the importance of the structural properties of galaxies and their correlation with physical properties in the local universe was already well established (e.g., Hubble, 1936; Zwicky, 1937). However, several factors led to the development of automatic classification methods that depart from classical visual classification. Initially, these reasons were linked to the subjectivity of the classifier and the quality of the image (limited photometric depth, resolution, signal-to-noise ratio, etc.), which simply did not allow for an appropriate galaxy classification. Later, towards the end of the last century, another crucial motivation for the development of these methods was the increasing capacity of telescopes to generate vast volumes of data, a trend that was also anticipated for future surveys.

As a result, the early methods for classifying galaxies were parametric approaches. The first of these corresponds to the De Vaucouleurs profile (de Vaucouleurs, 1948), later generalized with the Sersic profile (Sersic, 1968). Both methods involve modeling the surface brightness profile of galaxies using mathematical functions, with the Sersic profile being more versatile. When the parameters are left free in the fit, it has been shown that they serve precisely as good morphological indicators (e.g., Vika et al., 2015).

Decades later, the first non-parametric structural indices involving the light concentration of galaxies were defined (Abraham et al., 1994a; Bershady et al., 2000), along with their asymmetry (Abraham et al., 1996; Brinchmann et al., 1998). The mathematical expression for calculating these parameters evolved, culminating in the concentration-asymmetry-smoothness system (CAS, Conselice, 2003), which also incorporates a new non-parametric index related to the smoothness of galaxies. A year later, Lotz et al. (2004) introduced two new parameters and developed the G-M_{20} classification system, named after its non-parametric indices. For an extensive definition of these systems, refer to Section 3.5.

In the literature, the advantages and disadvantages of using parametric and non-parametric methods for galaxy classification have been extensively discussed (e.g., Abraham et al., 1996; Peng et al., 2002; Conselice, 2003; Lotz et al., 2004; Vikram et al., 2010). For instance, the use of non-parametric methods has an advantage in terms of computation time since it does not require fitting a model to the data, which typically involves an iterative process of minimizing some statistical variable (e.g., χ^2, χ^2_ν). Instead, these methods calculate values directly from the data. However, in terms of interpretation, it is more straightforward to relate the underlying physics to the results of parametric methods, as these models directly connect physical variables, something not achieved with non-parametric methods.

More recently, methodologies employed to determine the morphology of galaxies have been dominated by the use of Machine Learning techniques (e.g., Domínguez Sánchez et al., 2018; Zhu et al., 2019; Fischer et al., 2019; Farias et al., 2020; Bom et al., 2021; Cheng et al., 2021; Walmsley et al., 2022). In general, these techniques are divided into two main groups: unsupervised and supervised learning. The former is associated with handling data without prior knowledge of their labels (unlabeled data), where clustering, association, and dimensionality reduction algorithms come into play. The latter focuses on performing specific tasks like regressions and classifications using a training sample with well-known labels (labeled data). Initially, the morphological classification of galaxies was based on supervised machine learning techniques (e.g., Lahav et al., 1996; Fasano et al., 2012), but lately hybrid techniques that combine supervised and unsupervised learning have been used (e.g., Cheng et al., 2021; Kolesnikov et al., 2024).

Regardless of the learning algorithms used, these methods have the advantage that once the classification model is created, it is possible to determine the morphological type of a large number of objects in a considerably shorter time than with classical visual classifications (Reza, 2021). However, it is essential to establish a robust training sample with the least possible biases; otherwise, the model will replicate these biases, which could affect the reliability of the classification (Lintott et al., 2008; Cabrera-Vives et al., 2018).

1.2 Clusters of galaxies

Despite the "isolated" nature of galaxies described by Hubble (1936), these objects do not necessarily exist in solitude. Galaxies can cluster together to form larger systems, such as groups or clusters of galaxies (hereafter clusters, for simplicity). Galaxy clusters are the largest gravitationally bound objects in the Universe and serve as ideal laboratories for studying a broad range of physical phenomena.

In the context of the standard cosmological model, the cosmological principle states that the Universe is homogeneous and isotropic on large scales (Large-Scale Structure, LSS). This intricate LSS is composed of filaments that converge into overdense regions, known as nodes, and vast regions with very little or almost no matter, known as voids (Davis et al., 1985). Utilizing redshift surveys data, it has been demonstrated that these filaments have scales of at least 10 h^{-1} Mpc (Coil, 2013), with galaxy clusters as their primary constituents.

According to the ΛCDM model, the total density is dominated by the cosmological constant (Λ), and the matter density is dominated by cold dark matter (CDM). Similar to galaxies, large structures undergo hierarchical formation processes here. In the initial density field, small fluctuations collapse first due to gravitational instabilities, and then more massive structures form through mergers and smooth accretion. Evidence of this can be observed in the cosmic microwave background (CMB), where fluctuations reflect the inhomogeneities of the initial density field, which seeded the formation of large-scale structures in the universe (Efstathiou et al., 1992; Spergel et al., 2003; Planck Collaboration et al., 2014). The model predicts that a considerable number of galaxy clusters are in some stage of merger at any given time. During these merger processes, the gravitational potential energy of the accreting groups is dissipated, subsequently heating the gas associated with these systems (Molnar, 2016).

The typical scale of galaxy clusters is of the order of $R_{200} > 1.5\,h^{-1}$ Mpc, and the mass lays within the range of $10^{14} \lesssim M_{200}/M_{\odot} \lesssim 10^{15}$. Here, R_{200} denotes the radius containing 200 times the critical density of the Universe at the cluster redshift, and M_{200} represents the mass enclosed within that radius. In terms of mass, these structures are predominantly composed of dark matter (DM, approximately 80%), followed by hot gas at temperatures of $\sim 10^7$ - 10^8 K, known as the intracluster medium (ICM, approximately 18%), and stellar mass, mainly consisting of the stellar mass of galaxies and intracluster light (gravitational unbound stars not associated with any specific galaxy), contributing the smallest fraction (approximately 2%) (Schneider, 2015).

Given their characteristics, the components of galaxy clusters can be observed across various wavelengths. Galaxies in these systems can be studied in the ultraviolet (UV), optical, and infrared (IR) regimes. On the other hand, the ICM emits in the X-ray range as the high temperature of the gas ionizes the medium, causing electrons to lose energy through the Bremsstrahlung process. Furthermore, due to the inverse Compton interaction between high-energy electrons in the hot gas and photons from the CMB, the ICM can also be analyzed in the microwave regime through Sunyaev-Zeldovich effect maps (SZ effect, Sunyaev and Zeldovich, 1972). Considering that dark matter cannot be directly observed, the overall matter distribution within galaxy clusters, which is dominated by dark matter, can be inferred. This inference is typically achieved through methods such as weak and strong gravitational lensing. Additionally, the total mass of a galaxy cluster can be estimated using scaling relations that relate to the velocity dispersion of the member galaxies within the cluster.

Considering the aforementioned, various methods for detecting galaxy clusters have been developed across all mentioned wavelength regimes. Among these, the identification of clusters using optical images is particularly notable, with the Abell catalogs (Abell, 1958; Abell et al., 1989) standing out due to their comprehensive and pioneering approach. The Abell catalogs were the first galaxy cluster catalogs constructed systematically based on specific selection criteria. On the other hand, these structures have also been detected through X-rays, with significant efforts invested in developing satellites and launching them into space. A notable example is ROSAT, which, with its ROSAT All Sky Survey (RASS), successfully detected thousands of clusters (Böhringer, 2005), conducted analyses of their substructures (Schuecker et al., 2001) and determined their fundamental parameters to study their implications in cosmology (David et al., 1995). More recently, we have the successor, eROSITA (extended ROentgen Survey with an Imaging Telescope Array), which will provide X-ray information for approximately 100,000 galaxy clusters in the coming years with its eROSITA All Sky Survey (eRASS, Merloni et al., 2012, 2024), offering 25 times more sensitivity than its predecessor RASS (Liu et al., 2022).

In the microwave region of the electromagnetic spectrum, several telescopes have been utilized to map the sky and detect these systems. Perhaps the most significant among them are the South Pole Telescope (SPT), the Atacama Cosmology Telescope (ACT), and the Planck Satellite, all of which have generated several catalogs of massive clusters across a wide range of redshifts (Hasselfield et al., 2013; Bleem et al., 2015; Planck Collaboration et al., 2016).

A common feature shared by all these detection methods is their susceptibility to significant projection effects. To overcome this issue, photometric redshifts can be employed as a good approximation to ascertain whether galaxies that appear to be part of a cluster in the projected space truly belong to it. However, for confirmation, spectroscopic redshifts are required, as applied in studies that combine multiwavelength photometry and optical spectroscopy (e.g., Bayliss et al., 2016; Liu et al., 2022).

Another method for identifying these structures through sky mappings is through the color-magnitude diagram of galaxy clusters. In these systems, there is a mixture of morphologies, and in the case of early-type galaxies, they form a well-defined narrow linear relation called the red cluster sequence (RCS, Visvanathan and Sandage, 1977; Yee et al., 1999). This sequence is associated with the red peak of the galaxy color distribution (e.g., Blanton et al., 2003; Bell et al., 2004). In the local universe, this sequence is nearly horizontal, but has been shown to evolve with redshift (Kodama et al., 1998). The scatter of the RCS in a cluster provides information about the color difference among its early-type galaxies, and its small slope indicates that more massive galaxies are more metal-rich. Indeed, this metallicity is traced by the color when covering the important spectral feature D4000, corresponding to a break at a wavelength of 4000 Å in the rest frame, given by the absorption of light caused by an accumulation of metal absorption lines in the near ultraviolet, predominantly from iron ions, which block the emission of lines beyond 4000 Å (Hamilton, 1985). Based on this fundamental relation, surveys such as the Red-Sequence Cluster Survey (RCS-1, Gladders and Yee, 2000, 2005) and the Red-Sequence Cluster Survey 2 (RCS-2, Gilbank et al., 2011) were designed, providing valuable information about the history of cluster formation and the populations that make them up, as well as obtaining accurate photometric redshifts of these systems and constraining cosmological parameters.

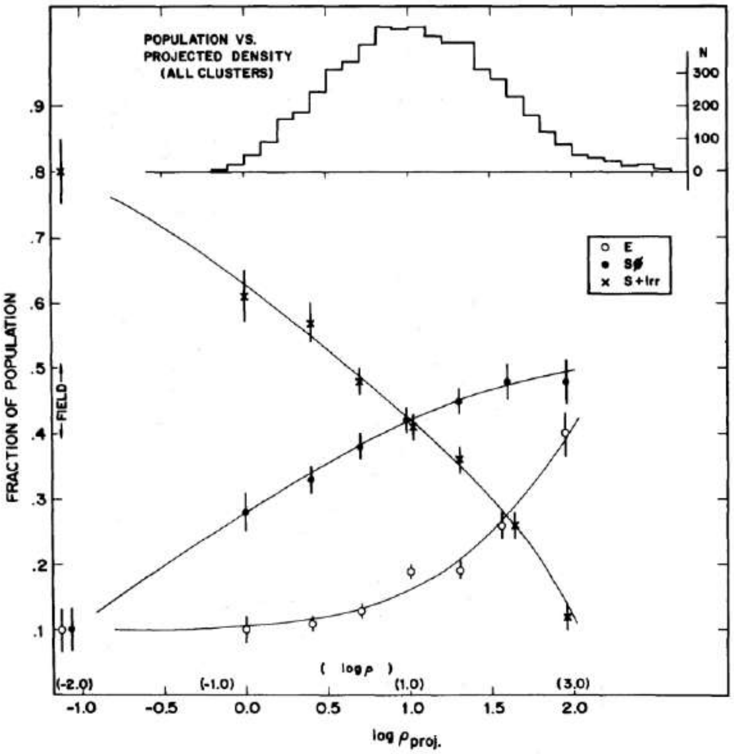

Figure 1.2: Morphology-density relation found by Dressler (1980) for galaxies in clusters and in the field. The upper histogram shows the distribution of galaxies of the projected density bins, and the main plot displays the fraction of morphological types as function of the same bins.

Dressler (1980), in his seminal article, demonstrated the existence of morphological segregation in local galaxy clusters ($z < 0.06$). In other words, different morphological types tend to be located in specific regions within these systems. On one hand, there is the morphology-density relation, where it is observed that in the denser regions of clusters, there is a higher fraction of elliptical galaxies, whereas in less dense regions, there is a higher fraction of spiral and irregular galaxies. In the case of lenticular galaxies, their fraction tends to increase in denser regions, similar to elliptical galaxies but with a less pronounced curve (Figure 1.2). Similarly, the morphology-clustercentric distance relation was found, where early-type galaxies tend to be located in the central regions of clusters, while late-type galaxies are more likely to be in the outskirts (Whitmore and Gilmore, 1991). Subsequently, Dressler et al. (1997) studied these relations at intermediate redshifts ($z \sim 0.5$), finding that the morphology-density relation appears to be more global, as it holds in all clusters, whether regular or irregular (with respect to the spatial distribution of galaxies), while the morphology-clustercentric distance relation is more prominent in regular clusters. Follow-up studies investigated these relations at even higher redshifts (e.g., Postman et al., 2005; Sazonova et al., 2020) and in hydrodynamical cosmological simulations (e.g., Teklu et al., 2017; Pfeffer et al., 2023). These works have shown that these relations begin to form at redshift $z \sim 2$ and persist until the local universe. This implies that the population of early-type galaxies forms very early in the Universe in environments that are sufficiently dense. Furthermore, it was shown that the fraction of lenticular galaxies decreases, and there is an excess of spiral and irregular galaxies at redshift $z \gtrsim 0.8$, compared to the local universe. Explanations for this include the transformation of spiral galaxies into lenticular ones through gas stripping in highly dense environments and the formation of lenticular galaxies through black hole feedback in low-density environments.

However, the relations found in clusters are associated not only with the morphology of galaxies but also with their physical properties. For example, studying the mass-size relation throughout cosmic time is crucial to trace the assembly history of galaxies (Chen et al., 2024). Considering the hierarchical formation of structures, it is natural to think that the primary factor for assembling the mass of these objects corresponds to mergers with their counterparts. However, this process is also associated with internal processes, such as the star formation rate (SFR, e.g., Ilbert et al., 2010). In fact, this latter property, often associated with the morphology of galaxies in the literature (e.g., Calvi et al., 2018), and the two aforementioned ones (mass and size), have differences not only in different regions of a galaxy cluster but also in the field (e.g., Poggianti et al., 2013; Yoon et al., 2017). In the mass-SFR parameter space, a sequence of star-forming galaxies can be found, while below them, passive or quiescent objects are observed (e.g., Noeske et al., 2007; Peng et al., 2010). On the mass-size plane, it has been shown that in different environments, mass ranges, and morphologies, the slopes of this relationship change significantly (e.g., van der Wel et al., 2014; Strazzullo et al., 2023; Chen et al., 2024).

The relationships between the physical and structural parameters of galaxies with the environments in which they are located can be explained by various physical processes occurring in dense environments. These processes can notably perturb the morphology of galaxies, generating, for example, fascinating cases of galaxies known as jellyfish (e.g., Poggianti et al., 2016).

The nature of these physical phenomena can be gravitational, hydrodynamical, or a combination of both (Boselli and Gavazzi, 2006). On the gravitational interaction side, galaxies in clusters can be affected by galaxy-galaxy interactions (Byrd and Valtonen, 1990), galaxy-cluster interactions (Valluri, 1993), and galaxy harassment (Moore et al., 1996). In the first two cases, galaxies are affected by tidal effects due to the potential wells of the involved objects, while in galaxy harassment, galaxies do not fully interact but are disturbed by high-speed encounters. On the hydrodynamic side, there are effects such as ram pressure stripping (Gunn and Gott, 1972), where galaxies can experience a removal of part of their interstellar medium due to the ram pressure exerted by the hot and dense intracluster medium (ICM); viscous stripping (Nulsen, 1982), where viscous momentum is transferred from the interstellar medium (ISM) to the intergalactic medium (IGM), causing losses of the gas reservoir and, consequently, the ability to form new stars; and thermal evaporation (Cowie and Songaila, 1977), a process in which if the temperature of the IGM is high compared to the velocity dispersion of galaxies, the gas temperature will rise, leading to evaporation and stripping of the host galaxy, combining with the IGM-ISM interface. Finally, regarding the consequences of combined effects of the previously discussed physical processes, two significant phenomena are observed: starvation/strangulation (Larson et al., 1980) and pre-processing (Zabludoff and Mulchaey, 1998). Starvation, also known as strangulation, results from gravitational and hydrodynamic processes that gradually deplete the gas reservoirs of galaxies, affecting them to a lesser extent. Pre-processing, on the other hand, refers to the accelerated evolution of galaxies within smaller systems such as groups or compact groups, and even within larger-scale structures like filaments, before they fall into the potential well of a cluster. As a result, these galaxies arrive at the cluster with diminished star formation rates or in a quenched state, and their physical and structural properties are already altered by the environmental effects of their previous locations.

1.3 Interaction of galaxy clusters

In a relaxed cluster, also known as virialized because it approximately satisfies the virial theorem, its three components (galaxies, dark matter, and intracluster medium or ICM) are in dynamic and hydrostatic equilibrium. Additionally, it is known that usually, due to dynamical friction effects, the deepest part of the potential well of these clusters contains a massive central galaxy; the brightest cluster galaxy (BCG, Tremaine, 1990). However, as explained earlier, the formation processes of these systems involve mergers and smooth accretion. In these circumstances, the equilibrium state of the clusters is affected. In the event of a merger between two massive galaxy clusters, we are dealing with the second most energetic process in the Universe after the Big Bang, releasing energy on the order of 10^{64} erg/s (Sarazin, 2002), with approximately 10% of its energy being dissipated in the ICM in the form of shocks, compression, and turbulence (Owers et al., 2014).

In such interactions, when analyzing systems on a large scale, galaxies can be considered point particles, and due to the large velocity dispersion that clusters have, the probability of collision is low. Additionally, it is inferred that dark matter is non-collisional on large scales, so in these processes, its distribution is not expected to be disturbed. On the other hand, the gas component interacts hydrodynamically, making it highly collisional and thus generating a delay in the displacement of collisional and non-collisional components when mergers occur (Massey et al., 2011).

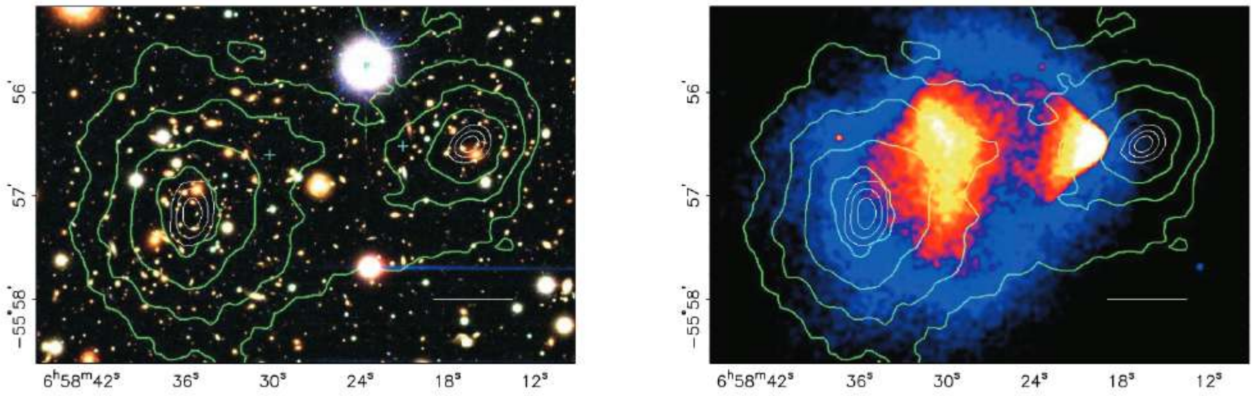

Figure 1.3: Optical (left) and X-ray (right) images of the 1E 0657-558 galaxy cluster (Bullet cluster) extracted from Clowe et al. (2006). The green contours correspond to the mass reconstruction through weak gravitational lensing, dominated by dark matter, and the white contours represent the errors in the position of the mass distribution peaks for the 68.3%, 95.5%, and 99.7% confidence levels, while the white solid line represents 200 kpc at the cluster distance. The blue plus signs show the locations of the centers of the plasma clouds (X-ray lobes).

A pioneering work that observationally demonstrated this cluster merger scenario and also provided the first direct evidence of the existence of dark matter is that of Clowe et al. (2006), where they studied 1E 0657-558, also known as the Bullet cluster. This is a distrubed galaxy cluster at redshift $z = 0.296$. Figure 1.3 shows the distribution of the total mass of the cluster (dominated by dark matter) reconstructed from weak gravitational lensing (green contours). It can be observed that galaxies are spatially distributed in a similar way to dark matter, but the gas (right panel) is completely offset. Moreover, two large lobes of galaxies, gas, and dark matter are clearly visible, supporting the cluster merger scenario. Thus, the offset between the centroid of the dark-matter distribution and the peak or centroid in X-rays serves as an approximation of the dynamic state of galaxy clusters, at least in the projected space of right ascension (RA) and declination (Dec).

However, as obtaining a massive sample of galaxy clusters with weak lensing analysis is not straightforward, the offset between the BCG and the X-ray peak or centroid can be used as a proxy for the dynamical state (e.g., Mann and Ebeling, 2012). This is because the BCG is considered a proxy for the non-collisional component, since it is expected that dark matter and galaxies move together during a merger. Additionally, as mentioned earlier, the BCG is located in the deepest region of the cluster gravitational potential well.

In addition to the dynamical state approximation involving optical and X-ray observations, these systems can also be classified using radio images (Cassano et al., 2010), utilizing the galaxy density distribution of the cluster (e.g., Wen and Han, 2015), and the X-ray surface brightness distribution (e.g., Jeltema et al., 2005; Nurgaliev et al., 2013). Similarly, to identify mergers of galaxy clusters along the line of sight, the shape of the velocity distribution can also be used as a proxy (e.g., Ribeiro et al., 2013; de Los Rios et al., 2016).

It has been determined that the impact of galaxy cluster mergers on their member galaxies is crucial for their evolution. For example, during these processes, galaxies can undergo extreme ram pressure stripping, significantly distorting their morphologies (e.g., Owers et al., 2012; Poggianti et al., 2016). Additionally, significant episodes of star formation can be triggered in galaxies (e.g., Stroe et al., 2017; Hernández-Lang et al., 2022) or, conversely, their star formation rates can be reduced (e.g., Mansheim et al., 2017). Currently, studies of interacting clusters range from a few dozen with the image quality of the Hubble Space Telescope (*HST*) (e.g., Harvey et al., 2015; Vulcani et al., 2023b) to thousands using surveys with lower image quality (e.g., Wen and Han, 2015; Tempel et al., 2017; Zenteno et al., 2020). Still, only a small fraction of them conducted a detailed study with a large sample of clusters on the impact of mergers on their populations.

One of the main motivations for this work comes from the results obtained by Zenteno et al. (2020). In that article, they estimate the dynamical state of 288 massive galaxy clusters within the redshift range $0.1 \lesssim z \lesssim 0.9$ using optical, X-ray, and microwave (SZ effect) information. They found that the galaxy luminosity function of disturbed clusters has a steeper faint-end slope α, with a brighter characteristic magnitude m^* than relaxed systems. Exploring different redshift ranges, they observed that the differences between relaxed and disturbed clusters become significant at redshift $z \gtrsim 0.55$. Furthermore, Aldás et al. (2023) found similar results regarding dynamics and redshift range, but this time using color-magnitude diagrams (CMDs) of the clusters. At low redshift, there is complete agreement between the characteristics of CMDs in relaxed and disturbed clusters, while at high redshift, disturbed clusters exhibit greater dispersion in the red sequence and a broader distribution of blue galaxies compared to relaxed systems.

1.4 Thesis goals

In this thesis, we evaluate the dynamical state of 87 massive galaxy clusters ($M_{500} \geq 1.5 \times 10^{14} M_{\odot}$) in the redshift range of $0.10 < z < 0.35$ and analyze their impact on the physical and structural properties of their member galaxies. The sample consists of galaxy clusters from the XMM-Newton and Chandra archives, including structures detected through optical observations (Abell, WHL), the SZ-effect in microwaves (SPT, ACT, Planck), and X-ray detections (RBS, RM, RXC).

The sample has deep optical images from the DESI Legacy Imaging Survey, which covers > 20,000 square degrees of the sky, carefully selected to include data in the g, r, i, and z bands of the Dark Energy Camera (DECam).

Here, we use X-ray, optical, and infrared data to address the following question: Does the dynamical state of galaxy clusters affect the morphological and physical properties of their member galaxies, and their fundamental relations at low redshift ($0.10 < z < 0.35$)? Investigating this relationship is crucial because it can shed light on the evolutionary processes that affect galaxy evolution within these clusters (e.g., Perez et al., 2009). Specifically, it can help clarify how interactions and environmental factors within clusters contribute to galaxy formation and evolution (e.g., Boselli and Gavazzi, 2006). This understanding is important for constructing more accurate models of galaxy behavior and cluster dynamics (e.g., Contreras et al., 2013). To answer it, we propose the following objectives:

- Identify member galaxies of galaxy clusters using a method that employs photometric redshift, quantifying its completeness and contamination.
- Classify the morphological type of galaxies using both parametric and non-parametric methods on DECam images with physical resolution greater than 1 kpc.
- Derive the physical properties of galaxies using spectral energy distribution (SED) fitting techniques with photometric data in the optical and infrared.
- Determine the dynamical state of galaxy clusters using different proxies across optical and X-ray wavelengths.

- Compare the physical and morphological properties of relaxed and disturbed cluster populations.

This thesis is organized as follows. In Chapter 2, we describe the nature of optical/infrared (photometry and spectroscopy) and X-ray data, as well as detail the sample selection. In Chapter 3, we describe the methods used to estimate the dynamical states of the clusters, determine their dynamic properties, and calculate the physical and structural properties of the galaxies. In Chapter 4 we present the results after applying those methods. Finally, in Chapter 5, we discuss the results and present the conclusions of the entire study in Chapter 6.

In this work, we adopt a Flat ΛCDM cosmology, asumming $H_0 = 69.3$ km s^{-1}, $\Omega_\Lambda = 0.721$ and $\Omega_m = 0.287$ (Hinshaw et al., 2013, WMAP-Y9).

Chapter 2

Data

In this chapter, we outline all the details concerning the data used in this thesis. We begin by describing the optical images that we use, which come primarily from the DESI Legacy Imaging Survey. Then, we explain the X-ray archive processed images and catalogs. Subsequently, we specify the content and source of the photometric and spectroscopic catalogs. Finally, we present the sample selection process for the study.

2.1 Optical images and catalogs

Legacy Surveys Data Release 10 (here after, LS DR10) is the result of the combined efforts of three different surveys that provide images and catalogs, initially planned for the g, r, and z filters. On one hand, there are surveys in the northern hemisphere ($\delta \gtrsim 32$); these include the Beijing Arizona Sky Survey, which provides photometric information in the g and r filters using the Bok 2.3m telescope (BASS, Zou et al., 2017), and the Mayall z-band Legacy Survey, which delivers data solely in the z filter using the 4m Mayall telescope (MzLS, Silva et al., 2016). On the other hand, for the southern hemisphere, there is the Dark Energy Camera Legacy Survey (DECaLS, Blum et al., 2016), observing in the g, r, and z filters through the 4m Blanco Telescope. It is worth mentioning that DECaLS is primarily composed of data from the Dark Energy Survey (DES, The Dark Energy Survey Collaboration, 2005), with the rest coming from public data of DECam, available in the online repository of NSF's National Optical-Infrared Astronomy Research Laboratory (NOIRLab)[1]. Among these programs, most notably are the DECam Local Volume Exploration Survey (DELVE; Drlica-Wagner et al., 2022) and the DECam eROSITA Survey (DeROSITAS; PI: A. Zenteno). The initial goal of LS was to select targets for the forthcoming DESI spectroscopic survey, with its spectrograph set to be

---

[1] https://noirlab.edu/public/projects/astrodataarchive/

installed on the 4m Mayall telescope, where MzLS is conducted.

The LS DR10 covers more than 20,000 square degrees of the sky, with the three surveys having similar design properties. They are typically at least ~ 1 magnitude deeper than the Panoramic Survey Telescope and Rapid Response System (Pan-STARRS) 3π Steradian Survey (Chambers et al., 2016) in each filter, achieving a uniform depth of 5σ at $m_g = 24.7$, $m_r = 23.9$, and $m_z = 23.0$ (Duncan, 2022).

All images in the LS DR10 are presented in “bricks”, which are regions of the sky measuring $0.25^\circ \times 0.25^\circ$, defined in terms of RA and Dec coordinates, with some degree of overlap. All of these data are publicly available on the National Energy Research Scientific Computer Center (NERSC) portal, access to which can be found on the official LS DR10 website[2]. Taking this into account, we develop Python codes that efficiently allow us to download the bricks corresponding to the area of interest for each cluster in our sample (see Section 2.5) and then join them.

Regarding the catalogs, we download the data from LS DR10 using Python codes that query the NOIRLab AstroDataLab portal[3]. We conduct a cone search centered on the X-ray peak with a radius of R_{200} for each cluster. The astrometry of these catalogs is tied directly to the Gaia Data Release 2, with astrometric residuals typically smaller than $0.03''$. Source detection in this survey was performed using `The Tractor` (Lang et al., 2016). This code employs a probabilistic method to fit models to the sources present in an image. These models can be point sources (PSF), round exponential galaxies with variable radius (REX), de Vaucouleurs (DEV) profiles (elliptical galaxies), exponential (EXP) profiles (spiral galaxies), and Sersic (SER) profiles, and these are fitted by means of a χ^2 minimization problem. Full details regarding calibrations, source detection, and photometry are available in Dey et al. (2019, and references therein).

2.2 X-ray images and catalogs

The X-ray images used in this study were obtained from the Chandra and XMM-Newton archives. However, these images have been downloaded, processed, and made available to the scientific community through online repositories by other authors. Specifically, Yuan and Han (2020) initiated their project with the aim of evaluating the dynamical state of galaxy clusters based on the distribution of the X-ray surface brightness, revealing the behavior of ICM in these systems. In their study, they explain that the Chandra satellite has observed approximately 1,000 galaxy clusters, and the high resolution of its images is ideal for detecting substructures in the ICM. They processed the data from these systems by filtering photons with energies in the

---

[2] `https://www.legacysurvey.org/`

[3] `https://datalab.noirlab.edu`

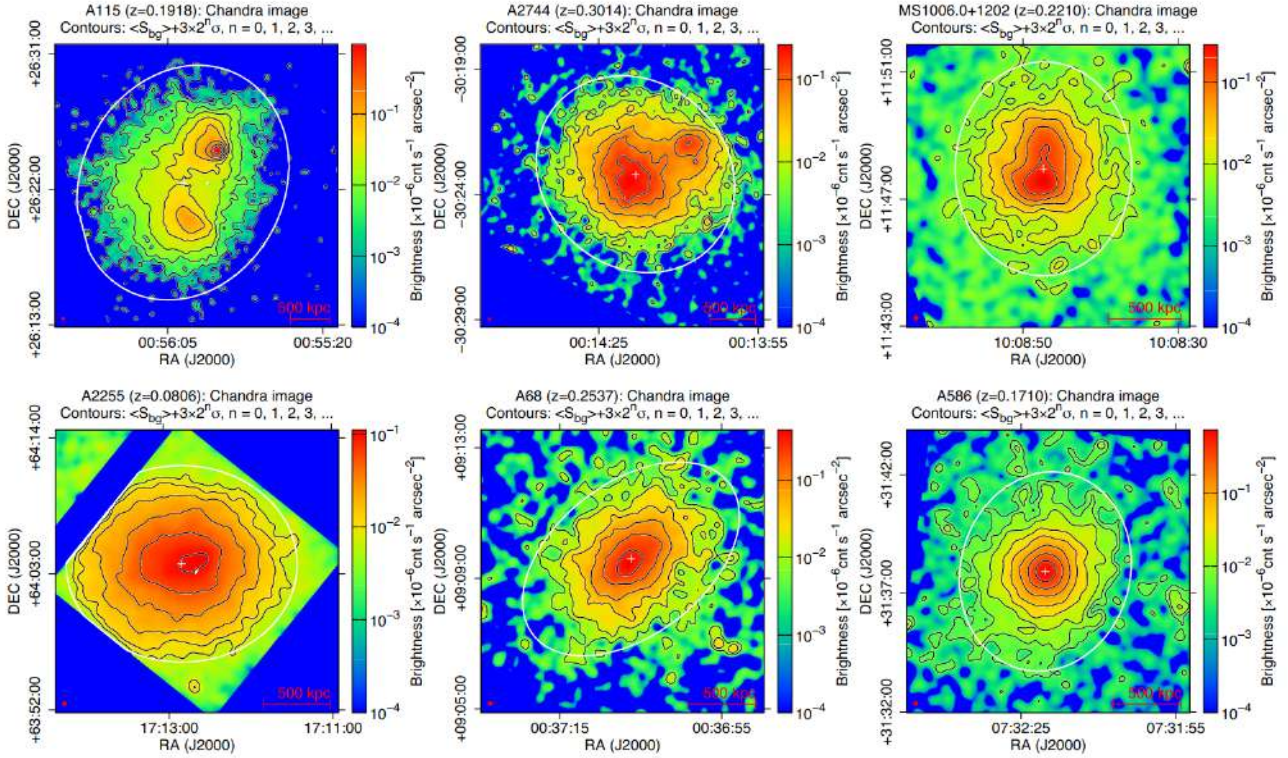

Figure 2.1: Example of the processed X-ray images given by Yuan and Han (2020). On the top of each panel, the cluster name, redshift and contour levels are specified. The colour bar on the right of each panel indicates the logarithmic surface brightness. The white cross and ellipse are the centre and the ellipse of the best-fitting model that they used in their work. The red circle in the bottom left corner of each panel indicates the smooth scale generally with 30 kpc of diameter, and the scale of 500 kpc is plotted on the bottom right corner to show the physical scale of every cluster.

Table 2.1: Dynamical parameters for the first 10 clusters extracted from Yuan et al. (2022).

Name (1)	obsID (2)	RA (3)	Dec (4)	z (5)	$\log_{10}(c)$ (6)	$\log_{10}(w)$ (7)	$\log_{10}(P_3/P_0)$ (8)	κ (9)	$\log_{10}(\alpha)$ (10)	δ (11)
RXCJ0000.1+0816	0741581501	0.02958	8.27444	0.0396	-0.14±0.01	-4.04±0.08	-6.50±0.01	0.89	-2.46±0.01	-0.81±0.01
A2690	0125310101	0.09120	-25.13822	0.0840	-0.60±0.01	-1.86±0.02	-6.66±0.05	2.54	-1.33±0.01	1.16±0.01
XMMXCSJ0002-3556	0145020201	0.56708	-35.94272	0.7704	-0.64±0.03	-1.41±0.03	-5.81±0.11	2.45	-1.19±0.01	1.19±0.01
A2715	0655300101	0.68944	-34.67154	0.1160	-0.76±0.01	-1.52±0.01	-5.64±0.03	2.30	-0.55±0.01	1.51±0.01
A2697	0145020201	0.79826	-6.09169	0.2484	-0.66±0.02	-2.38±0.02	-6.67±0.13	1.11	-1.90±0.01	-0.27±0.01
A2717	0145020201	0.80042	-35.92722	0.0490	-0.39±0.01	-3.32±0.01	-7.54±0.05	1.03	-1.93±0.01	-0.35±0.01
A2700	0201900101	0.96083	2.06333	0.0924	-0.51±0.01	-3.05±0.03	-7.88±0.10	1.40	-2.29±0.01	-0.33±0.01
ZGXJ000402-355635	0145020201	1.00742	-35.94317	0.4974	-0.58±0.04	-2.12±0.05	-6.15±0.13	2.17	-1.42±0.01	0.83±0.01
WHLJ000524+161309	0783270101	1.35000	16.21917	0.1160	-0.73±0.01	-1.66±0.01	-6.62±0.03	2.05	-1.39±0.01	0.76±0.01
A2734	0675470801	2.83625	-28.85500	0.0625	-0.63±0.01	-2.66±0.03	-6.72±0.02	1.85	-1.37±0.01	0.62±0.01

Notes. Columns: (1) galaxy cluster name; (2) XMM-Newton observation ID; (3-4) right ascension and declination in J2000; (5) redshift; (6) concentration index; (7) centroid shift; (8) power ratio; (9) profile parameter; (10) asymmetry factor; (11) morphology index.

0.5−5.0 keV band, carefully removing flares and point sources, and smoothing the images with a Gaussian function at a physical scale of 30 kpc. Initially, these scales varied for each cluster because of their different redshifts. Examples of the final results can be seen in Figure 2.1. They processed a total of 964 clusters, and both the images and catalogs of dynamical parameters derived from them can be found in the authors' web page repository[4]. Subsequently, Yuan et al. (2022) expanded the sample by including data from the XMM-Newton archive and adding 22 new Chandra clusters observed in the time period separating their two studies. The processing of the X-ray images remained exactly the same for consistency, resulting in images and dynamical parameters for 1,308 new galaxy clusters[5].

The aforementioned catalogs are also available in the same Web repositories. An illustration of their content can be seen in Table 2.1. These catalogs contain classic dynamical parameters such as the concentration index (Santos et al., 2008), the centroid shift (Poole et al., 2006), and the power ratio P_3/P_0 (Buote and Tsai, 1995). Moreover, they included a new morphological parameter to estimate the dynamical state: δ. A detailed description of this parameter is provided in Section 3.4.1.

2.3 Cluster catalog and photometric redshifts

Using data from the DES and the Wide-field Infrared Survey Explorer (WISE, Wright et al., 2010), Wen and Han (2022) estimated photometric redshifts for 105 million galaxies, identifying 151,244 galaxy clusters within the redshift range of $0.1 < z < 1.5$. The algorithms used are extensively outlined in their previous work (Wen and Han, 2021). In summary, they

---

[4] `http://zmtt.bao.ac.cn/galaxy_clusters/dyXimages/chandra.html`

[5] `http://zmtt.bao.ac.cn/galaxy_clusters/dyXimages/newton.html`

used publicly available DES DR2 data in the $grizY$ bands and data from the WISE five-year co-added image, also known as unWISE, in the $W1$ and $W2$ filters, to estimate the photometric redshifts. The data matching between both databases comprised 105 million objects.

Subsequently, photometric redshifts were derived on the basis of the colors and using the k-nearest neighbors algorithm with respect to the spectroscopic redshifts of a robust training sample. Specifically, the distances of the target galaxies to obtain their photometric redshifts in the color space ($g - r$, $r - i$, $i - z$, $z - y$, $i - W1$, and $W1 - W2$) to all galaxies in a training sample (galaxies with spectroscopic redshifts) were calculated, selecting the 20 nearest neighbors. The photometric redshifts were then calculated as the median value of these 20 galaxies with spectroscopic redshifts, and the error was computed as the standard deviation among these redshifts. This methodology is based on the premise that the color of galaxies is tightly related to their redshift when it covers spectral features such as the 4000 Å break or the Balmer jump. Galaxies located closely in multidimensional color space generally have similar redshifts (Wen and Han, 2021).

Regarding cluster identification, the authors also computed the stellar masses of galaxies using scaling relations with luminosity in the unWISE $W1$ band, following the procedures described in their previous work (Wen and Han, 2021). Then, the overdensities around each massive galaxy with $M_* \geq 5 \times 10^{10}$ $\mathrm{M}_\odot$ (at redshift z) were searched within the photometric redshift slice of $z \pm \Delta z$ and the radius of r_1 (defined below). The signal-to-noise ratio (SNR) of the overdensity of cluster galaxies was calculated as follows:

$$\mathrm{SNR} = (m_{\mathrm{stellar},0.5} - \langle m_{\mathrm{stellar},0.5} \rangle)/\sigma_{m_{\mathrm{stellar},0.5}}, \tag{2.1}$$

where $m_{\mathrm{stellar},0.5}$ is the sum of the stellar mass of member galaxy candidates within a projected radius of 0.5 Mpc from the BCG, $\langle m_{\mathrm{stellar},0.5} \rangle$ is the local background, and $\sigma_{m_{\mathrm{stellar},0.5}}$ is the fluctuation of the stellar mass within the same redshift slice.

From all the candidate member galaxies, R_{500} was obtained using a scaling relation:

$$\log R_{500} = 0.40 \log m_{\mathrm{stellar,r1}} - (0.96 \pm 0.03) + (0.33 \pm 0.12) \log(1 + z), \tag{2.2}$$

where $m_{\mathrm{stellar,r1}}$ is the total stellar mass within $r_1 = 1.0E(z)^{-2/3}$ Mpc, with the normalized Hubble function $E(z) = \sqrt{\Omega_\Lambda + \Omega_m(1 + z)^3}$.

Then, the total mass within R_{500} was computed as:

$$\log M_{500} = 0.96 \log m_{\mathrm{stellar},500} - (1.86 \pm 0.07) + (0.20 \pm 0.31) \log(1 + z), \tag{2.3}$$

where $m_{\text{stellar},500}$ is the total stellar mass within the recently defined R_{500}. Subsequently, the cluster richness within R_{500} was determined using:

$$\lambda_{500} = m_{\text{stellar},500}(1+z)^{0.21}/m^{*}_{\text{stellar}}, \tag{2.4}$$

where $m^{*}_{\text{stellar}} \sim 4 \times 10^{10}$ $\text{M}_{\odot}$ is the mean stellar mass of a galaxy with the luminosity of L^{*} at $z \sim 0.1$.

Hence, a cluster is identified with a threshold of SNR ≥ 0.5, a richness of $\lambda \geq 15$, and also a number of candidate member galaxies $N_{\text{gal}} \geq 6$.

As a result, these catalogs are publicly available in the authors' Web repository[6], and we show an example in Table 2.2. These catalogs encompass data for individual galaxies, identified clusters, and galaxies identified as potential cluster members based on their photometric redshift calculations.

Table 2.2: Clusters of galaxies identified from the DES×unWISE data extracted from Wen and Han (2022).

Cluster ID (1)	Name (2)	RA (3)	Dec (4)	z_{cl} (5)	i_{BCG} (6)	W1$_{BCG}$ (7)	SNR (8)	R_{500} (9)	λ_{500} (10)	M_{500} (11)	N_{gal} (12)	Other catalogs (13)
1	WH J000000.5+021911	0.00200	2.31979	0.4192	18.738	17.964	6.75	0.549	18.77	0.86	15	WH21
2	WH J000001.3-640959	0.00555	-64.16639	0.6423	18.565	17.360	10.17	0.673	36.48	1.62	12	
3	WH J000001.4-521956	0.00563	-52.33236	0.5829	19.249	18.207	6.00	0.590	21.61	0.98	12	redMaPPer
4	WH J000002.3-475113	0.00943	-47.85358	0.7734	20.239	18.481	5.48	0.487	17.47	0.80	13	CFSFDP
5	WH J000002.8-474415	0.01186	-47.73740	0.3169	17.305	17.307	7.53	0.548	17.18	0.79	11	
6	WH J000003.1-033245	0.01274	-3.54574	0.6056	18.754	17.483	14.00	0.722	43.60	1.92	22	WHL
7	WH J000003.8-010154	0.01592	-1.03153	0.7327	19.759	18.242	6.06	0.621	26.65	1.20	10	WaZP
8	WH J000003.9-525115	0.01610	-52.85407	0.7657	20.561	18.513	6.34	0.559	20.93	0.95	12	
9	WH J000004.2-393257	0.01733	-39.54926	0.6064	19.742	18.163	6.69	0.542	20.50	0.93	13	CFSFDP
10	WH J000004.2+021941	0.01742	2.32799	0.6228	19.247	17.721	6.47	0.541	20.33	0.92	9	WHL

Notes. Columns: (1) cluster ID; (2) cluster name with J2000 coordinates; (3-4) right ascension and declination in J2000; (5) redshift; (6)-(7) BCG magnitudes in i and W1 bands, respectively; (8) SNR for cluster detection; (9) R_{500} radius in Mpc; (10) richness; (11) derived M_{500} mass in units of 10^{14} $\text{M}_{\odot}$; (12) number of galaxy candidates within R_{500}; (13) reference for previously known clusters (see details in Wen and Han (2022)).

2.4 Spectroscopic redshift catalogs

In order to assess the reliability of the photometric redshifts for the galaxies that are specifically part of our sample and calibrate the membership assignation method, we conduct a comprehensive bibliographic research to identify clusters with spectroscopically confirmed member catalogs. The cluster selection process is detailed in Section 2.5, and Table 2.3 displays the sources from which the catalogs were obtained.

---

[6] `http://zmtt.bao.ac.cn/galaxy_clusters/catalogs.html`

Table 2.3: Galaxy clusters with spectroscopic redshifts available in the literature and databases.

Cluster	References
Abell 222	Proust et al. (2000)
Abell 223	Proust et al. (2000)
Abell 267	Rines et al. (2013); Tucker et al. (2017)
Abell 383	Geller et al. (2014)
Abell 402	Richard et al. (2021)
Abell 2537	Braglia et al. (2009)
Abell 2631	Rines et al. (2013)
Abell 2744	Braglia et al. (2009); Owers et al. (2011); Richard et al. (2021)
Abell 2813	Guzzo et al. (2009)
Abell 3088	Guzzo et al. (2009)
Abell 3364	Guzzo et al. (2009)
Abell 3378	Guzzo et al. (2009)
Abell 3739	Guzzo et al. (2009)
Abell 3827	Carrasco and Verdugo (2018)
Abell S295	Ruel et al. (2014); Bayliss et al. (2016)
Abell S520	Guzzo et al. (2009); Foëx et al. (2017)
Abell S579	Guzzo et al. (2009)
Abell S1063	Mercurio et al. (2021)
ACT-CLJ0235-5121	Sifón et al. (2016)
RBS 1748	Sifón et al. (2016)
RXC J0117.8-5455	Guzzo et al. (2009)
RXC J0220.9-3829	Guzzo et al. (2009)
RXC J0528.2-2942	Guzzo et al. (2009)
RXC J0532.9-3701	Guzzo et al. (2009)
RXC J2011.3-5725	Guzzo et al. (2009)
RXC J2023.4-5535	Guzzo et al. (2009)
SPT-CLJ0106-5943	Bayliss et al. (2016)
SPT-CLJ0348-4514	Bayliss et al. (2016)
SPT-CLJ2032-5627	Ruel et al. (2014)
SPT-CLJ2130-6458	Ruel et al. (2014)
SPT-CLJ2138-6007	Ruel et al. (2014)
ZwCl 2341.1+0000	Boschin et al. (2013)

2.5 Sample selection

If we aim to explore the effect of the dynamical state of clusters on the structural and physical properties of their member galaxies, it is crucial to have a robust and homogeneous sample. To achieve this, we perform a cross-match with a 2-arcminute radius between the galaxy clusters identified through clustering algorithms and estimated photometric redshifts by Wen and Han (2022), and the clusters found in the Chandra (Yuan and Han, 2020) and XMM-Newton (Yuan et al., 2022) X-ray catalogs, resulting in 471 systems.

We select the galaxy clusters that are in the redshift range of $0.10 < z < 0.35$, resulting in 152 clusters. At this point, Abell 3827 is added, which is at $z \sim 0.099$, and we have access to spectroscopic information. The reason for choosing the lower limit is due to the extensive spatial coverage required for nearby clusters. As for the upper limit, we rely on the work of de Albernaz Ferreira and Ferrari (2018), which demonstrated that reliable morphological studies can be conducted using DECam up to $z \sim 0.4$. However, we decide to be conservative and study up to the mentioned limit. Furthermore, within this interval, we ensure that we cover the 4000 Å break using the $(g - r)$ color index to separate early-type red galaxies from star-forming objects (e.g. Bruzual A., 1983; Nilo Castellón et al., 2014). Moreover, within this redshift range, the LS DR10 achieves enough photometric depth to conduct homogeneous studies up to three magnitudes fainter than the characteristic magnitude $(m^* + 3)$ of all clusters in the sample. This characteristic magnitude corresponds to the knee of the galaxy luminosity function, and it is modelled using composite stellar population (CSP) models. More details about this are found in Section 3.2.

Subsequently, to ensure that the matching of clusters between optical and X-ray databases is not affected by projection effects, we impose the condition that $z_{\mathrm{x}} - z_{\mathrm{phot}}/(1 + z_x) \leq 0.05$, where z_{x} is the redshift found in the X-ray catalogs of Yuan and Han (2020) and Yuan et al. (2022)[7], while z_{phot} is the photometric redshift estimated for the clusters identified in the optical by Wen and Han (2022), resulting in 119 galaxy clusters.

Next, we remove from the sample all systems that are very poor and low-mass by applying the condition $\lambda \geq 30$ and $M_{500} \geq 1.5 \times 10^{14} M_{\odot}$, where λ is the cluster richness estimated based on overdensities and fluctuations in the field, and M_{500} is the mass of the clusters estimated within R_{500}. This selection is made by observing the distributions of both parameters for the 119 galaxy clusters (see Figure 2.2). The respective peaks are close to the chosen thresholds, suggesting that with this criterion, we are selecting rich and massive systems with high completeness. Here

---

[7] The redshifts listed in these catalogs are the "best redshifts" found in the literature and databases such as NED. In some cases, the redshifts are spectroscopic, while in others, they are photometric.

we obtain 90 clusters of galaxies.

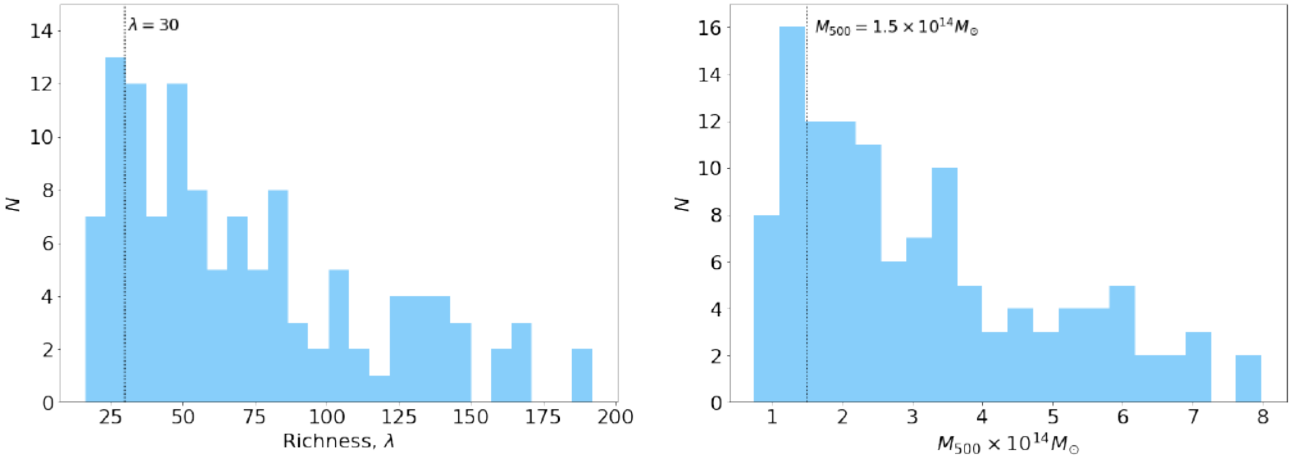

Figure 2.2: Richness λ (left) and mass M_{500} (right) distributions for the 119 galaxy clusters pre-selected at this point. The vertical black dotted lines denotes the peaks of the distributions.

Finally, we exclude from the sample, via visual inspection, all systems with field contamination due to a saturated star or lack of photometric information in the LS DR10 catalogs. Our final sample consists of 87 massive galaxy clusters (Table A.1).

Chapter 3

Analysis

3.1 Cluster membership

The most unequivocal way to select member galaxies of a cluster is by using spectroscopic redshifts. However, for our sample, less than half of the clusters have catalogs of this nature available in the literature or databases such as NASA/IPAC Extragalactic Database (NED) or Vizier. Additionally, there is the difficulty that the few systems with this information do not share the same observational designs. For example, some systems have more than 1,000 galaxies in the field with spectroscopic information due to the use of integral field spectroscopy (e.g., Mercurio et al., 2021), while others have fewer than 20 objects due to the use of slit or multi-object spectroscopy, mainly selecting galaxies that are on the Red Sequences in the CMDs of the clusters (e.g., Bayliss et al., 2016). These differences can directly affect sample analyses, leading to biased results due to inhomogeneities. However, this can be addressed by homogeneously assigning membership to the entire sample using photometric redshifts.

In this way, we follow a probabilistic method whose foundations were established by Brunner and Lubin (2000) and later developed by Pelló et al. (2009). The method consists of calculating the probability P_{member} that a galaxy is a member of a cluster at redshift z_{cl} within a redshift slice δ_z.

$$P_{\mathrm{member}} = \int_{z_{\mathrm{cl}}-\delta_z}^{z_{\mathrm{cl}}+\delta_z} P(z)\, dz. \tag{3.1}$$

To define the redshift slice, we follow Kesebonye et al. (2023), where they used $\delta_z = n\sigma_{\mathrm{bw}}(1+z_{\mathrm{cl}})$, with $n = 2$. To determine σ_{bw}, we use all galaxies with available spectroscopic redshifts (see Table 2.3) to compare them with photometric redshifts, obtaining a mean residual of $(z_{\mathrm{spec}} - z_{\mathrm{phot}})/(1 + z_{\mathrm{spec}}) = 0.008$. The robust biweight scale estimator (Beers et al., 1990) resulted in $\sigma_{\mathrm{bw}} = 0.02$.

$P(z)$ is the galaxy photometric redshift probability distribution in this context. This distribution has been discussed in the literature, which does not have to be Gaussian; instead, it can have multiple peaks or extended tails (Pelló et al., 2009). For this reason, in other works, the photometric redshift distributions provided as output in codes that calculate this value have been used. These distributions are usually obtained using algorithms that involve fitting SEDs to a library of templates (e.g., Arnouts et al., 1999; Ilbert et al., 2006; Hilton et al., 2018). However, we do not have access to this information; we only have the photometric redshift information and its corresponding error. Thus, we approximate this distribution as a Gaussian with median $\mu = z_{\mathrm{phot}}$ and standard deviation $\sigma = z_{\mathrm{phot,err}}$. While we recognize the mentioned disadvantages, at least we consider the measurement error, and it is feasible to apply this probabilistic method instead of making a simple selection within a photometric redshift slice.

The method requires a calibration of P_{member} with spectroscopic data, which, in turn, allows the calculation of the completeness of cluster member galaxies and contamination by field galaxies. This calibration is performed using clusters that have spectroscopic redshifts for a large number of both member and field galaxies, specifically Abell 267, Abell 383, Abell 2537, Abell 2631, Abell 2744, Abell S1063, and RBS 1748. Spectroscopically confirmed member galaxies are calculated using $|z_{\mathrm{cl}} - z_{\mathrm{spec}}| < 3\sigma_{\mathrm{cl}}(1 + z_{\mathrm{cl}})$, where σ_{cl} is the velocity dispersion of the cluster. More details about the spectroscopic membership method are found in Section 3.3.2.

We identify a total of 1,041 member galaxies and 1,328 galaxies that do not belong to the mentioned clusters. In Figure 3.1, the completeness and contamination fractions can be observed for a range of $P_{\mathrm{threshold}}$ values. We explore 100 variations for this parameter, from 0 to 1, in steps of 0.01. With this calibration, we decide to use the value of $P_{\mathrm{threshold}} = 0.65$, as this ensures completeness of at least 80% and contamination below 25%.

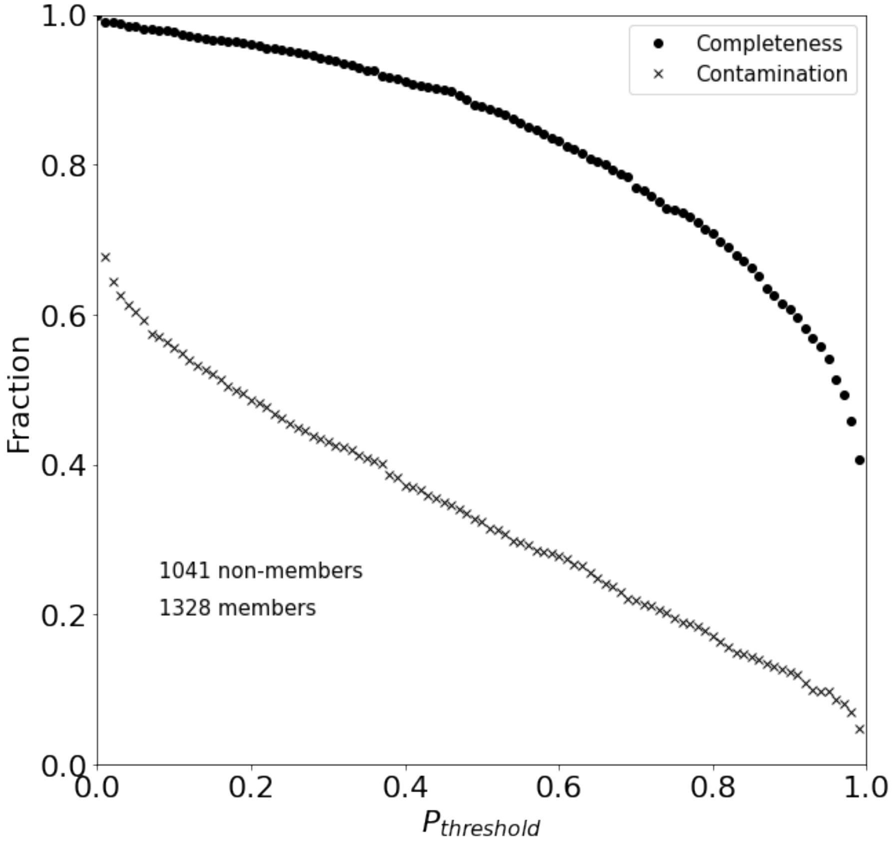

Figure 3.1: Fraction of retained members (completeness, black dots) and non-members (contamination, gray crosses) as function of the probability threshold $P_{\text{threshold}}$. This plot was created using only galaxies with secure z_{spec} measurements in clusters with enough spectroscopic data for members and the field.

3.2 BCG selection

The identification of the Brightest Cluster Galaxy (BCG) holds great importance for estimating the dynamical state of galaxy clusters. In this work, the BCG is selected using a combination of an automatic method and visual inspection.

The automatic method involves selecting the brightest cluster member galaxy within $\pm 1\sigma$ of the best fit to the red cluster sequence in the normalized color-magnitude diagram of each galaxy cluster. This process is conducted as follows. First, we determine the characteristic magnitude m^* for each galaxy cluster using the Python package EzGal (Mancone and Gonzalez, 2012), which allows us to generate observational parameters for any arbitrary stellar population synthesis (SPS) model. Specifically, we calculate m^* as a function of redshift for the DECam *griz* filters using the Bruzual and Charlot (2003) synthesis models, assuming a single burst of star formation at $z = 3$ followed by passive evolution to $z = 0$. This decision is supported by several works that have shown that the evolution of m^* can be well described using this method (e.g., de Propris et al., 1999, 2007; Mancone et al., 2010), and has been probed in massive clusters within the $0 < z < 1$ redshift range (Zenteno et al., 2016, 2020). Next, we define normalized magnitudes as

$$m_{\rm norm} = m - m^*, \tag{3.2}$$

where m is the magnitude of each galaxy. This allows us to compare the color-magnitude diagrams of galaxy clusters despite differences in redshift, as we consider the cluster redshift and K-corrections in the applied models. Note that we are inherently defining normalized colors, which essentially correspond to the subtraction of two normalized magnitudes.

Subsequently, we fit a double Gaussian model to the normalized color distribution $(g-r)_{\rm norm}$ of each galaxy cluster. This is based on the well-known bimodal color distribution in the member galaxies of these systems, featuring both the blue cloud and the red sequence (e.g., Baldry et al., 2004; Balogh et al., 2004; Menci et al., 2005). We define the *red_limit* as $\mu_{\rm red} - 3\sigma_{\rm red}$, where $\mu_{\rm red}$ and $\sigma_{\rm red}$ correspond to the mean value and standard deviation of the Gaussian fitted to the red component, respectively. An example of these double Gaussian fittings for a cluster from each dynamical state is shown in Figure 3.2.

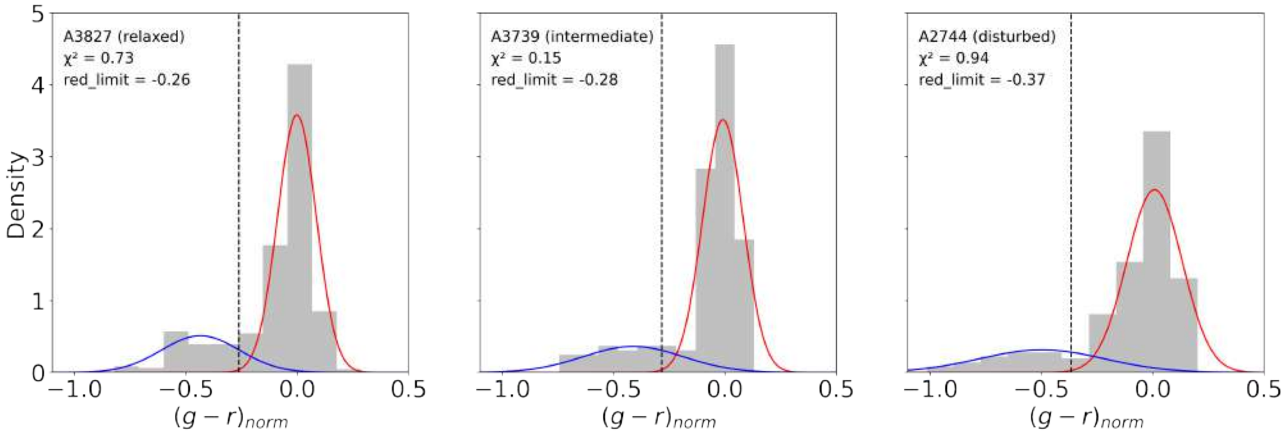

Figure 3.2: Double Gaussian fits applied to the color distribution of each cluster. From left to right, Abell 3827 (relaxed cluster), Abell 3739 (intermediate cluster), and Abell 2744 (disturbed cluster) are presented. The details of the classification of their dynamical states are found in Section 3.4. The red and blue Gaussians correspond to the components of the red sequence and the blue cloud, respectively. The vertical black dashed line indicates the `red_limit` in each panel. The specific value of this measure is located in the upper right corner of each panel along with the χ^2 statistic for each fit performed with `lmfit`.

Subsequently, selecting galaxies with a color $g - r \geq$ *red_limit*, a robust linear model was employed using the HuberRegressor (Pedregosa et al., 2011) to fit the red sequence (Figure 3.3).

This regression model has the advantage of being less influenced by the presence of outliers. To achieve this, the sample is divided into two groups, with inliers being those having an absolute error smaller than a certain threshold. Those not meeting this condition are considered outliers and given less weight.

Specifically, HuberRegressor optimizes the squared loss for the sub-sample where $|(y-Xw-c)/\sigma| < \epsilon$ (inliers) and the absolute loss for the sub-sample where $|(y-Xw-c)/\sigma| > \epsilon$ (outliers), where the model coefficient w, intercept c, and scale σ are the parameters to optimize. To achieve a 95% statistical efficiency, this threshold "ϵ" was set to 1.35.

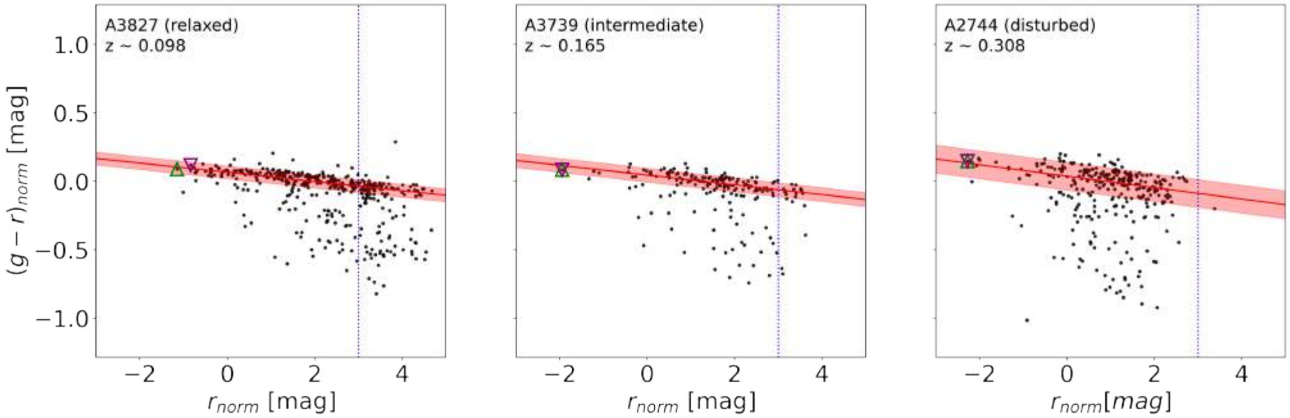

Figure 3.3: Normalized color-magnitude diagrams for the clusters mentioned in Figure 3.2. Black dots correspond to galaxies selected as members using the probabilistic method with photometric redshifts. Green triangles represent galaxies pre-selected as BCGs using the automated method, while purple inverted triangles denote visually confirmed BCGs. The solid red lines represent the best fits of the red sequences calculated with Huber Regressor, and the red shaded areas are the 1σ regions of the fits. The vertical blue dashed lines indicate the magnitude limit for studying physical and structural properties, i.e., $m^* + 3$, where m^* is the characteristic magnitude of each cluster.

The brightest galaxies of each cluster were selected as BCG candidates within 1σ of the best fit of their respective red sequences.

Finally, we visually inspected the BCGs to confirm that the selection is correct. To do this, we followed the approach of Zenteno et al. (2020), considering several properties, including size, colors, the number of neighboring galaxies, and their proximity to X-ray peaks.

3.3 Cluster properties

In this section we explain how we calculate the fundamental properties of galaxy clusters (i.e., R_{200} and M_{200}) and we detail in the selection of spectroscopic members and the computation of velocity dispersion for the clusters used for the calibration of the probabilistic membership method.

3.3.1 Fundamental properties

The galaxy cluster catalog from Wen and Han (2022) includes various characteristics of these systems, as seen in Table 2.2. Among these, the radius R_{500} is used to obtain an approximation of R_{200}, following the equation from Reiprich et al. (2013):

$$R_{500} \approx 0.65 R_{200}, \tag{3.3}$$

where R_{500} is the radius that contains 500 times the critical density of the universe at the redshift of the cluster.

Now, we can obtain a value of M_{200} associated with R_{200} assuming a spherical geometry:

$$\rho(R < R_{200}) = \frac{3M_{200}}{4\pi R_{200}^3} = \Delta_{\mathrm{c}}^{\mathrm{vir}} \rho_c(z), \tag{3.4}$$

where $\rho_c(z)$ is the critical density of the universe at the redshift of the cluster, and $\Delta_{\mathrm{c}}^{\mathrm{vir}}$ is the virial overdensity, usually approximated to 200 for a flat universe.

3.3.2 Spectroscopic members and velocity dispersion

For the galaxy clusters with available spectroscopic redshift used for the calibration of the membership method, we calculate the mean redshift and velocity dispersion using the robust biweight estimators (Beers et al., 1990). Specifically, we first pre-select the redshift of the cluster as the same of the Yuan and Han (2020) and Yuan et al. (2022) X-ray catalogs, and then we make a cut of ±6000 km s^{-1} in peculiar velocities. Next, we calculate the mean redshift z_{cl} as the biweight location σ_{cl}, and the velocity dispersion as the biweight scale, after convergence of 3σ-clipping. Subsequently, member galaxies are selected following a classical criteria of $|z_{\mathrm{cl}} - z_{\mathrm{spec}}| < 3\sigma_{\mathrm{cl}}(1 + z_{\mathrm{cl}})$ (e.g., Vulcani et al., 2023b).

3.4 Cluster dynamical states

3.4.1 Dynamical state proxies

In this section, we define the six dynamical state proxies that we utilize. The first two proxies correspond to the offset between the BCG and the X-ray peak and centroid, and are calculated directly by us. The next four were computed by Yuan and Han (2020) and Yuan et al. (2022), and we extract the values from their catalogs. The choice to use six parameters together is due to the fact that each of them individually has its limitations, as we describe below, and their combination can provide us with more robust results.

BCG-X-ray centroid/peak offset

Considering the highly hydrodynamically collisional nature of the hot gas composing the ICM of galaxy clusters, and the typical positioning of the BCG within the deepest region of its gravitational potential well, the BCG can be effectively used as a proxy for the non-collisional dark matter component. Thus, the offset between the position of the X-ray emission peak/centroid and the BCG provides a good approximation of the dynamical state of clusters, at least in the projected sky plane. This is because, in a merger process between these structures, the components would be noticeably displaced.

To determine the position of the X-ray peak, we simply identify the pixel with the highest X-ray flux in the image. This is performed using basic functions from the Python package `numpy`.

The X-ray centroid is calculated using tools from `photutils` Python package. Specifically, a 50x50-pixel grid is created over the original image. The median is then calculated in each block by convolving them with a 2D median filter of 5x5 pixels. Subsequently, the sky in each block is calculated using the same algorithm as the Source Extractor (SExtractor, Bertin and Arnouts, 1996), where the sky is equal to $(2.5 * \text{median}) - (1.5 * \text{mean})$. If $(\text{mean} - \text{median})/\text{std} > 0.3$, the median is used instead. The calculated low-resolution map is then interpolated to obtain another one with the same dimensions as the image. Next, the sky was subtracted from the image and it is convolved with a 5x5 pixel Gaussian kernel to enhance the X-ray emission from galaxy clusters relative to the background. Then, a 3σ threshold is applied, where σ is the RMS of the background over which pixels are considered signals. Additionally, a criterion of 900 connected pixels above the threshold is used to segment an object (in this case, galaxy clusters) from the background. This is done to detect clusters as a single system and not separate possible substructures within clusters that may interact. Finally, the centroid of each structure is determined as the center of mass of the pixels belonging to the source segment.

Following Mann and Ebeling (2012), we use a threshold to distinguish between relaxed and disturbed clusters, with a value of $D_{\text{BCG-X}} = 42(71)$ kpc for the X-ray peak (centroid) offset.

Morphological parameter δ

This parameter is a morphological indicator of the X-ray surface brightness distribution. The definition of Yuan and Han (2020) mentions that the great advantage of this dynamical parameter is its adaptability to the properties of each cluster, allowing a direct comparison between them. The first step in calculating the value of δ is to fit a 2D elliptical β model to the X-ray surface brightness distribution. This model is defined as (Cavaliere and Fusco-Femiano, 1976; Guennou et al., 2014):

$$f_{\mathrm{mod}}(x_i, y_i) = f_{\mathrm{mod}}(r) = A\left(1 + \left(\frac{r}{r_0}\right)^2\right)^{-\beta} + C, \tag{3.5}$$

where

$$r(x_i, y_i) = \frac{\sqrt{x^2(1-\epsilon)^2 + y^2}}{1-\epsilon}, \tag{3.6}$$

and

$$x = (x_i - x_0)\,\cos(\theta) + (y_i - y_0)\,\sin(\theta), \tag{3.7}$$

$$y = (y_i - y_0)\,\cos(\theta) - (x_i - x_0)\,\sin(\theta). \tag{3.8}$$

Here, (x_0, y_0) are the coordinates of the centre of the model, A is the model amplitude, r_0 corresponds to the core radius, β is the power-law index, and C is a constant adjusting the count number for the average background. ϵ is the ellipticity of cluster, and θ is the position angle of the system, defined as the direction of the major axis from north to east. All these model parameters can be determined by the least χ^2 fitting.

Then, a new parameter of the X-ray distribution profile is calculated:

$$\kappa = \frac{1+\epsilon}{\beta}, \tag{3.9}$$

Based on the observation that disturbed clusters tend to have a more asymmetric geometry than relaxed clusters (e.g., Okabe et al., 2010; Zhang et al., 2010), the asymmetry factor α is used as an auxiliary variable.

$$\alpha = \frac{\sum_{x_i,y_i}[f_{\mathrm{obs}}(x_i, y_i) - f_{\mathrm{obs}}(x_i', y_i')]^2}{\sum_{x_i,y_i} f_{\mathrm{obs}}^2(x_i, y_i)} \times 100 \text{ per cent}, \tag{3.10}$$

where, $f_{\text{obs}}(x_i', y_i')$ is the observed flux in the pixel symmetric to $f_{\text{obs}}(x_i, y_i)$ with respect to the center of the cluster (x_0, y_0), which is obtained from the fitting of the β-model.

With a combination of these parameters that quantify the properties of the profiles and the asymmetry of the X-ray surface brightness distribution, the morphological index δ is defined as:

$$\delta = A\kappa + B\alpha + C. \tag{3.11}$$

To find appropriate values for the free parameters, Yuan and Han (2020) used a homogeneous calibration sample of 125 clusters qualitatively classified by Mann and Ebeling (2012), finding that the values of $A = 0.68$, $B = 0.73$, and $C = 0.21$ can separate the sample into relaxed systems ($\delta < 0$) and disturbed systems ($\delta \geq 0$) with a success rate of 88%.

Concentration c

Galaxy clusters in a non-virialized state may exhibit various substructures or extended geometries. However, when these systems are very close to virialization, most of the matter is concentrated in their centre, with some even having very luminous cool cores (e.g., Fabian et al., 1994; McDonald et al., 2012, 2013). The concentration index, c, quantifies this characteristic by being calculated as the ratio of the integrated X-ray flux within an inner aperture to that within an outer aperture. In this thesis, the definition of Cassano et al. (2010, 2013) is followed, who used apertures of 100 kpc and 500 kpc:

$$c = \frac{S_{100\text{ kpc}}}{S_{500\text{ kpc}}} = \frac{\sum_{R<100\text{ kpc}} f_{\text{obs}}(x_i, y_i)}{\sum_{R<500\text{ kpc}} f_{\text{obs}}(x_i, y_i)}, \tag{3.12}$$

where $f_{\text{obs}}(x_i, y_i)$ is the observed flux in the pixel (x_i, y_i).

Cassano et al. (2010) found that the median of the distribution of the concentration parameter $\log(c) = -0.7$ is a good threshold to distinguish galaxy clusters in different dynamical states. These states were classified on the basis of their features observed in radio images.

Centroid shift ω

In relaxed clusters, there is an almost negligible deviation between the positions of the X-ray peak and the X-ray centroid. However, in clusters undergoing mergers, these two positions can exhibit a considerable shift. Poole et al. (2006) quantified the deviation between the X-ray peak and the center of a model fit within 20 apertures of different sizes centered on the X-ray peak. The aim was to obtain a value that helps determine the dynamical state of the cluster. This is an iterative process that starts from 0.05 R_{ap} and increases to R_{ap} in increments of $0.05R_{\text{ap}}$. In other words,

$$\omega = \left[\frac{1}{n-1}\sum_i (\Delta_i - \langle\Delta\rangle)^2\right]^{\frac{1}{2}} \times \frac{1}{R_{\text{ap}}}. \tag{3.13}$$

Here, $R_{\text{ap}} = 500$ kpc, $n = 20$, Δ_i is the distance between the peak of the X-ray surface brightness and the center of the fitted model in the i-th aperture, and $\langle\Delta\rangle$ is the mean value of all Δ_i.

Similarly to concentration c, Cassano et al. (2010) found that $\log(\omega) = -1.92$ is a good threshold for separating relaxed and disturbed systems.

Power ratio P_3/P_0

Another way to characterize the dynamics of galaxy clusters based on the X-ray surface brightness distribution was defined by Buote and Tsai (1995). Grounded in the observation that systems undergoing mergers or with substructures exhibit more fluctuations in surface brightness in this range of the electromagnetic spectrum, they developed a method to categorize clusters into different morphological types in the projected plane of the sky.

These authors defined multiclusters as systems that have two or more components with a considerable size ($> 10\%$) of the total gravitational potential of the cluster within approximately 1 Mpc from its center. Thus, they started from the basis of the two-dimensional multipole expansion of the projected gravitational potential. Let $\Sigma(R, \phi)$ be the two-dimensional projection of the mass density of the multicluster, where (R, ϕ) are the conventional polar coordinates. Then, a two-dimensional potential $\Psi(R, \phi)$ is generated due to $\Sigma(R, \phi)$:

$$\nabla^2\Psi(R, \phi) = 4\pi G\Sigma(R, \phi), \tag{3.14}$$

where ∇^2 is the two-dimensional Laplacian and G is the gravitational constant. Following a standard analysis using Green's functions, the potential due to the mass enclosed within R is

$$\Psi(R, \phi) = -2Ga_0 \ln\left(\frac{1}{R}\right) - 2G\sum_{m=1}^{\infty} \frac{1}{mR^m} \times (a_m \cos(m\phi) + b_m \sin(m\phi)), \tag{3.15}$$

where the moments a_m and b_m are given by:

$$a_m(R) = \int_{R' \leq R} \Sigma(R', \phi')(R')^m \cos(m\phi')\, dR'\, d\phi', \tag{3.16}$$

$$b_m(R) = \int_{R' \leq R} \Sigma(R', \phi')(R')^m \sin(m\phi')\, dR'\, d\phi'. \tag{3.17}$$

If the origin is defined at the center of an apparently virialized cluster in the projected plane of the sky, i.e., with nearly completely elliptical geometry, then it only contributes to the even terms in the multipole expansion of the gravitational potential Ψ. Consequently, a significant contribution to the odd multipole terms unambiguously reflects the asymmetry in the projected cluster. These odd multipole terms are also important because multiclusters differ in their relative contributions to even terms, given their distinct morphologies. Taking this into account, Buote and Tsai (1995) propose considering only the first few multipole moments ($m = 0, 1, 2, 3, 4$) since higher order terms contribute to a smaller scale fluctuations that are less significant in terms of dynamics.

The next step is to define the region over which multipole expansion will be carried out, as each term is a function of position (R, ϕ). A simple solution is to compute the moments within a circular aperture R_{ap}. In the case of Yuan and Han (2020) and Yuan et al. (2022), they used $R_{\text{ap}} = 500$ kpc as it is a value commonly used in the literature, facilitating comparisons between different studies.

Because terms with $m > 1$ in the multipole expansion vanish when integrated over ϕ, their magnitude integrated over ϕ is considered instead. If Ψ_m is the m-th term in the multipole expansion of Ψ, then the quantity is defined as:

$$P_{m,m'}(R_{\text{ap}}) = \frac{1}{2\pi} \int_0^{2\pi} \Psi_{m'}(R_{\text{ap}}, \phi)\Psi_m(R_{\text{ap}}, \phi) d\phi. \tag{3.18}$$

Thus, only terms with $m = m'$ do not vanish, and $P_m \equiv P_{m,m}$ is a measure of the "power" of terms of order m within R_{ap}. Ignoring the factors of $2G$, these are given by:

$$P_0 = [a_0 \ln(R_{\text{ap}})]^2, \tag{3.19}$$

for $m = 0$, and

$$P_m = \frac{1}{2m^2 R_{\text{ap}}^{2m}}(a_m^2 + b_m^2), \tag{3.20}$$

for $m > 0$.

Because the projected gravitational potential is directly related to the dynamical state of the cluster, the P_m precisely measures the substructure that is being sought. Thus, if we know the projected mass density Σ of these systems, we can have a direct physical interpretation of P_m. However, due to the absence of this information and considering that we are working with the projected X-ray distribution, the interpretation becomes more complex. Additionally, we must adapt the moments a_m and b_m in such a way that:

$$a_m = \int_{r \leq R_{\rm ap}} f_{\rm obs}(x_i, y_i)(r)^m \, \cos(m\phi) \, dx_i \, dy_i, \tag{3.21}$$

$$b_m = \int_{r \leq R_{\rm ap}} f_{\rm obs}(x_i, y_i)(r)^m \, \sin(m\phi) \, dx_i \, dy_i, \tag{3.22}$$

where r is the distance to the pixel (x_i, y_i) from the center of the cluster (x_0, y_0), and $f_{\rm obs}(x_i, y_i)$ is the observed flux in that pixel.

It has been empirically found that specifically the power ratio P_3/P_0 is a good parameter to separate clusters according to their dynamical states. In this thesis, we use $\log(P_3/P_0) = -6.92$ as a threshold, considering clusters with a value lower (higher) than this threshold as relaxed (disturbed) systems. This choice, like the parameters c and ω, is based on the article by Cassano et al. (2010), where the thresholds are defined as the medians of the distributions.

3.4.2 Weighted boolean sum

As mentioned earlier, dynamical parameters alone do not robustly separate galaxy cluster samples. This is due to various factors discussed appropriately in the articles in which they were developed (i.e., Buote and Tsai, 1995; Poole et al., 2006; Cassano et al., 2010; Mann and Ebeling, 2012; Yuan and Han, 2020). For example, parameters such as c, ω, and P_3/P_0 are calculated on fixed apertures. However, clusters have different sizes, so the values derived from these apertures may not be entirely comparable. In fact, that is the reason why Yuan and Han (2020) decide to develop a new parameter (δ), which is adaptable to the size of these systems. Despite this, the parameter alone still has a considerable overlapping region.

If we add the offsets of the BCG with the X-ray peak and centroid to the aforementioned parameters, which are quite robust proxies due to their multiwavelength nature and the components they approximate in each structure, then we propose that we can more robustly approximate the dynamical state of galaxy clusters.

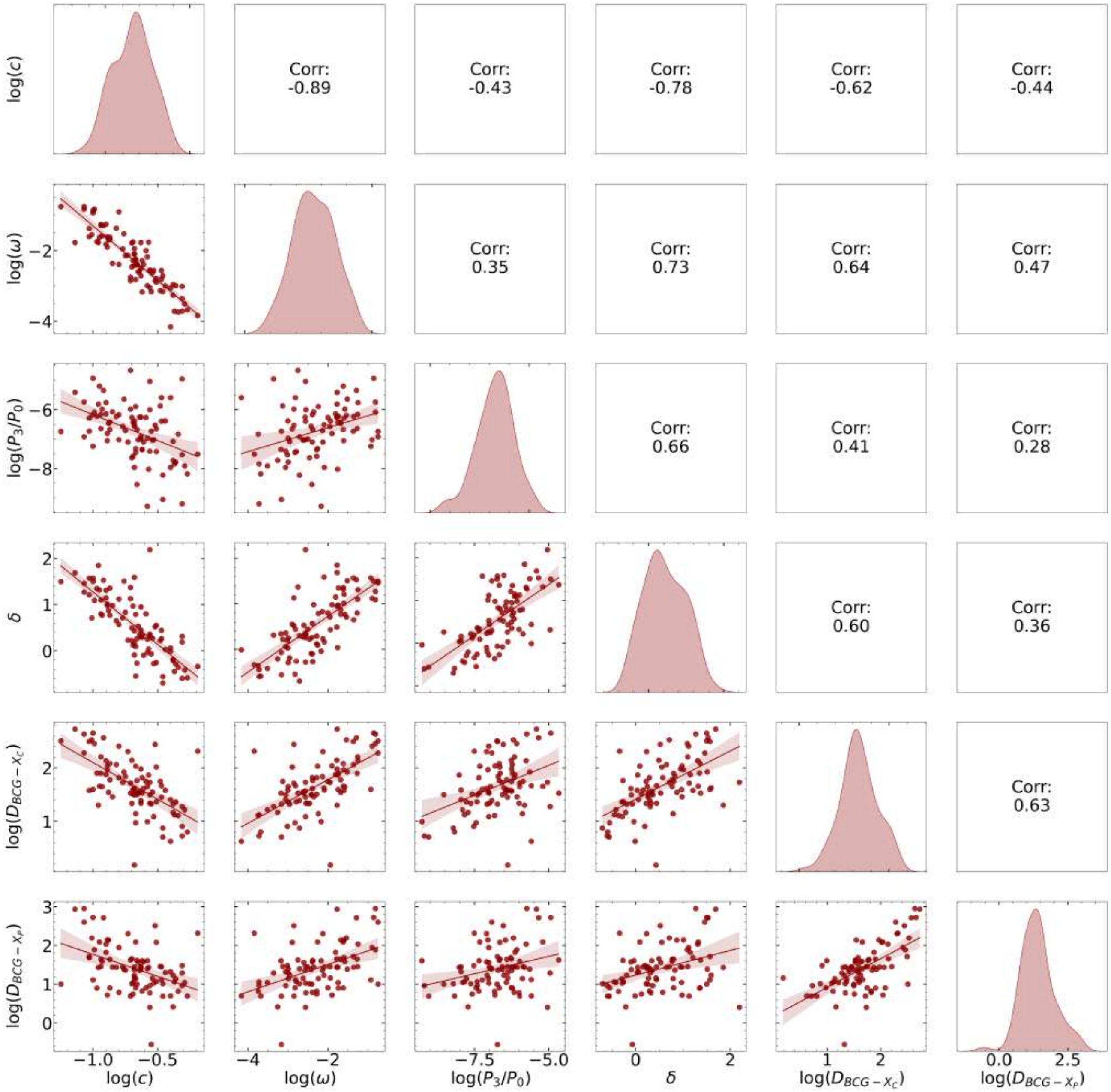

Figure 3.4: Pairgrid of the six dynamical state proxies used in this thesis. The diagonal displays the kernel density estimation (KDE) of each variable. Below the diagonal, scatter plots with linear fits and their corresponding confidence intervals are presented for all combinations of these parameters. Above the diagonal, Pearson correlation coefficients associated with each parameter space are shown.

A method that might initially seem effective is to create a Boolean sum of disturbance conditions. Then, one could observe the distribution of this Boolean sum and categorize the sample into relaxed and disturbed clusters, perhaps with an intermediate region. However, as seen in Figure 3.4, several parameters are correlated with each other, either positively or negatively. Therefore, using this method could potentially give more statistical weight to one parameter over another, leading to biased results.

To address this situation, we search in the literature for clusters in our study sample with dynamical states determined using other methods, such as visual inspection of features in radio, a combination of optical and X-ray observations, among others. This subset consists of 26 systems with well-defined dynamical states.

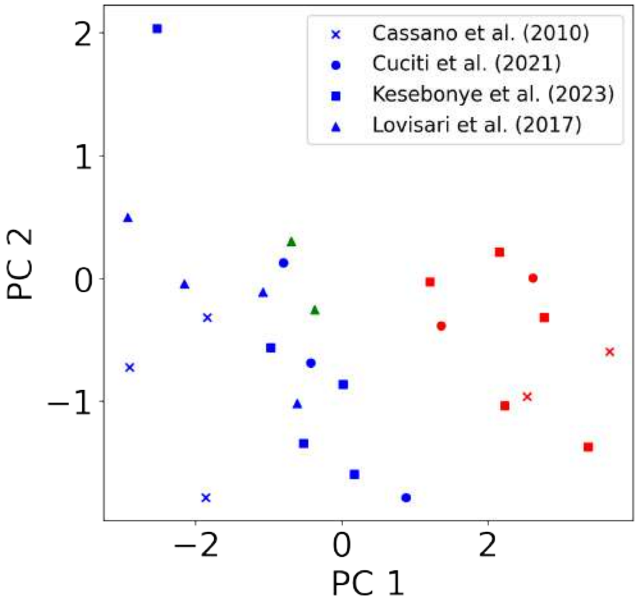

Figure 3.5: Parameter space of the first two principal components (PC 1 and PC 2) obtained from the six dynamic parameters described in Section 3.4.1 for the 26 clusters in the sample that have a well-defined dynamical state in the literature. Blue dots represent relaxed clusters, red crosses represent disturbed clusters, and green squares denote systems with intermediate dynamics.

Subsequently, we apply Principal Component Analysis (PCA) to this subsample. PCA is a statistical tool that, using a linear transformation, can reduce the dimensionality of a dataset by identifying (linearly) correlated variables and eliminating noise and redundancy in the data. The advantage of this technique is that it can transform a set of possibly related variables into another set of more fundamental independent variables (Hotelling, 1933). Additionally, if the redundancy is significant and hence there is correlation between the variables, it might be possible to reproduce the original values of the variables with fewer principal components than the original number of variables in the dataset, without losing their features.

To perform PCA, the values of the original data set must first be scaled. A common way to do this is to use $z = (x-\mu)/\sigma$, where μ and σ are the mean and standard deviation of the variable x, respectively, and z is the new scaled variable. Next, the correlation matrix between the variables must be found, which is symmetric by definition. Subsequently, the eigenvalues and eigenvectors of the covariance matrix are calculated and the eigenvectors are ordered from highest to lowest, using the eigenvalue associated with each as the metric. The principal components are in fact the eigenvectors found, and the associated eigenvalue corresponds to the relative statistical weight of that principal component in this new data set.

Table 3.1: Normalized statistical weight of the dynamical parameters associated to the first principal component.

Parameter	Statistical weight
$D_{\mathrm{BCG\text{-}X_P}}$	0.21
$D_{\mathrm{BCG\text{-}X_C}}$	0.28
δ	0.30
c	-0.30
ω	0.30
P_3/P_0	0.21

Thus, we apply PCA to our set of variables $\{D_{\mathrm{BCG\text{-}X_P}}$, $D_{\mathrm{BCG\text{-}X_P}}$,$\delta$, c, ω, $P_3/P_0\}$. To do this, we use the Python package `scikit-learn`, which includes all the necessary functions and classes for scaling and performs the linear transformation. As seen in Figure 3.5, the first principal component (PC 1) is able to roughly separate the sample into relaxed and disturbed clusters. With this observation, we extract the statistical weights of each dynamical parameter associated with PC 1 (see Table 3.1). Subsequently, we perform a weighted Boolean sum to determine the dynamic state of the clusters.

$$\texttt{wbs} = \sum_i w_i \, B_i, \tag{3.23}$$

where w_i is the statistical weight extracted from PCA and B_i is the Boolean value. In our definition, if a perturbation condition for a specific parameter is met, then the Boolean value for this parameter is 1. Otherwise, the Boolean value is 0.

As observed in the distribution of the weighted Boolean sum (`wbs`) for the full sample in Figure 3.6, it is suggestive to divide the sample into three categories: relaxed clusters ($\texttt{wbs} < 0$), intermediate clusters ($0 \leq \texttt{wbs} \leq 1$), and disturbed clusters ($\texttt{wbs} > 1$). This is the criterion we use in this thesis.

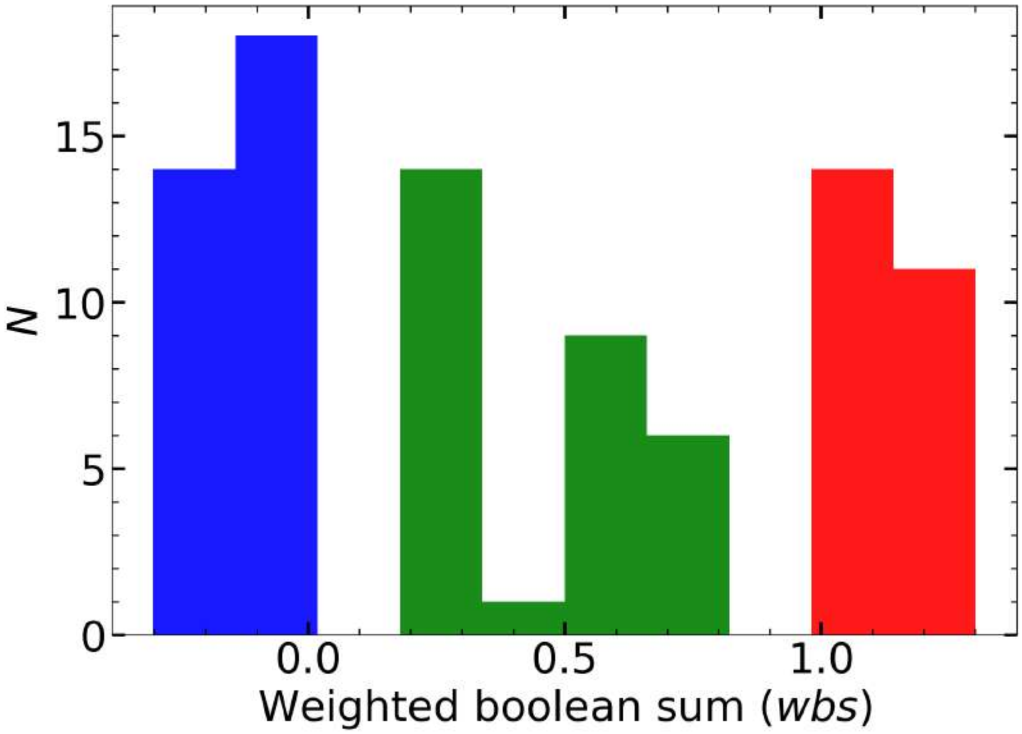

Figure 3.6: Distribution of the weighted Boolean sum (`wbs`) for the whole galaxy clusters sample.

3.5 Structural properties of galaxies

In this section, we describe the parameters used to define a morphological classification system. To calculate these parameters, it was necessary to run several codes that will be described later. What the inputs of these software have in common is that they require cutouts of the images, segmentation maps, and weight images, either necessarily or optionally. Additionally, for parametric methods, it was also necessary to reconstruct the point-spread function (PSF) and calculate the zero-point magnitude of the images. The following details how these files were obtained.

Science images, weight images, and maps of FWHM and N_{exp}

As mentioned in Section 2.1, several Python codes are created to download and crop images from the LS DR10 repositories. The final size of the images for each cluster is $2.4R_{200}$. This size is chosen because the studies in this thesis are limited to a distance of R_{200} from the centers of the clusters, and by giving a extra size, we ensure that none of our galaxies of interest ends up positioned at the boundaries of the images. For each cluster, science images, weight images, full width half maximum (FWHM) and exposure maps (N_{exp}) are downloaded. It is important to note that the images associated with each LS DR10 brick are not entirely homogeneous, as they were stacked from DES DR2 images and all those from DECam that were made public. Therefore, there may be regions with different exposure times in the same brick. Determining the median of FWHM and $N_{\rm exp}$ is necessary to obtain segmentation maps using SExtractor, as explained below.

Segmentation maps

Segmentation maps are useful on their own to provide input to the algorithms used in the calculation of non-parametric methods and also to generate masks from them. These masks are useful for making measurements on our object of interest, ensuring that it is not contaminated by neighboring objects.

Table 3.2: `SExtractor` parameters used to obtain the photometric catalogs and segmentation maps.

Parameter	Value
`DETECT_MINAREA`	5
`DETECT_THRESH`	3.0
`DEBLEND_THRESH`	64
`DEBLEND_MINCONT`	0.000015
`BACK_SIZE`	64
`BACK_FILTERSIZE`	3
`FILTER_NAME`	gauss_5.0_9x9.conv

To obtain them, we utilize the `SExtractor` program (Bertin and Arnouts, 1996), following the configurations outlined in Table 3.2, which are based on the ones used to construct catalogs in the Legacy Surveys[1]. Originally designed to detect sources and compile photometric catalogs, `SExtractor` performs several processes towards this end. One such intermediate process is the creation of segmentation maps, analogous to the procedure described in Section 3.4.1 for calculating centroids of X-ray emissions from galaxy clusters (see Figure 3.7).

It is worth mentioning that other important parameters not listed in Table 3.2 were determined from the $N_{\rm exp}$ and FWHM maps. The gain provided as input is `GAIN` $= 4\overline{N_{\rm exp}}$, with 4 e/pixel being the gain of the DECam and $\overline{N_{\rm exp}}$ being the median of the number of exposures in the image. Additionally, for the seeing, `FWHM` $= \overline{\rm fwhm}$ is used, where $\overline{\rm fwhm}$ is the median of the FWHM map associated with each science image.

---

[1] While the final catalogs delivered by the Legacy Survey are made with `Tractor`, the algorithm requires a PSF to run. This PSF was constructed with PSF Extractor (PSFEX Bertin, 2011), and requires as input catalogs that come from a SExtractor run. Therefore, this configuration file is the one we refer to.

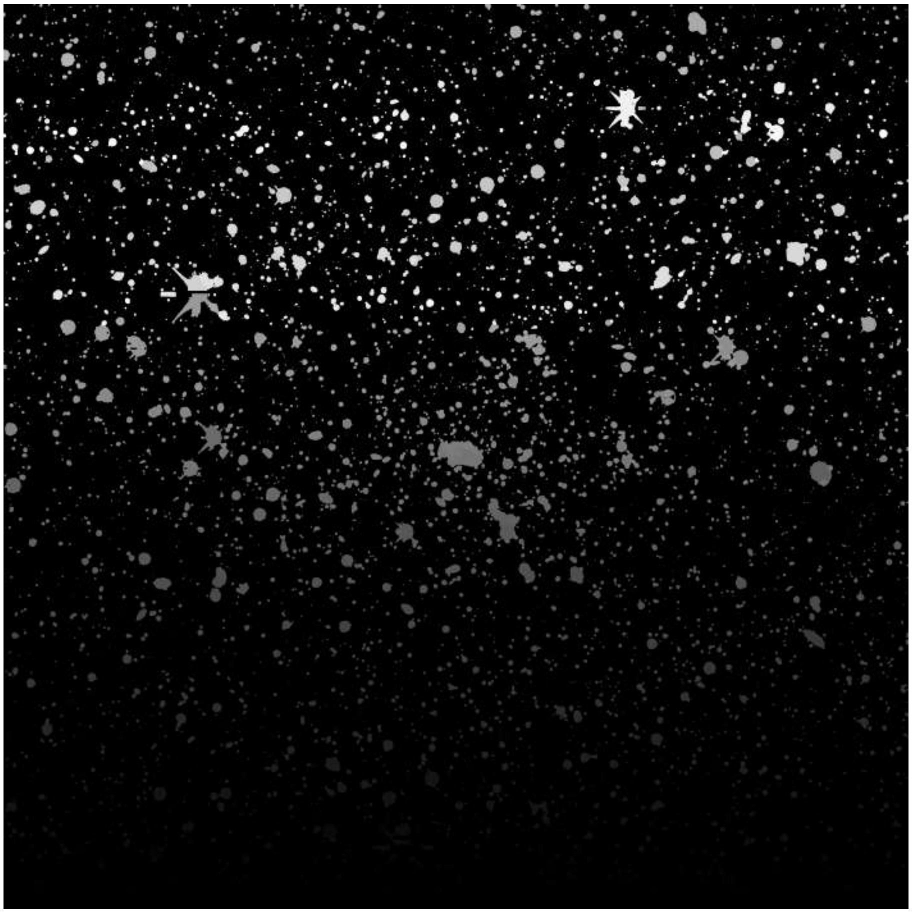

Figure 3.7: Example of segmentation map generated by SExtractor[2] for SPT-CLJ2138-6007. All sources detected by this algorithm are separated from the sky background.

`SExtractor` photometric catalogs

In addition to the segmentation maps, another product obtained from SExtractor, which is indeed the main one, corresponds to the photometric catalogs. Table 3.3 details all the parameters obtained as output in the `SExtractor` run. The function of each of these variables will be explained as they are used.

Cutouts

In the case of all the galaxy cutouts (science images, weight images, and segmentation maps), these are made following the idea of Häussler et al. (2007), where these stamps have an adaptable size. The center of the cutouts corresponds to the positions (`X_IMAGE`, `Y_IMAGE`) of each galaxy. To determine the size, some morphometric parameters obtained with `SExtractor` are used as input. These include the RMS profile along the semi-major axis (`A_IMAGE`, A), the Kron radius

Table 3.3: Output parameters given by `SExtractor`

Parameter	Description [unit]
`X_IMAGE`	Object position along x [pixel]
`Y_IMAGE`	Object position along y [pixel]
`MAG_APER`	Magnitude from aperture photometry [mag]
`MAG_AUTO`	Magnitude from Kron photometry [mag]
`FLUX_RADIUS_20`	Fraction-of-light radii (20%) [pixel]
`FLUX_RADIUS_50`	Fraction-of-light radii (50%) [pixel]
`FLUX_RADIUS_80`	Fraction-of-light radii (80%) [pixel]
`THETA_IMAGE`	Position angle [deg]
`A_IMAGE`	Profile RMS along major axis [pixel]
`B_IMAGE`	Profile RMS along minor axis [pixel]
`KRON_RADIUS`	Kron apertures in units of A or B
`ALPHA_SKY`	Right ascension of barycenter [deg]
`DELTA_SKY`	Declination of barycenter [deg]
`FWHM_IMAGE`	FWHM assuming a gaussian core [pixel]
`ELLIPTICITY`	1 - `B_IMAGE`/`A_IMAGE`
`SNR_WIN`	SNR measured using a window function
`ISOAREA_IMAGE`	Isophotal area above analysis threshold [pixel^2]
`FLAGS`	Extraction flags
`FLAGS_WIN`	Flags for windowed parameters

(`KRON_RADIUS`, K), the position angle (`THETA_IMAGE`, θ), and the ellipticity (`ELLIPTICITY`, E).

$$\texttt{size} = 5AK[|\sin(\theta)| + (1-E)|\cos(\theta)|]. \tag{3.24}$$

While the definition of Häussler et al. (2007) uses a factor of 2.5, we decide to increase it to 5. The idea of the aforementioned author was to create cutouts to obtain morphological parameters only with `GALFITM` (Vika et al., 2013, 2015). However, in this thesis, `statmorph` (Rodriguez-Gomez et al., 2019) is also used, and this larger size allow us to find an appropriate sky box relative to the size of the galaxies (for more details, see Section 3.5.1).

Photometric calibration

`GALFITM` requires several parameters as input that we receive as output from `SExtractor`. One of them corresponds to the integrated magnitude of the galaxy. Regardless of the type of magnitude chosen (i.e., `MAG_APER` or `MAG_AUTO`), it is necessary to perform photometric calibration to find the zero point of the images. Although the flux units in each pixel of the LS DR10 images (nanomaggies[3]) are designed to standardize the combination of the three surveys and thus have a common zero-point (i.e., 22.5 mag), in practice, there can be variations of the order of 0.5 magnitudes. This is an empirical result found in this thesis that can be seen in Figure 3.8. Therefore, we decide to calculate the zero-point of all downloaded science images ourselves.

The procedure to calculate it is as follows. First, a match is made between the `SExtractor` detected source catalog and GAIA DR3. To perform this match, we use `STILTS`[4]. This is a set of command-line tools based on `STIL` (Starlink Tables Infrastructure Library). In fact, `STILTS` is the command-line counterpart to the well-known table analysis tool `TOPCAT`, which is used through a GUI. The reason for using `STILTS` is that, when executed through the terminal, it allows for automation within a pipeline, which is essential for the efficiency of this work. The match is executed with the `cdsskymatch` command, which allows matching a local catalog with another in Vizier, or any other database from the CDS (Centre de Donnés astronomiques de Strasbourg).

Subsequently, only the stars are selected from this new catalog, using the condition `Pstar` $>$ 0.99. The robust parameter `Pstar` from GAIA precisely measures the probability that the detected source is a star, based on its photometry, morphology, and proper motions, among other features (Gaia Collaboration et al., 2023). With the selected stars, we then perform another match with the new catalog. This time, the match is made with the DES DR2 database. The aim of this is to compare the magnitudes of point sources with the same filters, and there is even the advantage that we also have data from the same telescope and CCD imager.

This final catalog, which includes information from `SExtractor`, GAIA DR3, and DES DR2, allows us to perform the desired photometric calibration. However, before doing so, we must ensure that we select well-behaved stars to obtain a good calibration. That is, stars that are not saturated and belong to the main sequence. The first condition can be applied by analyzing the half-light radius vs. the magnitude plane, something that is commonly done in the field of weak lensing (e.g., Kaiser et al., 1995; Okabe et al., 2010; Gonzalez et al., 2015). These parameters are precisely the `FLUX_RADIUS_50` and `MAG_APER` from `SExtractor`, respectively. Regarding the second condition, the main sequence stars can be selected in the color-color diagram, specifically $g - r$ vs. $r - i$. In this case, DES DR2 magnitudes were used, as photometric calibrations were already done, and this is a necessary requirement in this procedure. In order to achieve greater efficiency in this method, a semi-automatic pipeline is developed in Python that uses the DBSCAN clustering algorithm[5] through the `scikit-learn` library and specific thresholds

---

[3] A maggie is a unit of linear flux, where a source with AB magnitude of 22.5 has a flux of 1×10^{-9} maggie or 1.0 nanomaggie.

[4] https://www.star.bris.ac.uk/~mbt/stilts/

[5] The DBSCAN algorithm is used to find the star locus in the color-color diagram.

for each parameter.

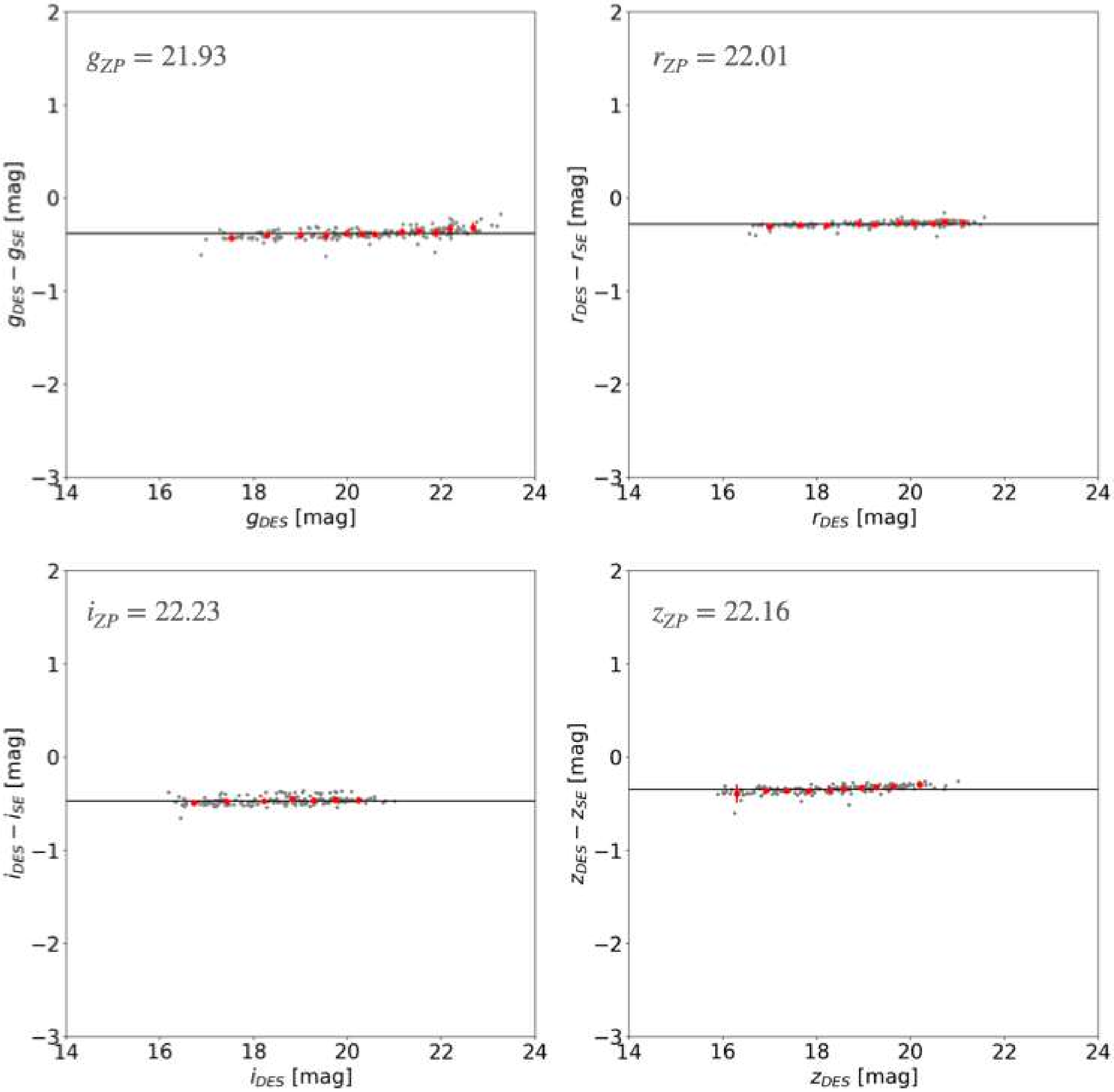

Figure 3.8: Example of the photometric calibrations carried out. The data corresponds to the Abell 3038 galaxy cluster. The gray points correspond to the data of the selected stars for the calibrations, and the red points represent the bins of the data. The black horizontal line is the best fit to the binned data. The zero-points found are displayed as text in the upper left corners of each panel.

Finally, to complete the photometric calibration, we use the parameter space $\texttt{MAG}_{\text{DES}}$ vs. $\texttt{MAG}_{\text{DES}} - \texttt{MAG}_{\text{SE}}$, where $\texttt{MAG}_{\text{DES}}$ and $\texttt{MAG}_{\text{SE}}$ are the magnitudes from the DES DR2 and `SExtractor` catalogs, respectively. Here, we bin the data and then fit a constant function (horizontal line) to the binned data (Figure 3.8). This constant obtained in the fit corresponds to the excess or deficit of magnitudes from the empirically found zero-point, with respect to the default preselected value, i.e. 22.5 magnitudes. This procedure is applied to all four filters ($griz$), and for homogeneity, the same stars are selected in all four DECam bands.

Point-spread function (PSF)

The PSF of the images is also a requirement for `GALFITM`, in this case optional, but we use it to strengthen the results (see Section 3.5.2). We construct an effective PSF (ePSF) using the tools of the Python package `photutils`, following the prescription of Anderson and King (2000). To begin with, we select the same ("well-behaved") stars to those employed for calibrating the zero-point of the science images. Additionally, we impose a criterion to exclude any stars with nearby sources within a 50-pixel radius. Then 25x25 pixel cutouts are made (see Figure 3.9), and the ePSF is constructed with the `EPSFBuilder` class, with an oversampling factor `oversampling` = 1, since for our purposes it is not necessary to have a sub-pixel resolution PSF. Also, we set a maximum of 10 iterations until convergence.

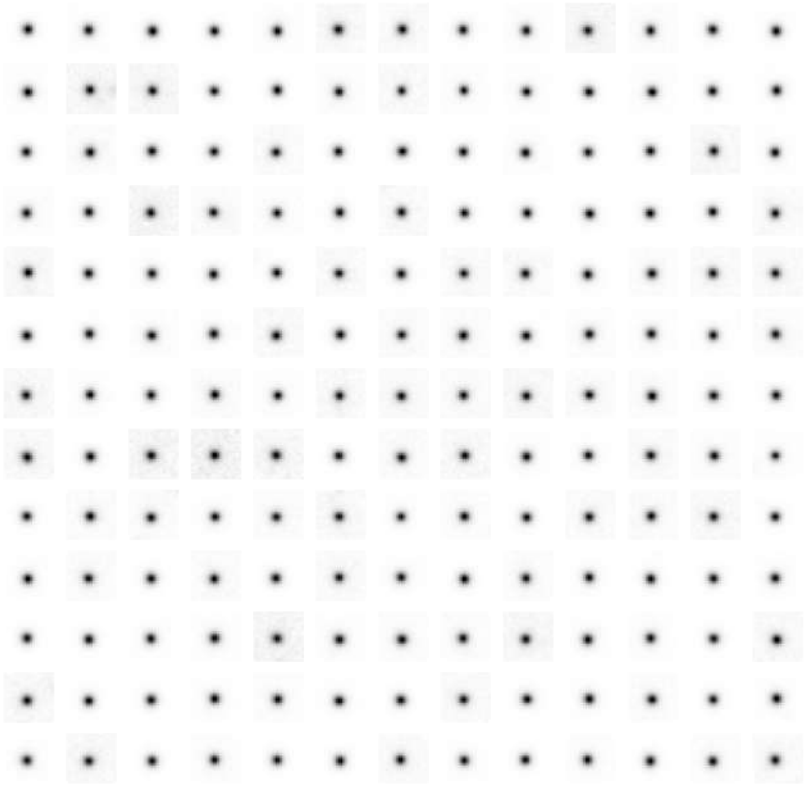

Figure 3.9: Selected stars used to reconstruct the ePSF in the Abell 3038 cluster. The image cutouts correspond to the r-filter.

3.5.1 Non-parametric approach

In this work, we utilize four parameters obtained through non-parametric methods: concentration index (C), asymmetry (A), Gini coefficient (G) and the moment of light (M_{20}) The definition and mathematical formulation of each of them are described below. To calculate them, we use the Python package `statmorph`. This code allows for the computation of several morphological parameters (e.g., CAS statistics, Conselice, 2003; G-M_{20} statistics, Lotz et al., 2004; MID statistics, Freeman et al., 2013). As input, it requires providing a cutout of the science image, a segmentation map indicating which pixels belong to the galaxy, and the CCD gain with which the image was generated or the weight map associated with the observation.

Additionally, an optional mask can be added to reduce contamination from nearby objects or the contribution of flux from bad pixels. All these mentioned input elements are obtained as described at the beginning of this section.

It is worth noting that, regarding the CAS statistics developed by Conselice (2003), we only use the C and A parameters. This choice is made because the resolution and signal-to-noise ratio in our data are not sufficient to obtain robust and reliable results for the smoothness parameter (S).

Examples of the outputs obtained from `statmorph` can be seen in the Figures 3.10 and 3.11 for a disk-dominated and a bulge-dominated galaxy, respectively. The morphological types are assigned using the morphological classification system detailed in Section 3.5.3.

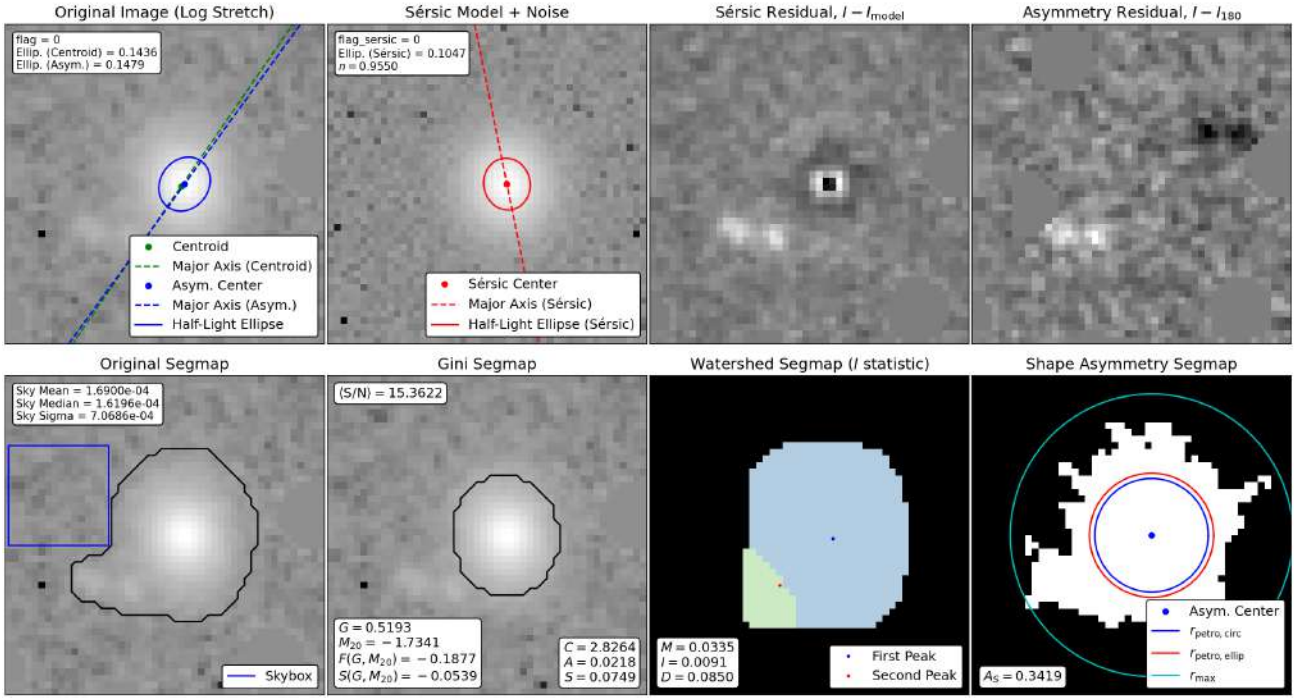

Figure 3.10: Example of `statmorph` output for the bulge-dominated galaxy J002712.03-343901.38 belonging to the Abell 2715 cluster.

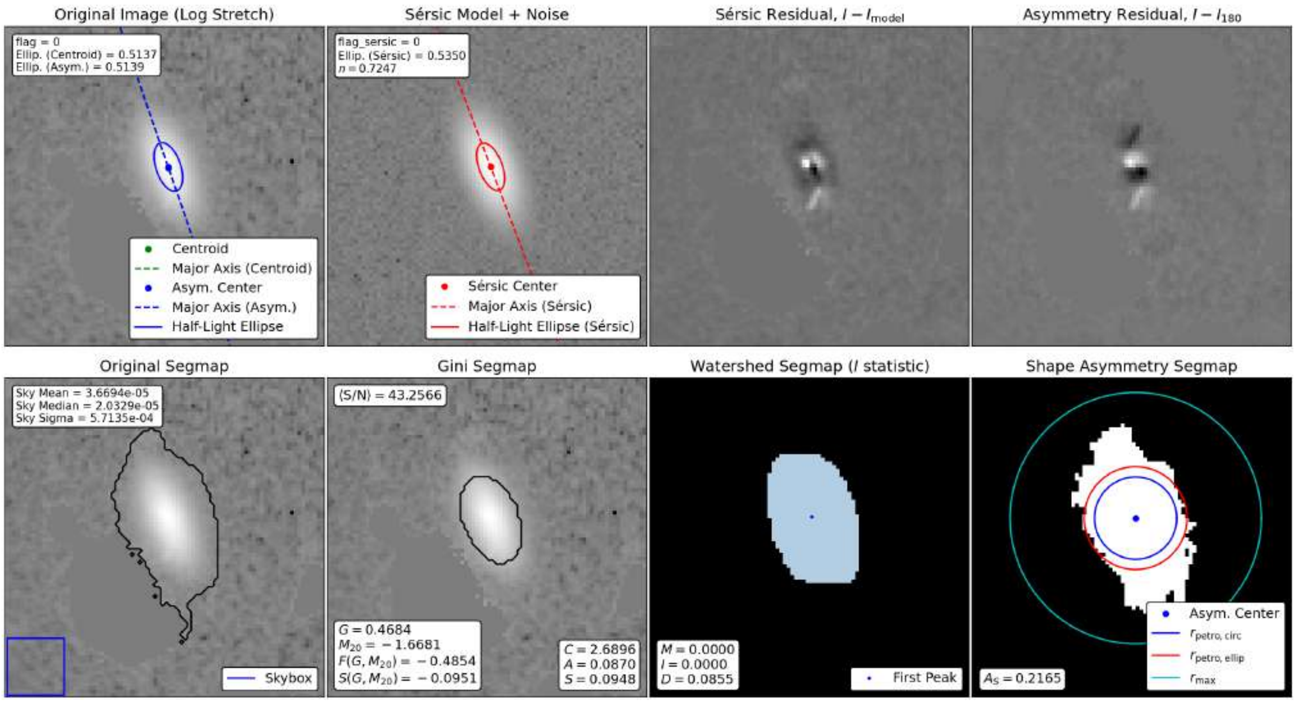

Figure 3.11: Example of `statmorph` output for the disk-dominated galaxy J220241.77-600131.8, belonging to the Abell 3827 cluster.

Concentration index C

The concentration index is a parameter that has been widely used in classification systems. It is defined as the ratio between an outer and an inner radii that encloses a particular physical quantity. In the area of automated galaxy classification, this quantity is a fraction of the total flux, and it was first introduced by Abraham et al. (1994b), but over the years the mathematical expression has been changing, until it has reached the form defined by Conselice (2003):

$$C = 5\,\log\left(\frac{r_{80}}{r_{20}}\right). \tag{3.25}$$

where r_{80} and r_{20} are the radii enclosing 80% and 20% of the galaxy light, respectively.

It is important to note that, when a radius that encloses a fraction of the total flux is defined, we are actually establishing a limit to the galaxy. It has been shown in the literature (e.g., Conselice, 2003; Lotz et al., 2004) that using $1.5R_{\rm P}$ as the "total radius" of the galaxy, where $R_{\rm P}$ is the Petrosian radius, is representative for galaxies at different redshifts and allows comparison between them, since this radius is based on a curve of growth, which makes it largely insensitive to variations in the limiting surface brightness and S/N of observations (Lotz et al., 2004).

The Petrosian radius is defined as

$$\eta = \frac{\mu(R_\mathrm{P})}{\bar{\mu}(R < R_\mathrm{P})}, \tag{3.26}$$

i.e., the radius at which the ratio of the surface brightness (μ) at R_P to the mean surface brightness within the same radius is equal to a fixed value, η, usually set to 0.2 (Petrosian, 1976).

The last important consideration to calculate this parameter is the choice of the center. For homogeneity, the center of asymmetry (see below) is used in the concentration and asymmetry calculations.

Asymmetry A

The asymmetry index allows us to quantify asymmetries in terms of the shape and flux distribution of the galaxy. To calculate the value of this parameter, the image of the galaxy must be rotated by a specific angle. Although different angles of rotation have been proposed in the literature, the most widely used is the 180° angle. Then, the asymmetry is calculated as follows (Abraham et al., 1996; Brinchmann et al., 1998; Conselice, 2003):

$$A = \frac{\Sigma_{i,j}|I_{ij} - I_{ij}^{180}|}{\Sigma_{i,j}|I_{ij}|} - A_\mathrm{bg}, \tag{3.27}$$

where I_{ij} and I_{ij}^{180} are the pixel flux values within $1.5R_\mathrm{P}$ of the original and rotated images, respectively, and A_bg is the asymmetry of the background, which is calculated over a square region of an area similar to that covered by the galaxy.

Finally, it is imperative to find a proper center of asymmetry to perform these calculations, which do not necessarily coincide with the centroid of the galaxy. Shifting this center by a few pixels can greatly alter the obtained value (Conselice et al., 2000). For this task, the downhill simplex algorithm is used to find the center that minimizes the asymmetry of the galaxy in a region close to its centroid.

Gini coefficient G

The Gini coefficient is widely used in economy, as it shows the rank-ordered cumulative distribution function of a population's wealth. This statistic is based on the Lorenz curve, defined as

$$L(p) = \frac{1}{\bar{X}} \int_0^p F^{-1}(u)\, du, \tag{3.28}$$

where p is the fraction of the poorest citizens, $F(x)$ is the cumulative distribution function, and $\bar{X}$ is the mean over all X_i values (Lorenz, 1905).

Naturally, this definition was adapted in such a way that G is a parameter to estimate the morphology of a galaxy, considering the flux (wealth) distribution in pixels that corresponds to the galaxy (population), rather than its application in economics (Abraham et al., 2003; Lotz et al., 2004). As with the previous non-parametric statistics, the mathematical expression evolved until it reached the form described by Lotz et al. (2004):

$$G = \frac{1}{|\bar{X}|n(n-1)} \sum_i^n (2i - n - 1)|X_i|, \tag{3.29}$$

where n is the number of pixels belonging to a galaxy. In this context, the X_i corresponds to the pixel values.

The moment of light M_{20}

The second-order moment of the brightest 20% region of a galaxy is the last non-parametric index used in this thesis. As introduced by Lotz et al. (2004), in order to measure this parameter, first $M_{\rm tot}$ must be found, which corresponds to the total second-order moment of the galaxy:

$$M_{\rm tot} = \sum_i^n M_i = \sum_i^n f_i \left[(x_i - x_c)^2 + (y_i - y_c)^2 \right],$$

where f_i is the flux in each pixel, $(x_i,\, y_i)$ the position of each pixel, and $(x_c,\, y_c)$ is the center of the galaxy, calculated in such a way that $M_{\rm tot}$ is minimized.

Then, to compute the second-order moment of the brightest 20% of the galaxy's flux, it is necessary to rank-order the galaxy pixels by flux, and then:

$$M_{20} \equiv \log \left(\frac{\Sigma_i M_i}{M_{\rm tot}} \right), \text{ while} \sum_i f_i < 0.2 f_{\rm tot}.$$

In this equation, $f_{\rm tot}$ is the total flux of pixels belonging to the galaxy, and f_i are the fluxes for each pixel i, arranged in such a way that f_1 is the brightest pixel, f_2 is the second brightest pixel, and so on.

It is important to note that both in the calculation of G and in that of M_{20}, it is necessary to identify the pixels that belong to the galaxy, and in fact, the values of these parameters are very sensitive to this detection. A segmentation map is used to perform this task, which has been defined in at least two different ways. For example, Abraham et al. (2003) used a constant surface brightness threshold to determine which pixels are part of the galaxy, i.e., pixels that lie above that threshold, and Lotz et al. (2004) proposed a method in which the "Gini" segmentation map depends only on the Petrosian radius, becoming insensitive to the surface brightness dimming of distant galaxies and allowing better comparison. In this thesis, we lean towards the second option, supported by the advantage that this method allows for a better comparison between galaxies at different redshifts, and it is also the default method used in `statmorph`.

Specifically, to create the "Gini" segmentation map the galaxy image is first convolved with a Gaussian with $\sigma = R_P/5$. This step arises the signal of the galaxy pixels above the background noise, making low surface brightness galaxy pixels more detectable. Next, the surface brightness μ at R_P is measured and pixels in the smoothed image with flux values greater than $\mu(R_P)$ and less than 10σ from their neighboring pixels are assigned to the galaxy. This last step assures that any remaining contamination (e.g., cosmic rays or spurious noise pixels) in the image are not included in the "Gini" segmentation map (Lotz et al., 2004).

3.5.2 Parametric approach

On the side of parametric methods for determining the morphology of galaxies, we determin the Sersic index and the effective radius of these systems using `GALFITM`. This code is an adaptation of `GALFIT` (Peng et al., 2002, 2010), which enables fitting two-dimensional surface brightness profiles through a minimization of the χ^2 statistic. The advantage of `GALFITM` is that it allows simultaneous fits in images of different filters of the same galaxy, thus constraining these wavelength-dependent models.

`GALFITM` needs as input a configuration file that contains the path to the files needed to perform the fits, some characteristics of the images, the initial parameters on which to start fitting the surface brightness profiles, the models to be applied and an optional constraints file.

In our work, we provide the science images (mandatory) and the weight images, masks, and PSF of the image (optional). Weight images are added due to the inhomogeneity of the images mentioned at the beginning of the section; the masks, created from segmentation maps, are considered to avoid contamination by nearby objects; and the PSF is used to convolve the best-fit model found by `GALFITM` to obtain more robust results.

Regarding the characteristics of the images, the required inputs include the photometric bands with their respective central wavelengths, the size of the images in pixels, the pixel scale of the camera, the magnitude zero-point, and the size of the convolution box where the model fitting will take place. In our case, the size of the convolution box is the same as that of the stamp.

On the side of the initial parameters, most of them are obtained from the `SExtractor` catalog. Specifically, the positions of the objects (x, y) in the images are required, which are determined as half the size of the stamp calculated with Equation 3.24. Additionally, the object magnitudes in all bands are needed, which are determined with the `MAG_AUTO` parameter and corrected for the empirically found zero-point. The axis ratio (b/a) is also provided, which is derived from the `ELLIPTICITY` parameter. Similarly, the position angle is provided, which does not directly correspond to the `THETA_IMAGE` variable but requires a suitable transformation since the origins from which the angles are measured in `SExtractor` and `GALFITM` are different. Finally, the Sersic index $n = 4.0$ is set as the initial value in all bands and all possible degrees of freedom are given for all the mentioned parameters. The only constraint used is that the resulting Sersic indices are within the range $0 < n < 10$, to avoid losing physical meaning in cases where this parameter takes excessively high values.

In Figures 3.12 and 3.13 an example of the `GALFITM` outputs and the masks used are shown for the same bulge-dominated and disk-dominated utilized to display the `statmorph` outputs.

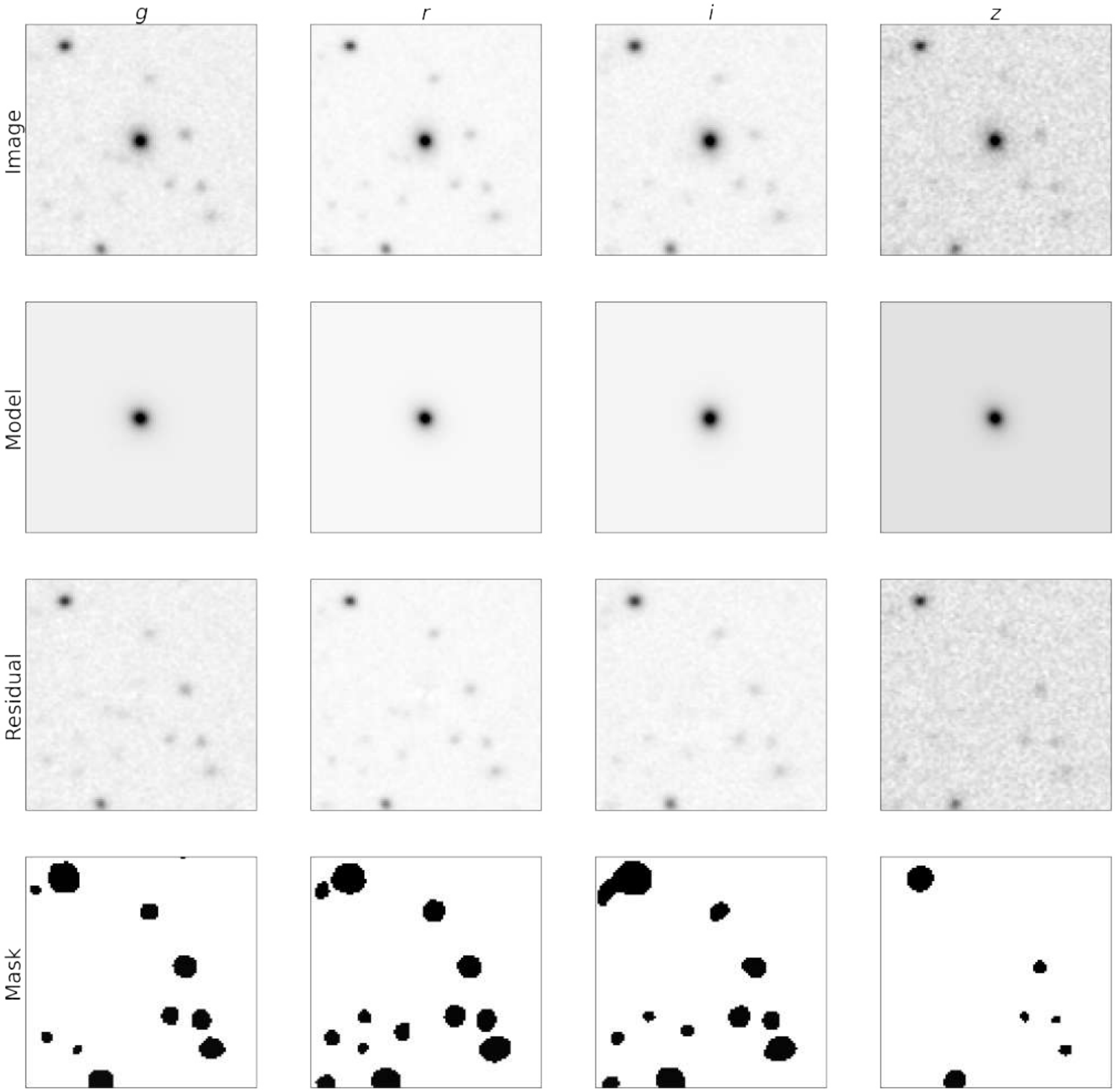

Figure 3.12: Example of `GALFITM` output for the bulge-dominated galaxy J002712.03-343901.38 belonging to the Abell 2715 cluster.

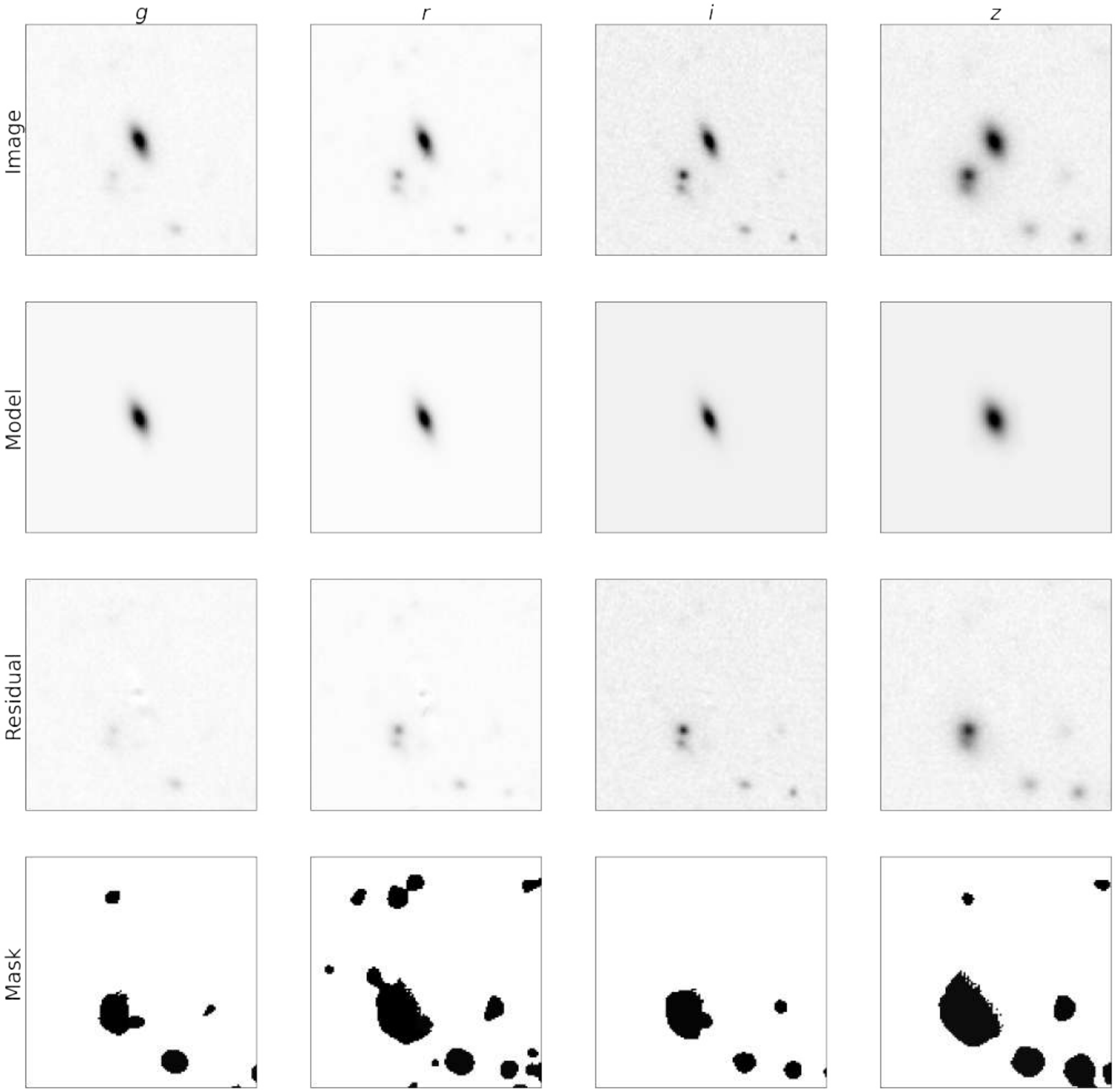

Figure 3.13: Example of `GALFITM` output for the disk-dominated galaxy J220241.77-600131.8, belonging to the Abell 3827 cluster.

Sérsic index n and effective radius r_e

The Sérsic profile (Sersic, 1968) is a mathematical function that describes the intensity profile of a galaxy. This can be expressed using the following formulation:

$$I(r) = I_{\mathrm{e}} \exp\left\{-b_n \left[\left(\frac{r}{r_{\mathrm{e}}}\right)^{(1/n)} - 1\right]\right\}, \tag{3.30}$$

where I is the intensity at position $r(x,y)$, r is the radius from the center that corresponds to (x,y), r_e is the effective radius (half-light radius), I_{e} is the intensity at the half-light radius ($I_{\mathrm{e}} = I(r_{\mathrm{e}})$), and n is the Sérsic index which determines the slope of the profile. Values of $n = 4$ correspond to a de Vaucouleurs' profile, and $n = 1$ indicates an exponential profile.

The constant b_n is defined so that r_{e} contains half of the total flux and can be solved numerically using:

$$\Gamma(2n) = 2\gamma(2n, b_n), \tag{3.31}$$

where Γ and γ are the complete and incomplete gamma functions, respectively.

The Sersic index has been extensively used in the literature to distinguish between spheroidal and disk-type galaxies (e.g., Buitrago et al., 2013), or in conjunction with the effective radius to identify populations in different environments (e.g., Montaguth et al., 2023).

Compactness

Although the effective radius obtained from two-dimensional surface brightness Sersic models is a parameter commonly used for galaxy comparisons, the results may be misleading, as the galaxy radius is strongly dependent on its mass (Sazonova et al., 2020). Therefore, we employ the definition of compactness, which is very similar to the surface mass density of galaxies:

$$\Sigma = \frac{M_*}{\pi R_e^2}, \tag{3.32}$$

where M_* is the stellar mass of the galaxy and R_e is the effective radius obtained from Sersic models.

3.5.3 Morphological classification of galaxies

The culmination of this section corresponds to the definition of the classification system used to determine the morphology of galaxies.

In addition to defining the parameters of the G-M_{20} system, Lotz et al. (2004) created a classification system based on these two variables. They used a calibration compilation of catalogs that includes: 104 objects from the catalog of Frei et al. (1996) and 44 galaxies from SDSS DR1 classified as normal Hubble types; 22 irregular dwarf galaxies from the sample of van

Zee (2001); and 73 ultraluminous infrared galaxies (ULIRGs), whose images were obtained from the HST archive. ULIRGs usually exhibit morphological signatures of ongoing or recent mergers (e.g., Wu et al., 1998; Conselice et al., 2000). By calculating the morphological parameters G and M_{20}, Lotz et al. (2004) found that early-type, late-type, and merger galaxies can be separated on this plane using certain empirically obtained lines.

Later, in a study at higher redshift, Lotz et al. (2008) found that while this classification system is valid, it is highly dependent on the redshift, or more specifically, on the spatial (or physical) resolution of the images. One way to re-calibrate this system is to have a training sample with robust visual classification and the calculation of morphological parameters G and M_{20}. Then, the best linear fit to the data is determined, and by shifting its zero-point $+0.06$ in G (which is 3 times the typical uncertainty of this parameter), the separation between merger candidates and normal Hubble-type galaxies is obtained. Subsequently, with an appropriate density contour, a straight line is empirically drawn passing right through the middle of the two lobes representing the regions of early-type and late-type galaxies (see Figure 7 in Lotz et al. 2008).

Although the method for calibrating the morphological classification system of Lotz et al. (2004) and Lotz et al. (2008) works, it is not applicable in our case, as it would require a robust visual classification, which involves multiple classifiers and complex methods to obtain reliable results, something beyond the scope of this thesis. Instead, we follow the approach of Sazonova et al. (2020), where they used PCA to scale the data set G, M_{20} and then classify galaxies.

The mathematical background of PCA has been detailed in Section 3.4.2, and in this case, the main goal of applying this statistical tool is to normalize the data and find the main sequence that divides normal Hubble-type galaxies and mergers, as well as the separation between early-type and late-type galaxies. When PCA is applied to only two variables, the first component corresponds to the main sequence of the data and the second component corresponds to the standard deviation of this sequence. This method offers the benefit that once there are sufficiently reliable measurements for the morphological parameters, the spatial resolution no longer plays a crucial role in the classification system since the dataset for G, M_{20} is standardized.

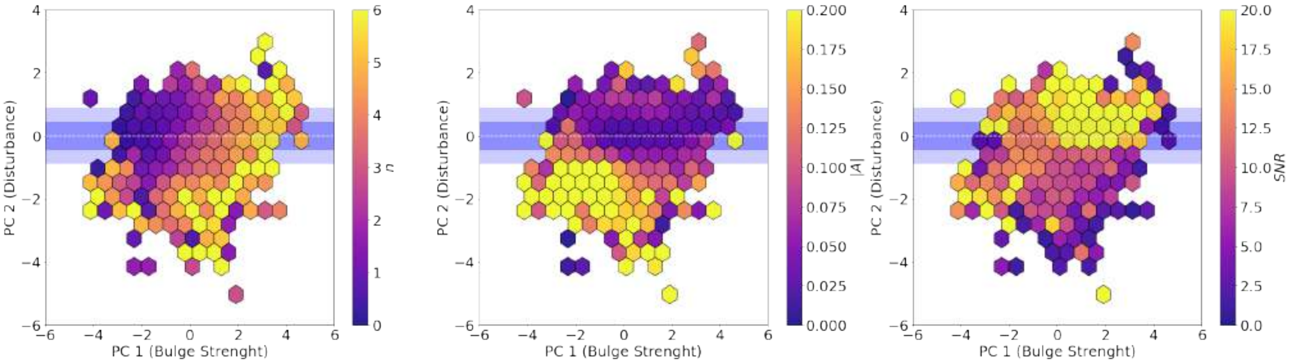

Figure 3.14: Principal components (PC 1 and PC2) of the morphological parameters G and M_{20} for approximately 17,000 galaxies. A hexagonal binning has been applied with a grid size of (30, 9). The horizontal white dashed line corresponds to the main sequence in this plane, and the shaded regions in dark and light blue correspond to the 1σ and 2σ zones, respectively. The hexbins follow a color map associated with three different variables. From left to right, we have: the Sersic index n, asymmetry A, and signal-to-noise ratio SNR.

In Figure 3.14, we have the results of the PCA. In the left panel, we notice that within the 2σ confidence interval, there is a clear trend of galaxies to increase the value of PC 1 along with the Sersic index n. For this reason, we interpret the first principal component as the bulge strength, as indicated in the X-axis label. Then, observing the middle panel, we see that within this same confidence interval, galaxies have an absolute value of asymmetry very close to zero. This leads us to interpret the second principal component as the degree of disturbance that galaxies exhibit. However, as we can see in the right panel, there is also a trend for galaxies below the 2σ confidence zone to have a lower signal-to-noise ratio. Therefore, considering this, we can conclude that a galaxy with a very positive value of PC 2 implies that it is an asymmetric galaxy and then a merger candidate. But if the value of PC 2 is very negative, then it is a diffuse or unresolved galaxy (Sazonova et al., 2020).

However, terms like “very high/low PC 2” are not precise at all. Although there is a trend for bulge strength to increase with PC 1, it is pertinent to define the classification system clearly. Galaxies with PC $2 > 1$ are considered candidates for mergers, and those with PC $2 < -2$ are classified as diffuse/unresolved galaxies. Galaxies with $-2 \leq$ PC $2 \leq 1$ are considered normal Hubble-type galaxies. Those with PC $1 \leq 0$ are disk-dominated and those with PC $1 > 0$ are bulge-dominated. The reason for choosing the threshold PC $1 = 0$ to separate bulge and disk galaxies, instead the value of PC $1 = 1$ used by Sazonova et al. (2020), is because in our data, this bin has a mean value for the Sersic index of $n \sim 2.5$, a value commonly used in the literature to separate early-type and late-type galaxies (e.g., Buitrago et al., 2013).

3.6 Physical properties of galaxies

3.6.1 Normalized colors

The colors of galaxies are a fundamental property. As mentioned earlier in this thesis, it has been shown that it is possible to clearly separate populations using this physical parameter, as it exhibits a notable bimodality (i.e., red galaxies and blue galaxies). However, because we are working with clusters located at different redshifts, it is necessary to apply corrections to compare populations across all systems. Essentially, we are taking into account the Doppler effect, where the light from galaxies is redshifted as they are moving away from us due to the expansion of the universe.

To carry out this process, we subtract the characteristic magnitudes of the galaxy clusters in which they are located from the magnitudes of the galaxies. The characteristic magnitudes (m^*) of these structures are calculated using `EzGal`, modelling CSP as explained in Section 3.2.

Thus, the corrected (or normalized) colors $(g-r)_{\rm norm}$ can be expressed as

$$(g-r)_{\rm norm} = (g-m_g^*) - (r-m_r^*), \tag{3.33}$$

where m_g^* and m_r^* are the characteristic magnitudes in the g and r bands, respectively.

3.6.2 Stellar mass and specific star formation rate

To determine the mass and specific star formation rate of galaxies, we use the `Le Phare` code (Arnouts et al., 1999; Ilbert et al., 2006). This `Fortran` code was designed to perform SED fitting to obtain the photometric redshift of galaxies, as well as some of their physical properties.

This program requires, as input, a catalog containing magnitudes of galaxies and their respective errors, along with certain parameter values set in a configuration file. The output is a catalog of the same dimensions as the input, providing the photometric redshift measurement of the best fit and various parameters selected in another file[6]. Subsequently, the execution of the code consists of three phases:

1. Preparation Phase: Here, the SED template libraries are selected and the set of filters is defined.

---

[6] All possible physical parameters that can be obtained as output are detailed in the `Le Phare` documentation: `https://www.cfht.hawaii.edu/~arnouts/LEPHARE/DOWNLOAD/lephare_doc.pdf`.

2. Magnitude Library Creation Phase: Using the ingredients mentioned earlier, the magnitudes are computed based on the redshift and then interpolated to obtain the final result. In addition, simulated multi-color catalogs can be created as an option in this stage.

3. Fitting Phase: By utilizing a conventional χ^2 minimization technique, a comparison is conducted between the theoretical values present in the libraries generated in the preceding stage and the observed values from the input catalog.

Table 3.4: Parameters used to create the SED libraries.

Parameter	Value(s)
Stellar population synthesis model	Bruzual and Charlot (2003)
Initial mass function	Chabrier
Metallicity Z	0.02, 0.04, 0.008
Star formation history	Exponentially declining
Characteristic duration τ [Gyr]	0.1, 0.3, 1, 2, 3, 5, 10, 30
Extinction curve	Calzetti et al. (2000)
Color excess $E(B-V)$ [mag]	0, 0.05, 0.1, 0.2, 0.3, 0.4, 0.5, 0.6, 0.7, 0.8, 0.9, 1
Emission lines	[$\mathrm{O_{II}}$], [$\mathrm{O_{III}}$], H_β, H_α, Ly_α

In our case, we utilize a library of synthetic spectra generated with the stellar population synthesis model by Bruzual and Charlot (2003) with a Chabrier initial mass function (IMF). Three different metallicities are used (0.02, 0.04, and 0.008). We assume an exponentially declining star formation history (SFH) with nine values for the characteristic timescale τ, ranging from 0.1 to 30 Gyr. The extinction curve of Calzetti et al. (2000) is considered, with twelve possible values for $E(B-V)$, ranging from 0.0 to 1.0 mag. Additionally, the contribution of emission lines to the SEDs is included, specifically modeling the lines of [OII], [OIII], Hβ, Hα, and Ly$_\alpha$. The characteristics of the generated SED libraries are summarized in Table 3.4.

To obtain a library of magnitudes as a function of redshift, all these synthetic spectra libraries are convolved with the filters used for this SED fitting process. As shown in Figure 3.15, these correspond to the set of $grizY$ filters of the DECam[7] and the $W1$ and $W2$ bands of WISE[8].

---

[7] `https://noirlab.edu/science/index.php/programs/ctio/filters/Dark-Energy-Camera`

[8] `https://wise2.ipac.caltech.edu/docs/release/allsky/expsup/sec4_4h.html`

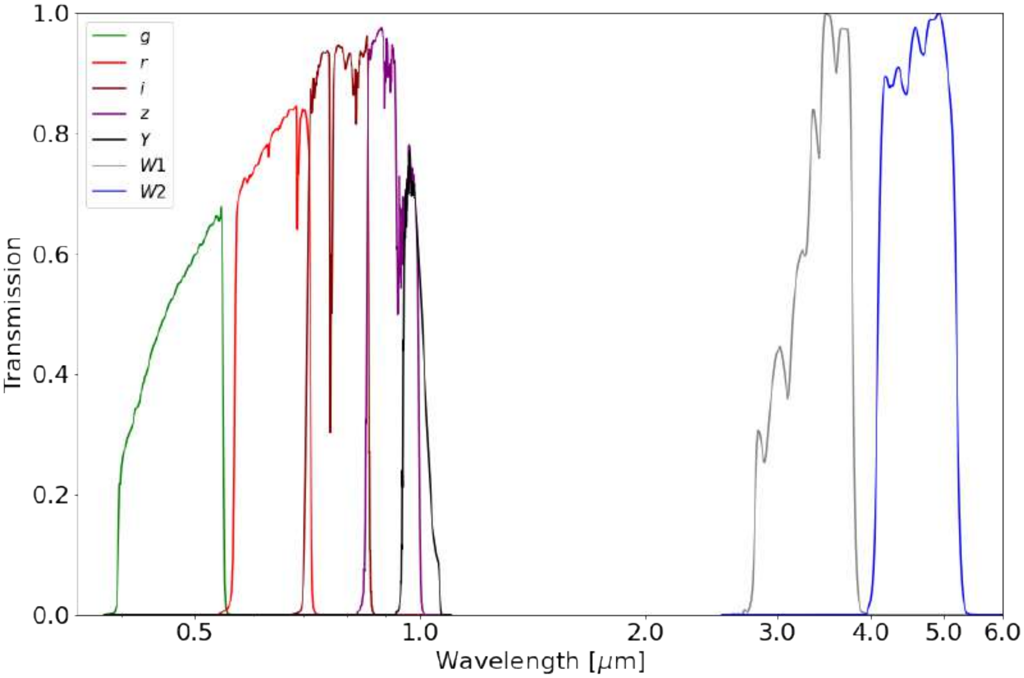

Figure 3.15: Set of filters used in the observations of galaxies, provided by DES DR2 and unWISE. These filters were also employed by the `Le Phare` code to convolve the synthetic spectra and generate magnitude libraries as a function of redshift.

3.7 Quality cuts

To ensure the robustness of our results, we decide to apply several quality cuts. Firstly (1), we apply the criterion $\sigma_{z_{\rm phot}} < 0.05(1 + z_{\rm phot})$, thereby excluding galaxies with imprecise photometric redshifts, where $\sigma_{z_{\rm phot}}$ represents the error of the photometric redshift.

Subsequently, following the recommendations from the documentation of `statmorph`, we decide to eliminate from the sample those galaxies with low signal-to-noise ratio (2) using the condition `sn_per_pixel`$(r) < 2.5$. Furthermore, this code provides a `flag` indicating the quality of the morphological measurements, taking values of 0 (good), 1 (suspicious), 2 (bad), and 4 (catastrophic). We apply the criterion `flag`$(r) \leq 1$.

Next, considering that `GALFITM` (3) and `Le Phare` (4) both use a minimization method of a statistic (χ^2_ν and χ^2, respectively), we chose a threshold below which we select galaxies for the study. We understand that this value had to be as low as possible, but to avoid arbitrary selection, we chose the maximum non-outlier values[9] of both as thresholds (see Figure 3.16).

---

[9] In a boxplot, the whiskers represent the non-outlier minimum and maximum values. Without loss of generality, the non-outlier minimum is calculated as Q1 - 1.5 IQR, where Q1 is the first quartile and IQR is the interquartile range, defined as Q3 - Q1, with Q3 being the third quartile.

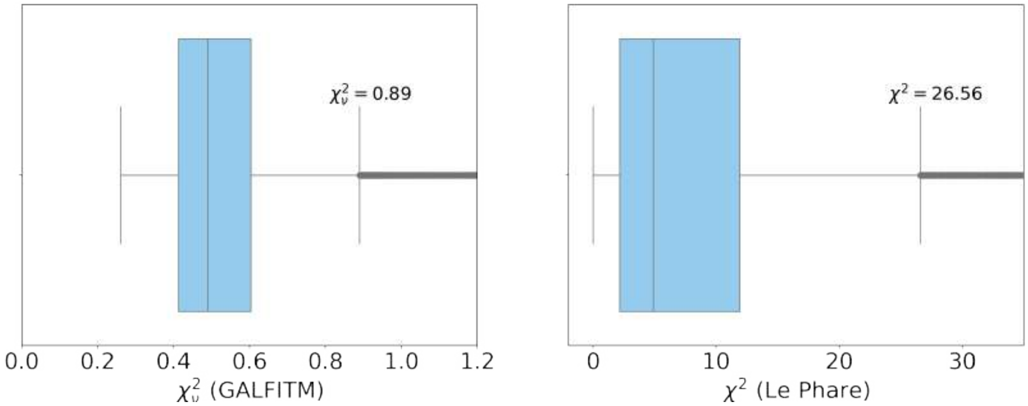

Figure 3.16: *Left*: Boxplot of the χ^2_ν parameter outputted by the `GALFITM` software. *Right*: Boxplot of the χ^2 statistic outputted by the `Le Phare` code. In both cases, we display text regarding the maximum non-outlier extremes, indicating their numerical values.

However, for the case of χ^2_ν, we use a threshold value of 1, as this represents the case of ideal fit.

Finally, we make three cuts that are directly related to measurements of galaxy properties. The first, following the work of Chen et al. (2024), is regarding the specific star formation rate of these systems (5), retaining only those within the range $-15 \leq \log(\mathrm{sSFR}) \leq -8$. The second cut is related to the mass (6), where we cut at $\log(M_*/M_\odot) \geq 8.5$ to minimize the issue of mass completeness (e.g., Chen et al., 2019; Liu et al., 2019). The last cut is about photometric depth (7). In this thesis, we only work with galaxies that had a magnitude $m < m^* + 3$ in the r-band filter, where m^* is the characteristic magnitude of each cluster. This ensures a homogeneous study in terms of photometric depth and also ensures the reliability of the LS DR10 photometric measurements[10].

Our final sample consists of 8,412 galaxies in 87 different clusters, with an average of $N_{\mathrm{mem}} = 97$, where N_{mem} represents reliable cluster members (i.e., after applying the quality cuts). Figure 3.17 illustrates the number of galaxies excluded in each quality cut stage.

---

[10] Although Figure 3.3 shows a potential incompleteness at fainter magnitudes for Abell 2744, this is the most extreme case in our sample. We have verified that using a photometric limit of $m^* + 2$ and $m^* + 3$ yields similar results.

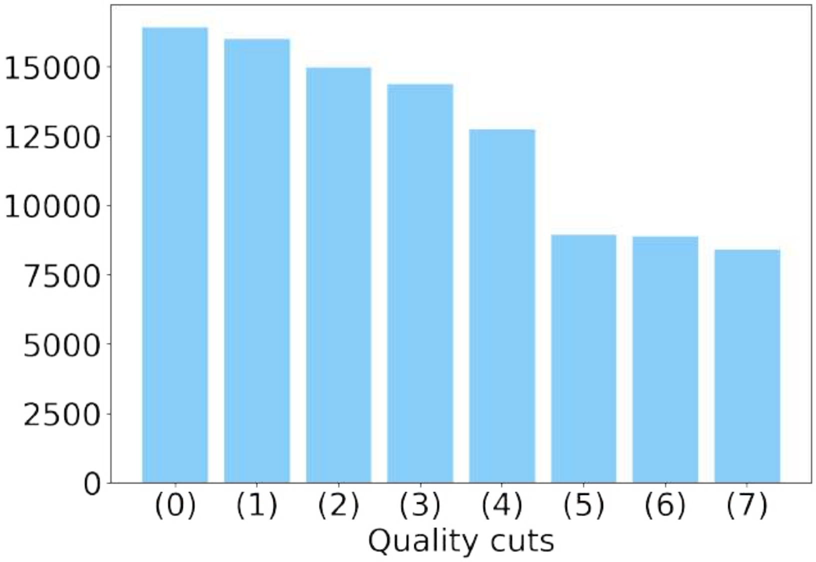

Figure 3.17: Galaxy counts for each quality cut. The (0) label corresponds to the total sample of galaxies before applying any quality cut.

Chapter 4

Results

4.1 Photometric redshifts quality

In this thesis, we have photometric redshifts available from two different methods. The first is obtained from the catalogs of Wen and Han (2022), whose method employs a statistic with the k-nearest neighbors in the multidimensional color space, as explained in Section 2.3. The second involve running the `Le Phare` code, which is based on SED fitting.

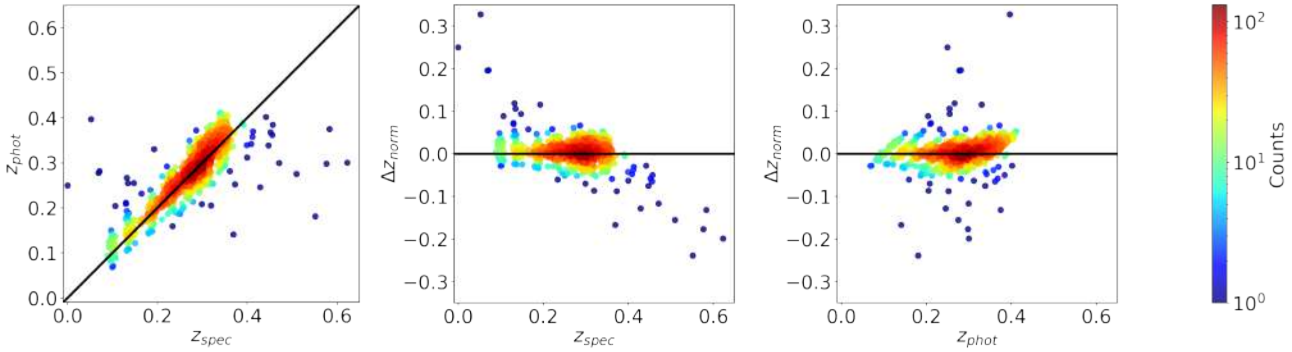

Figure 4.1: Left: Comparison between z_{spec} and z_{phot}. The solid blue line represents the identity line ($z_{\text{spec}} = z_{\text{phot}}$). Middle: Δz_{norm} as function of z_{spec}. Right: Δz_{norm} as function of z_{spec}. In the latter two cases, the solid blue line corresponds to the constant function where $\Delta z_{\text{norm}} = 0$.

Figure 4.1 shows the comparison between the photometric redshifts obtained from the catalogs of Wen and Han (2022) and the spectroscopic redshifts obtained in the literature for member galaxies of the clusters. We define $\Delta z_{\text{norm}} = (z_{\text{phot}} - z_{\text{spec}})/(1 + z_{\text{spec}})$. This method proved to be more accurate in calculating photometric redshifts for our data than the SED fitting performed by `Le Phare`. We find a mean value of $\Delta z_{\text{norm}} = 0.005$ with a dispersion of $\sigma_{\text{z}} = 0.02$, using robust biweight estimators. Table 4.1 compares the quality of the photometric redshifts obtained with each method. It is worth noting that for the case of `Le Phare`, this code is only run using galaxies already selected as members, while for the photometric redshifts of Wen and Han (2022), it is also compared with all galaxies present in the fields of view of the images of each cluster.

Table 4.1: Comparison of the photometric redshift quality obtained by Wen and Han (2021) using the *kNN* method and those obtained through SED fitting with the `Le Phare` code.

Method	Mean	σ
kNN	0.005	0.02
kNN (all galaxies)	0.004	0.03
`Le Phare`	0.043	0.06

4.2 Characterization of galaxy clusters

As mentioned in Section 3.4.2, the 87 galaxy clusters are separated following the weighted Boolean sum criterion. We obtain 32 relaxed clusters, 30 systems with intermediate dynamics, and 25 disturbed galaxy clusters. In Figure 4.2, the scaled value of each proxy is shown, with the dynamical states of each system represented by colors. The values of each parameter are scaled using the StandardScaler class from the `scikit-learn` package. All the characteristics of the galaxy clusters, including their positions, redshifts, R_{200}, M_{200}, and dynamical states, can be found in Table A.1.

Figure 4.2: Radar charts with the six dynamical parameters used in this thesis for all clusters in the sample. The colors blue, green, and red indicate the relaxed, intermediate, and disturbed dynamical states, respectively. The parameters are standardized, and the radar charts are on the same scale for all clusters for comparison purposes. This scale corresponds to $-3.30 \leq$ `param_value` ≤ 2.60, where `param_value` is the dimensionless scaled value of any dynamical parameter.

An important step in estimating the dynamical states of the clusters was the selection of the BCG to obtain the X-ray peak/centroid offset. The automatic method achieved an accuracy of 70%, with respect to the visual inspection. Since we are measuring the accuracy of the automatic method with respect to visual inspection, we must ensure that the selection of the BCG using this latter method is indeed correct. To this end, we have spectroscopic information from the literature (Table 2.3). In Figure 4.3, we present as an example the peculiar velocities of six galaxy clusters from the sample within the range of ±6000 km s^{-1}, and we observe that all the BCGs selected visually indeed belong to the cluster. This occurs for the 30 systems for which we have spectroscopic information for the BCG selected by visual inspection, which gives us confidence in the method.

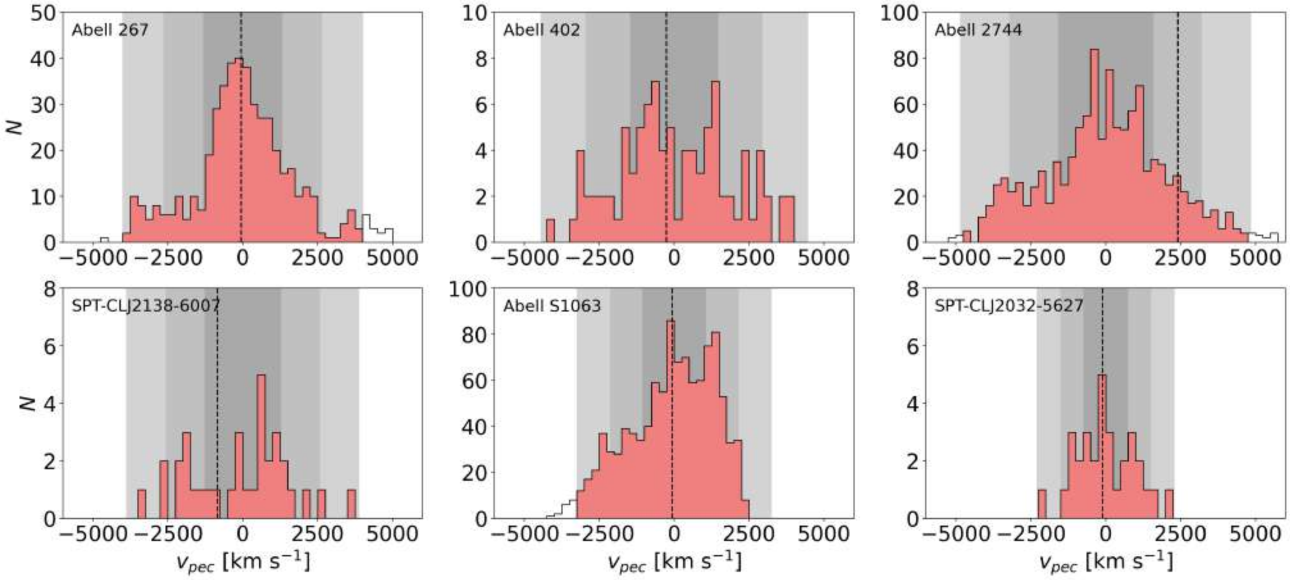

Figure 4.3: Peculiar velocity distributions of galaxies within 6000 km s^{-1} of six example galaxy clusters. The members are marked with red bars. The black dashed lines indicate the positions of the BCGs selected by visual inspection. The shaded areas represent the 1σ, 2σ, and 3σ regions from darkest to lightest. The cluster names are indicated in the upper left corners of each panel. The bin sizes are 250 km s^{-1}.

4.3 Galaxy properties

In Figure 4.4, we present the galaxy stellar mass distributions of the three dynamical states subsamples. Qualitative differences are observed, and then corroborated by applying the Kolmogorov-Smirnov test (the details of this hypothesis test are provided below) in 10,000 Monte Carlo simulations. This may affect our study, as the morphology is strongly influences by mass (e.g., Calvi et al., 2012; Bluck et al., 2019). Therefore, to compare the physical and structural parameters of galaxies, we first perform a mass-match between the subsamples of relaxed, intermediate and disturbed clusters. From now on, all analyses are conducted on this mass-matched sample.

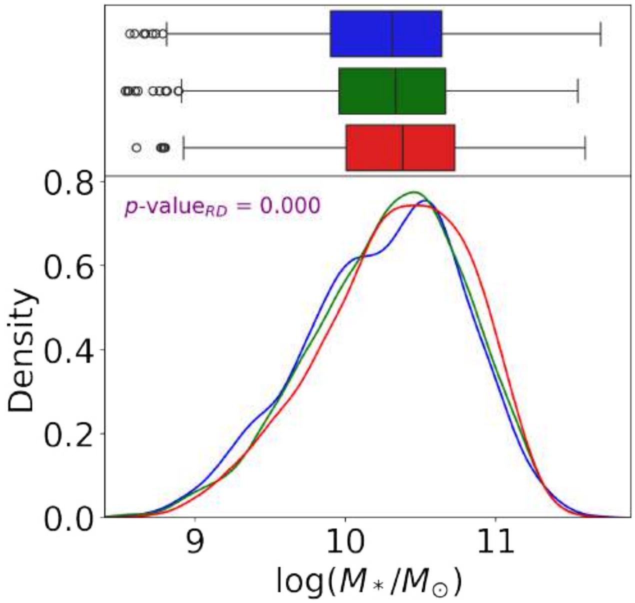

Figure 4.4: Top: Boxplots of the distributions of stellar masses of the galaxies for the three studied dynamical states. Bottom: Kernel Density Estimates (KDE) of the stellar mass distributions. The text indicates the p-values of the K-S test applied to relaxed and disturbed clusters. In both panels, the colors blue, green, and red represent the relaxed, intermediate, and disturbed clusters, respectively.

4.3.1 Overall results

In general, the morphological and physical parameters of galaxies exhibit similar distributions across the three environments studied (see Figures 4.5 and 4.6). The median values and their respective standard deviations for all parameters in each environment are listed in Table 4.2.

However, there are some parameters in which the distributions exhibit qualitative differences when observed (e.g., Sersic index, compactness). To quantitatively determine these differences, we use the Kolmogorov-Smirnov hypothesis test. This test allows us to calculate the probability (p-value) of obtaining a difference equal to or as large as the one observed with a certain level of confidence under the null hypothesis that both distributions are equal. In this thesis, we use a confidence level of 95%, which means that if we obtain a p-value ≤ 0.05, there is sufficient evidence to reject the null hypothesis, thus accepting the alternative hypothesis (two-sided) that the distributions exhibit statistically significant differences. The results of these tests are presented in Table 4.3.

We find that, in general, the concentration, asymmetry M_{20}, Sersic index and specific star formation rate of galaxies present significant differences between relaxed and disturbed clusters. The comparison between relaxed-intermediate and disturbed-intermediate are shown for completeness, but the analysis of that results are beyond the scope of this thesis.

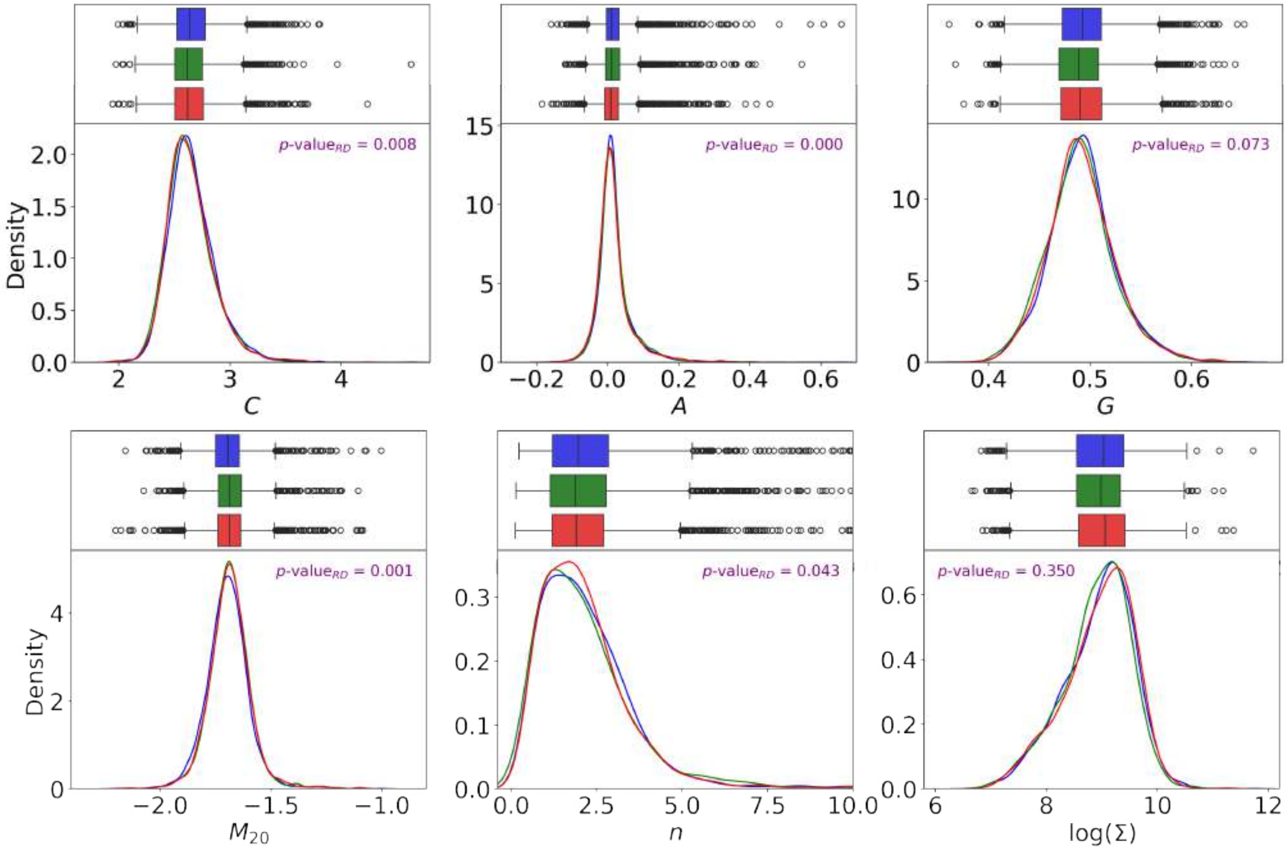

Figure 4.5: Distributions of the structural parameters for all galaxies in the three studied environments (i.e., relaxed, intermediate, and disturbed galaxy clusters). In all upper panels, boxplots are presented, and in the lower panels, the densities of the distributions estimated with KDE are shown. The colors blue, green, and red represent the relaxed, intermediate, and disturbed galaxy clusters, respectively. Additionally, the results of the K-S test for the relaxed and disturbed clusters are also shown in text in the lower panels.

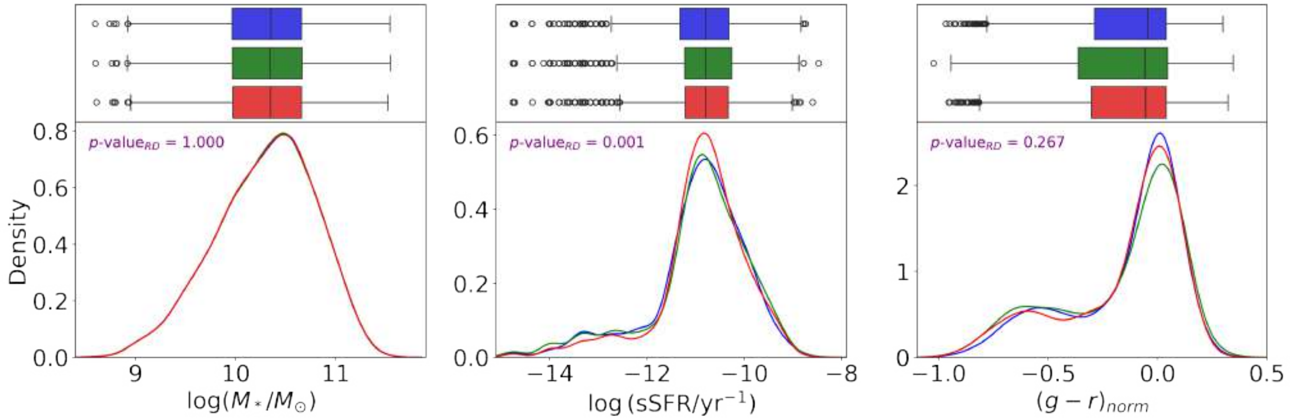

Figure 4.6: Distributions of the physical parameters for all galaxies in the three studied environments (i.e., relaxed, intermediate, and disturbed galaxy clusters). In all upper panels, boxplots are presented, and in the lower panels, the densities of the distributions estimated with KDE are shown. The colors blue, green, and red represent the relaxed, intermediate, and disturbed galaxy clusters, respectively. Additionally, the results of the K-S test for the relaxed and disturbed clusters are also shown in text in the lower panels.

Table 4.2: Median values (M) and standard deviations (σ) of the structural and physical parameters in the three environments studied for all galaxies.

Parameter	Relaxed clusters	Intermediate clusters	Disturbed clusters
C	$M = 2.63$, $\sigma = 0.22$	$M = 2.61$, $\sigma = 0.21$	$M = 2.62$, $\sigma = 0.22$
A	$M = 0.01$, $\sigma = 0.06$	$M = 0.01$, $\sigma = 0.05$	$M = 0.01$, $\sigma = 0.06$
G	$M = 0.49$, $\sigma = 0.03$	$M = 0.49$, $\sigma = 0.03$	$M = 0.49$, $\sigma = 0.03$
M_{20}	$M = -1.70$, $\sigma = 0.10$	$M = -1.69$, $\sigma = 0.09$	$M = -1.69$, $\sigma = 0.10$
n	$M = 1.96$, $\sigma = 1.65$	$M = 1.88$, $\sigma = 1.92$	$M = 1.90$, $\sigma = 1.55$
$\log(\Sigma)$	$M = 9.03$, $\sigma = 0.63$	$M = 8.98$, $\sigma = 0.62$	$M = 9.06$, $\sigma = 0.63$
$\log(M_*/M_\odot)$	$M = 10.35$, $\sigma = 0.50$	$M = 10.34$, $\sigma = 0.50$	$M = 10.35$, $\sigma = 0.50$
$\log(\mathrm{sSFR/yr^{-1}})$	$M = -10.80$, $\sigma = 1.00$	$M = -10.80$, $\sigma = 1.07$	$M = -10.80$, $\sigma = 0.94$
$(g-r)_{\mathrm{norm}}$	$M = -0.05$, $\sigma = 0.26$	$M = -0.06$, $\sigma = 0.28$	$M = -0.06$, $\sigma = 0.27$

Table 4.3: Results of the Kolmogorov-Smirnov hypothesis tests applied to the physical and morphological parameters for all galaxies in the sample.

Parameter	p-value$_{\mathrm{KS,\ RI}}$	p-value$_{\mathrm{KS,\ RD}}$	p-value$_{\mathrm{KS,\ ID}}$
C	0.001	0.008	0.629
A	0.407	0.000	0.005
G	0.002	0.073	0.238
M_{20}	0.000	0.001	0.935
n	0.059	0.043	0.097
$\log(\Sigma)$	0.016	0.350	0.000
$\log(M_*/M_\odot)$	1.000	1.000	1.000
sSFR	0.298	0.001	0.034
$(g-r)_{\mathrm{norm}}$	0.192	0.267	0.047

Table 4.4: Abundances of galaxies for all the sample.

Fraction (%)	Bulge	Disk	Quiescent	Star-forming
Relaxed	39.2	60.2	39.9	60.1
Intermediate	34.2	65.5	39.0	61.0
Disturbed	35.5	63.9	37.5	62.6

In Table 4.4 we observe the galaxy fractions as we separate the galaxies by quenching state and morphological types. We note that between relaxes and disturbed clusters, there is a 3.7% difference in the morphological type abundances, and 2.5% difference when separating in quiescent and star-forming galaxies.

4.3.2 Mass dependence

To explore the dependence of morphological and physical parameters on galaxy masses, we divide the sample into low-mass ($\log(M_*/M_\odot) \leq 10.41$) and high-mass ($\log(M_*/M_\odot) > 10.41$) galaxies. This threshold corresponds to the median of the entire sample after making a cut at 90% completeness. In Figures 4.7 and 4.8 we present the distributions of structural parameters for low-mass and high-mass galaxies, respectively. Next, in Figures 4.9 and 4.10 we display the distribution of physical parameters in the same order. The median values and standard deviations of these properties are tabulated in Table 4.5, and the results of the Kolmogorov-Smirnov tests comparing the galaxy properties between relaxed and disturbed clusters in Table 4.6.

Before comparing the subsamples (relaxed, intermediate and disturbed clusters), we notice that, in general, the median values of some morphological parameters are different for low-mass and high-mass galaxies. Specifically, the concentration, compactness and Sersic index are higher for high-mass galaxies. On the physical properties side, we note that low-mass galaxies are more star-forming, and bluer than the high-mass counterpart.

Now, focusing on the differences between the three environments, we observe that low-mass galaxies are more affected by the dynamical state of galaxy clusters, at least on morphological transformations. This is supported by the fact that the concentration, asymmetry, Gini coefficient and M_{20} of galaxies present significant differences between relaxed and disturbed clusters. However, high-mass galaxies only show differences in the asymmetry and the specific star formation rate of galaxies.

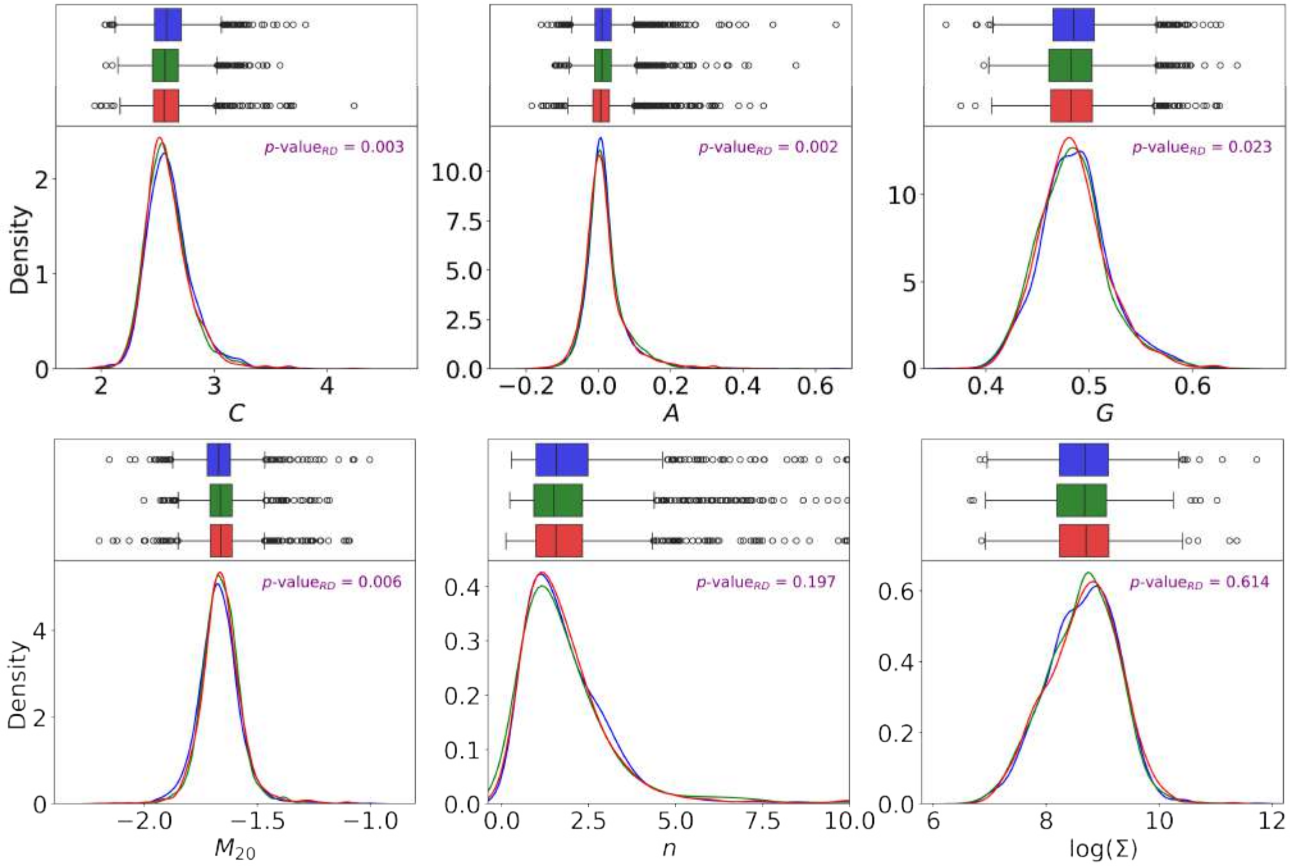

Figure 4.7: Similar to Figure 4.5, but only for low-mass galaxies.

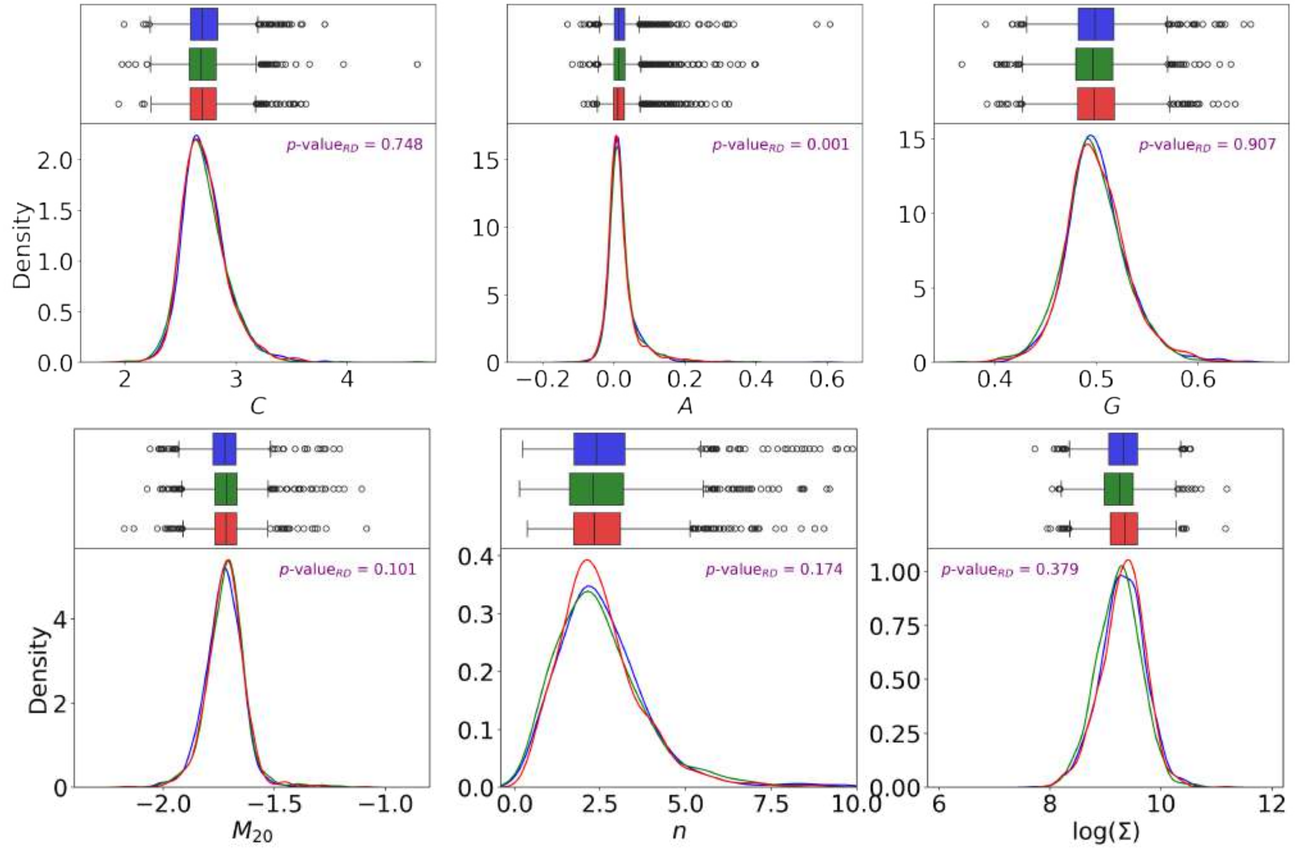

Figure 4.8: Similar to Figure 4.5, but only for high-mass galaxies

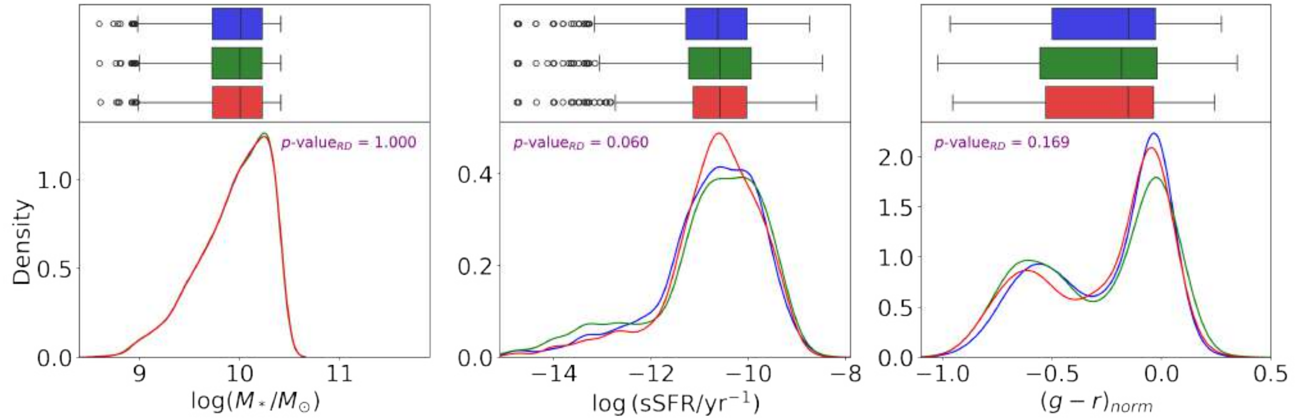

Figure 4.9: Similar to Figure 4.6, but only for low-mass galaxies.

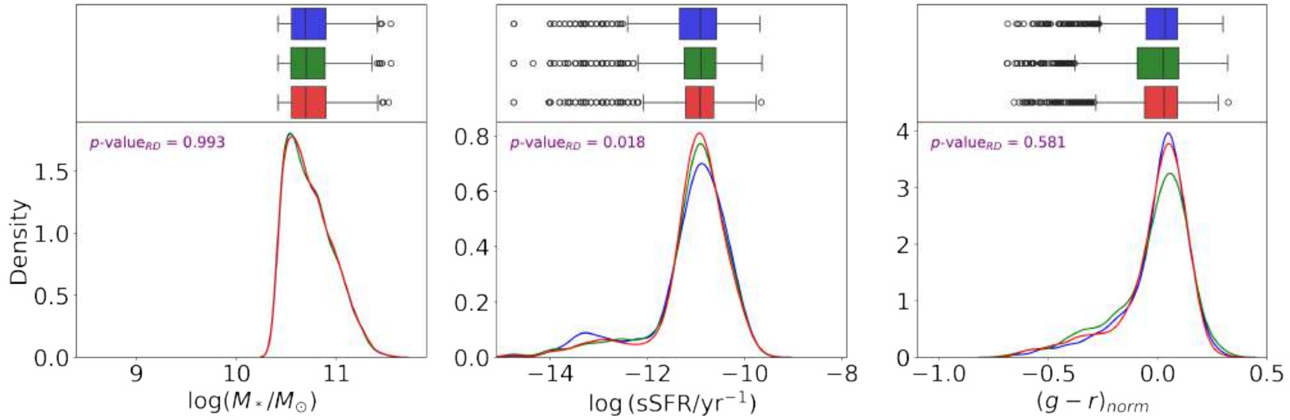

Figure 4.10: Similar to Figure 4.6, but only for high-mass galaxies.

Table 4.5: Median values (M) and standard deviations (σ) of the morphological and physical parameters in the three studied environments. Here, we separate between high and low mass galaxies.

Parameter	Relaxed clusters	Intermediate clusters	Disturbed clusters
Low-mass			
C	$M = 2.58$, $\sigma = 0.21$	$M = 2.56$, $\sigma = 0.19$	$M = 2.56$, $\sigma = 0.21$
A	$M = 0.01$, $\sigma = 0.06$	$M = 0.01$, $\sigma = 0.06$	$M = 0.01$, $\sigma = 0.06$
G	$M = 0.48$, $\sigma = 0.03$	$M = 0.48$, $\sigma = 0.03$	$M = 0.48$, $\sigma = 0.03$
M_{20}	$M = -1.67$, $\sigma = 0.10$	$M = -1.66$, $\sigma = 0.09$	$M = -1.66$, $\sigma = 0.10$
n	$M = 1.56$, $\sigma = 1.58$	$M = 1.49$, $\sigma = 2.07$	$M = 1.55$, $\sigma = 1.67$
$\log(\Sigma)$	$M = 8.69$, $\sigma = 0.62$	$M = 8.68$, $\sigma = 0.63$	$M = 8.70$, $\sigma = 0.64$
$\log(M_*/M_\odot)$	$M = 10.01$, $\sigma = 0.35$	$M = 10.00$, $\sigma = 0.35$	$M = 10.00$, $\sigma = 0.35$
$\log(\mathrm{sSFR/yr^{-1}})$	$M = -10.62$, $\sigma = 1.08$	$M = -10.58$, $\sigma = 1.21$	$M = -10.58$, $\sigma = 1.01$
$(g-r)_{\mathrm{norm}}$	$M = -0.15$, $\sigma = 0.27$	$M = -0.18$, $\sigma = 0.30$	$M = -0.15$, $\sigma = 0.29$
High-mass			
C	$M = 2.69$, $\sigma = 0.21$	$M = 2.68$, $\sigma = 0.21$	$M = 2.69$, $\sigma = 0.21$
A	$M = 0.01$, $\sigma = 0.05$	$M = 0.01$, $\sigma = 0.05$	$M = 0.01$, $\sigma = 0.04$
G	$M = 0.50$, $\sigma = 0.03$	$M = 0.50$, $\sigma = 0.03$	$M = 0.50$, $\sigma = 0.03$
M_{20}	$M = -1.72$, $\sigma = 0.09$	$M = -1.71$, $\sigma = 0.09$	$M = -1.72$, $\sigma = 0.09$
n	$M = 2.38$, $\sigma = 1.65$	$M = 2.30$, $\sigma = 1.66$	$M = 2.32$, $\sigma = 1.30$
$\log(\Sigma)$	$M = 9.32$, $\sigma = 0.40$	$M = 9.25$, $\sigma = 0.40$	$M = 9.35$, $\sigma = 0.39$
$\log(M_*/M_\odot)$	$M = 10.69$, $\sigma = 0.23$	$M = 10.70$, $\sigma = 0.23$	$M = 10.69$, $\sigma = 0.23$
$\log(\mathrm{sSFR/yr^{-1}})$	$M = -10.91$, $\sigma = 0.87$	$M = -10.91$, $\sigma = 0.83$	$M = -10.92$, $\sigma = 0.78$
$(g-r)_{\mathrm{norm}}$	$M = 0.03$, $\sigma = 0.15$	$M = 0.02$, $\sigma = 0.17$	$M = 0.03$, $\sigma = 0.16$

Table 4.6: Results of the Kolmogorov-Smirnov hypothesis tests applied to the physical and morphological parameters for galaxies separated into high and low mass.

Parameter	p-value$_{\text{KS, RI}}$	p-value$_{\text{KS, RD}}$	p-value$_{\text{KS, ID}}$
Low-mass			
C	0.007	0.003	0.888
A	0.551	0.002	0.038
G	0.035	0.023	0.571
M_{20}	0.010	0.006	0.874
n	0.203	0.197	0.492
$\log(\Sigma)$	0.354	0.614	0.172
$\log(M_*/M_\odot)$	0.999	1.000	1.000
$\log(\text{sSFR}/\text{yr}^{-1})$	0.125	0.060	0.013
$(g-r)_{\text{norm}}$	0.015	0.169	0.023
High-mass			
C	0.125	0.748	0.723
A	0.536	0.001	0.029
G	0.066	0.907	0.226
M_{20}	0.008	0.101	0.516
n	0.186	0.174	0.171
$\log(\Sigma)$	0.001	0.379	0.000
$\log(M_*/M_\odot)$	0.999	0.993	0.996
$\log(\text{sSFR}/\text{yr}^{-1})$	0.159	0.018	0.803
$(g-r)_{\text{norm}}$	0.008	0.581	0.109

Table 4.7: Abundances of galaxies for low-mass and high-mass populations.

Fraction (%)	Bulge	Disk	Quiescent	Star-forming
Low-mass				
Relaxed	28.3	71.1	34.8	65.2
Intermediate	24.8	74.7	33.8	65.9
Disturbed	24.4	75.2	30.7	69.3
High-mass				
Relaxed	42.6	37.9	37.5	43.7
Intermediate	37.2	43.9	36.7	44.7
Disturbed	39.8	40.6	37.1	44.0

In Table 4.7 we observe the galaxy abundances separating them by quenching state and morphological types, for low-mass and high-mass galaxies. We notice that, for low-mass galaxies, between relaxed and disturbed galaxy clusters, there is a 3.7% difference in morphological type fractions, and 1.1% difference when separating in quiescent and star-forming galaxies. In the same comparison, but for high-mass galaxies, we observe a 3.3% difference in the fraction of morphological types, and 0.9% difference in the abundances of quenched galaxies.

4.3.3 Morphology dependence

Now we study the dependence of structural and physical parameters on the morphological type of each galaxy. We use the classifications of bulge-dominated and disk-dominated defined in Section 3.5.3. It is worth noting that the fraction of mergers in our work is less than 1%, so we do not include this type of galaxies in our analysis. For more details about this, refer to Section 5.3.

In Figures 4.11 and 4.12 we display the distributions of structural parameters for bulge-dominated and disk-dominated galaxies, respectively. Next, in Figures 4.13 and 4.14 we present the distribution of physical properties in the same order. The median values and standard deviations of these parameters are shown in Table 4.8, and the results of the Kolmogorov-Smirnov tests comparing the galaxy properties between relaxed and disturbed clusters in Table 4.9.

Similar to the previous subsection, we first notice that, in general, regardless of the environment, the median values of the several morphological and physical parameters are different for each morphological type. Specifically, the concentration, Gini coefficient, Sersic index compactness, and stellar mass is higher for bulge-dominated galaxies than for the disk-dominated ones. On the contrary, the M_{20} and specific star formation rate are lower. Additionally, bulge-dominated galaxies are redder than the disk-dominated counterpart.

But, focusing on the comparison between the different environments, we observe that when we separate galaxies into morphological types, the dependency on the dynamical state of clusters almost disappears. We only find statistically significant differences in the specific star formation rate of bulge-dominated galaxies, and in the asymmetry of the disk-dominated galaxies, between relaxed and disturbed galaxy clusters.

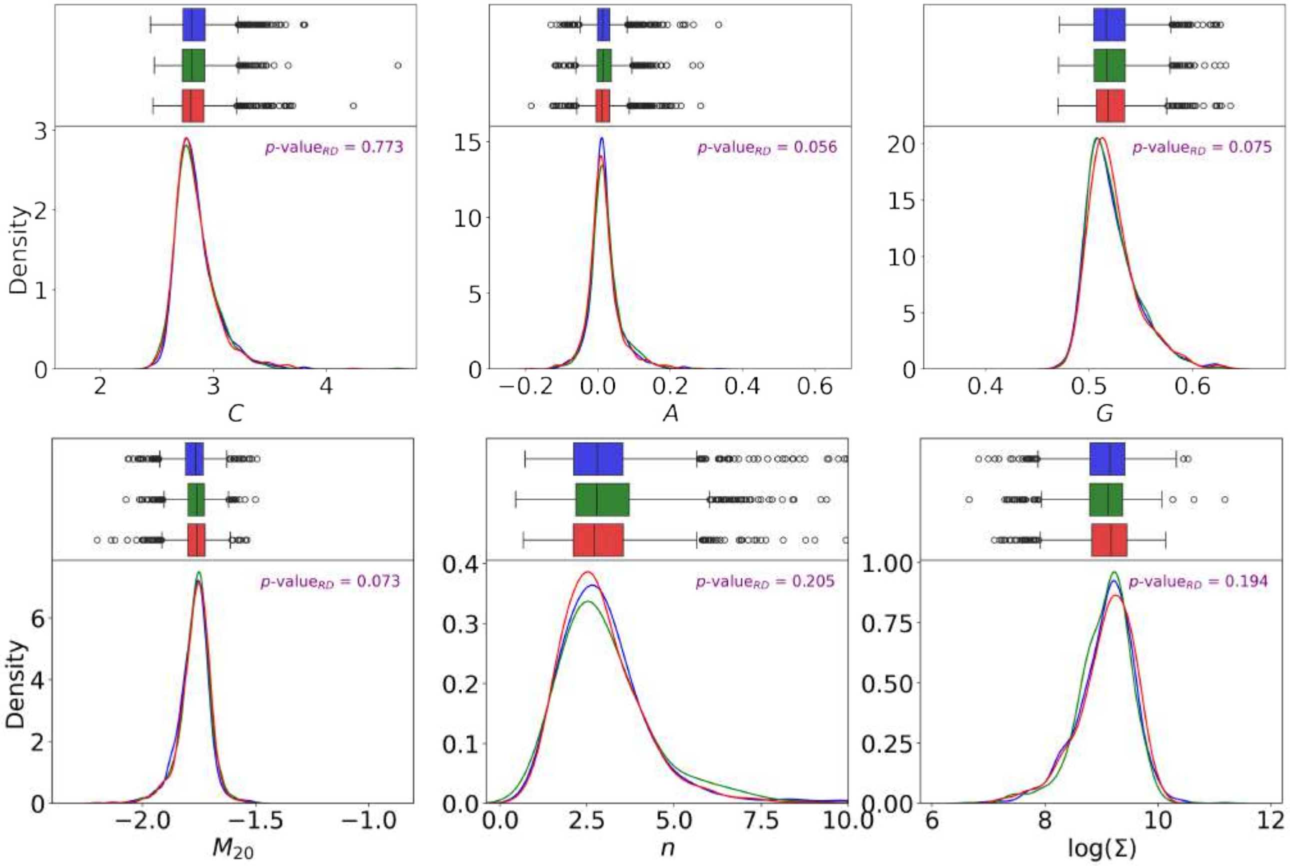

Figure 4.11: Similar to Figure 4.5, but only for bulge-dominated galaxies.

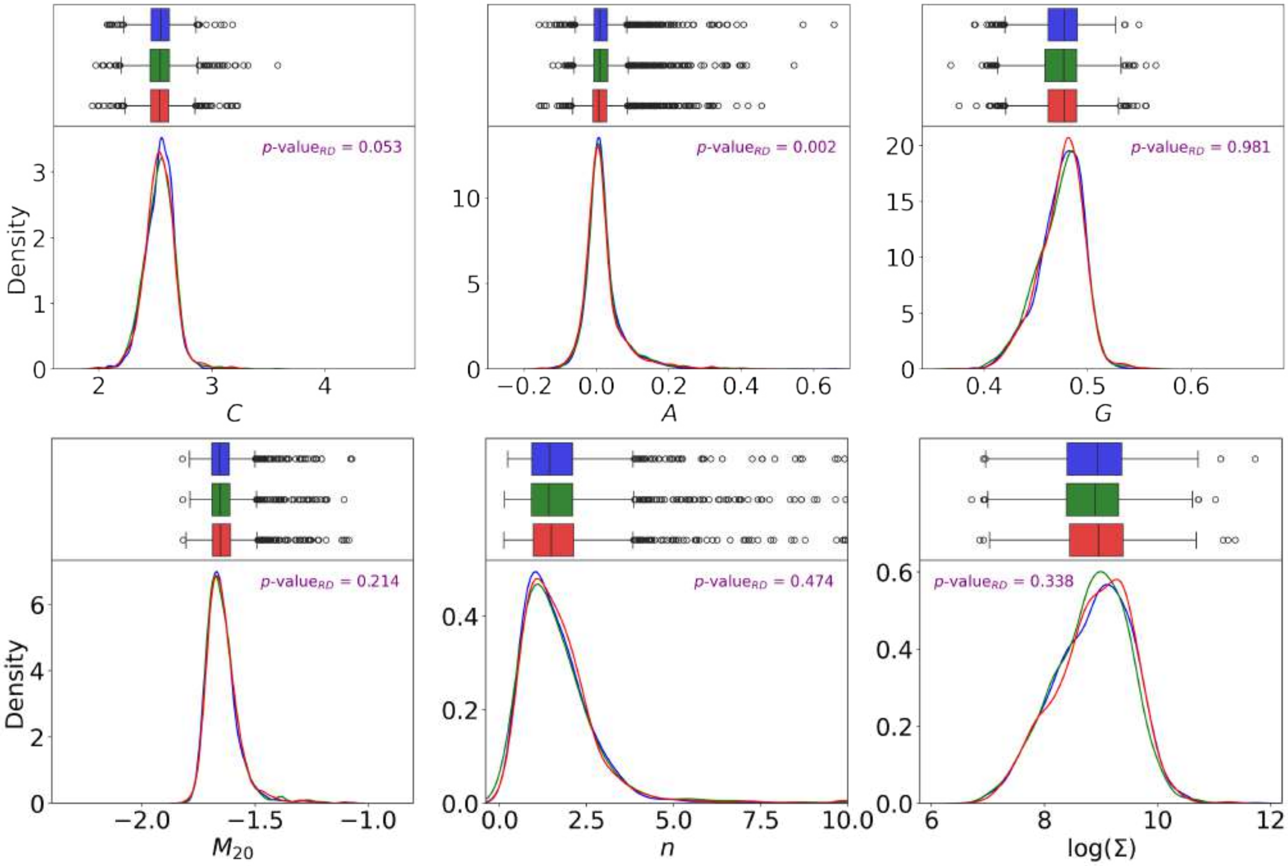

Figure 4.12: Similar to Figure 4.5, but only for disk-dominated galaxies.

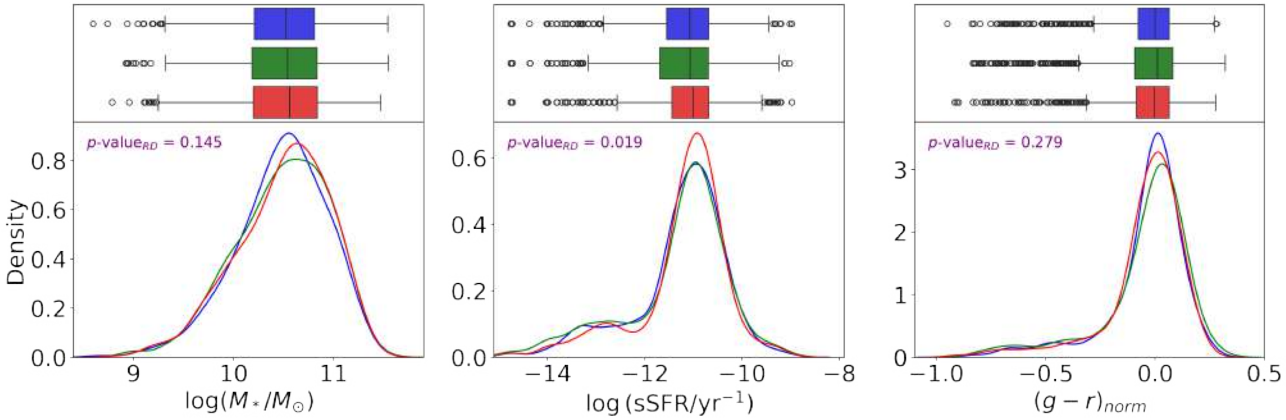

Figure 4.13: Similar to Figure 4.6, but only for bulge-dominated galaxies.

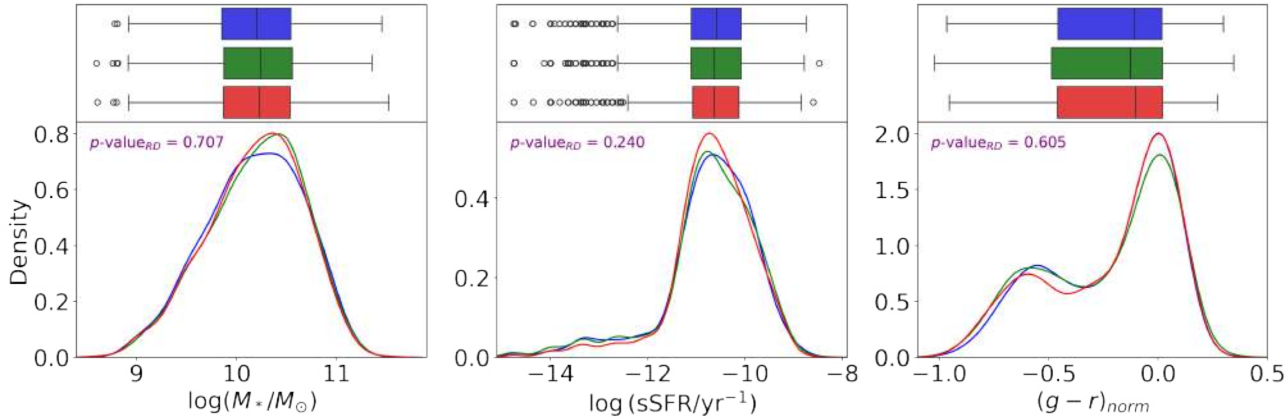

Figure 4.14: Similar to Figure 4.6, but only for disk-dominated galaxies.

Table 4.8: Median values (M) and standard deviations (σ) of the morphological and physical parameters in the three studied environments. Here, we separate between bulge-dominated and disk-dominated galaxies.

Parameter	Relaxed clusters	Intermediate clusters	Disturbed clusters
Bulges			
C	$M = 2.81$, $\sigma = 0.18$	$M = 2.81$, $\sigma = 0.18$	$M = 2.80$, $\sigma = 0.19$
A	$M = 0.01$, $\sigma = 0.04$	$M = 0.01$, $\sigma = 0.04$	$M = 0.01$, $\sigma = 0.05$
G	$M = 0.52$, $\sigma = 0.02$	$M = 0.52$, $\sigma = 0.02$	$M = 0.52$, $\sigma = 0.02$
M_{20}	$M = -1.77$, $\sigma = 0.07$	$M = -1.76$, $\sigma = 0.07$	$M = -1.76$, $\sigma = 0.07$
n	$M = 2.80$, $\sigma = 1.70$	$M = 2.78$, $\sigma = 2.02$	$M = 2.70$, $\sigma = 1.52$
$\log(\Sigma)$	$M = 9.15$, $\sigma = 0.50$	$M = 9.12$, $\sigma = 0.48$	$M = 9.17$, $\sigma = 0.51$
$\log(M_*/M_\odot)$	$M = 10.52$, $\sigma = 0.45$	$M = 10.54$, $\sigma = 0.47$	$M = 10.56$, $\sigma = 0.47$
$\log(\mathrm{sSFR/yr^{-1}})$	$M = -11.08$, $\sigma = 0.97$	$M = -11.07$, $\sigma = 1.07$	$M = -11.01$, $\sigma = 0.95$
$(g-r)_{\mathrm{norm}}$	$M = 0.00$, $\sigma = 0.18$	$M = 0.01$, $\sigma = 0.21$	$M = -0.01$, $\sigma = 0.19$
Disks			
C	$M = 2.55$, $\sigma = 0.12$	$M = 2.54$, $\sigma = 0.14$	$M = 2.54$, $\sigma = 0.13$
A	$M = 0.01$, $\sigma = 0.06$	$M = 0.01$, $\sigma = 0.06$	$M = 0.01$, $\sigma = 0.06$
G	$M = 0.48$, $\sigma = 0.02$	$M = 0.48$, $\sigma = 0.02$	$M = 0.48$, $\sigma = 0.02$
M_{20}	$M = -1.66$, $\sigma = 0.07$	$M = -1.66$, $\sigma = 0.08$	$M = -1.65$, $\sigma = 0.08$
n	$M = 1.43$, $\sigma = 1.32$	$M = 1.41$, $\sigma = 1.66$	$M = 1.47$, $\sigma = 1.33$
$\log(\Sigma)$	$M = 8.94$, $\sigma = 0.69$	$M = 8.89$, $\sigma = 0.66$	$M = 8.95$, $\sigma = 0.68$
$\log(M_*/M_\odot)$	$M = 10.20$, $\sigma = 0.49$	$M = 10.24$, $\sigma = 0.48$	$M = 10.23$, $\sigma = 0.48$
$\log(\mathrm{sSFR/yr^{-1}})$	$M = -10.58$, $\sigma = 0.97$	$M = -10.64$, $\sigma = 1.00$	$M = -10.64$, $\sigma = 0.87$
$(g-r)_{\mathrm{norm}}$	$M = -0.11$, $\sigma = 0.28$	$M = -0.13$, $\sigma = 0.29$	$M = -0.10$, $\sigma = 0.29$

Table 4.9: Results of the Kolmogorov-Smirnov hypothesis tests applied to the physical and morphological parameters for galaxies separated into bulge-dominated and disk-dominated.

Parameter	p-value$_{\text{KS, RI}}$	p-value$_{\text{KS, RD}}$	p-value$_{\text{KS, ID}}$
Bulge			
C	0.693	0.773	0.979
A	0.103	0.056	0.006
G	0.910	0.075	0.233
M_{20}	0.093	0.073	0.923
n	0.316	0.205	0.137
$\log(\Sigma)$	0.165	0.194	0.007
$\log(M_*/M_\odot)$	0.245	0.145	0.864
$\log(\text{sSFR}/\text{yr}^{-1})$	0.568	0.019	0.081
$(g-r)_{\text{norm}}$	0.042	0.279	0.101
Disk			
C	0.190	0.053	0.471
A	0.760	0.002	0.035
G	0.162	0.981	0.189
M_{20}	0.560	0.214	0.785
n	0.952	0.474	0.189
$\log(\Sigma)$	0.049	0.338	0.005
$\log(M_*/M_\odot)$	0.252	0.707	0.701
$\log(\text{sSFR}/\text{yr}^{-1})$	0.754	0.240	0.295
$(g-r)_{\text{norm}}$	0.293	0.605	0.149

4.4 Fundamental relations of galaxy clusters

Considering that we have at our disposal measurements of galaxy properties with which we can characterize the fundamental relations of the clusters they belong to, we compare these relations in systems of different dynamical states. Specifically, we compare the CMDs, the mass-size relation, and the morphology/SFR vs. local environment relation (i.e., morphology/SFR-density relation and morphology/SFR-clustercentric distance relation).

4.4.1 Color magnitude diagram

In all three subsamples (i.e., relaxed, intermediate, and disturbed clusters), we employ the same robust linear regression model as in Section 3.2. The normalized CMDs for each environment are shown in Figure 4.15, along with the regression parameters and their respective errors. These errors are calculated using 10,000 bootstrap iterations and robust biweight estimators. In this context, we use the t-test to determine if there are significant differences between the slopes of the RCS. This statistical method allows us to calculate the probability (p-value) of finding a difference between the slopes equal to or greater than the observed under the null hypothesis that they are equal, using a certain level of confidence. Similar to the Kolmogorov-Smirnov test, we use a confidence level of 95%. Therefore, with a p-value less than or equal to 0.05, we have sufficient evidence to reject the null hypothesis. The results of this test are presented in Table 4.10, in which no significant differences between relaxed and disturbed clusters are observed, whether in the slope or the intercept of the robust regression model. However, interestingly, we find significant differences between relaxed-intermediate and disturbed-intermediate clusters.

Table 4.10: Results of the t-tests applied to the parameters of robust linear regressions applied to red galaxies in the three types of clusters.

Paramter	p-value$_{\text{t, RI}}$	p-value$_{\text{t, RD}}$	p-value$_{\text{t, ID}}$
Slope	0.033	0.406	0.005
Intercept	0.015	0.701	0.059

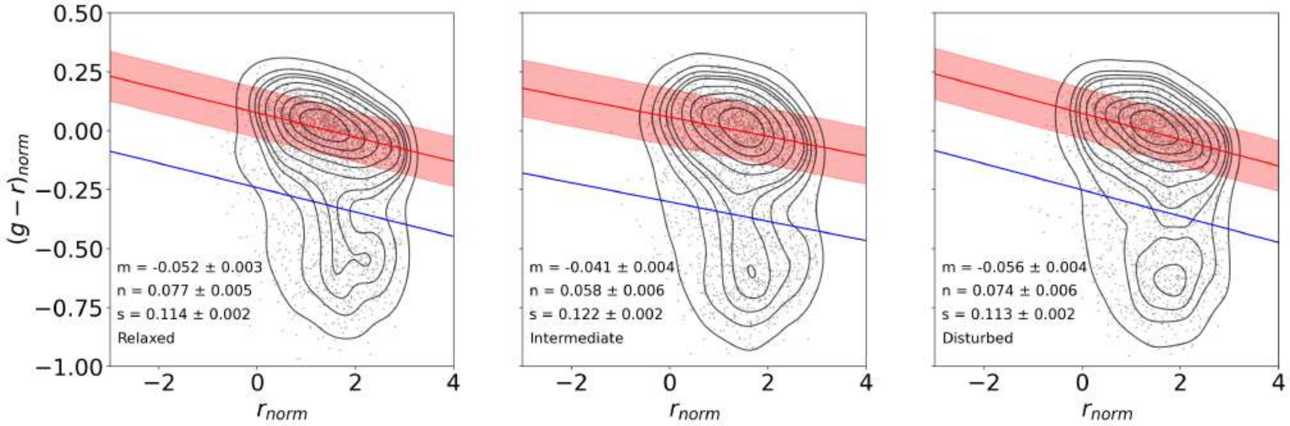

Figure 4.15: Normalized and stacked color-magnitude diagrams, separating the sample into relaxed, intermediate, and disturbed clusters. Each gray point corresponds to a galaxy. The solid red line represents the best-fit Red Sequence, while the red shaded area represents the $\pm 1\sigma$ region. The solid blue line is the same best-fit Red Sequence line but shifted 3σ downwards. The text shows the parameters of the robust linear regressions with their respective errors.

On the other hand, we can use the CMDs to delineate subpopulations within each cluster type. We define Red Sequence galaxies as those falling within $\pm 1\sigma$ of the best fit, while Blue Cloud galaxies are identified as those lying beyond 3σ from the best fit. Meanwhile, we define the Green Valley as the intermediate zone between these two populations. This can be expressed as

$$\begin{aligned}
&\text{Red Sequence: } m_{\text{model}} r_{\text{norm}} + n_{\text{model}} - \sigma_{\text{model}} \leq (g-r)_{\text{norm}} \leq m_{\text{model}} r_{\text{norm}} + n_{\text{model}} + \sigma_{\text{model}} \\
&\text{Green Valley: } m_{\text{model}} r_{\text{norm}} + n_{\text{model}} - 3\sigma_{\text{model}} < (g-r)_{\text{norm}} < m_{\text{model}} r_{\text{norm}} + n_{\text{model}} + \sigma_{\text{model}} \\
&\text{Blue Cloud: } (g-r) \leq m_{\text{model}} r_{\text{norm}} - 3\sigma_{\text{model}},
\end{aligned} \tag{4.1}$$

where m_{model}, n_{model} and σ_{model} correspond to the slope, the intercept, and the scatter of the best fit, respectively.

Next, we compare the structural and physical parameters in these three populations for the three different environments, analogously to Section 4.3. We display the distribution of the structural parameters of galaxies for the Red Sequence, Green Valley and Blue Cloud in Figures 4.16, 4.17 and 4.18, respectively. Also, we present the distribution of the physical properties of galaxies in Figures 4.19, 4.20 and 4.21, following the same order. The median values and standard deviations of these parameters are tabulated in Table 4.11, and the results of the Kolmogorov-Smirnov tests comparing the galaxy properties for different dynamical states of clusters in Table 4.12.

Regardless of the environment, we observe that the median values for the concentration, Gini coefficient, Sersic index, compactness and stellar mass increase as the galaxies become redder (i.e., following the sequence blue cloud-green valley-red sequence). On the other side, M_{20} and specific star formation rate decrease.

Now, focusing on the differences between the relaxed and disturbed clusters, we find that Red Sequence galaxies are the most affected by the dynamical states. The concentration index, asymmetry, M_{20}, Sersic index, specific star formation rate and normalized color present significant differences between relaxed and disturbed clusters. In the case of Green Valley and Blue Cloud galaxies, they are only affected in their specific star formation rates.

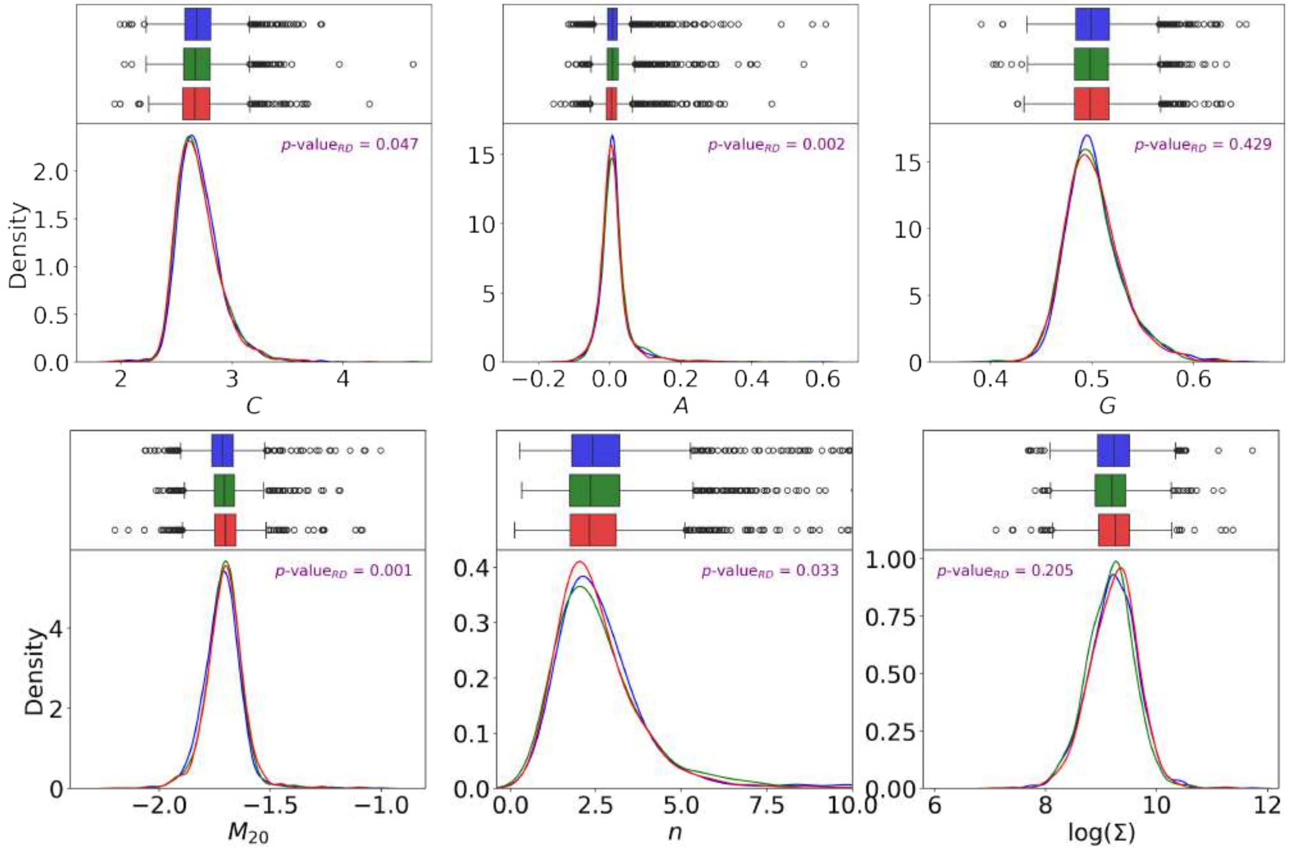

Figure 4.16: Similar to 4.5, but only for Red Sequence galaxies.

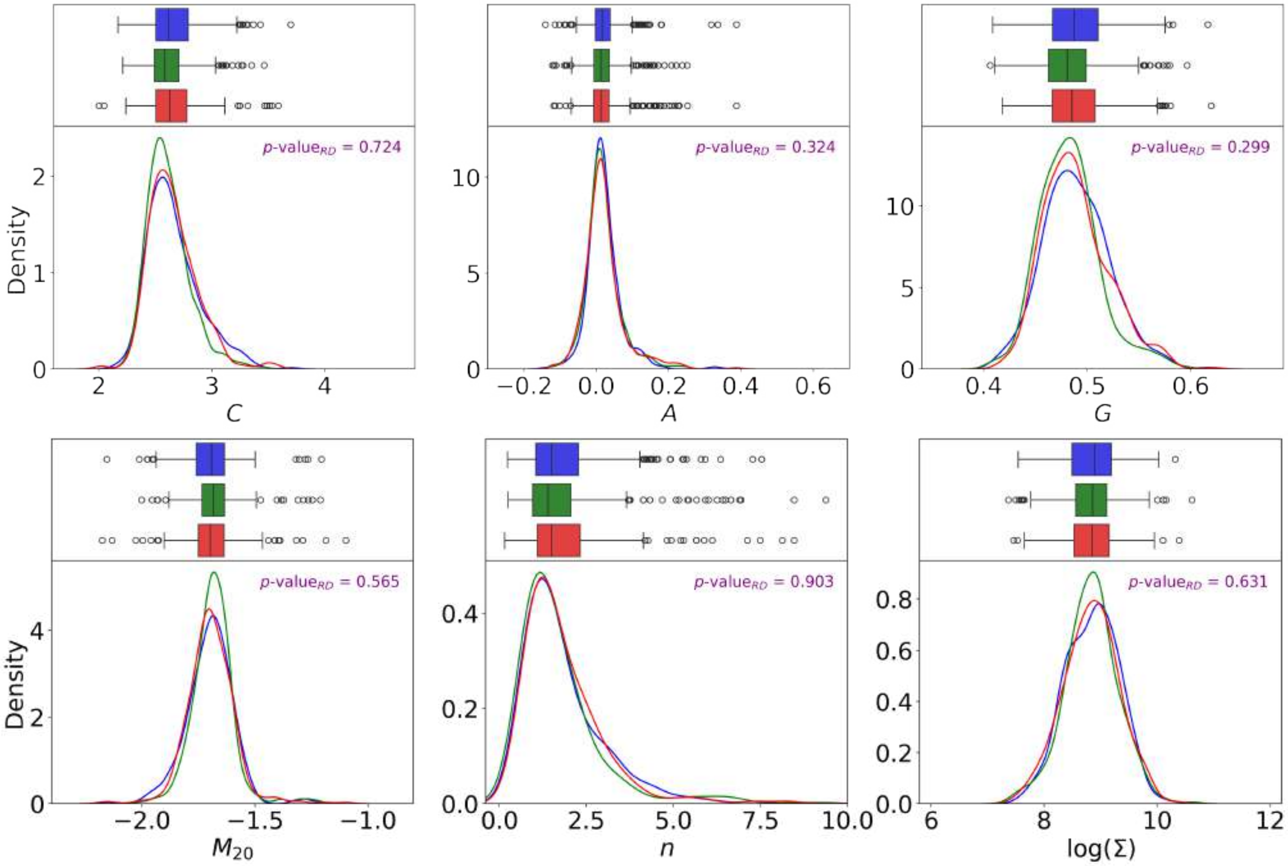

Figure 4.17: Similar to 4.5, but only for Green Valley galaxies.

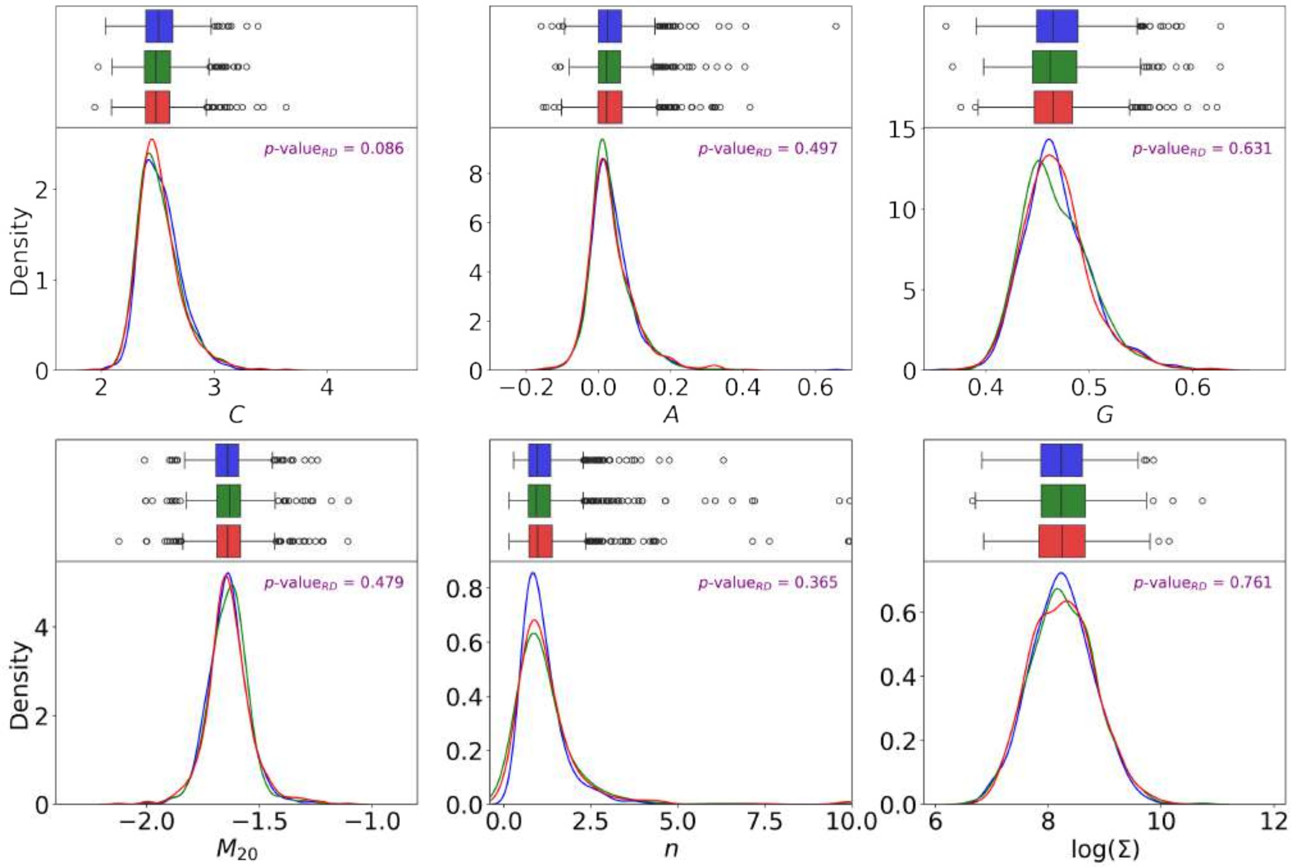

Figure 4.18: Similar to 4.5, but only for Blue Cloud galaxies.

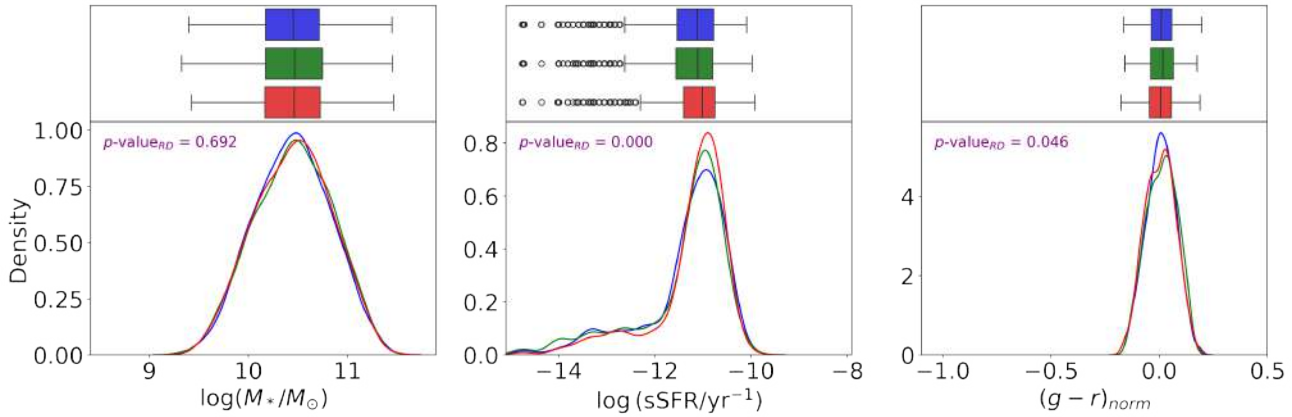

Figure 4.19: Similar to 4.6, but only for Red Sequence galaxies.

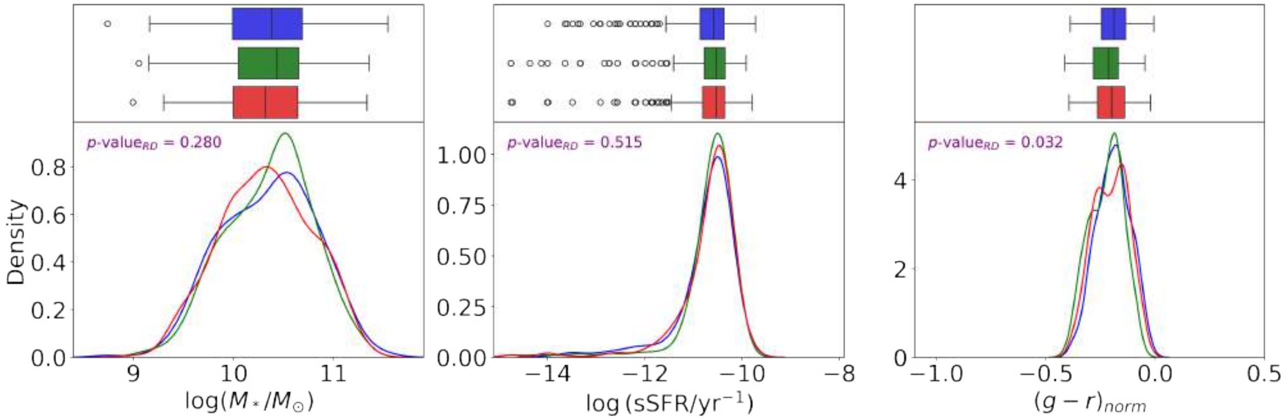

Figure 4.20: Similar to 4.6, but only for Green Valley galaxies.

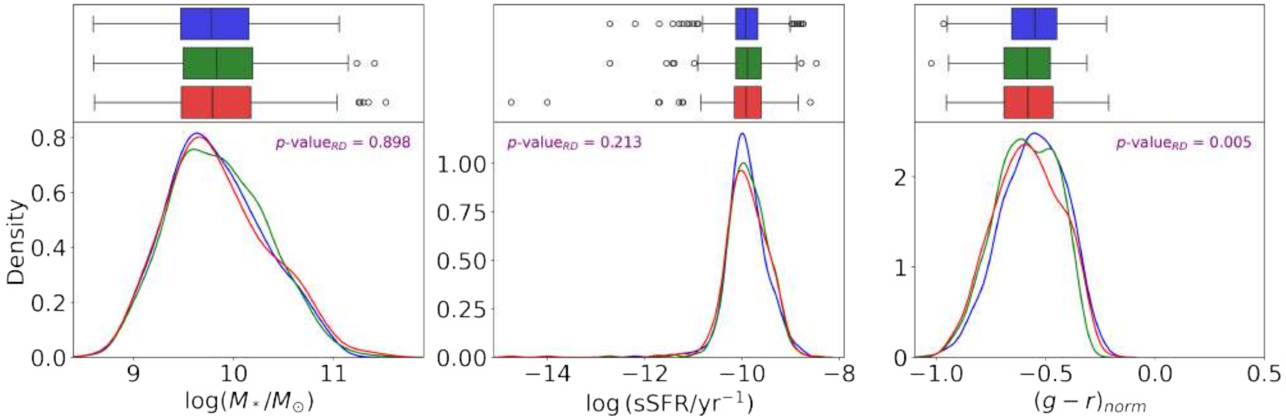

Figure 4.21: Similar to 4.6, but only for Blue Cloud galaxies.

Table 4.11: Median values (M) and standard deviations (σ) of the structural and physical parameters in the three studied environments. Here, we separate between Red Sequence, Green Valley and Blue Cloud galaxies.

Parameter	Relaxed clusters	Intermediate clusters	Disturbed clusters
Red Sequence			
C	$M = 2.68$, $\sigma = 0.20$	$M = 2.67$, $\sigma = 0.20$	$M = 2.67$, $\sigma = 0.20$
A	$M = 0.01$, $\sigma = 0.05$	$M = 0.01$, $\sigma = 0.05$	$M = 0.01$, $\sigma = 0.05$
G	$M = 0.50$, $\sigma = 0.03$	$M = 0.50$, $\sigma = 0.03$	$M = 0.50$, $\sigma = 0.03$
M_{20}	$M = -1.71$, $\sigma = 0.09$	$M = -1.71$, $\sigma = 0.09$	$M = -1.70$, $\sigma = 0.09$
n	$M = 2.40$, $\sigma = 1.73$	$M = 2.34$, $\sigma = 1.95$	$M = 2.30$, $\sigma = 1.53$
$\log(\Sigma)$	$M = 9.23$, $\sigma = 0.44$	$M = 9.19$, $\sigma = 0.42$	$M = 9.26$, $\sigma = 0.44$
$\log(M_*/M_\odot)$	$M = 10.45$, $\sigma = 0.38$	$M = 10.46$, $\sigma = 0.39$	$M = 10.46$, $\sigma = 0.39$
sSFR	$M = -11.11$, $\sigma = 0.89$	$M = -11.11$, $\sigma = 0.96$	$M = -11.01$, $\sigma = 0.82$
$(g-r)_{\rm norm}$	$M = 0.01$, $\sigma = 0.07$	$M = 0.02$, $\sigma = 0.07$	$M = 0.01$, $\sigma = 0.07$
Green Valley			
C	$M = 2.62$, $\sigma = 0.23$	$M = 2.58$, $\sigma = 0.19$	$M = 2.62$, $\sigma = 0.22$
A	$M = 0.02$, $\sigma = 0.05$	$M = 0.01$, $\sigma = 0.05$	$M = 0.01$, $\sigma = 0.06$
G	$M = 0.49$, $\sigma = 0.03$	$M = 0.48$, $\sigma = 0.03$	$M = 0.49$, $\sigma = 0.03$
M_{20}	$M = -1.69$, $\sigma = 0.11$	$M = -1.69$, $\sigma = 0.09$	$M = -1.70$, $\sigma = 0.11$
n	$M = 1.49$, $\sigma = 1.29$	$M = 1.39$, $\sigma = 1.45$	$M = 1.49$, $\sigma = 1.25$
$\log(\Sigma)$	$M = 8.89$, $\sigma = 0.47$	$M = 8.85$, $\sigma = 0.47$	$M = 8.85$, $\sigma = 0.49$
$\log(M_*/M_\odot)$	$M = 10.38$, $\sigma = 0.47$	$M = 10.43$, $\sigma = 0.43$	$M = 10.32$, $\sigma = 0.45$
sSFR	$M = -10.58$, $\sigma = 0.65$	$M = -10.54$, $\sigma = 0.66$	$M = -10.54$, $\sigma = 0.67$
$(g-r)_{\rm norm}$	$M = -0.19$, $\sigma = 0.08$	$M = -0.21$, $\sigma = 0.08$	$M = -0.20$, $\sigma = 0.08$
Blue Cloud			
C	$M = 2.51$, $\sigma = 0.18$	$M = 2.48$, $\sigma = 0.19$	$M = 2.48$, $\sigma = 0.19$
A	$M = 0.02$, $\sigma = 0.07$	$M = 0.02$, $\sigma = 0.06$	$M = 0.02$, $\sigma = 0.07$
G	$M = 0.46$, $\sigma = 0.03$	$M = 0.46$, $\sigma = 0.03$	$M = 0.46$, $\sigma = 0.03$
M_{20}	$M = -1.64$, $\sigma = 0.09$	$M = -1.63$, $\sigma = 0.09$	$M = -1.64$, $\sigma = 0.10$
n	$M = 0.95$, $\sigma = 0.85$	$M = 0.93$, $\sigma = 1.50$	$M = 0.97$, $\sigma = 1.28$
$\log(\Sigma)$	$M = 8.23$, $\sigma = 0.54$	$M = 8.23$, $\sigma = 0.58$	$M = 8.23$, $\sigma = 0.57$
$\log(M_*/M_\odot)$	$M = 9.78$, $\sigma = 0.48$	$M = 9.83$, $\sigma = 0.48$	$M = 9.79$, $\sigma = 0.51$
sSFR	$M = -9.92$, $\sigma = 0.42$	$M = -9.89$, $\sigma = 0.40$	$M = -9.92$, $\sigma = 0.49$
$(g-r)_{\rm norm}$	$M = -0.55$, $\sigma = 0.14$	$M = -0.59$, $\sigma = 0.14$	$M = -0.58$, $\sigma = 0.15$

Table 4.12: Results of the Kolmogorov-Smirnov hypothesis tests applied to the physical and morphological parameters for galaxies separated into Red Sequence, Green Valley and Blue Cloud.

Parameter	p-value$_{\text{KS, RI}}$	p-value$_{\text{KS, RD}}$	p-value$_{\text{KS, ID}}$
Red Sequence			
C	0.113	0.047	0.847
A	0.041	0.002	0.002
G	0.132	0.429	0.623
M_{20}	0.012	0.001	0.455
n	0.255	0.033	0.349
$\log(\Sigma)$	0.008	0.205	0.000
$\log(M_*/M_\odot)$	0.546	0.692	0.943
sSFR	0.046	0.000	0.007
$(g-r)_{\text{norm}}$	0.121	0.046	0.035
Green Valley			
C	0.014	0.724	0.030
A	0.307	0.324	0.901
G	0.001	0.299	0.020
M_{20}	0.067	0.565	0.043
n	0.192	0.903	0.121
$\log(\Sigma)$	0.185	0.631	0.376
$\log(M_*/M_\odot)$	0.573	0.280	0.085
sSFR	0.106	0.515	0.032
$(g-r)_{\text{norm}}$	0.085	0.300	0.001
Blue Cloud			
C	0.113	0.086	0.671
A	0.528	0.497	0.871
G	0.036	0.631	0.272
M_{20}	0.134	0.479	0.123
n	0.468	0.365	0.666
$\log(\Sigma)$	0.738	0.761	0.787
$\log(M_*/M_\odot)$	0.370	0.898	0.300
sSFR	0.064	0.213	0.494
$(g-r)_{\text{norm}}$	0.002	0.005	0.167

Table 4.13: Abundances of galaxies for color-magnitude diagram populations.

Fraction (%)	Bulge	Disk	Quiescent	Star-forming
Red Sequence				
Relaxed	49.6	49.9	58.1	41.5
Intermediate	45.1	54.6	58.8	41.2
Disturbed	45.8	53.8	53.2	46.8
Green Valley				
Relaxed	36.2	63.0	20.3	79.7
Intermediate	25.8	74.0	13.7	86.3
Disturbed	33.1	66.1	19.8	80.2
Blue Cloud				
Relaxed	14.5	84.7	1.4	98.7
Intermediate	14.0	85.7	0.6	99.4
Disturbde	12.8	86.0	1.4	98.6

In Table 4.13 we observe the galaxy fractions as we separate galaxies by quenching state and morphological types, for Red Sequence, Green valley, and Blue Cloud galaxies. Separating by morphological type, we find a 3.4&, 3.1% and 1.7% difference between relaxed and disturbed clusters, for RS, GV and BC galaxies, respectively. In the same comparison, we note that there is a difference of 0.8%, 3.1% and 0.9% in the abundances of quenched galaxies, following the same order.

4.4.2 Mass-size relation

We study the mass-size relation by classifying galaxies in two different ways. On one hand, we separate galaxies by morphological types, and on the other hand, according to their quenching state. For the latter, we employ the criteria where quenched galaxies are those with $\log(\mathrm{sSFR/yr^{-1}}) < -10.5$, and star-forming galaxies are those with $\log(\mathrm{sSFR/yr^{-1}}) \geq -10.5$ (Brown et al., 2017; Cora et al., 2018; Lacerna et al., 2022).

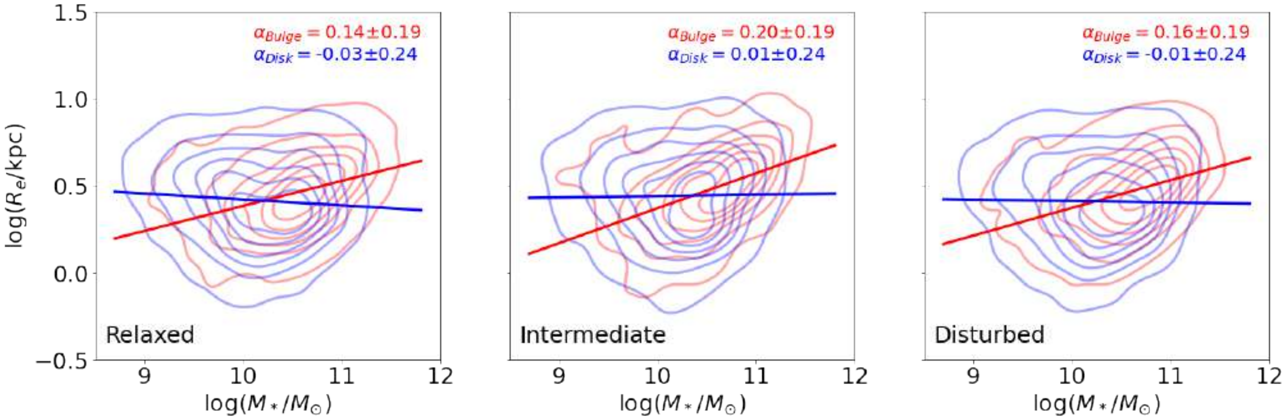

Figure 4.22: Distribution of bulge galaxies (red contours) and disk galaxies (blue contours) in the logarithmic mass-size space, separated into the three studied environments. The solid lines show the linear regressions applied to the data (following the same color code), and the text indicates the slopes with their respective errors for each type of galaxy.

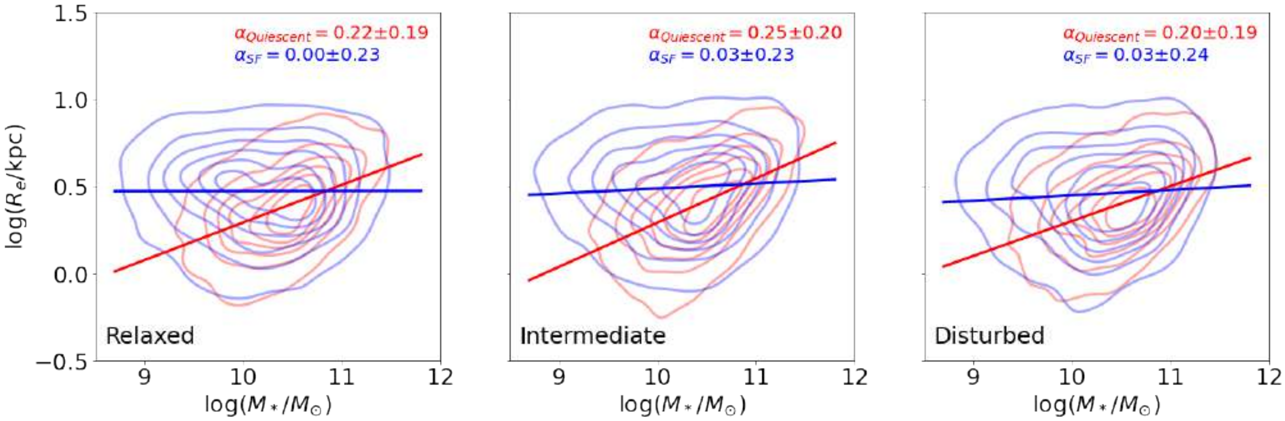

Figure 4.23: Similar to Figure 4.22, but separating galaxies into quiescent and star-forming.

In Figures 4.22 and 4.23, the mass-size relations for morphology and sSFR, respectively, are depicted. They show the slopes of the linear regressions fitted with the Huber Regressor and their respective errors calculated using bootstrap.

While some differences are observed among the various environments for the mass-size relations, quantifying them is necessary. For this purpose, we again utilize the t-test to determine if there are statistically significant differences among the slopes. The results of these tests are presented in Table 4.14. We find no statistically significant differences between relaxed and disturbed clusters. However, similar to the results of the CMDs, we notice that differences between relaxed-intermediate and disturbed-intermediate clusters are present.

Finally, we study the mass-size plane by separating it into morphological types and using

Table 4.14: Results of the t-tests applied to the slopes of the linear regressions for the three types of clusters in the mass-size plane.

Galaxy type	p-value$_{\text{t, RI}}$	p-value$_{\text{t, RD}}$	p-value$_{\text{t, ID}}$
Morphology			
Bulge	0.006	0.837	0.010
Disk	0.052	0.982	0.055
Star-formation rate			
Quiescent	0.006	0.842	0.010
Star-forming	0.054	0.986	0.057

two different parameters as controls. Firstly, we employ the Sersic index (Figure 4.24), followed by the specific star formation rate (Figure 4.25). In both figures, we use bins of width 0.2 dex in masses and width 0.1 dex in sizes (R_e). The color of each bin represents the average within it. If there are insufficient elements to form a bin (a value of 7 was arbitrarily chosen), then individual data points appear with the same color scale.

In disk-dominated galaxies, we observe a gradient from low-mass, high-size galaxies to high-mass, low-size galaxies, in which the Sersic index increases and the specific star formation rate decreases. This is not observed in bulge-dominated galaxies, so as we discuss later (Section 5), this behavior may be due to the fact that we have a morphological mix in this category.

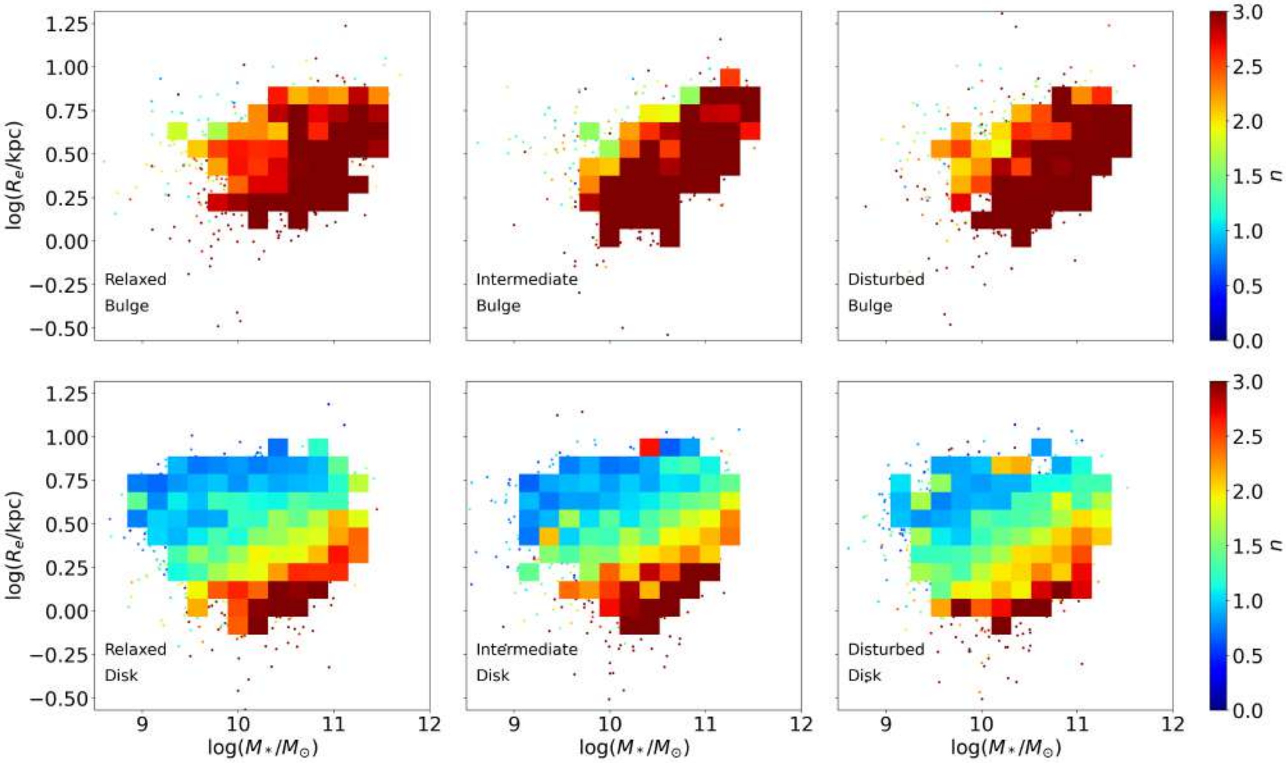

Figure 4.24: Mass-size relation using Sersic index as control parameter and separating galaxies into morphological types. The data are grouped into bins of size 0.2 for stellar mass, and of size 0.1 for effective radius. The number of elements required to form a bin was arbitrarily chosen as seven. If not met, the isolated points are displayed, following the same color scale.

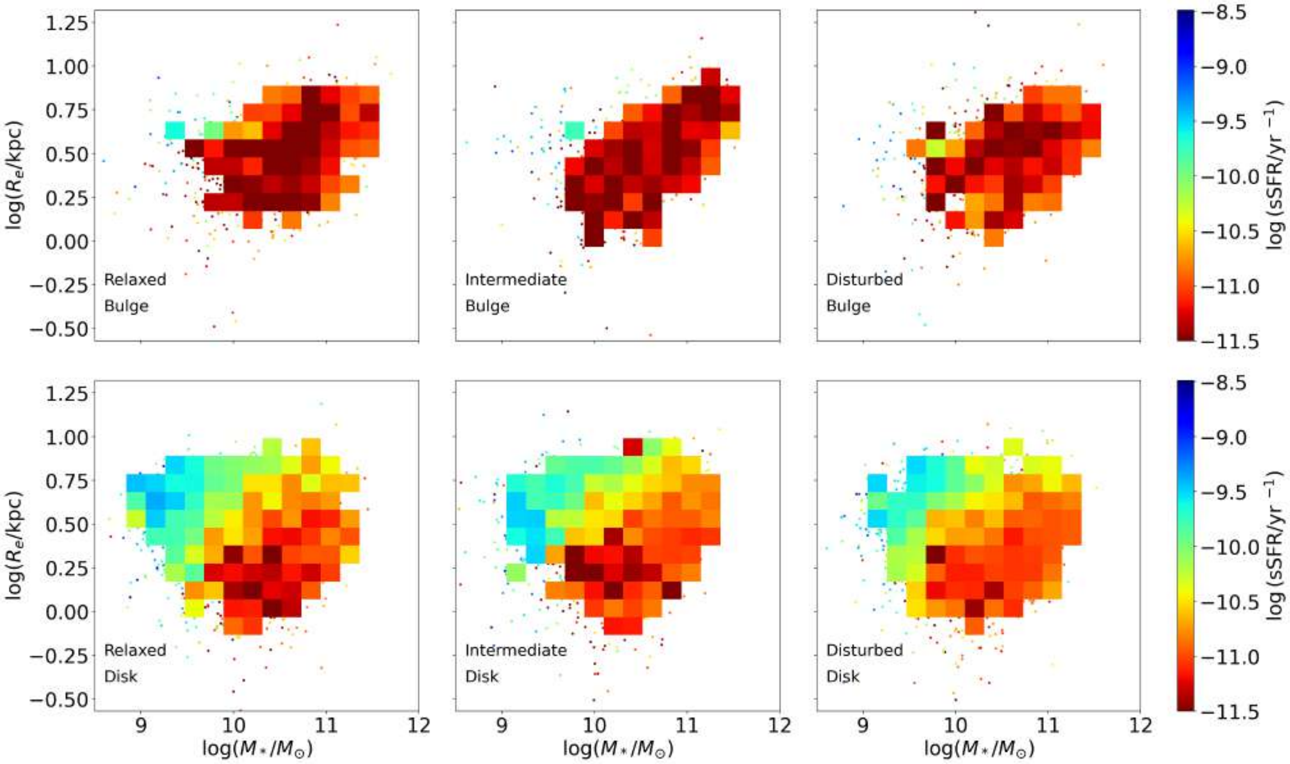

Figure 4.25: Mass-size relation using sSFR as control parameter and separating galaxies into morphological types. The data are grouped into bins of size 0.2 for stellar mass, and of size 0.1 for effective radius. The number of elements required to form a bin was arbitrarily chosen as seven. If not met, the isolated points are displayed, following the same color scale.

4.4.3 Morphology/SFR vs local environment

To investigate whether there are differences in the relationship between galaxies and their local environment, we have used parameters such as the normalized clustercentric distance (R/R_{200}) and the local density. The latter parameter is defined as $\log(\Sigma_{10}) = 10/A$, where A is the circular area containing the 10 nearest neighbors of a galaxy (Dressler, 1980; Vulcani et al., 2023a).

Figure 4.26 displays the fractions of galaxy types according to morphology (solid lines) and star formation rate (SFR) (dashed lines) as a function of local density, whereas Figure 4.27 presents the same fractions but as a function of the clustercentric distance. The position of the X-ray peak has been utilized as the center of these systems.

For the morphology-density relation, we observe that the fraction of bulge-dominated galaxies increases to the densest regions of the clusters, regarding the dynamical state, but this behavior is less pronounced in intermediate clusters. In the case of the sSFR-density relation, the

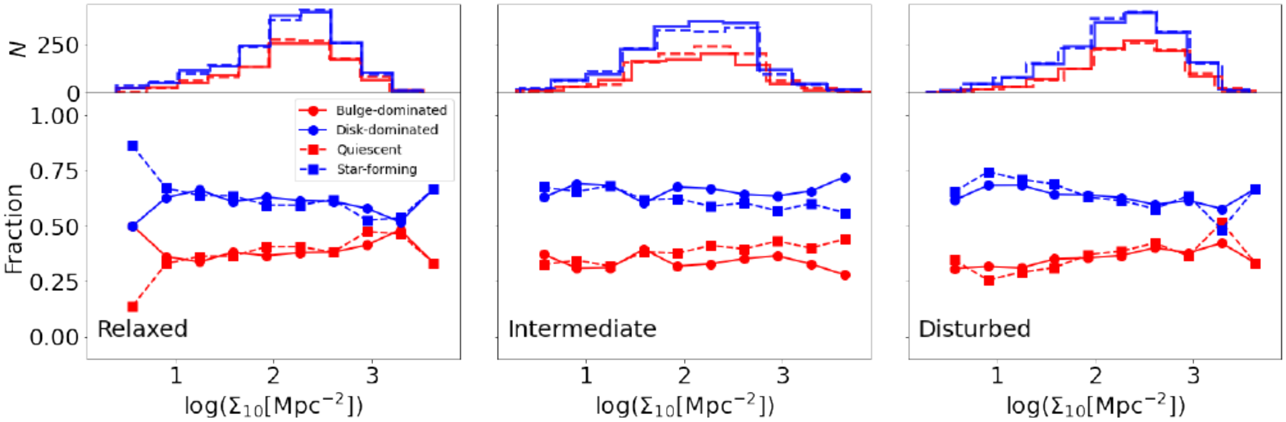

Figure 4.26: The Morphology/SFR-density relation for relaxed, intermediate, and disturbed clusters (from left to right). Data are binned into 10 categories. Solid blue (red) lines correspond to disk (bulge) galaxies, while the dashed blue and red lines represent star-forming and quiescent galaxies, respectively. Upper panels display histograms indicating the number of elements in each bin. Lower panels show the fraction of galaxies per bin.

quiescent fraction increases to the densest regions in the three different environments. On the other hand, the morphology-clustercentric distance relation and sSFR-clustercentric distance relations are clearly seen, with the bulge-dominated and quiescent galaxy fractions increasing to the centers of the clusters.

However, it is important to note that the bulge-dominated galaxy fractions are unusually low for galaxy clusters, as reported by previous findings (e.g., Dressler, 1980; Postman and Geller, 1984; Dressler et al., 1997; Blanton and Moustakas, 2009; Vulcani et al., 2023a,b). This is appropriately discussed in Section 5.

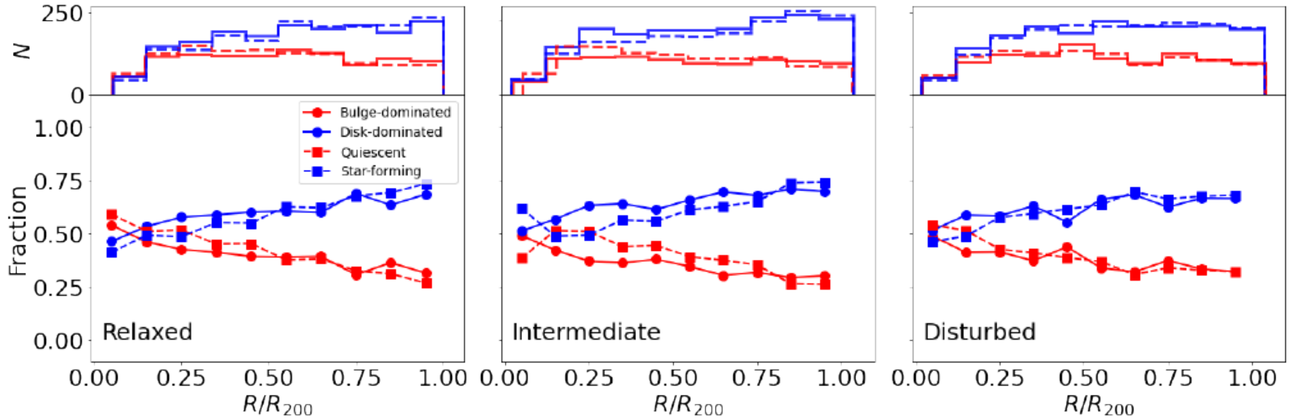

Figure 4.27: The Morphology/SFR-clustercentric distance relation for relaxed, intermediate, and disturbed clusters (from left to right). Data are binned into 10 categories. Solid blue (red) lines correspond to disk (bulge) galaxies, while the dashed blue and red lines represent star-forming and quiescent galaxies, respectively. Upper panels display histograms indicating the number of elements in each bin. Lower panels show the fraction of galaxies per bin.

Chapter 5

Discussion

5.1 Photometric redshifts and cluster membership

As shown in Section 4.1, the photometric redshifts determined by Wen and Han (2022) exhibit high precision, reflected in their residuals ($\text{mean}_{\text{BW}} = 0.005$, $\sigma_{\text{BW}} = 0.03$). However, for the purposes for which they were used, they have a disadvantage, as mentioned in Section 3.1. Following the photometric member assignment method developed by Pelló et al. (2009), in addition to having the photometric redshift of candidate galaxies, the probability distribution of this value is also required to assign membership to a given object. One solution to this problem could have been to use the photometric redshifts calculated by `Le Phare`. However, as observed in Table 4.1, this method has a lower precision than the one used by Wen and Han (2022). Considering this, we decide to approximate the probability distribution of the photometric redshifts of galaxies using a Gaussian function with mean $\mu = z_{\text{phot}}$ and standard deviation $\sigma = z_{\text{phot,err}}$. Although we are aware that these distributions may not necessarily follow this form (Pelló et al., 2009), we are willing to sacrifice this information in exchange for greater precision in determining the photometric redshifts. With these choices, we ensure at least 80% completeness in assigning members to galaxy clusters, with contamination reaching a maximum of 25%.

In Figure 5.1, we show the probability threshold used in other works as a reference. In Pelló et al. (2009), the authors focused on the completeness of the membership selection, rather than the contamination. In the case of Rodríguez-Muñoz et al. (2019), their aim was to achieve a contamination level lower than 20%. As a result, a subsample of their data has a completeness lower than 70%, but for the rest of the data, they achieved a good balance. In this thesis, similar to Kesebonye et al. (2023), we seek a compromise between completeness and contamination. Although we use similar photometric data to Kesebonye et al. (2023), we attribute our slightly

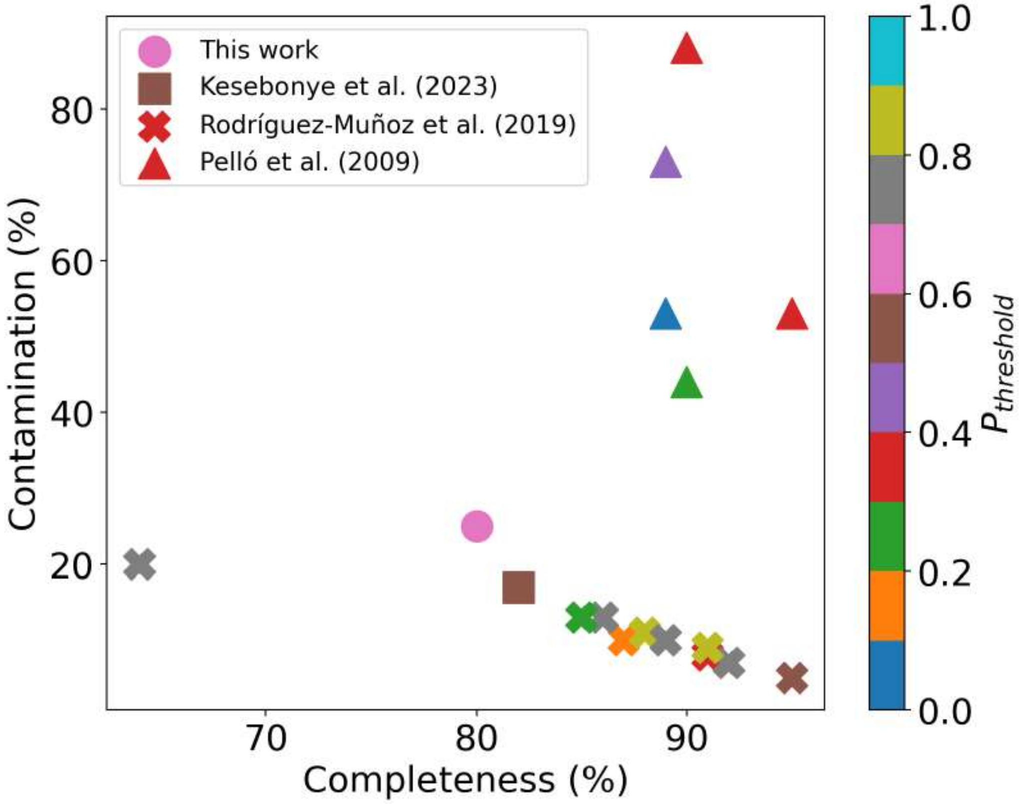

Figure 5.1: Completeness-contamination plane for the probabilistic cluster membership method. The color code indicates the probability threshold used in each case. Our work is marked with a dot, and for reference, we include the thresholds used by Pelló et al. (2009, triangles), Rodríguez-Muñoz et al. (2019, X-markers) and Kesebonye et al. (2023, square).

lower quality of membership assignment (i.e., higher contamination, lower completeness) to the fact that we do not have the probability distribution of photometric redshifts. In their case, they used the `ZCLUSTER` package (Hilton et al., 2021; Pillay et al., 2021) to estimate the maximum likelihood galaxy photo-zs and their probability distribution using the template-fitting method.

5.2 Dynamical state of galaxy clusters

5.2.1 BCG selection method

As mentioned earlier, the BCG selection is a crucial step in classifying the dynamical state of galaxy clusters. Considering this, we use an automatic method to pre-select the BCG, which is then confirmed or rejected through visual inspection. This approach yields a 70% accuracy for the automatic method. Previous studies have reported that the three common characteristics of

BCGs (being the brightest, most extended, and most central member) can conflict in up to 20% of cases, especially when shallow photometry is used or when dealing with unrelaxed clusters (Von Der Linden et al., 2007; Kluge et al., 2020). Additionally, Kluge et al. (2024) employed `eROMaPPer`, an enhanced version of `redMaPPer` (Rykoff et al., 2014), for BCG selection. By reanalyzing different literature samples, they found that the BCG is correctly identified in $\sim 80\%$ of cases.

Our method's accuracy is lower but consistent with previous works, given that we use a simpler automatic approach. Specifically, we select the brightest galaxy within $\pm 1\sigma$ of the best RS fit as the BCG. Interestingly, when we calculate the accuracy of the method separately for relaxed and unrelaxed clusters, we find no significant differences, obtaining 62% and 64% agreement with visual inspection, respectively.

We propose several explanations for the incorrect selections. In the case of relaxed cool-core clusters, cold gas can directly reach the BCG, triggering significant star formation and/or nuclear activity (e.g., Rawle et al., 2012), resulting in bluer BCGs. Additionally, specific clusters may have central dominant galaxies still forming, with another galaxy farther from the center being redder than the central one, leading to incorrect BCG selection (e.g., Abell 3827, Carrasco et al., 2024, in prep.). Moreover, irrespective of the cluster dynamical state, non-member galaxies might be included due to the 25% contamination of the membership method, causing a foreground galaxy to be misclassified as the BCG. Furthermore, the photometry of some BCGs might be contaminated by nearby sources, as in the case of RXC J0138.0-2155 and Abell 3017 (see Figure 5.2).

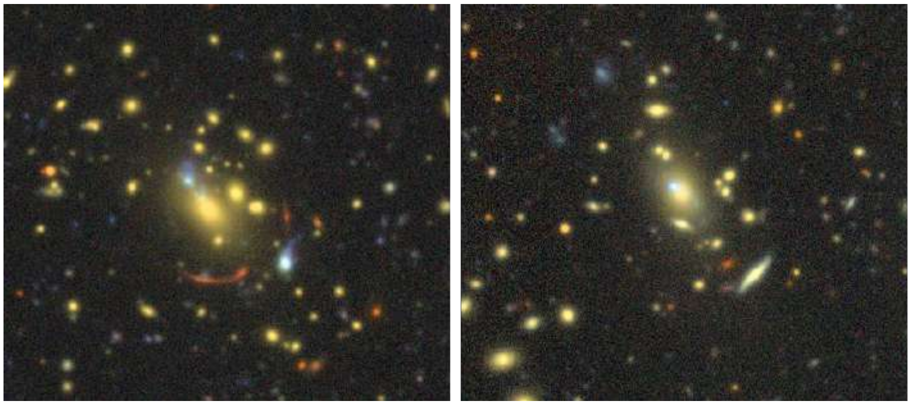

Figure 5.2: RGB images created using the g, r, and i filters, exctracted from the *Legacy Survey Sky Browser*[1]. Examples of clusters with BCGs that have contamination are shown. Left: RXC J0138.0-2155 (relaxed cluster). Right: Abell 3017 (intermediate cluster).

5.2.2 Dynamical parameters

While classifying dynamical states based on a single parameter can be quite useful for distinguishing the most extreme cases, a proper combination of these indices can be more robust. To quantify this, we compare our results with those obtained by Yuan and Han (2020) and Yuan et al. (2022). For the disturbed clusters, we find consistent results between our classification system and that used by Yuan and Han (2020) and Yuan et al. (2022) ($\delta > 0$). However, we note a discrepancy for the relaxed clusters. Of the 32 relaxed galaxy clusters in our sample, 13 do not fall into this category according to the Yuan and Han (2020) and Yuan et al. (2022) criteria ($\delta < 0$). This fraction corresponds to 40%, and given that this is a rather high value, we have individually analyze these 13 systems. All of them have a wbs value of -0.0057, which is almost at the threshold of our separation between relaxed and intermediate clusters. However, upon inspection, only Abell 3322, Abell 3783 and MCXCJ0528.9-3927 exhibit interaction features typical of a disturbed cluster (see Figures A.1, A.2 and A.3). This indicates the need for an intermediate systems category, rather than opting for a binary classification between relaxed and disturbed cluster, and our combined use of dynamical state proxies allows us to do this robustly.

The binary separation between relaxed and disturbed clusters arises from the bimodalities found in the distributions of these dynamical parameters, but in some cases, the bimodalities may be absent, making the classification task more challenging (e.g., Campitiello et al., 2022). It has been shown that using two dynamical state proxies together in a two-dimensional parameter space can aid in this classification task (e.g., Cassano et al., 2010, 2013). However, even more robust results can be obtained by combining multiple dynamical parameters, such as with the M statistic (e.g., Rasia et al., 2013; Lovisari et al., 2017). In our case, we have chosen to use PCA with our set of six proxies, finding that the first principal component can effectively separate the dynamical states of the clusters, which is consistent with Campitiello et al. (2022).

5.2.3 Classification of dynamical states

To determine the dynamical state of the galaxy clusters in our sample, we jointly use six commonly employed dynamical parameters from the literature. We decide not to utilize other proxies of dynamical state, such as the magnitude gap between the first and second BCG (e.g., Dariush et al., 2007; Raouf et al., 2019; Lourenço et al., 2023). Considering the percentage of failures in BCG selection and the contamination of the membership method, we deemed the number of clusters where the parameter $\Delta m_{1,2}$ could be contaminated by non-member galaxies to be sufficiently high to potentially affect the results.

However, the set of parameters we have is quite robust, and, as can be observed in the principal component analysis (see Figure 3.5), its first principal component traces the dynamical state of these systems. While one could argue that the training sample to generate this classification is small, it is true that at least in the projected plane of the sky, the results are, in general, consistent with what is expected for different dynamical states, in terms of their gas and member galaxy distributions (see Appendix A.2). Specifically, the X-ray contours are more irregular for disturbed clusters (Yuan and Han, 2020; Yuan et al., 2022), and the RS contours are more consistent with the gas distribution in relaxed clusters (Zenteno et al., 2020).

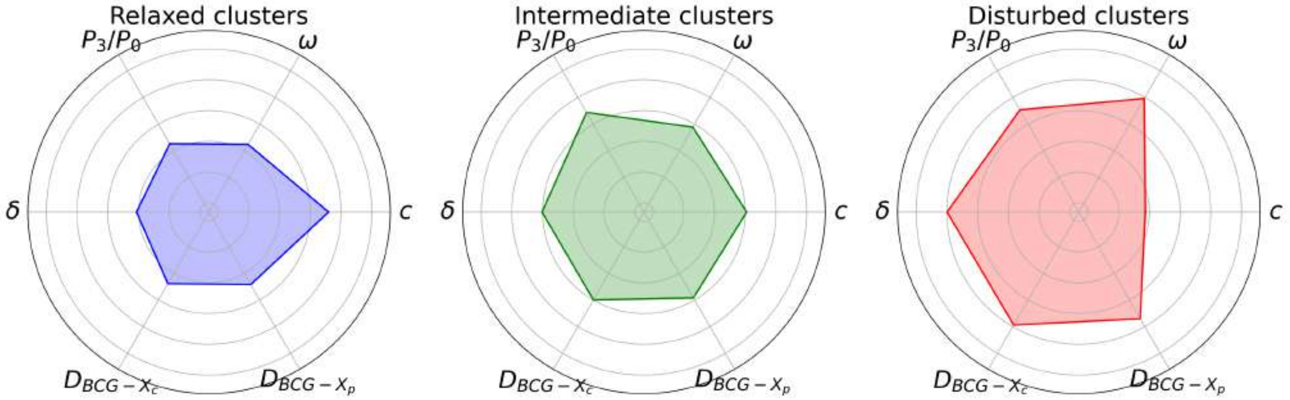

Figure 5.3: Radar charts with the medians of the six dynamical parameters used in this thesis for the three subsamples. The colors blue, green, and red indicate the relaxed, intermediate, and disturbed dynamical states, respectively. The parameters are standardized, and the radar charts are on the same scale for all clusters for comparison purposes. This scale corresponds to $-3.30 \leq$ `param_value` ≤ 2.60, where `param_value` is the dimensionless scaled value of any dynamical parameter.

Furthermore, in Figure 5.3, one can observe that the shape of the radar charts with the median values of the dynamical state proxies is nearly opposite for the relaxed and disturbed clusters, leaving the clusters with intermediate dynamics as a transition zone, giving us confidence in the results. Moreover, in Figure 5.4, we see the median values of each dynamical parameter with their respective standard errors for each dynamical state. We observe a significant difference between relaxed and disturbed clusters, placing the intermediate clusters in a transitional zone between them, which gives us confidence in the methodology employed (i.e., PCA). It is important to mention that the sign of the concentration values has been inverted in Figure 5.4. This was done to facilitate visualization, as this is the only proxy where higher values indicate relaxation, and this can lead to misinterpretations when observing an overlapping zone between relaxed and disturbed clusters that does not actually exist.

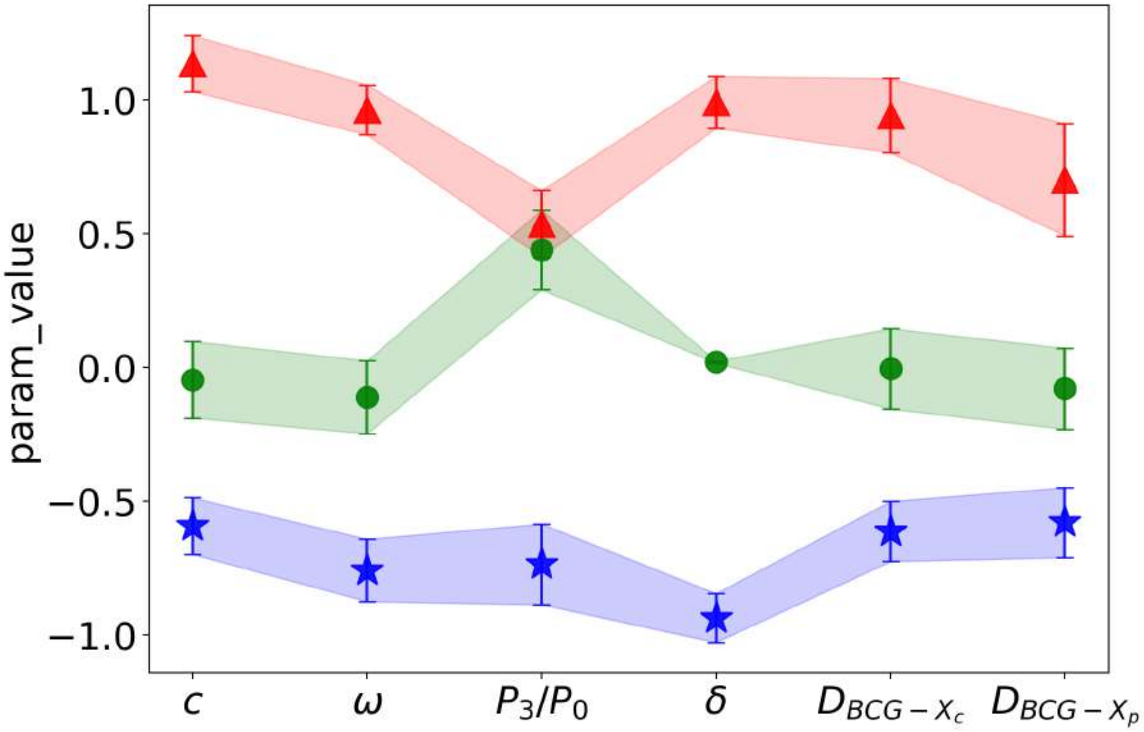

Figure 5.4: Median values of the six dynamical state proxies for the subsamples of relaxed clusters (blue stars), intermediate clusters (green dots), and disturbed clusters (red triangles). The parameter values are scaled in the same way as in Figure 4.2. The concentration parameter c is inverted for visualization purposes only. The shaded areas and error bars represent the 1σ regions.

From our full sample of 87 galaxy clusters, we classifiy 32 ($\sim$ 36%) as relaxed clusters, 30 ($\sim$ 34%) as systems with an intermediate dynamical state, and 25 ($\sim$ 29%) as disturbed clusters of galaxies. Thus, we identify a fraction of $\sim$ 63% of galaxy clusters in an unrelaxed state (intermediate and disturbed), which is consistent with the expected range of $30 - 80\%$ according to previous studies (e.g., Dressler and Shectman, 1988; Santos et al., 2008; Fakhouri et al., 2010; Wen and Han, 2013; Yuan and Han, 2020; Yuan et al., 2022).

5.3 Structural parameters of galaxies

To determine the structural properties of the galaxies, several steps are necessary, as explained in Section 3.5. After downloading the images, the first step was to process them with `SExtractor` to obtain segmentation maps and catalogs with relevant morphological and photometric properties for our study. As mentioned earlier, our `SExtractor` configuration file is based on the one used to construct catalogs in the Legacy Surveys and on the one used in the DES DR2 (Abbott et al., 2021), aiming to make direct comparisons and build catalogs based on configurations that have already been tested and widely used.

Regarding the cutouts of the images, we ensure that there are no issues with galaxies near the boundaries of our study range (R_{200} from the center of the clusters). This is done by downloading images of the clusters with a side length of $2.4R_{200}$.

On the other hand, concerning the selection of an adaptable stamp size for all galaxies, the choice to use a factor of 5 in Equation 3.24 instead of a factor of 2.5, as proposed by Häussler et al. (2007), is based on empirical results where we found that this factor ensures that codes calculating parametric and non-parametric morphology can find the necessary sky box to perform robust statistics. Additionally, considering that statmorph creates a new segmentation map (i.e., Gini segmentation map), in cases where the S/N is low, this map tends to encompass more pixels, which could risk reaching the stamp limits if its size is small.

Regarding the photometric calibrations, we emphasize that the fixed aperture magnitudes used for comparison between the magnitudes obtained by `SExtractor` and those extracted from the DES DR2 catalogs are the same. Additionally, since the configuration files of this algorithm used in this work are similar, we are confident in the robustness of the calibration. Another reason for our confidence is the careful selection of stars. We ensure to select objects with a probability of being a star greater than 99% according to GAIA DR3 data (Gaia Collaboration et al., 2023), and we identifiy main sequence stars to carry out the calibrations. This is done using the DBSCAN clustering algorithm. It is important to clarify that this clustering algorithm is less efficient in images of clusters where the number of stars in the field was small, and even when the number of stars is high, there is a contamination rate close to 1%. Furthermore, another criterion used to select good stars in the context of photometric calibrations (which would later be used for PSF construction as well) is to exclude those with nearby objects within a radius of 25 pixels. This radius is chosen because it coincides with the length of the stamps used for PSF creation. However, diffuse objects that were not detected by `SExtractor` due to low S/N or areas with higher than average statistical noise could not be excluded by our algorithm, adding a certain degree of contamination.

Subsequently, we compute the non-parametric indices using statmorph. As mentioned in the analysis, the input files consisted of science images, weight maps, segmentation maps, and masks. This code provides flags to determine the reliability of the results. In total, we obtain a 0.44% galaxies with unreliable measurements. The unreliable measurements (i.e., `FLAG` > 1; `S/N` < 2.5) indicate issues with the calculation of the parameters. For example, the asymmetry minimizer attempts to leave the edges of the stamps, there are negative fluxes in the science images, or their surface brightness is so low that the random background noise predominates over the galaxy. In Figure 5.5, some examples of galaxies with unreliable measurements are shown. Additionally, `SERSIC_FLAGS` are provided, associated with the fits of these models. Since in this work we use `GALFITM` to fit parametric models, we are not interested in whether the measurements made by statmorph are erroneous or unreliable. In fact, in Figures 3.10 and 3.11, strange residuals are observed after fitting Sersic models to galaxies, but the analysis and discussion of this are beyond the scope of this thesis.

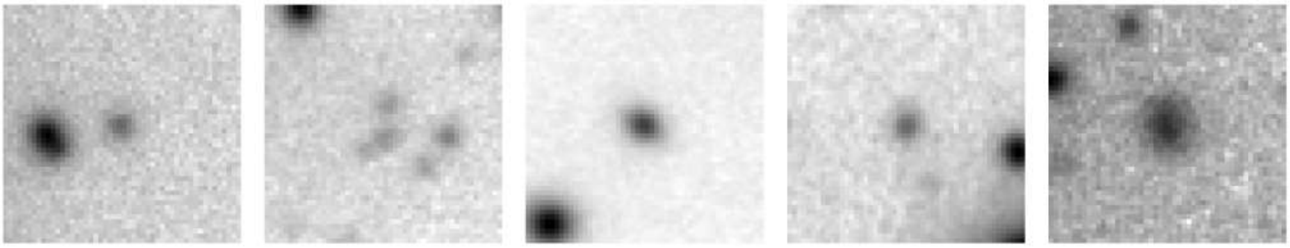

Figure 5.5: Some example of unreliable morphology measurements flagged by `statmorph`. From left to right, we have J001937.55+033607.2 (CL0019.6+0336), J010626.08-594313.9 (SPT-CLJ0106-5943), J030704.23-284026.4 (Abell 3088), J040414.95-270521.0 (Abell 3213) and J052851.36-392809.4 (MCXC J0528.9-3927). In general, these galaxies are too dim; therefore their Gini segmentation maps are contaminated by background fluctuations.

On the parametric measurements side, we use `GALFITM`. In other works, multiple two-dimensional models are often fitted to galaxies. For instance, fitting a Sersic profile and an exponential one allows decomposing galaxies into their bulge and disk components (e.g., Häußler et al., 2022; Lima-Dias et al., 2024). In our case, we opt for Single Sersic Models, as the resolution of our images does not allow us to fit more than one component reliably. We notic in the distribution of χ^2_ν (see Figure 3.16) that the majority of our fits have a value lower than 1, indicating overfitting. Generally, overfitting is undesired as models fit the data so well that they might include noise, and most importantly, they might not generalize well to new data. However, in our case, this is not of major concern since we do not plan to use the fitted model to predict new information; rather, we aim to obtain all the information associated with the model for a single galaxy in each fit. Hence, the observed overfitting does not have significant implications for the results, and as seen in Figures 4.11 and 4.12, the distribution of the Sersic index for bulge and disk galaxies is consistent with what is reported in the literature, i.e., bulge-dominated galaxies have higher Sersic indices that the disk-dominated counterpart (e.g., Shen et al., 2003; Lange et al., 2015).

Regarding the morphological classification, where use the Gini and M_{20} parameters directly, and indirectly the Sersic index, asymmetry, and SNR, we generally obtain results consistent with what is expected in the literature for bulge and disk galaxies, i.e., the bulge galaxies are redder, less star-forming, more compact, more concentrated and less disturbed that disk galaxies (Conselice, 2003; Lotz et al., 2004; Conselice, 2014). In the case of merger galaxies, we notice that the detected fraction is very small ($< 1\%$). We attribute this to the masks used as input for `statmorph`. If `SExtractor` is capable of detecting and separating sources near an object, then these will be masked, and we will not be able to detect a high M_{20} value, which is characteristic of irregular or merging galaxies. Thus, we prefer not to consider these galaxies in the analyses, as our detection capability for them is not reliable.

It is worth noting that the method used for morphologically classify galaxies follows the idea of Sazonova et al. (2020). In the data used in that work, the spatial resolution is better than ours by a factor of ~ 2. Therefore, to determine how much the difference in resolution affects, we use an image of Abell 3827 in the r filter obtained with GMOS and perform the same morphological classification as in the data obtained with DECam. In this cluster, the difference in spatial resolution between both instruments is also a factor of ~ 2. As shown in Figure 5.6, 9% of galaxies are detected as bulges in DECam and disks in GMOS, while 6% are detected as disks in DECam and bulges in GMOS. Therefore, we found an error rate of $\sim 15\%$ in differentiating between bulge and disk galaxies.

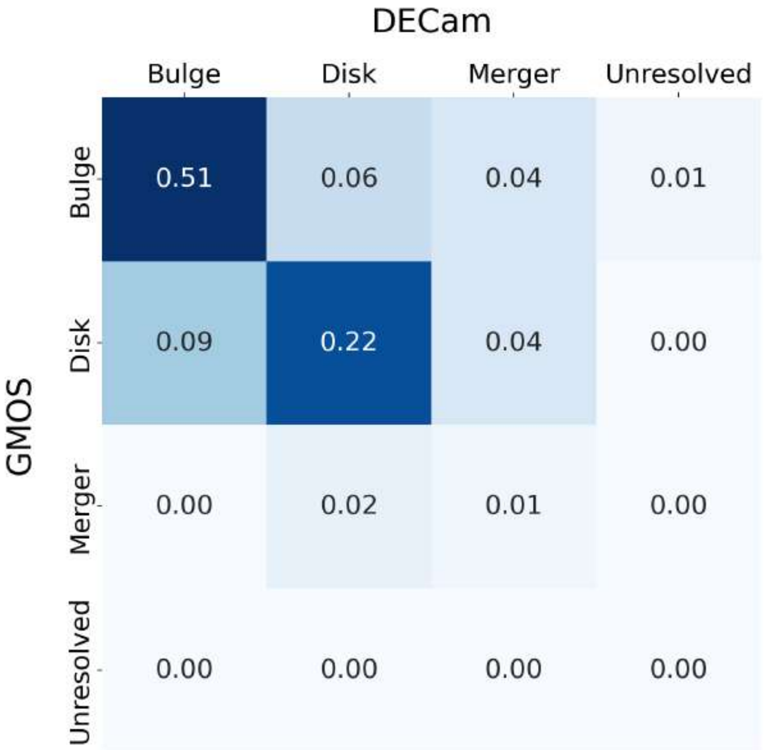

GMOS \ DECam	Bulge	Disk	Merger	Unresolved
Bulge	0.51	0.06	0.04	0.01
Disk	0.09	0.22	0.04	0.00
Merger	0.00	0.02	0.01	0.00
Unresolved	0.00	0.00	0.00	0.00

Figure 5.6: Comparison of the morphological classification carried out using GMOS and DECam in the Abell 3827 galaxy cluster. The confusion matrix shows the fractions of classified member galaxies for each morphological type.

Something important to mention is that all analyses of galaxy structural properties are conducted in the r-band. The reason for this is that historically, CAS and G-M_{20} systems have classified galaxies in filters covering a similar range of rest-frame wavelengths (Conselice, 2003; Lotz et al., 2004). Nevertheless, for completeness, in Figure 5.7 we show the differences in the morphological parameters of the other filters compared to the r-band. We notice that the asymmetry has a very broad distribution in the g-filter, and we attribute this behavior to the lower signal-to-noise ratio in this band compared to the others. Another reason responsible for the differences in the other filters and parameters is that while `SExtractor` can detect and separate nearby sources, this capability decreases if the S/N of a galaxy is low. For this reason, it may happen that in some filters a galaxy close to another one for which morphological parameters are being calculated is detected and masked, while in other bands, this does not occur. This is visually confirmed with the checkplots obtained from the output of statmorph.

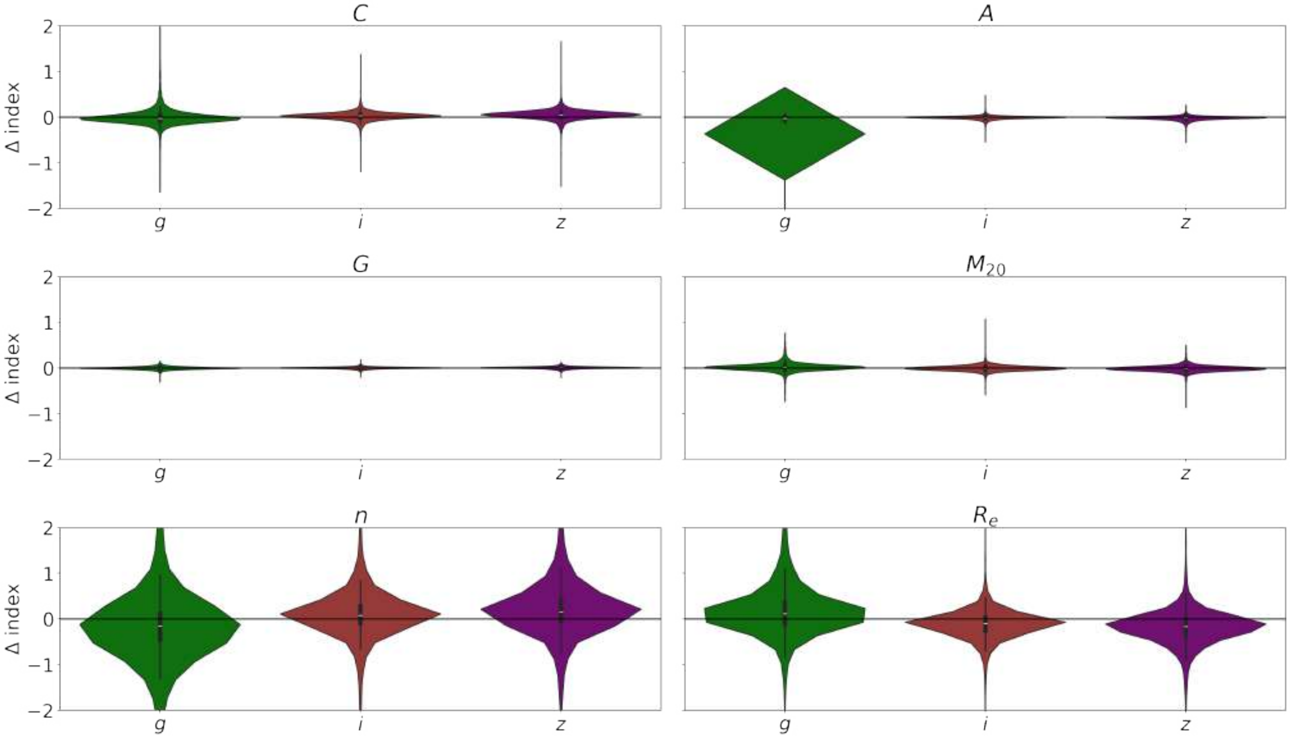

Figure 5.7: Comparison of structural parameters between different photometric bands with respect to the r-band.

5.4 Physical parameters of galaxies

Regarding the physical properties of galaxies, these are determined using the `Le Phare` code, applying SED fitting with photometric data using the g, r, i, z, Y, $W1$, and $W2$ filters. In Table

4.1, we note that the mean of the residuals of the photometric redshift derived with this code in relation to the spectroscopic redshifts is 0.043. Additionally, in Figure 5.8, the distribution of uncertainties for the masses and sSFR determined with `Le Phare` is shown, indicating that the mass calculations are generally good (uncertainty ≤ 0.12 dex) and acceptable for the sSFR (uncertainty ≤ 0.92 dex) for 75% of the data.

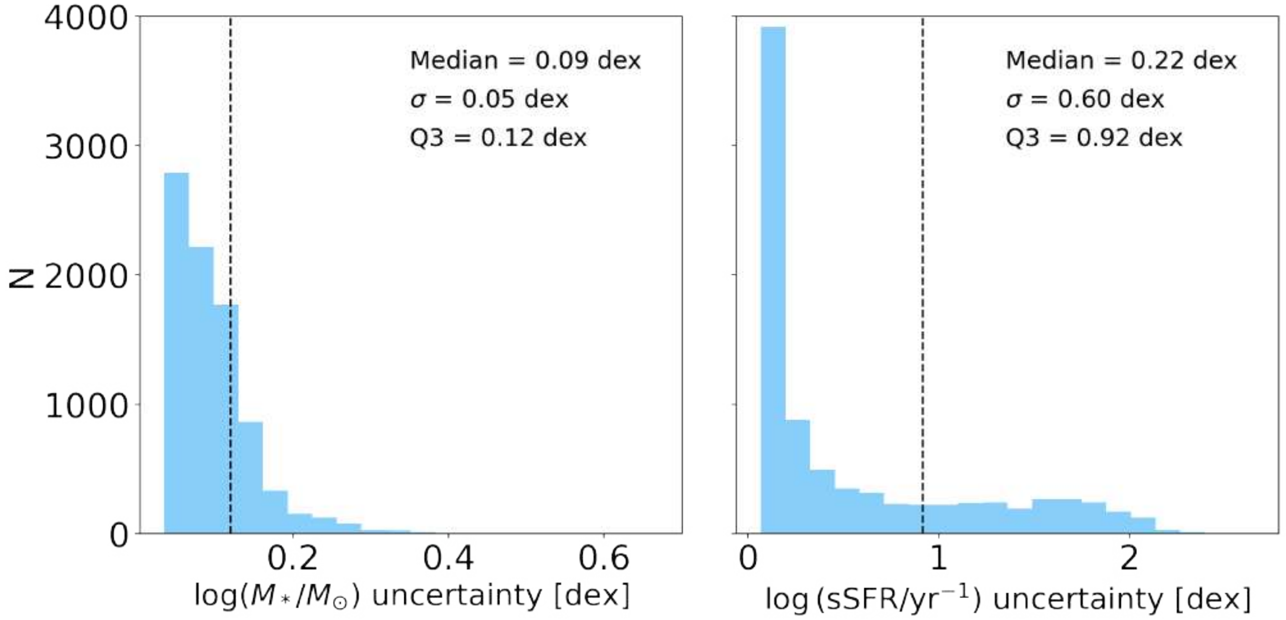

Figure 5.8: Uncertainties for mass and sSFR.

Additionally, in other works such as Chen et al. (2024), it has been shown that the SED fitting for obtaining photometric redshift and the physical properties used in this work (i.e., stellar mass and specific star formation rate) yields reliable results with the same bands used in this thesis. Furthermore, when we separate galaxies according to morphology or color, we find that their physical properties are consistent with what is expected from previous knowledge provided by the literature (e.g., van der Wel, 2008; Blanton and Moustakas, 2009; Wijesinghe et al., 2010; Schneider, 2015). Specifically, in Figures 4.13 and 4.14, it can be seen that bulge galaxies are more massive and have less active star formation compared to disk galaxies. On the other hand, in Figures 4.19, 4.20 and 4.21, it is observed that stellar mass increases from blue to red galaxies, and the specific star formation rate decreases. This consistency provides us with confidence in the results obtained.

On the other hand, let us recall that the χ^2 statistic measures the difference between the expected (best-fit) and observed magnitude, divided by the standard error of the observed magnitude. In the case of an excellent fit, we would expect to obtain χ^2 values very close to zero. However, as observed in Figure 3.16, the χ^2 statistic takes values that may seem quite high. Nonetheless, upon visually inspecting the fits, we do not notice anything particularly unusual, such as a data point that is an outlier compared to the rest. Additionally, in Coupon et al. (2009), it is noted that among the conditions to consider the photometric redshifts reliable, is that $\chi^2 < 1000$, using five filters. Therefore, we trust that a cut-off at $\chi^2 \sim 26$ is more than sufficient to obtain reliable results using seven filters.

5.5 Galaxy properties on different environments

With the obtained results, we can argue that the effect of cluster dynamics on their member galaxies is complex, and may or may not influence their physical and structural properties, depending on the type of galaxy under consideration. On one hand, we observe significant differences between relaxed and disturbed clusters in the distributions of concentration, asymmetry, M_{20}, Sersic index, and star formation rate, in general. As a summary for all the results find in Sections 4.3.1, 4.3.2 and 4.3.3, we present in Figure 5.9 a matrix with the p-values of the KS tests applied to compare the galaxy properties between relaxed and disturbed clusters. We observe that the effect of cluster dynamical state on galaxies is differential. Concerning mass dependence, we observe that low-mass galaxies are more susceptible to structural changes due to cluster dynamics. Regarding morphological types, disk galaxies are predominantly impacted in terms of asymmetry, whereas bulge galaxies are affected in their star formation rate. Lastly, concerning the classification based on the normalized CMD, galaxies in the red sequence experience the most significant physical and structural changes. Other populations show minimal effects, except for some color variations in the Green Valley and the Blue Cloud.

Combining the information from both the boxplots and the KS-tests (summarized in Figure 5.9), we propose that in relaxed clusters, galaxies tend to exhibit higher concentration, lower irregularity (as evidenced by lower asymmetry and M_{20} values), and more prominent bulges, compared to galaxies in disturbed clusters.

Regarding clusters with intermediate dynamical states, we observe that there is no clear trend, suggesting that these systems are not precisely in an intermediate evolutionary stage between relaxed and disturbed clusters. This could imply that these galaxy clusters indeed possess a more complex dynamics, which may not be fully captured using the six proxies of the dynamical state employed in this study.

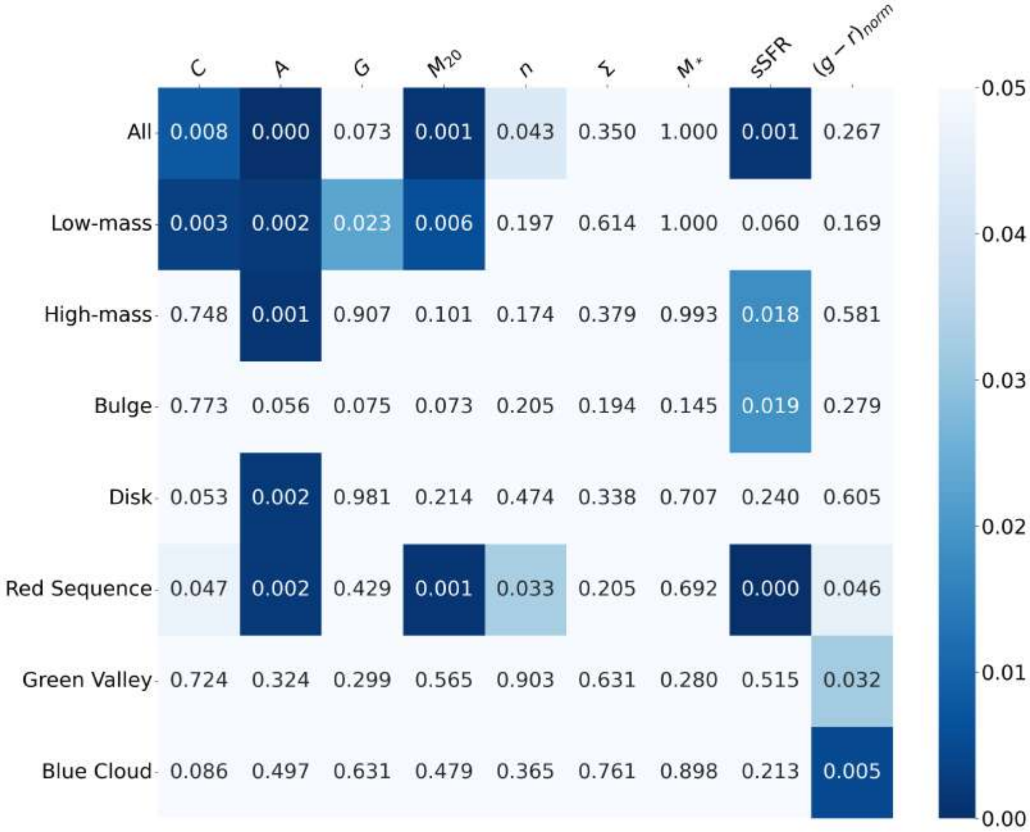

	C	A	G	M_{20}	n	Σ	M_*	sSFR	$(g-r)_{norm}$
All	0.008	0.000	0.073	0.001	0.043	0.350	1.000	0.001	0.267
Low-mass	0.003	0.002	0.023	0.006	0.197	0.614	1.000	0.060	0.169
High-mass	0.748	0.001	0.907	0.101	0.174	0.379	0.993	0.018	0.581
Bulge	0.773	0.056	0.075	0.073	0.205	0.194	0.145	0.019	0.279
Disk	0.053	0.002	0.981	0.214	0.474	0.338	0.707	0.240	0.605
Red Sequence	0.047	0.002	0.429	0.001	0.033	0.205	0.692	0.000	0.046
Green Valley	0.724	0.324	0.299	0.565	0.903	0.631	0.280	0.515	0.032
Blue Cloud	0.086	0.497	0.631	0.479	0.365	0.761	0.898	0.213	0.005

Figure 5.9: Summary of the results of applying the Kolmogorov-Smirnov test to all the cluster populations studied in this thesis. This heatmap presents the p-values that result from comparing relaxed clusters with disturbed ones.

On the other hand, we can observe form Table 4.4 that our results show a higher fraction of disk-dominated galaxies compared to bulge-dominated in the three environments studied. This may seem surprising, as one might expect the opposite when studying galaxies in dense environments such as galaxy clusters (Dressler, 1980; Postman and Geller, 1984; Dressler et al., 1997; Blanton and Moustakas, 2009). he reason for having more disk-dominated morphological types is that, using this classification system, this category includes galaxies that have a disk and also transitional galaxies (Sazonova et al., 2020). Thus, this category may include lenticular galaxies, and considering the large number of such galaxies at low redshifts (Dressler, 1980; Fasano et al., 2012; Vulcani et al., 2023a), it is not unreasonable for the fraction of disk galaxies to increase in our sample. In Figure 4.22, we observe a gradient in disk galaxies where the Sersic index increases from galaxies with lower mass and larger effective radius to those that are more massive and smaller. This behavior is not observed in bulge galaxies, which would support the scenario that the disk-dominated classification includes lenticular and transitional systems.

Nonetheless, even taking this into account, our results indicate that the fractions of quenched and bulge-dominated galaxies do not show significant differences between relaxed and disturbed clusters. The result concerning the quenching fraction contrasts with Kesebonye et al. (2023), who found that this fraction is $\sim 23\%$ higher in merging clusters. However, they used radio images to classify the dynamical state of clusters and radio luminosity to estimate the galaxy star formation rates, which is quite different from our methods.

5.6 Fundamental relations of galaxy clusters

Color-magnitude diagram

The Red Cluster Sequence is a fundamental relation in the CMD and can provide important insights into the formation and evolution of clusters and their populations (e.g., Martin et al., 2007; Faber et al., 2007; Wetzel et al., 2012; Mei et al., 2012; Nilo Castellón et al., 2014). In our study, we find that the slopes and zero-points between relaxed and disturbed clusters do not show significant differences. However, clusters with intermediate dynamical states exhibit significant differences. In fact, the slope in these clusters is significantly less steep than in the others, and the zero-point is significantly lower. This may seem counterintuitive because if we were in a scenario of an evolutionary sequence from relaxed clusters, through intermediate, and finally to disturbed clusters, where the dynamical state alters this fundamental relation, we would expect the slopes to become less steep in this order, and the zero-points to increase progressively. Recalling that the zero-point reflects the intrinsic color of red sequence galaxies, and the slope provides information about the relationship between mass and metallicity of galaxies, one possible scenario is that in environments with intermediate dynamics, the fainter galaxies (less massive) still do not experience a decrease in their star formation processes, preventing quenching and metal enrichment. This could explain the significant differences in the sSFR distributions for red galaxies in the three environments (Figure 4.19 and Table 4.11). However, we must be careful with this interpretation, as we are working within a constrained radius of R_{200}, considering the center of the clusters as their peak X-ray emission. Therefore, we cannot rule out the possibility that if we considered galaxies located further from the center ($R > R_{200}$), the expected behavior could be reproduced. Whatever the case, these results are consistent with Aldás et al. (2023), where the RCS of a sample of relaxed and disturbed clusters was compared, finding no significant differences at low redshift, within R_{200}.

Regarding the Blue Cloud, we observe in Figure 4.15 that this population gradually stands out in the density contours, from relaxed clusters, to intermediate ones, and finally to disturbed clusters. In fact, this is one of the few cases where our results suggest that intermediate clusters could be an evolutionary stage between relaxed and perturbed clusters. On the other hand, the results of the KS tests (Table 4.12) show us that the color distribution for Blue Cloud galaxies is significantly different between relaxed and disturbed clusters. This is reflected in Figure 4.21, where we notice that in disturbed clusters, this population is bluer than in relaxed systems.

Finally, for the Green Valley, no significant differences are observed in any physical or structural parameters between relaxed and disturbed clusters. However, it is interesting to note the bimodal nature in the color distribution in intermediate and disturbed clusters, which is not observed in relaxed systems. This may support a scenario where relaxed clusters provide an environment in which the conditions are ideal for accelerating the evolution of galaxies, suppressing the bimodalities observed in disturbed and intermediate clusters, which result from a more "natural" evolution, i.e., less affected by the environment.

Mass-size relation

In the case of the mass-size relation, this has also been extensively studied in the literature (e.g., Shen et al., 2003; Mowla et al., 2019; Strazzullo et al., 2023). Following the approach of van der Wel et al. (2014), we fit a single power law to this relation ($R_e \propto M_*^\alpha$) using the robust Huber Regressor regression model, separating galaxies according to their morphologies. Similar to Shen et al. (2003), we find that the slope of early-type galaxies (bulge-dominated) is significantly steeper than that of late-type galaxies (disk-dominated) in any environment (Figure 4.22). Furthermore, when separating galaxies according to their specific star formation rate, we find consistent results with Chen et al. (2024), where quiescent galaxies have a steeper slope than star-forming galaxies (Figure 4.23).

Now, when comparing across different environments, we notice that there are no significant differences in the slopes of the mass-size relation between relaxed and disturbed clusters for bulge, disk, quiescent, and star-forming galaxies. However, for clusters with intermediate dynamics, we do find significant differences in some cases. This again suggests that the dynamics in these systems are more complex and may affect this fundamental relation differently.

On the other hand, we highlight that in Figure 4.24 a clear gradient of the Sersic index can be observed in a diagonal direction, which is more noticeable for disk galaxies. We propose that with adequate separation, it is possible to differentiate morphological types in the logarithmic mass-size parameter space. This behavior is also observed for the specific star formation rate in Figure 4.25, which strengthens this proposed galaxy classification, because as discussed, morphology has a known correlation with sSFR.

Morphology/SFR vs local environment

Regarding galaxy morphology, it is well-established in the literature that there exists a dependence on the environment (e.g., Dressler, 1980; Dressler et al., 1997; Fasano et al., 2012; Sazonova et al., 2020; Vulcani et al., 2023a). Furthermore, this dependency is also strongly related to the quenching state of galaxies (e.g., Gómez et al., 2003; Kauffmann et al., 2004; Quadri et al., 2012). In our findings (Figure 4.26), we observe that the relationship between galaxy morphology and sSFR with local density is reproduced. That is, the fraction of bulge/quiescent galaxies increases in the denser regions of both relaxed and perturbed clusters. However, there appears to be a decoupling between the fraction of quenched galaxies and bulge galaxies in intermediate clusters. This behavior could be attributed to the low completeness in the bins at the extremes (see histograms in Figure 4.26). However, upon examining the morphology/SFR vs. clustercentric distance relationship (Figure 4.27), where the expected behavior for relaxed and disturbed clusters is also reproduced, we note that this decoupling also occurs, despite all bins exhibiting more consistent completeness (Figure 4.27). Thus, once again, we observe a fundamental relationship altered in intermediate clusters.

Chapter 6

Summary, conclusions and outlook

In this research, we addressed the impact of the dynamical state of galaxy clusters on their respective populations, analyzing in detail their physical and structural properties, as well as the fundamental relations in relaxed and perturbed systems. To conduct this study, we use optical data from the Legacy Survey DR10, infrared data obtained from unWISE, along with X-ray information provided by the Chandra and XMM-Newton archives. Additionally, we use spectroscopic data available in the literature, as well as from recognized databases such as Vizier and NED. In the following, we summarize the main results:

- We identified cluster member galaxies using a probabilistic method based on photometric redshifts, which ensured a completeness of at least 80% and contamination lower than 25%.

- We classified galaxies into morphological types (bulge and disk) using both parametric and non-parametric approaches, along with PCA. In our study, we can resolve galaxies at scales larger than 1 kpc, resulting in a 15% misclassification rate. Regarding mergers, our methods do not allow reliable identification of them, so they were not considered in the analyses.

- We derived the physical properties of galaxies by applying SED fitting with the Le Phare code. We obtained errors of 0.12 dex and 0.92 dex for the masses and specific star formation rates obtained, respectively, for the 75% of the data. With this, we separated the galaxies according to their masses and quenching states.

- We determined the dynamical state of galaxy clusters using a combination of six proxies. We employed PCA to calculate the statistical weights for each, and through a weighted boolean sum (`wbs`), classified these systems as relaxed, intermediate, and disturbed.

- We compared the physical and structural properties of member galaxies in galaxy clusters with different dynamical states. We found significant differences in concentration, irregularity (asymmetry and M_{20}, bulge prominence (Sersic index), and star formation rates between the populations of relaxed and disturbed clusters, suggesting that dynamics have an effect on their distributions. However, this impact is differential, and we observed that disk-dominated galaxies, less massive and belonging to the Red Sequence, are more susceptible to being affected. Furthermore, the fundamental relationships of relaxed and disturbed clusters show no significant differences.

Taking all of this into account, we can conclude that the dynamical state of massive galaxy clusters at low redshift ($z < 0.55$) does not significantly alter their more global properties, such as their fundamental relationships, within R_{200}. This is in agreement with the hypothesis proposed by Zenteno et al. (2020), suggesting that significant differences begin to emerge at $z > 0.55$, and with the findings of Aldás et al. (2023), who confirm this for the red sequence of clusters. However, despite the fact that dynamics do not have a large effect on the median values of the physical and structural parameters of galaxies within the redshift range of our study, they do have a significant impact on their distributions. Specifically, in these systems, we find galaxies that are less concentrated, more irregular, and with a higher specific star formation rate. This could suggest, for example, that the scenario of a merger process between two clusters could alter the structures of galaxies, making them more irregular through physical processes such as extreme ram pressure stripping and/or tidal stripping, and also triggering star formation.

Furthermore, we noticed that the clusters initially classified as intermediate do not behave precisely like systems in an intermediate evolutionary stage between relaxed and disturbed clusters in most cases. Instead, these structures appear to be peculiar and perhaps we cannot reliably determine their dynamical states with the methods used in this thesis. A deeper analysis of these galaxy clusters could be very interesting, but it is beyond the scope of this thesis.

In light of the conclusions drawn from this research, the next logical steps in this field would involve conducting a similar study at higher redshifts ($z \geq 0.55$). However, this adds complexity, as good spatial resolution is required for morphological studies. This can be addressed by using *HST* images. Additionally, it would also be interesting to expand the study radius ($3R_{200}$-$5R_{200}$) to include the outskirts of galaxy clusters and determine whether the results obtained are related to the study radius or are intrinsic to the systems. Finally, characterizing the physical processes responsible for the observed differences between relaxed and perturbed clusters would be intriguing, which could be achieved using cosmological simulations.

Bibliography

Abbott, T. M. C., Adamów, M., Aguena, M., Allam, S., Amon, A., Annis, J., Avila, S., Bacon, D., Banerji, M., Bechtol, K., Becker, M. R., Bernstein, G. M., Bertin, E., Bhargava, S., Bridle, S. L., Brooks, D., Burke, D. L., Carnero Rosell, A., Carrasco Kind, M., Carretero, J., Castander, F. J., Cawthon, R., Chang, C., Choi, A., Conselice, C., Costanzi, M., Crocce, M., da Costa, L. N., Davis, T. M., De Vicente, J., DeRose, J., Desai, S., Diehl, H. T., Dietrich, J. P., Drlica-Wagner, A., Eckert, K., Elvin-Poole, J., Everett, S., Evrard, A. E., Ferrero, I., Ferté, A., Flaugher, B., Fosalba, P., Friedel, D., Frieman, J., García-Bellido, J., Gaztanaga, E., Gelman, L., Gerdes, D. W., Giannantonio, T., Gill, M. S. S., Gruen, D., Gruendl, R. A., Gschwend, J., Gutierrez, G., Hartley, W. G., Hinton, S. R., Hollowood, D. L., Honscheid, K., Huterer, D., James, D. J., Jeltema, T., Johnson, M. D., Kent, S., Kron, R., Kuehn, K., Kuropatkin, N., Lahav, O., Li, T. S., Lidman, C., Lin, H., MacCrann, N., Maia, M. A. G., Manning, T. A., Maloney, J. D., March, M., Marshall, J. L., Martini, P., Melchior, P., Menanteau, F., Miquel, R., Morgan, R., Myles, J., Neilsen, E., Ogando, R. L. C., Palmese, A., Paz-Chinchón, F., Petravick, D., Pieres, A., Plazas, A. A., Pond, C., Rodriguez-Monroy, M., Romer, A. K., Roodman, A., Rykoff, E. S., Sako, M., Sanchez, E., Santiago, B., Scarpine, V., Serrano, S., Sevilla-Noarbe, I., Smith, J. A., Smith, M., Soares-Santos, M., Suchyta, E., Swanson, M. E. C., Tarle, G., Thomas, D., To, C., Tremblay, P. E., Troxel, M. A., Tucker, D. L., Turner, D. J., Varga, T. N., Walker, A. R., Wechsler, R. H., Weller, J., Wester, W., Wilkinson, R. D., Yanny, B., Zhang, Y., Nikutta, R., Fitzpatrick, M., Jacques, A., Scott, A., Olsen, K., Huang, L., Herrera, D., Juneau, S., Nidever, D., Weaver, B. A., Adean, C., Correia, V., de Freitas, M., Freitas, F. N., Singulani, C., Vila-Verde, G., and Linea Science Server (2021). The Dark Energy Survey Data Release 2. *ApJS*, 255(2):20.

Abell, G. O. (1958). The Distribution of Rich Clusters of Galaxies. *ApJS*, 3:211.

Abell, G. O., Corwin, Harold G., J., and Olowin, R. P. (1989). A Catalog of Rich Clusters of Galaxies. *ApJS*, 70:1.

Abraham, R. G., Valdes, F., Yee, H. K. C., and van den Bergh, S. (1994a). The Morphologies of Distant Galaxies. I. an Automated Classification System. *ApJ*, 432:75.

Abraham, R. G., Valdes, F., Yee, H. K. C., and van den Bergh, S. (1994b). The Morphologies of Distant Galaxies. I. an Automated Classification System. *ApJ*, 432:75.

Abraham, R. G., van den Bergh, S., Glazebrook, K., Ellis, R. S., Santiago, B. X., Surma, P., and Griffiths, R. E. (1996). The Morphologies of Distant Galaxies. II. Classifications from the Hubble Space Telescope Medium Deep Survey. *ApJS*, 107:1.

Abraham, R. G., van den Bergh, S., and Nair, P. (2003). A New Approach to Galaxy Morphology. I. Analysis of the Sloan Digital Sky Survey Early Data Release. *ApJ*, 588(1):218–229.

Aldás, F., Zenteno, A., Gómez, F. A., Hernandez-Lang, D., Carrasco, E. R., Vega-Martínez, C. A., and Nilo Castellón, J. L. (2023). Clash of Titans: the impact of cluster mergers in the galaxy cluster red sequence. *MNRAS*, 525(2):1769–1778.

Anderson, J. and King, I. R. (2000). Toward High-Precision Astrometry with WFPC2. I. Deriving an Accurate Point-Spread Function. *PASP*, 112(776):1360–1382.

Arnouts, S., Cristiani, S., Moscardini, L., Matarrese, S., Lucchin, F., Fontana, A., and Giallongo, E. (1999). Measuring and modelling the redshift evolution of clustering: the Hubble Deep Field North. *MNRAS*, 310(2):540–556.

Baldry, I. K., Glazebrook, K., Brinkmann, J., Ivezić, Ž., Lupton, R. H., Nichol, R. C., and Szalay, A. S. (2004). Quantifying the Bimodal Color-Magnitude Distribution of Galaxies. *ApJ*, 600(2):681–694.

Balogh, M. L., Baldry, I. K., Nichol, R., Miller, C., Bower, R., and Glazebrook, K. (2004). The Bimodal Galaxy Color Distribution: Dependence on Luminosity and Environment. *ApJ*, 615(2):L101–L104.

Barnes, J. and Efstathiou, G. (1987). Angular Momentum from Tidal Torques. *ApJ*, 319:575.

Barnes, J. E. (1989). Evolution of compact groups and the formation of elliptical galaxies. *Nature*, 338(6211):123–126.

Bayliss, M. B., Ruel, J., Stubbs, C. W., Allen, S. W., Applegate, D. E., Ashby, M. L. N., Bautz, M., Benson, B. A., Bleem, L. E., Bocquet, S., Brodwin, M., Capasso, R., Carlstrom, J. E., Chang, C. L., Chiu, I., Cho, H. M., Clocchiatti, A., Crawford, T. M., Crites, A. T., de Haan, T., Desai, S., Dietrich, J. P., Dobbs, M. A., Doucouliagos, A. N., Foley, R. J., Forman, W. R., Garmire, G. P., George, E. M., Gladders, M. D., Gonzalez, A. H., Gupta, N., Halverson, N. W., Hlavacek-Larrondo, J., Hoekstra, H., Holder, G. P., Holzapfel, W. L., Hou, Z., Hrubes, J. D., Huang, N., Jones, C., Keisler, R., Knox, L., Lee, A. T., Leitch, E. M., von der Linden, A., Luong-Van, D., Mantz, A., Marrone, D. P., McDonald, M., McMahon, J. J., Meyer, S. S., Mocanu, L. M., Mohr, J. J., Murray, S. S., Padin, S., Pryke, C., Rapetti, D., Reichardt, C. L., Rest, A., Ruhl, J. E., Saliwanchik, B. R., Saro, A., Sayre, J. T., Schaffer, K. K., Schrabback, T., Shirokoff, E., Song, J., Spieler, H. G., Stalder, B., Stanford, S. A., Staniszewski, Z., Stark, A. A., Story, K. T., Vanderlinde, K., Vieira, J. D., Vikhlinin, A., Williamson, R., and Zenteno, A. (2016). SPT-GMOS: A Gemini/GMOS-South Spectroscopic Survey of Galaxy Clusters in the SPT-SZ Survey. *ApJS*, 227(1):3.

Beers, T. C., Flynn, K., and Gebhardt, K. (1990). Measures of Location and Scale for Velocities in Clusters of Galaxies—A Robust Approach. *AJ*, 100:32.

Bell, E. F., Wolf, C., Meisenheimer, K., Rix, H.-W., Borch, A., Dye, S., Kleinheinrich, M., Wisotzki, L., and McIntosh, D. H. (2004). Nearly 5000 Distant Early-Type Galaxies in COMBO-17: A Red Sequence and Its Evolution since z~1. *ApJ*, 608(2):752–767.

Benson, A. J. (2010). Galaxy formation theory. *Phys. Rep.*, 495(2-3):33–86.

Bershady, M. A., Jangren, A., and Conselice, C. J. (2000). Structural and Photometric Classification of Galaxies. I. Calibration Based on a Nearby Galaxy Sample. *AJ*, 119(6):2645–2663.

Bertin, E. (2011). Automated Morphometry with SExtractor and PSFEx. In Evans, I. N., Accomazzi, A., Mink, D. J., and Rots, A. H., editors, *Astronomical Data Analysis Software and Systems XX*, volume 442 of *Astronomical Society of the Pacific Conference Series*, page 435.

Bertin, E. and Arnouts, S. (1996). SExtractor: Software for source extraction. *A&AS*, 117:393–404.

Blanton, M. R., Hogg, D. W., Bahcall, N. A., Baldry, I. K., Brinkmann, J., Csabai, I., Eisenstein, D., Fukugita, M., Gunn, J. E., Ivezić, Ž., Lamb, D. Q., Lupton, R. H., Loveday, J., Munn, J. A., Nichol, R. C., Okamura, S., Schlegel, D. J., Shimasaku, K., Strauss, M. A., Vogeley, M. S., and Weinberg, D. H. (2003). The Broadband Optical Properties of Galaxies with Redshifts 0.02¡z¡0.22. *ApJ*, 594(1):186–207.

Blanton, M. R. and Moustakas, J. (2009). Physical Properties and Environments of Nearby Galaxies. *ARA&A*, 47(1):159–210.

Bleem, L. E., Stalder, B., de Haan, T., Aird, K. A., Allen, S. W., Applegate, D. E., Ashby, M. L. N., Bautz, M., Bayliss, M., Benson, B. A., Bocquet, S., Brodwin, M., Carlstrom, J. E., Chang, C. L., Chiu, I., Cho, H. M., Clocchiatti, A., Crawford, T. M., Crites, A. T., Desai, S., Dietrich, J. P., Dobbs, M. A., Foley, R. J., Forman, W. R., George, E. M., Gladders, M. D., Gonzalez, A. H., Halverson, N. W., Hennig, C., Hoekstra, H., Holder, G. P., Holzapfel, W. L., Hrubes, J. D., Jones, C., Keisler, R., Knox, L., Lee, A. T., Leitch, E. M., Liu, J., Lueker, M., Luong-Van, D., Mantz, A., Marrone, D. P., McDonald, M., McMahon, J. J., Meyer, S. S., Mocanu, L., Mohr, J. J., Murray, S. S., Padin, S., Pryke, C., Reichardt, C. L., Rest, A., Ruel, J., Ruhl, J. E., Saliwanchik, B. R., Saro, A., Sayre, J. T., Schaffer, K. K., Schrabback, T., Shirokoff, E., Song, J., Spieler, H. G., Stanford, S. A., Staniszewski, Z., Stark, A. A., Story, K. T., Stubbs, C. W., Vanderlinde, K., Vieira, J. D., Vikhlinin, A., Williamson, R., Zahn, O., and Zenteno, A. (2015). Galaxy Clusters Discovered via the Sunyaev-Zel'dovich Effect in the 2500-Square-Degree SPT-SZ Survey. *ApJS*, 216(2):27.

Bluck, A. F. L., Bottrell, C., Teimoorinia, H., Henriques, B. M. B., Mendel, J. T., Ellison, S. L., Thanjavur, K., Simard, L., Patton, D. R., Conselice, C. J., Moreno, J., and Woo, J. (2019). What shapes a galaxy? - unraveling the role of mass, environment, and star formation in forming galactic structure. *MNRAS*, 485(1):666–696.

Blum, R. D., Burleigh, K., Dey, A., Schlegel, D. J., Meisner, A. M., Levi, M., Myers, A. D., Lang, D., Moustakas, J., Patej, A., Valdes, F., Kneib, J.-P., Huanyuan, S., Nord, B., Olsen, K. A., Delubac, T., Saha, A., James, D., Walker, A. R., and DECaLS Team (2016). The DECam Legacy Survey. In *American Astronomical Society Meeting Abstracts #228*, volume 228 of *American Astronomical Society Meeting Abstracts*, page 317.01.

Blumenthal, G. R., Faber, S. M., Primack, J. R., and Rees, M. J. (1984). Formation of galaxies and large-scale structure with cold dark matter. *Nature*, 311:517–525.

Böhringer, H. (2005). Rosat observations of clusters of galaxies. In *New Insights into the Universe: Proceeding of a Summer School Held in València, Spain 23–27 September 1991*, pages 219–246. Springer.

Bom, C. R., Cortesi, A., Lucatelli, G., Dias, L. O., Schubert, P., Oliveira Schwarz, G. B., Cardoso, N. M., Lima, E. V. R., Mendes de Oliveira, C., Sodre, L., Smith Castelli, A. V., Ferrari, F., Damke, G., Overzier, R., Kanaan, A., Ribeiro, T., and Schoenell, W. (2021). Deep

Learning assessment of galaxy morphology in S-PLUS Data Release 1. *MNRAS*, 507(2):1937–1955.

Boschin, W., Girardi, M., and Barrena, R. (2013). The dynamical status of ZwCl 2341.1+0000: a very elongated galaxy structure with a complex radio emission. *MNRAS*, 434(1):772–783.

Boselli, A. and Gavazzi, G. (2006). Environmental Effects on Late-Type Galaxies in Nearby Clusters. *PASP*, 118(842):517–559.

Bournaud, F., Jog, C. J., and Combes, F. (2007). Multiple minor mergers: formation of elliptical galaxies and constraints for the growth of spiral disks. *A&A*, 476(3):1179–1190.

Braglia, F. G., Pierini, D., Biviano, A., and Böhringer, H. (2009). Multi-wavelength study of X-ray luminous clusters at z ~0.3. I. Star-formation activity of cluster galaxies. *A&A*, 500(3):947–963.

Brinchmann, J., Abraham, R., Schade, D., Tresse, L., Ellis, R. S., Lilly, S., Le Fèvre, O., Glazebrook, K., Hammer, F., Colless, M., Crampton, D., and Broadhurst, T. (1998). Hubble Space Telescope Imaging of the CFRS and LDSS Redshift Surveys. I. Morphological Properties. *ApJ*, 499(1):112–133.

Brown, T., Catinella, B., Cortese, L., Lagos, C. d. P., Davé, R., Kilborn, V., Haynes, M. P., Giovanelli, R., and Rafieferantsoa, M. (2017). Cold gas stripping in satellite galaxies: from pairs to clusters. *MNRAS*, 466(2):1275–1289.

Brunner, R. J. and Lubin, L. M. (2000). A Probabilistic Quantification of Galaxy Cluster Membership. *AJ*, 120(6):2851–2858.

Bruzual, G. and Charlot, S. (2003). Stellar population synthesis at the resolution of 2003. *MNRAS*, 344(4):1000–1028.

Bruzual A., G. (1983). Spectral evolution of galaxies. I. Early-type systems. *ApJ*, 273:105–127.

Buitrago, F., Trujillo, I., Conselice, C. J., and Häußler, B. (2013). Early-type galaxies have been the predominant morphological class for massive galaxies since only z $\sim$ 1. *MNRAS*, 428(2):1460–1478.

Buote, D. A. and Tsai, J. C. (1995). Quantifying the Morphologies and Dynamical Evolution of Galaxy Clusters. I. The Method. *ApJ*, 452:522.

Byrd, G. and Valtonen, M. (1990). Tidal Generation of Active Spirals and S0 Galaxies by Rich Clusters. *ApJ*, 350:89.

Cabrera-Vives, G., Miller, C. J., and Schneider, J. (2018). Systematic Labeling Bias in Galaxy Morphologies. *AJ*, 156(6):284.

Calvi, R., Poggianti, B. M., Fasano, G., and Vulcani, B. (2012). The distribution of galaxy morphological types and the morphology-mass relation in different environments at low redshift. *MNRAS*, 419(1):L14–L18.

Calvi, R., Vulcani, B., Poggianti, B. M., Moretti, A., Fritz, J., and Fasano, G. (2018). Morphology rather than environment drives the SFR-mass relation in the local universe. *MNRAS*, 481(3):3456–3469.

Calzetti, D., Armus, L., Bohlin, R. C., Kinney, A. L., Koornneef, J., and Storchi-Bergmann, T. (2000). The Dust Content and Opacity of Actively Star-forming Galaxies. *ApJ*, 533(2):682–695.

Campitiello, M. G., Ettori, S., Lovisari, L., Bartalucci, I., Eckert, D., Rasia, E., Rossetti, M., Gastaldello, F., Pratt, G. W., Maughan, B., Pointecouteau, E., Sereno, M., Biffi, V., Borgani, S., De Luca, F., De Petris, M., Gaspari, M., Ghizzardi, S., Mazzotta, P., and Molendi, S. (2022). CHEX-MATE: Morphological analysis of the sample. *A&A*, 665:A117.

Carrasco, E. R. and Verdugo, T. (2018). Revisiting the monster: the mass profile of the galaxy cluster Abell 3827 using dynamical and strong lensing constrains. In *American Astronomical Society Meeting Abstracts #231*, volume 231 of *American Astronomical Society Meeting Abstracts*, page 258.08.

Cassano, R., Ettori, S., Brunetti, G., Giacintucci, S., Pratt, G. W., Venturi, T., Kale, R., Dolag, K., and Markevitch, M. (2013). Revisiting Scaling Relations for Giant Radio Halos in Galaxy Clusters. *ApJ*, 777(2):141.

Cassano, R., Ettori, S., Giacintucci, S., Brunetti, G., Markevitch, M., Venturi, T., and Gitti, M. (2010). On the Connection Between Giant Radio Halos and Cluster Mergers. *ApJ*, 721(2):L82–L85.

Cavaliere, A. and Fusco-Femiano, R. (1976). X-rays from hot plasma in clusters of galaxies. *A&A*, 49:137–144.

Chambers, K. C., Magnier, E. A., Metcalfe, N., Flewelling, H. A., Huber, M. E., Waters, C. Z., Denneau, L., Draper, P. W., Farrow, D., Finkbeiner, D. P., Holmberg, C., Koppenhoefer, J., Price, P. A., Rest, A., Saglia, R. P., Schlafly, E. F., Smartt, S. J., Sweeney, W., Wainscoat, R. J., Burgett, W. S., Chastel, S., Grav, T., Heasley, J. N., Hodapp, K. W., Jedicke, R., Kaiser, N., Kudritzki, R. P., Luppino, G. A., Lupton, R. H., Monet, D. G., Morgan, J. S., Onaka, P. M., Shiao, B., Stubbs, C. W., Tonry, J. L., White, R., Bañados, E., Bell, E. F., Bender, R., Bernard, E. J., Boegner, M., Boffi, F., Botticella, M. T., Calamida, A., Casertano, S., Chen, W. P., Chen, X., Cole, S., Deacon, N., Frenk, C., Fitzsimmons, A., Gezari, S., Gibbs, V., Goessl, C., Goggia, T., Gourgue, R., Goldman, B., Grant, P., Grebel, E. K., Hambly, N. C., Hasinger, G., Heavens, A. F., Heckman, T. M., Henderson, R., Henning, T., Holman, M., Hopp, U., Ip, W. H., Isani, S., Jackson, M., Keyes, C. D., Koekemoer, A. M., Kotak, R., Le, D., Liska, D., Long, K. S., Lucey, J. R., Liu, M., Martin, N. F., Masci, G., McLean, B., Mindel, E., Misra, P., Morganson, E., Murphy, D. N. A., Obaika, A., Narayan, G., Nieto-Santisteban, M. A., Norberg, P., Peacock, J. A., Pier, E. A., Postman, M., Primak, N., Rae, C., Rai, A., Riess, A., Riffeser, A., Rix, H. W., Röser, S., Russel, R., Rutz, L., Schilbach, E., Schultz, A. S. B., Scolnic, D., Strolger, L., Szalay, A., Seitz, S., Small, E., Smith, K. W., Soderblom, D. R., Taylor, P., Thomson, R., Taylor, A. N., Thakar, A. R., Thiel, J., Thilker, D., Unger, D., Urata, Y., Valenti, J., Wagner, J., Walder, T., Walter, F., Watters, S. P., Werner, S., Wood-Vasey, W. M., and Wyse, R. (2016). The Pan-STARRS1 Surveys. *arXiv e-prints*, page arXiv:1612.05560.

Chen, Y., Mo, H. J., Li, C., Wang, H., Yang, X., Zhou, S., and Zhang, Y. (2019). ELUCID. VI. Cosmic Variance of the Galaxy Distribution in the Local Universe. *ApJ*, 872(2):180.

Chen, Z., Gu, Y., Zou, H., and Yuan, Q. (2024). Galaxy Clusters from the DESI Legacy Imaging Surveys. II. Environmental Effects on the Size–Mass Relation. *ApJ*, 961(2):253.

Cheng, T.-Y., Conselice, C. J., Aragón-Salamanca, A., Aguena, M., Allam, S., Andrade-Oliveira, F., Annis, J., Bluck, A. F. L., Brooks, D., Burke, D. L., Carrasco Kind, M., Carretero, J., Choi, A., Costanzi, M., da Costa, L. N., Pereira, M. E. S., De Vicente, J., Diehl, H. T., Drlica-Wagner, A., Eckert, K., Everett, S., Evrard, A. E., Ferrero, I., Fosalba, P., Frieman, J., García-Bellido, J., Gerdes, D. W., Giannantonio, T., Gruen, D., Gruendl, R. A., Gschwend, J., Gutierrez, G., Hinton, S. R., Hollowood, D. L., Honscheid, K., James, D. J., Krause, E., Kuehn, K., Kuropatkin, N., Lahav, O., Maia, M. A. G., March, M., Menanteau, F., Miquel, R., Morgan, R., Paz-Chinchón, F., Pieres, A., Plazas Malagón, A. A., Roodman, A., Sanchez, E., Scarpine, V., Serrano, S., Sevilla-Noarbe, I., Smith, M., Soares-Santos, M., Suchyta, E., Swanson, M. E. C., Tarle, G., Thomas, D., and To, C. (2021). Galaxy morphological classification catalogue of the Dark Energy Survey Year 3 data with convolutional neural networks. *MNRAS*, 507(3):4425–4444.

Clowe, D., Bradač, M., Gonzalez, A. H., Markevitch, M., Randall, S. W., Jones, C., and Zaritsky, D. (2006). A Direct Empirical Proof of the Existence of Dark Matter. *ApJ*, 648(2):L109–L113.

Coil, A. L. (2013). The Large-Scale Structure of the Universe. In Oswalt, T. D. and Keel, W. C., editors, *Planets, Stars and Stellar Systems. Volume 6: Extragalactic Astronomy and Cosmology*, volume 6, page 387.

Cole, S., Aragon-Salamanca, A., Frenk, C. S., Navarro, J. F., and Zepf, S. E. (1994). A recipe for galaxy formation. *MNRAS*, 271:781–806.

Conselice, C. J. (2003). The Relationship between Stellar Light Distributions of Galaxies and Their Formation Histories. *ApJS*, 147(1):1–28.

Conselice, C. J. (2014). The Evolution of Galaxy Structure Over Cosmic Time. *ARA&A*, 52:291–337.

Conselice, C. J., Bershady, M. A., and Jangren, A. (2000). The Asymmetry of Galaxies: Physical Morphology for Nearby and High-Redshift Galaxies. *ApJ*, 529(2):886–910.

Contreras, S., Baugh, C. M., Norberg, P., and Padilla, N. (2013). How robust are predictions of galaxy clustering? *MNRAS*, 432(4):2717–2730.

Cora, S. A., Vega-Martínez, C. A., Hough, T., Ruiz, A. N., Orsi, Á. A., Muñoz Arancibia, A. M., Gargiulo, I. D., Collacchioni, F., Padilla, N. D., Gottlöber, S., and Yepes, G. (2018). Semi-analytic galaxies - I. Synthesis of environmental and star-forming regulation mechanisms. *MNRAS*, 479(1):2–24.

Coupon, J., Ilbert, O., Kilbinger, M., McCracken, H. J., Mellier, Y., Arnouts, S., Bertin, E., Hudelot, P., Schultheis, M., Le Fèvre, O., Le Brun, V., Guzzo, L., Bardelli, S., Zucca, E., Bolzonella, M., Garilli, B., Zamorani, G., Zanichelli, A., Tresse, L., and Aussel, H. (2009). Photometric redshifts for the CFHTLS T0004 deep and wide fields. *A&A*, 500(3):981–998.

Cowie, L. L. and Songaila, A. (1977). Thermal evaporation of gas within galaxies by a hot intergalactic medium. *Nature*, 266:501–503.

Dariush, A., Khosroshahi, H. G., Ponman, T. J., Pearce, F., Raychaudhury, S., and Hartley, W. (2007). The mass assembly of fossil groups of galaxies in the Millennium simulation. *MNRAS*, 382(1):433–442.

David, L. P., Jones, C., and Forman, W. (1995). Cosmological Implications of ROSAT Observations of Groups and Clusters of Galaxies. *ApJ*, 445:578.

Davis, M., Efstathiou, G., Frenk, C. S., and White, S. D. M. (1985). The evolution of large-scale structure in a universe dominated by cold dark matter. *ApJ*, 292:371–394.

de Albernaz Ferreira, L. and Ferrari, F. (2018). The impact of redshift on galaxy morphometric classification: case studies for SDSS, DES, LSST and HST with MORFOMETRYKA. *MNRAS*, 473(2):2701–2713.

de Los Rios, M., Domínguez R., M. J., Paz, D., and Merchán, M. (2016). The MeSsI (merging systems identification) algorithm and catalogue. *MNRAS*, 458(1):226–232.

de Propris, R., Stanford, S. A., Eisenhardt, P. R., Dickinson, M., and Elston, R. (1999). The K-Band Luminosity Function in Galaxy Clusters to Z ~1. *AJ*, 118(2):719–729.

de Propris, R., Stanford, S. A., Eisenhardt, P. R., Holden, B. P., and Rosati, P. (2007). The Rest-Frame K-Band Luminosity Function of Galaxies in Clusters to z = 1.3. *AJ*, 133(5):2209–2215.

de Vaucouleurs, G. (1948). Recherches sur les Nebuleuses Extragalactiques. *Annales d'Astrophysique*, 11:247.

de Vaucouleurs, G., de Vaucouleurs, A., Corwin, Herold G., J., Buta, R. J., Paturel, G., and Fouque, P. (1991). *Third Reference Catalogue of Bright Galaxies.*

Dey, A., Schlegel, D. J., Lang, D., Blum, R., Burleigh, K., Fan, X., Findlay, J. R., Finkbeiner, D., Herrera, D., Juneau, S., Landriau, M., Levi, M., McGreer, I., Meisner, A., Myers, A. D., Moustakas, J., Nugent, P., Patej, A., Schlafly, E. F., Walker, A. R., Valdes, F., Weaver, B. A., Yèche, C., Zou, H., Zhou, X., Abareshi, B., Abbott, T. M. C., Abolfathi, B., Aguilera, C., Alam, S., Allen, L., Alvarez, A., Annis, J., Ansarinejad, B., Aubert, M., Beechert, J., Bell, E. F., BenZvi, S. Y., Beutler, F., Bielby, R. M., Bolton, A. S., Briceño, C., Buckley-Geer, E. J., Butler, K., Calamida, A., Carlberg, R. G., Carter, P., Casas, R., Castander, F. J., Choi, Y., Comparat, J., Cukanovaite, E., Delubac, T., DeVries, K., Dey, S., Dhungana, G., Dickinson, M., Ding, Z., Donaldson, J. B., Duan, Y., Duckworth, C. J., Eftekharzadeh, S., Eisenstein, D. J., Etourneau, T., Fagrelius, P. A., Farihi, J., Fitzpatrick, M., Font-Ribera, A., Fulmer, L., Gänsicke, B. T., Gaztanaga, E., George, K., Gerdes, D. W., Gontcho, S. G. A., Gorgoni, C., Green, G., Guy, J., Harmer, D., Hernandez, M., Honscheid, K., Huang, L. W., James, D. J., Jannuzi, B. T., Jiang, L., Joyce, R., Karcher, A., Karkar, S., Kehoe, R., Kneib, J.-P., Kueter-Young, A., Lan, T.-W., Lauer, T. R., Le Guillou, L., Le Van Suu, A., Lee, J. H., Lesser, M., Perreault Levasseur, L., Li, T. S., Mann, J. L., Marshall, R., Martínez-Vázquez, C. E., Martini, P., du Mas des Bourboux, H., McManus, S., Meier, T. G., Ménard, B., Metcalfe, N., Muñoz-Gutiérrez, A., Najita, J., Napier, K., Narayan, G., Newman, J. A., Nie, J., Nord, B., Norman, D. J., Olsen, K. A. G., Paat, A., Palanque-Delabrouille, N., Peng, X., Poppett, C. L., Poremba, M. R., Prakash, A., Rabinowitz, D., Raichoor, A., Rezaie, M., Robertson, A. N., Roe, N. A., Ross, A. J., Ross, N. P., Rudnick, G., Safonova, S., Saha, A., Sánchez, F. J., Savary, E., Schweiker, H., Scott, A., Seo, H.-J., Shan, H., Silva, D. R., Slepian, Z., Soto, C., Sprayberry, D., Staten, R., Stillman, C. M., Stupak, R. J., Summers, D. L., Sien Tie, S., Tirado, H., Vargas-Magaña, M., Vivas, A. K., Wechsler, R. H., Williams, D., Yang, J., Yang, Q., Yapici, T., Zaritsky, D., Zenteno, A., Zhang, K., Zhang, T., Zhou, R., and Zhou, Z. (2019). Overview of the DESI Legacy Imaging Surveys. *AJ*, 157(5):168.

Domínguez Sánchez, H., Huertas-Company, M., Bernardi, M., Tuccillo, D., and Fischer, J. L. (2018). Improving galaxy morphologies for SDSS with Deep Learning. *MNRAS*, 476(3):3661–3676.

Dressler, A. (1980). Galaxy morphology in rich clusters: implications for the formation and evolution of galaxies. *ApJ*, 236:351–365.

Dressler, A., Oemler, Augustus, J., Couch, W. J., Smail, I., Ellis, R. S., Barger, A., Butcher, H., Poggianti, B. M., and Sharples, R. M. (1997). Evolution since z = 0.5 of the Morphology-Density Relation for Clusters of Galaxies. *ApJ*, 490(2):577–591.

Dressler, A. and Shectman, S. A. (1988). Evidence for Substructure in Rich Clusters of Galaxies from Radial-Velocity Measurements. *AJ*, 95:985.

Drlica-Wagner, A., Ferguson, P. S., Adamów, M., Aguena, M., Allam, S., Andrade-Oliveira, F., Bacon, D., Bechtol, K., Bell, E. F., Bertin, E., Bilaji, P., Bocquet, S., Bom, C. R., Brooks, D., Burke, D. L., Carballo-Bello, J. A., Carlin, J. L., Carnero Rosell, A., Carrasco Kind, M., Carretero, J., Castander, F. J., Cerny, W., Chang, C., Choi, Y., Conselice, C., Costanzi, M., Crnojević, D., da Costa, L. N., de Vicente, J., Desai, S., Esteves, J., Everett, S., Ferrero, I., Fitzpatrick, M., Flaugher, B., Friedel, D., Frieman, J., García-Bellido, J., Gatti, M., Gaztanaga, E., Gerdes, D. W., Gruen, D., Gruendl, R. A., Gschwend, J., Hartley, W. G., Hernandez-Lang, D., Hinton, S. R., Hollowood, D. L., Honscheid, K., Hughes, A. K., Jacques, A., James, D. J., Johnson, M. D., Kuehn, K., Kuropatkin, N., Lahav, O., Li, T. S., Lidman, C., Lin, H., March, M., Marshall, J. L., Martínez-Delgado, D., Martínez-Vázquez, C. E., Massana, P., Mau, S., McNanna, M., Melchior, P., Menanteau, F., Miller, A. E., Miquel, R., Mohr, J. J., Morgan, R., Mutlu-Pakdil, B., Muñoz, R. R., Neilsen, E. H., Nidever, D. L., Nikutta, R., Nilo Castellon, J. L., Noël, N. E. D., Ogando, R. L. C., Olsen, K. A. G., Pace, A. B., Palmese, A., Paz-Chinchón, F., Pereira, M. E. S., Pieres, A., Plazas Malagón, A. A., Prat, J., Riley, A. H., Rodriguez-Monroy, M., Romer, A. K., Roodman, A., Sako, M., Sakowska, J. D., Sanchez, E., Sánchez, F. J., Sand, D. J., Santana-Silva, L., Santiago, B., Schubnell, M., Serrano, S., Sevilla-Noarbe, I., Simon, J. D., Smith, M., Soares-Santos, M., Stringfellow, G. S., Suchyta, E., Suson, D. J., Tan, C. Y., Tarle, G., Tavangar, K., Thomas, D., To, C., Tollerud, E. J., Troxel, M. A., Tucker, D. L., Varga, T. N., Vivas, A. K., Walker, A. R., Weller, J., Wilkinson, R. D., Wu, J. F., Yanny, B., Zaborowski, E., Zenteno, A., Delve Collaboration, Des Collaboration, and Astro Data Lab (2022). The DECam Local Volume Exploration Survey Data Release 2. *ApJS*, 261(2):38.

Duncan, K. J. (2022). All-purpose, all-sky photometric redshifts for the Legacy Imaging Surveys Data Release 8. *MNRAS*, 512(3):3662–3683.

Efstathiou, G., Bond, J. R., and White, S. D. M. (1992). COBE background radiation anisotropies and large-scale structure in the universe. *MNRAS*, 258(1):1P–6P.

Faber, S. M., Willmer, C. N. A., Wolf, C., Koo, D. C., Weiner, B. J., Newman, J. A., Im, M., Coil, A. L., Conroy, C., Cooper, M. C., Davis, M., Finkbeiner, D. P., Gerke, B. F., Gebhardt, K., Groth, E. J., Guhathakurta, P., Harker, J., Kaiser, N., Kassin, S., Kleinheinrich, M., Konidaris, N. P., Kron, R. G., Lin, L., Luppino, G., Madgwick, D. S., Meisenheimer, K., Noeske, K. G., Phillips, A. C., Sarajedini, V. L., Schiavon, R. P., Simard, L., Szalay, A. S., Vogt, N. P., and Yan, R. (2007). Galaxy Luminosity Functions to z~1 from DEEP2 and COMBO-17: Implications for Red Galaxy Formation. *ApJ*, 665(1):265–294.

Fabian, A. C., Johnstone, R. M., and Daines, S. J. (1994). The effects of dust in cold clouds embedded in cooling flows. *MNRAS*, 271:737–742.

Fakhouri, O., Ma, C.-P., and Boylan-Kolchin, M. (2010). The merger rates and mass assembly histories of dark matter haloes in the two Millennium simulations. *MNRAS*, 406(4):2267–2278.

Farias, H., Ortiz, D., Damke, G., Jaque Arancibia, M., and Solar, M. (2020). Mask galaxy: Morphological segmentation of galaxies. *Astronomy and Computing*, 33:100420.

Fasano, G., Vanzella, E., Dressler, A., Poggianti, B. M., Moles, M., Bettoni, D., Valentinuzzi, T., Moretti, A., D'Onofrio, M., Varela, J., Couch, W. J., Kjærgaard, P., Fritz, J., Omizzolo, A., and Cava, A. (2012). Morphology of galaxies in the WINGS clusters. *MNRAS*, 420(2):926–948.

Fischer, J. L., Domínguez Sánchez, H., and Bernardi, M. (2019). SDSS-IV MaNGA PyMorph Photometric and Deep Learning Morphological Catalogues and implications for bulge properties and stellar angular momentum. *MNRAS*, 483(2):2057–2077.

Foëx, G., Chon, G., and Böhringer, H. (2017). From the core to the outskirts: structure analysis of three massive galaxy clusters. *A&A*, 601:A145.

Freeman, P. E., Izbicki, R., Lee, A. B., Newman, J. A., Conselice, C. J., Koekemoer, A. M., Lotz, J. M., and Mozena, M. (2013). New image statistics for detecting disturbed galaxy morphologies at high redshift. *MNRAS*, 434(1):282–295.

Frei, Z., Guhathakurta, P., Gunn, J. E., and Tyson, J. A. (1996). A Catalog of Digital Images of 113 Nearby Galaxies. *AJ*, 111:174.

Gaia Collaboration, Vallenari, A., Brown, A. G. A., Prusti, T., de Bruijne, J. H. J., Arenou, F., Babusiaux, C., Biermann, M., Creevey, O. L., Ducourant, C., Evans, D. W., Eyer, L., Guerra, R., Hutton, A., Jordi, C., Klioner, S. A., Lammers, U. L., Lindegren, L., Luri, X., Mignard, F., Panem, C., Pourbaix, D., Randich, S., Sartoretti, P., Soubiran, C., Tanga, P., Walton, N. A., Bailer-Jones, C. A. L., Bastian, U., Drimmel, R., Jansen, F., Katz, D., Lattanzi, M. G., van Leeuwen, F., Bakker, J., Cacciari, C., Castañeda, J., De Angeli, F., Fabricius, C., Fouesneau, M., Frémat, Y., Galluccio, L., Guerrier, A., Heiter, U., Masana, E., Messineo, R., Mowlavi, N., Nicolas, C., Nienartowicz, K., Pailler, F., Panuzzo, P., Riclet, F., Roux, W., Seabroke, G. M., Sordo, R., Thévenin, F., Gracia-Abril, G., Portell, J., Teyssier, D., Altmann, M., Andrae, R., Audard, M., Bellas-Velidis, I., Benson, K., Berthier, J., Blomme, R., Burgess, P. W., Busonero, D., Busso, G., Cánovas, H., Carry, B., Cellino, A., Cheek, N., Clementini, G., Damerdji, Y., Davidson, M., de Teodoro, P., Nuñez Campos, M., Delchambre, L., Dell'Oro, A., Esquej, P., Fernández-Hernández, J., Fraile, E., Garabato, D., García-Lario, P., Gosset, E., Haigron, R., Halbwachs, J. L., Hambly, N. C., Harrison, D. L., Hernández, J., Hestroffer, D., Hodgkin, S. T., Holl, B., Janßen, K., Jevardat de Fombelle, G., Jordan, S., Krone-Martins, A., Lanzafame, A. C., Löffler, W., Marchal, O., Marrese, P. M., Moitinho, A., Muinonen, K., Osborne, P., Pancino, E., Pauwels, T., Recio-Blanco, A., Reylé, C., Riello, M., Rimoldini, L., Roegiers, T., Rybizki, J., Sarro, L. M., Siopis, C., Smith, M., Sozzetti, A., Utrilla, E., van Leeuwen, M., Abbas, U., Ábrahám, P., Abreu Aramburu, A., Aerts, C., Aguado, J. J., Ajaj, M., Aldea-Montero, F., Altavilla, G., Álvarez, M. A., Alves, J., Anders, F., Anderson, R. I., Anglada Varela, E., Antoja, T., Baines, D., Baker, S. G., Balaguer-Núñez, L., Balbinot, E., Balog, Z., Barache, C., Barbato, D., Barros, M., Barstow, M. A., Bartolomé, S., Bassilana, J. L., Bauchet, N., Becciani, U., Bellazzini, M., Berihuete, A., Bernet, M., Bertone, S., Bianchi, L., Binnenfeld, A., Blanco-Cuaresma, S., Blazere, A., Boch, T., Bombrun, A., Bossini, D., Bouquillon, S., Bragaglia, A., Bramante, L., Breedt, E., Bressan, A., Brouillet, N., Brugaletta, E., Bucciarelli, B., Burlacu, A., Butkevich, A. G., Buzzi, R., Caffau, E., Cancelliere, R., Cantat-Gaudin, T., Carballo, R., Carlucci, T., Carnerero, M. I., Carrasco, J. M., Casamiquela, L., Castellani, M., Castro-Ginard, A., Chaoul, L., Charlot, P., Chemin, L., Chiaramida, V., Chiavassa, A., Chornay, N., Comoretto, G., Contursi, G., Cooper, W. J., Cornez, T., Cowell, S., Crifo, F., Cropper, M., Crosta, M., Crowley, C., Dafonte, C., Dapergolas, A., David, M., David, P., de Laverny, P., De Luise, F., De March, R., De Ridder, J., de Souza, R., de Torres, A., del Peloso, E. F., del Pozo, E., Delbo, M., Delgado, A., Delisle, J. B., Demouchy, C., Dharmawardena, T. E., Di Matteo, P., Diakite, S., Diener, C., Distefano, E., Dolding, C., Edvardsson, B., Enke, H., Fabre, C., Fabrizio, M., Faigler, S., Fedorets, G., Fernique, P., Fienga, A., Figueras, F., Fournier, Y., Fouron, C., Fragkoudi, F., Gai, M., Garcia-Gutierrez, A., Garcia-Reinaldos, M., García-Torres, M., Garofalo, A., Gavel, A., Gavras, P., Gerlach, E., Geyer, R., Giacobbe, P., Gilmore, G., Girona, S., Giuffrida, G., Gomel, R., Gomez, A., González-Núñez, J., González-Santamaría, I., González-Vidal, J. J., Granvik, M., Guillout, P., Guiraud, J., Gutiérrez-Sánchez, R., Guy, L. P., Hatzidimitriou, D., Hauser, M., Haywood, M., Helmer, A., Helmi, A., Sarmiento, M. H., Hidalgo, S. L., Hilger, T., Hładczuk, N., Hobbs, D., Holland, G., Huckle, H. E., Jardine, K., Jasniewicz, G., Jean-Antoine Piccolo, A., Jiménez-Arranz, Ó., Jorissen, A., Juaristi Campillo, J., Julbe, F., Karbevska, L., Kervella, P., Khanna, S., Kontizas, M., Kordopatis, G., Korn, A. J., Kóspál, Á., Kostrzewa-Rutkowska, Z., Kruszyńska, K., Kun, M., Laizeau, P., Lambert, S., Lanza, A. F., Lasne, Y., Le Campion, J. F., Lebreton, Y., Lebzelter, T., Leccia, S., Leclerc, N., Lecoeur-Taibi, I., Liao, S., Licata, E. L., Lindstrøm, H. E. P., Lister, T. A., Livanou, E., Lobel, A., Lorca, A., Loup, C., Madrero Pardo, P., Magdaleno Romeo, A., Managau, S., Mann, R. G., Manteiga, M., Marchant, J. M., Marconi, M., Marcos, J., Marcos Santos, M. M. S., Marín Pina, D., Marinoni, S., Marocco, F., Marshall, D. J., Martin Polo, L., Martín-Fleitas, J. M., Marton, G., Mary, N., Masip, A., Massari, D., Mastrobuono-Battisti, A., Mazeh, T., McMillan, P. J., Messina, S., Michalik, D., Millar, N. R., Mints, A., Molina, D., Molinaro, R., Molnár, L., Monari, G., Monguió, M., Montegriffo, P., Montero, A., Mor, R., Mora, A., Morbidelli, R., Morel, T., Morris, D., Muraveva, T., Murphy, C. P., Musella, I., Nagy, Z., Noval, L., Ocaña, F., Ogden, A., Ordenovic, C., Osinde, J. O., Pagani, C., Pagano, I., Palaversa, L., Palicio, P. A., Pallas-Quintela, L., Panahi, A., Payne-Wardenaar, S., Peñalosa Esteller, X., Penttilä, A., Pichon, B., Piersimoni, A. M., Pineau, F. X., Plachy, E., Plum, G., Poggio, E., Prša, A., Pulone, L., Racero, E., Ragaini, S., Rainer, M., Raiteri, C. M., Rambaux, N., Ramos, P., Ramos-Lerate, M., Re Fiorentin, P., Regibo, S., Richards, P. J., Rios Diaz, C., Ripepi, V., Riva, A., Rix, H. W., Rixon, G., Robichon, N., Robin, A. C., Robin, C., Roelens, M., Rogues, H. R. O., Rohrbasser, L., Romero-Gómez, M., Rowell, N., Royer, F., Ruz Mieres, D., Rybicki, K. A., Sadowski, G., Sáez Núñez, A., Sagristà Sellés, A., Sahlmann, J., Salguero, E., Samaras, N., Sanchez Gimenez, V., Sanna, N., Santoveña, R., Sarasso, M., Schultheis, M., Sciacca, E., Segol, M., Segovia, J. C., Ségransan, D., Semeux, D., Shahaf, S., Siddiqui, H. I., Siebert, A., Siltala, L., Silvelo, A., Slezak, E., Slezak, I., Smart, R. L., Snaith, O. N., Solano, E., Solitro, F., Souami, D., Souchay, J., Spagna, A., Spina, L., Spoto, F., Steele, I. A., Steidelmüller, H., Stephenson, C. A., Süveges, M., Surdej, J., Szabados, L., Szegedi-Elek, E., Taris, F., Taylor, M. B., Teixeira, R., Tolomei, L., Tonello, N., Torra, F., Torra, J., Torralba Elipe, G., Trabucchi, M., Tsounis, A. T., Turon, C., Ulla, A., Unger, N., Vaillant, M. V., van Dillen, E., van Reeven, W., Vanel, O., Vecchiato, A., Viala, Y., Vicente, D., Voutsinas, S., Weiler, M., Wevers, T., Wyrzykowski, Ł., Yoldas, A., Yvard, P., Zhao, H., Zorec, J., Zucker, S., and Zwitter, T. (2023). Gaia Data Release 3. Summary of the content and survey properties. *A&A*, 674:A1.

Geller, M. J., Hwang, H. S., Diaferio, A., Kurtz, M. J., Coe, D., and Rines, K. J. (2014). A Redshift Survey of the Strong-lensing Cluster Abell 383. *ApJ*, 783(1):52.

Gilbank, D. G., Gladders, M. D., Yee, H. K. C., and Hsieh, B. C. (2011). The Red-sequence Cluster Survey-2 (RCS-2): Survey Details and Photometric Catalog Construction. *AJ*, 141(3):94.

Gladders, M. D. and Yee, H. K. C. (2000). A New Method For Galaxy Cluster Detection. I. The Algorithm. *AJ*, 120(4):2148–2162.

Gladders, M. D. and Yee, H. K. C. (2005). The Red-Sequence Cluster Survey. I. The Survey and Cluster Catalogs for Patches RCS 0926+37 and RCS 1327+29. *ApJS*, 157(1):1–29.

Gómez, P. L., Nichol, R. C., Miller, C. J., Balogh, M. L., Goto, T., Zabludoff, A. I., Romer, A. K., Bernardi, M., Sheth, R., Hopkins, A. M., Castander, F. J., Connolly, A. J., Schneider, D. P., Brinkmann, J., Lamb, D. Q., SubbaRao, M., and York, D. G. (2003). Galaxy Star

Formation as a Function of Environment in the Early Data Release of the Sloan Digital Sky Survey. *ApJ*, 584(1):210–227.

Gonzalez, E. J., Foëx, G., Nilo Castellón, J. L., Domínguez Romero, M. J., Alonso, M. V., García Lambas, D., Moreschi, O., and Gallo, E. (2015). Low X-ray luminosity galaxy clusters - III. Weak lensing mass determination at 0.18 ¡ z ¡ 0.70. *MNRAS*, 452(3):2225–2235.

Guennou, L., Adami, C., Durret, F., Lima Neto, G. B., Ulmer, M. P., Clowe, D., LeBrun, V., Martinet, N., Allam, S., Annis, J., Basa, S., Benoist, C., Biviano, A., Cappi, A., Cypriano, E. S., Gavazzi, R., Halliday, C., Ilbert, O., Jullo, E., Just, D., Limousin, M., Márquez, I., Mazure, A., Murphy, K. J., Plana, H., Rostagni, F., Russeil, D., Schirmer, M., Slezak, E., Tucker, D., Zaritsky, D., and Ziegler, B. (2014). Structure and substructure analysis of DAFT/FADA galaxy clusters in the [0.4-0.9] redshift range. *A&A*, 561:A112.

Gunn, J. E. and Gott, J. Richard, I. (1972). On the Infall of Matter Into Clusters of Galaxies and Some Effects on Their Evolution. *ApJ*, 176:1.

Guzzo, L., Schuecker, P., Böhringer, H., Collins, C. A., Ortiz-Gil, A., de Grandi, S., Edge, A. C., Neumann, D. M., Schindler, S., Altucci, C., and Shaver, P. A. (2009). The REFLEX galaxy cluster survey. VIII. Spectroscopic observations and optical atlas,. *A&A*, 499(2):357–369.

Hamilton, D. (1985). The spectral evolution of galaxies. I. an observational approach. *ApJ*, 297:371–389.

Harvey, D., Massey, R., Kitching, T., Taylor, A., and Tittley, E. (2015). The nongravitational interactions of dark matter in colliding galaxy clusters. *Science*, 347(6229):1462–1465.

Hasselfield, M., Hilton, M., Marriage, T. A., Addison, G. E., Barrientos, L. F., Battaglia, N., Battistelli, E. S., Bond, J. R., Crichton, D., Das, S., Devlin, M. J., Dicker, S. R., Dunkley, J., Dünner, R., Fowler, J. W., Gralla, M. B., Hajian, A., Halpern, M., Hincks, A. D., Hlozek, R., Hughes, J. P., Infante, L., Irwin, K. D., Kosowsky, A., Marsden, D., Menanteau, F., Moodley, K., Niemack, M. D., Nolta, M. R., Page, L. A., Partridge, B., Reese, E. D., Schmitt, B. L., Sehgal, N., Sherwin, B. D., Sievers, J., Sifón, C., Spergel, D. N., Staggs, S. T., Swetz, D. S., Switzer, E. R., Thornton, R., Trac, H., and Wollack, E. J. (2013). The Atacama Cosmology Telescope: Sunyaev-Zel'dovich selected galaxy clusters at 148 GHz from three seasons of data. *J. Cosmology Astropart. Phys.*, 2013(7):008.

Häussler, B., McIntosh, D. H., Barden, M., Bell, E. F., Rix, H.-W., Borch, A., Beckwith, S. V. W., Caldwell, J. A. R., Heymans, C., Jahnke, K., Jogee, S., Koposov, S. E., Meisenheimer, K., Sánchez, S. F., Somerville, R. S., Wisotzki, L., and Wolf, C. (2007). GEMS: Galaxy Fitting Catalogs and Testing Parametric Galaxy Fitting Codes: GALFIT and GIM2D. *ApJS*, 172(2):615–633.

Häußler, B., Vika, M., Bamford, S. P., Johnston, E. J., Brough, S., Casura, S., Holwerda, B. W., Kelvin, L. S., and Popescu, C. (2022). GALAPAGOS-2/GALFITM/GAMA - Multi-wavelength measurement of galaxy structure: Separating the properties of spheroid and disk components in modern surveys. *A&A*, 664:A92.

Hernández-Lang, D., Zenteno, A., Diaz-Ocampo, A., Cuevas, H., Clancy, J., Prado, P. H., Aldás, F., Pallero, D., Monteiro-Oliveira, R., Gómez, F. A., Ramirez, A., Wynter, J., Carrasco, E. R., Hau, G. K. T., Stalder, B., McDonald, M., Bayliss, M., Floyd, B., Garmire, G., Katzenberger, A., Kim, K. J., Klein, M., Mahler, G., Nilo Castellon, J. L., Saro, A., and Somboonpanyakul, T. (2022). Clash of Titans: A MUSE dynamical study of the extreme cluster merger SPT-CL J0307-6225. *MNRAS*, 517(3):4355–4378.

Hilton, M., Hasselfield, M., Sifón, C., Battaglia, N., Aiola, S., Bharadwaj, V., Bond, J. R., Choi, S. K., Crichton, D., Datta, R., Devlin, M. J., Dunkley, J., Dünner, R., Gallardo, P. A., Gralla, M., Hincks, A. D., Ho, S.-P. P., Hubmayr, J., Huffenberger, K. M., Hughes, J. P., Koopman, B. J., Kosowsky, A., Louis, T., Madhavacheril, M. S., Marriage, T. A., Maurin, L., McMahon, J., Miyatake, H., Moodley, K., Næss, S., Nati, F., Newburgh, L., Niemack, M. D., Oguri, M., Page, L. A., Partridge, B., Schmitt, B. L., Sievers, J., Spergel, D. N., Staggs, S. T., Trac, H., van Engelen, A., Vavagiakis, E. M., and Wollack, E. J. (2018). The Atacama Cosmology Telescope: The Two-season ACTPol Sunyaev-Zel'dovich Effect Selected Cluster Catalog. *ApJS*, 235(1):20.

Hilton, M., Sifón, C., Naess, S., Madhavacheril, M., Oguri, M., Rozo, E., Rykoff, E., Abbott, T. M. C., Adhikari, S., Aguena, M., Aiola, S., Allam, S., Amodeo, S., Amon, A., Annis, J., Ansarinejad, B., Aros-Bunster, C., Austermann, J. E., Avila, S., Bacon, D., Battaglia, N., Beall, J. A., Becker, D. T., Bernstein, G. M., Bertin, E., Bhandarkar, T., Bhargava, S., Bond, J. R., Brooks, D., Burke, D. L., Calabrese, E., Carrasco Kind, M., Carretero, J., Choi, S. K., Choi, A., Conselice, C., da Costa, L. N., Costanzi, M., Crichton, D., Crowley, K. T., Dünner, R., Denison, E. V., Devlin, M. J., Dicker, S. R., Diehl, H. T., Dietrich, J. P., Doel, P., Duff, S. M., Duivenvoorden, A. J., Dunkley, J., Everett, S., Ferraro, S., Ferrero, I., Ferté, A., Flaugher, B., Frieman, J., Gallardo, P. A., García-Bellido, J., Gaztanaga, E., Gerdes, D. W., Giles, P., Golec, J. E., Gralla, M. B., Grandis, S., Gruen, D., Gruendl, R. A., Gschwend, J., Gutierrez, G., Han, D., Hartley, W. G., Hasselfield, M., Hill, J. C., Hilton, G. C., Hincks,

A. D., Hinton, S. R., Ho, S. P. P., Honscheid, K., Hoyle, B., Hubmayr, J., Huffenberger, K. M., Hughes, J. P., Jaelani, A. T., Jain, B., James, D. J., Jeltema, T., Kent, S., Knowles, K., Koopman, B. J., Kuehn, K., Lahav, O., Lima, M., Lin, Y. T., Lokken, M., Loubser, S. I., MacCrann, N., Maia, M. A. G., Marriage, T. A., Martin, J., McMahon, J., Melchior, P., Menanteau, F., Miquel, R., Miyatake, H., Moodley, K., Morgan, R., Mroczkowski, T., Nati, F., Newburgh, L. B., Niemack, M. D., Nishizawa, A. J., Ogando, R. L. C., Orlowski-Scherer, J., Page, L. A., Palmese, A., Partridge, B., Paz-Chinchón, F., Phakathi, P., Plazas, A. A., Robertson, N. C., Romer, A. K., Carnero Rosell, A., Salatino, M., Sanchez, E., Schaan, E., Schillaci, A., Sehgal, N., Serrano, S., Shin, T., Simon, S. M., Smith, M., Soares-Santos, M., Spergel, D. N., Staggs, S. T., Storer, E. R., Suchyta, E., Swanson, M. E. C., Tarle, G., Thomas, D., To, C., Trac, H., Ullom, J. N., Vale, L. R., Van Lanen, J., Vavagiakis, E. M., De Vicente, J., Wilkinson, R. D., Wollack, E. J., Xu, Z., and Zhang, Y. (2021). The Atacama Cosmology Telescope: A Catalog of ¿4000 Sunyaev-Zel'dovich Galaxy Clusters. *ApJS*, 253(1):3.

Hinshaw, G., Larson, D., Komatsu, E., Spergel, D. N., Bennett, C. L., Dunkley, J., Nolta, M. R., Halpern, M., Hill, R. S., Odegard, N., Page, L., Smith, K. M., Weiland, J. L., Gold, B., Jarosik, N., Kogut, A., Limon, M., Meyer, S. S., Tucker, G. S., Wollack, E., and Wright, E. L. (2013). Nine-year Wilkinson Microwave Anisotropy Probe (WMAP) Observations: Cosmological Parameter Results. *ApJS*, 208(2):19.

Hotelling, H. (1933). Analysis of a complex of statistical variables into principal components. *Journal of educational psychology*, 24(6):417.

Hubble, E. P. (1936). *Realm of the Nebulae.*

Huertas-Company, M., Bernardi, M., Pérez-González, P. G., Ashby, M. L. N., Barro, G., Conselice, C., Daddi, E., Dekel, A., Dimauro, P., Faber, S. M., Grogin, N. A., Kartaltepe, J. S., Kocevski, D. D., Koekemoer, A. M., Koo, D. C., Mei, S., and Shankar, F. (2016). Mass assembly and morphological transformations since z $\sim$ 3 from CANDELS. *MNRAS*, 462(4):4495–4516.

Ilbert, O., Arnouts, S., McCracken, H. J., Bolzonella, M., Bertin, E., Le Fèvre, O., Mellier, Y., Zamorani, G., Pellò, R., Iovino, A., Tresse, L., Le Brun, V., Bottini, D., Garilli, B., Maccagni, D., Picat, J. P., Scaramella, R., Scodeggio, M., Vettolani, G., Zanichelli, A., Adami, C., Bardelli, S., Cappi, A., Charlot, S., Ciliegi, P., Contini, T., Cucciati, O., Foucaud, S., Franzetti, P., Gavignaud, I., Guzzo, L., Marano, B., Marinoni, C., Mazure, A., Meneux, B., Merighi, R., Paltani, S., Pollo, A., Pozzetti, L., Radovich, M., Zucca, E., Bondi, M., Bongiorno, A., Busarello, G., de La Torre, S., Gregorini, L., Lamareille, F., Mathez, G., Merluzzi, P., Ripepi, V., Rizzo, D., and Vergani, D. (2006). Accurate photometric redshifts for the CFHT legacy survey calibrated using the VIMOS VLT deep survey. *A&A*, 457(3):841–856.

Ilbert, O., Salvato, M., Le Floc'h, E., Aussel, H., Capak, P., McCracken, H. J., Mobasher, B., Kartaltepe, J., Scoville, N., Sanders, D. B., Arnouts, S., Bundy, K., Cassata, P., Kneib, J. P., Koekemoer, A., Le Fèvre, O., Lilly, S., Surace, J., Taniguchi, Y., Tasca, L., Thompson, D., Tresse, L., Zamojski, M., Zamorani, G., and Zucca, E. (2010). Galaxy Stellar Mass Assembly Between 0.2 ¡ z ¡ 2 from the S-COSMOS Survey. *ApJ*, 709(2):644–663.

Jeltema, T. E., Canizares, C. R., Bautz, M. W., and Buote, D. A. (2005). The Evolution of Structure in X-Ray Clusters of Galaxies. *ApJ*, 624(2):606–629.

Kaiser, N., Squires, G., and Broadhurst, T. (1995). A Method for Weak Lensing Observations. *ApJ*, 449:460.

Kauffmann, G., White, S. D. M., Heckman, T. M., Ménard, B., Brinchmann, J., Charlot, S., Tremonti, C., and Brinkmann, J. (2004). The environmental dependence of the relations between stellar mass, structure, star formation and nuclear activity in galaxies. *MNRAS*, 353(3):713–731.

Kesebonye, K. C., Hilton, M., Knowles, K., Cotton, W. D., Clarke, T. E., Loubser, S. I., Moodley, K., and Sikhosana, S. P. (2023). The MeerKAT Galaxy Clusters Legacy Survey: star formation in massive clusters at 0.15 ¡ z ¡ 0.35. *MNRAS*, 518(2):3004–3016.

Kluge, M., Comparat, J., Liu, A., Balzer, F., Bulbul, E., Ider Chitham, J., Ghirardini, V., Garrel, C., Bahar, Y. E., Artis, E., Bender, R., Clerc, N., Dwelly, T., Fabricius, M. H., Grandis, S., Hernández-Lang, D., Hill, G. J., Joshi, J., Lamer, G., Merloni, A., Nandra, K., Pacaud, F., Predehl, P., Ramos-Ceja, M. E., Reiprich, T. H., Salvato, M., Sanders, J. S., Schrabback, T., Seppi, R., Zelmer, S., Zenteno, A., and Zhang, X. (2024). The First SRG/eROSITA All-Sky Survey: Optical Identification and Properties of Galaxy Clusters and Groups in the Western Galactic Hemisphere. *arXiv e-prints*, page arXiv:2402.08453.

Kluge, M., Neureiter, B., Riffeser, A., Bender, R., Goessl, C., Hopp, U., Schmidt, M., Ries, C., and Brosch, N. (2020). Structure of Brightest Cluster Galaxies and Intracluster Light. *ApJS*, 247(2):43.

Kodama, T., Arimoto, N., Barger, A. J., and Arag'on-Salamanca, A. (1998). Evolution of the colour-magnitude relation of early-type galaxies in distant clusters. *A&A*, 334:99–109.

Kolesnikov, I., Sampaio, V. M., de Carvalho, R. R., Conselice, C., Rembold, S. B., Mendes, C. L., and Rosa, R. R. (2024). Unveiling galaxy morphology through an unsupervised-supervised hybrid approach. *MNRAS*, 528(1):82–107.

Lacerna, I., Rodriguez, F., Montero-Dorta, A. D., O'Mill, A. L., Cora, S. A., Artale, M. C., Ruiz, A. N., Hough, T., and Vega-Martínez, C. A. (2022). On the environmental influence of groups and clusters of galaxies beyond the virial radius: Galactic conformity at few Mpc scales. *MNRAS*, 513(2):2271–2284.

Lahav, O., Naim, A., Sodré, L., J., and Storrie-Lombardi, M. C. (1996). Neural computation as a tool for galaxy classification: methods and examples. *MNRAS*, 283:207.

Lang, D., Hogg, D. W., and Mykytyn, D. (2016). The Tractor: Probabilistic astronomical source detection and measurement. Astrophysics Source Code Library, record ascl:1604.008.

Lange, R., Driver, S. P., Robotham, A. S. G., Kelvin, L. S., Graham, A. W., Alpaslan, M., Andrews, S. K., Baldry, I. K., Bamford, S., Bland-Hawthorn, J., Brough, S., Cluver, M. E., Conselice, C. J., Davies, L. J. M., Haeussler, B., Konstantopoulos, I. S., Loveday, J., Moffett, A. J., Norberg, P., Phillipps, S., Taylor, E. N., López-Sánchez, Á. R., and Wilkins, S. M. (2015). Galaxy And Mass Assembly (GAMA): mass-size relations of z ¡ 0.1 galaxies subdivided by Sérsic index, colour and morphology. *MNRAS*, 447(3):2603–2630.

Larson, R. B., Tinsley, B. M., and Caldwell, C. N. (1980). The evolution of disk galaxies and the origin of S0 galaxies. *ApJ*, 237:692–707.

Lima-Dias, C., Monachesi, A., Torres-Flores, S., Cortesi, A., Hernández-Lang, D., P. Montaguth, G., Jiménez-Teja, Y., Panda, S., Menéndez-Delmestre, K., Gonçalves, T. S., Méndez-Hernández, H., Telles, E., Dimauro, P., Bom, C. R., Mendes de Oliveira, C., Kanaan, A., Ribeiro, T., and Schoenell, W. (2024). Bulge-disc decomposition of the Hydra cluster galaxies in 12 bands. *MNRAS*, 527(3):5792–5807.

Lin, C. C. and Shu, F. H. (1964). On the Spiral Structure of Disk Galaxies. *ApJ*, 140:646.

Lin, C. C. and Shu, F. H. (1966). On the Spiral Structure of Disk Galaxies, II. Outline of a Theory of Density Waves. *Proceedings of the National Academy of Science*, 55(2):229–234.

Lintott, C. J., Schawinski, K., Slosar, A., Land, K., Bamford, S., Thomas, D., Raddick, M. J., Nichol, R. C., Szalay, A., Andreescu, D., Murray, P., and Vandenberg, J. (2008). Galaxy Zoo: morphologies derived from visual inspection of galaxies from the Sloan Digital Sky Survey. *MNRAS*, 389(3):1179–1189.

Liu, A., Bulbul, E., Ghirardini, V., Liu, T., Klein, M., Clerc, N., Özsoy, Y., Ramos-Ceja, M. E., Pacaud, F., Comparat, J., Okabe, N., Bahar, Y. E., Biffi, V., Brunner, H., Brüggen, M., Buchner, J., Ider Chitham, J., Chiu, I., Dolag, K., Gatuzz, E., Gonzalez, J., Hoang, D. N., Lamer, G., Merloni, A., Nandra, K., Oguri, M., Ota, N., Predehl, P., Reiprich, T. H., Salvato, M., Schrabback, T., Sanders, J. S., Seppi, R., and Thibaud, Q. (2022). The eROSITA Final Equatorial-Depth Survey (eFEDS). Catalog of galaxy clusters and groups. *A&A*, 661:A2.

Liu, C., Hao, L., Wang, H., and Yang, X. (2019). The Morphological Transformation and the Quenching of Galaxies. *ApJ*, 878(1):69.

Lorenz, M. O. (1905). Methods of measuring the concentration of wealth. *Publications of the American statistical association*, 9(70):209–219.

Lotz, J. M., Davis, M., Faber, S. M., Guhathakurta, P., Gwyn, S., Huang, J., Koo, D. C., Le Floc'h, E., Lin, L., Newman, J., Noeske, K., Papovich, C., Willmer, C. N. A., Coil, A., Conselice, C. J., Cooper, M., Hopkins, A. M., Metevier, A., Primack, J., Rieke, G., and Weiner, B. J. (2008). The Evolution of Galaxy Mergers and Morphology at z ¡ 1.2 in the Extended Groth Strip. *ApJ*, 672(1):177–197.

Lotz, J. M., Primack, J., and Madau, P. (2004). A New Nonparametric Approach to Galaxy Morphological Classification. *AJ*, 128(1):163–182.

Lourenço, A. C. C., Jaffé, Y. L., Vulcani, B., Biviano, A., Poggianti, B., Moretti, A., Kelkar, K., Crossett, J. P., Gitti, M., Smith, R., Laganá, T. F., Gullieuszik, M., Ignesti, A., McGee, S., Wolter, A., Sonkamble, S., and Müller, A. (2023). The effect of cluster dynamical state on ram-pressure stripping. *MNRAS*, 526(4):4831–4847.

Lovisari, L., Forman, W. R., Jones, C., Ettori, S., Andrade-Santos, F., Arnaud, M., Démoclès, J., Pratt, G. W., Randall, S., and Kraft, R. (2017). X-Ray Morphological Analysis of the Planck ESZ Clusters. *ApJ*, 846(1):51.

Mancone, C. L. and Gonzalez, A. H. (2012). EzGal: A Flexible Interface for Stellar Population Synthesis Models. *PASP*, 124(916):606.

Mancone, C. L., Gonzalez, A. H., Brodwin, M., Stanford, S. A., Eisenhardt, P. R. M., Stern, D., and Jones, C. (2010). The Formation of Massive Cluster Galaxies. *ApJ*, 720(1):284–298.

Mann, A. W. and Ebeling, H. (2012). X-ray-optical classification of cluster mergers and the evolution of the cluster merger fraction. *MNRAS*, 420(3):2120–2138.

Mansheim, A. S., Lemaux, B. C., Tomczak, A. R., Lubin, L. M., Rumbaugh, N., Wu, P. F., Gal, R. R., Shen, L., Dawson, W. A., and Squires, G. K. (2017). Suppressed star formation by a merging cluster system. *MNRAS*, 469(1):L20–L25.

Martin, D. C., Wyder, T. K., Schiminovich, D., Barlow, T. A., Forster, K., Friedman, P. G., Morrissey, P., Neff, S. G., Seibert, M., Small, T., Welsh, B. Y., Bianchi, L., Donas, J., Heckman, T. M., Lee, Y.-W., Madore, B. F., Milliard, B., Rich, R. M., Szalay, A. S., and Yi, S. K. (2007). The UV-Optical Galaxy Color-Magnitude Diagram. III. Constraints on Evolution from the Blue to the Red Sequence. *ApJS*, 173(2):342–356.

Massey, R., Kitching, T., and Nagai, D. (2011). Cluster bulleticity. *MNRAS*, 413(3):1709–1716.

McDonald, M., Bayliss, M., Benson, B. A., Foley, R. J., Ruel, J., Sullivan, P., Veilleux, S., Aird, K. A., Ashby, M. L. N., Bautz, M., Bazin, G., Bleem, L. E., Brodwin, M., Carlstrom, J. E., Chang, C. L., Cho, H. M., Clocchiatti, A., Crawford, T. M., Crites, A. T., de Haan, T., Desai, S., Dobbs, M. A., Dudley, J. P., Egami, E., Forman, W. R., Garmire, G. P., George, E. M., Gladders, M. D., Gonzalez, A. H., Halverson, N. W., Harrington, N. L., High, F. W., Holder, G. P., Holzapfel, W. L., Hoover, S., Hrubes, J. D., Jones, C., Joy, M., Keisler, R., Knox, L., Lee, A. T., Leitch, E. M., Liu, J., Lueker, M., Luong-van, D., Mantz, A., Marrone, D. P., McMahon, J. J., Mehl, J., Meyer, S. S., Miller, E. D., Mocanu, L., Mohr, J. J., Montroy, T. E., Murray, S. S., Natoli, T., Padin, S., Plagge, T., Pryke, C., Rawle, T. D., Reichardt, C. L., Rest, A., Rex, M., Ruhl, J. E., Saliwanchik, B. R., Saro, A., Sayre, J. T., Schaffer, K. K., Shaw, L., Shirokoff, E., Simcoe, R., Song, J., Spieler, H. G., Stalder, B., Staniszewski, Z., Stark, A. A., Story, K., Stubbs, C. W., Šuhada, R., van Engelen, A., Vanderlinde, K., Vieira, J. D., Vikhlinin, A., Williamson, R., Zahn, O., and Zenteno, A. (2012). A massive, cooling-flow-induced starburst in the core of a luminous cluster of galaxies. *Nature*, 488(7411):349–352.

McDonald, M., Benson, B. A., Vikhlinin, A., Stalder, B., Bleem, L. E., de Haan, T., Lin, H. W., Aird, K. A., Ashby, M. L. N., Bautz, M. W., Bayliss, M., Bocquet, S., Brodwin, M., Carlstrom, J. E., Chang, C. L., Cho, H. M., Clocchiatti, A., Crawford, T. M., Crites, A. T., Desai, S., Dobbs, M. A., Dudley, J. P., Foley, R. J., Forman, W. R., George, E. M., Gettings, D., Gladders, M. D., Gonzalez, A. H., Halverson, N. W., High, F. W., Holder, G. P., Holzapfel, W. L., Hoover, S., Hrubes, J. D., Jones, C., Joy, M., Keisler, R., Knox, L., Lee, A. T., Leitch, E. M., Liu, J., Lueker, M., Luong-Van, D., Mantz, A., Marrone, D. P., McMahon, J. J., Mehl, J., Meyer, S. S., Miller, E. D., Mocanu, L., Mohr, J. J., Montroy, T. E., Murray, S. S., Nurgaliev, D., Padin, S., Plagge, T., Pryke, C., Reichardt, C. L., Rest, A., Ruel, J., Ruhl, J. E., Saliwanchik, B. R., Saro, A., Sayre, J. T., Schaffer, K. K., Shirokoff, E., Song, J., Šuhada, R., Spieler, H. G., Stanford, S. A., Staniszewski, Z., Stark, A. A., Story, K., van Engelen, A., Vanderlinde, K., Vieira, J. D., Williamson, R., Zahn, O., and Zenteno, A. (2013). The Growth of Cool Cores and Evolution of Cooling Properties in a Sample of 83 Galaxy Clusters at 0.3 ¡ z ¡ 1.2 Selected from the SPT-SZ Survey. *ApJ*, 774(1):23.

Mei, S., Stanford, S. A., Holden, B. P., Raichoor, A., Postman, M., Nakata, F., Finoguenov, A., Ford, H. C., Illingworth, G. D., Kodama, T., Rosati, P., Tanaka, M., Huertas-Company, M., Rettura, A., Shankar, F., Carrasco, E. R., Demarco, R., Eisenhardt, P., Jee, M. J., Koyama, Y., and White, R. L. (2012). Early-type Galaxies at z = 1.3. I. The Lynx Supercluster: Cluster and Groups at z = 1.3. Morphology and Color-Magnitude Relation. *ApJ*, 754(2):141.

Menci, N., Fontana, A., Giallongo, E., and Salimbeni, S. (2005). Bimodal Color Distribution in Hierarchical Galaxy Formation. *ApJ*, 632(1):49–57.

Mercurio, A., Rosati, P., Biviano, A., Annunziatella, M., Girardi, M., Sartoris, B., Nonino, M., Brescia, M., Riccio, G., Grillo, C., Balestra, I., Caminha, G. B., De Lucia, G., Gobat, R., Seitz, S., Tozzi, P., Scodeggio, M., Vanzella, E., Angora, G., Bergamini, P., Borgani, S., Demarco, R., Meneghetti, M., Strazzullo, V., Tortorelli, L., Umetsu, K., Fritz, A., Gruen, D., Kelson, D., Lombardi, M., Maier, C., Postman, M., Rodighiero, G., and Ziegler, B. (2021). CLASH-VLT: Abell S1063. Cluster assembly history and spectroscopic catalogue. *A&A*, 656:A147.

Merloni, A., Lamer, G., Liu, T., Ramos-Ceja, M. E., Brunner, H., Bulbul, E., Dennerl, K., Doroshenko, V., Freyberg, M. J., Friedrich, S., Gatuzz, E., Georgakakis, A., Haberl, F., Igo, Z., Kreykenbohm, I., Liu, A., Maitra, C., Malyali, A., Mayer, M. G. F., Nandra, K., Predehl, P., Robrade, J., Salvato, M., Sanders, J. S., Stewart, I., Tubín-Arenas, D., Weber, P., Wilms, J., Arcodia, R., Artis, E., Aschersleben, J., Avakyan, A., Aydar, C., Bahar, Y. E., Balzer, F., Becker, W., Berger, K., Boller, T., Bornemann, W., Brüggen, M., Brusa, M., Buchner, J., Burwitz, V., Camilloni, F., Clerc, N., Comparat, J., Coutinho, D., Czesla, S., Dannhauer, S. M., Dauner, L., Dauser, T., Dietl, J., Dolag, K., Dwelly, T., Egg, K., Ehl, E., Freund, S., Friedrich, P., Gaida, R., Garrel, C., Ghirardini, V., Gokus, A., Grünwald, G., Grandis, S., Grotova, I., Gruen, D., Gueguen, A., Hämmerich, S., Hamaus, N., Hasinger, G., Haubner, K., Homan, D., Ider Chitham, J., Joseph, W. M., Joyce, A., König, O., Kaltenbrunner, D. M., Khokhriakova, A., Kink, W., Kirsch, C., Kluge, M., Knies, J., Krippendorf, S., Krumpe, M., Kurpas, J., Li, P., Liu, Z., Locatelli, N., Lorenz, M., Müller, S., Magaudda, E., Mannes, C., McCall, H., Meidinger, N., Michailidis, M., Migkas, K., Muñoz-Giraldo, D., Musiimenta, B., Nguyen-Dang, N. T., Ni, Q., Olechowska, A., Ota, N., Pacaud, F., Pasini, T., Perinati, E., Pires, A. M., Pommranz, C., Ponti, G., Poppenhaeger, K., Pühlhofer, G., Rau, A., Reh, M., Reiprich, T. H., Roster, W., Saeedi, S., Santangelo, A., Sasaki, M., Schmitt, J., Schneider, P. C., Schrabback, T., Schuster, N., Schwope, A., Seppi, R., Serim, M. M., Shreeram, S., Sokolova-Lapa, E., Starck, H., Stelzer, B., Stierhof, J., Suleimanov, V., Tenzer, C., Traulsen, I., Trümper, J., Tsuge, K., Urrutia, T., Veronica, A., Waddell, S. G. H., Willer, R., Wolf, J., Yeung, M. C. H., Zainab, A., Zangrandi, F., Zhang, X., Zhang, Y., and Zheng, X. (2024). The SRG/eROSITA all-sky survey. First X-ray catalogues and data release of the western Galactic hemisphere. *A&A*, 682:A34.

Merloni, A., Predehl, P., Becker, W., Böhringer, H., Boller, T., Brunner, H., Brusa, M., Dennerl, K., Freyberg, M., Friedrich, P., Georgakakis, A., Haberl, F., Hasinger, G., Meidinger, N., Mohr, J., Nandra, K., Rau, A., Reiprich, T. H., Robrade, J., Salvato, M., Santangelo, A., Sasaki, M., Schwope, A., Wilms, J., and German eROSITA Consortium, t. (2012). eROSITA Science Book: Mapping the Structure of the Energetic Universe. *arXiv e-prints*, page arXiv:1209.3114.

Molnar, S. M. (2016). Cluster physics with merging galaxy clusters. *Frontiers in Astronomy and Space Sciences*, 2:7.

Montaguth, G. P., Torres-Flores, S., Monachesi, A., Gómez, F. A., Lima-Dias, C., Cortesi, A., Mendes de Oliveira, C., Telles, E., Panda, S., Grossi, M., Lopes, P. A. A., Hernandez-Jimenez, J. A., Kanaan, A., Ribeiro, T., and Schoenell, W. (2023). Galaxy evolution in compact groups - I. Revealing a transitional galaxy population through a multiwavelength approach. *MNRAS*, 524(4):5340–5356.

Moore, B., Katz, N., Lake, G., Dressler, A., and Oemler, A. (1996). Galaxy harassment and the evolution of clusters of galaxies. *Nature*, 379(6566):613–616.

Mowla, L. A., van Dokkum, P., Brammer, G. B., Momcheva, I., van der Wel, A., Whitaker, K., Nelson, E., Bezanson, R., Muzzin, A., Franx, M., MacKenty, J., Leja, J., Kriek, M., and Marchesini, D. (2019). COSMOS-DASH: The Evolution of the Galaxy Size-Mass Relation since z $\sim$ 3 from New Wide-field WFC3 Imaging Combined with CANDELS/3D-HST. *ApJ*, 880(1):57.

Nilo Castellón, J. L., Alonso, M. V., García Lambas, D., O'Mill, A. L., Valotto, C., Carrasco, E. R., Cuevas, H., and Ramírez, A. (2014). Low X-ray luminosity galaxy clusters - II. Optical properties and morphological content at 0.18 ¡ z ¡ 0.70. *MNRAS*, 437(3):2607–2620.

Noeske, K. G., Weiner, B. J., Faber, S. M., Papovich, C., Koo, D. C., Somerville, R. S., Bundy, K., Conselice, C. J., Newman, J. A., Schiminovich, D., Le Floc'h, E., Coil, A. L., Rieke, G. H., Lotz, J. M., Primack, J. R., Barmby, P., Cooper, M. C., Davis, M., Ellis, R. S., Fazio, G. G., Guhathakurta, P., Huang, J., Kassin, S. A., Martin, D. C., Phillips, A. C., Rich, R. M., Small, T. A., Willmer, C. N. A., and Wilson, G. (2007). Star Formation in AEGIS Field Galaxies since z=1.1: The Dominance of Gradually Declining Star Formation, and the Main Sequence of Star-forming Galaxies. *ApJ*, 660(1):L43–L46.

Nulsen, P. E. J. (1982). Transport processes and the stripping of cluster galaxies. *MNRAS*, 198:1007–1016.

Nurgaliev, D., McDonald, M., Benson, B. A., Miller, E. D., Stubbs, C. W., and Vikhlinin, A. (2013). A Robust Quantification of Galaxy Cluster Morphology Using Asymmetry and Central Concentration. *ApJ*, 779(2):112.

Okabe, N., Takada, M., Umetsu, K., Futamase, T., and Smith, G. P. (2010). LoCuSS: Subaru Weak Lensing Study of 30 Galaxy Clusters. *PASJ*, 62:811.

Owers, M. S., Couch, W. J., Nulsen, P. E. J., and Randall, S. W. (2012). Shocking Tails in the Major Merger Abell 2744. *ApJ*, 750(1):L23.

Owers, M. S., Nulsen, P. E. J., Couch, W. J., Ma, C.-J., David, L. P., Forman, W. R., Hopkins, A. M., Jones, C., and van Weeren, R. J. (2014). A Merger Shock in A2034. *ApJ*, 780(2):163.

Owers, M. S., Randall, S. W., Nulsen, P. E. J., Couch, W. J., David, L. P., and Kempner, J. C. (2011). The Dissection of Abell 2744: A Rich Cluster Growing Through Major and Minor Mergers. *ApJ*, 728(1):27.

Pedregosa, F., Varoquaux, G., Gramfort, A., Michel, V., Thirion, B., Grisel, O., Blondel, M., Müller, A., Nothman, J., Louppe, G., Prettenhofer, P., Weiss, R., Dubourg, V., Vanderplas, J., Passos, A., Cournapeau, D., Brucher, M., Perrot, M., and Duchesnay, É. (2011). Scikit-learn: Machine Learning in Python. *Journal of Machine Learning Research*, 12:2825–2830.

Pelló, R., Rudnick, G., De Lucia, G., Simard, L., Clowe, D. I., Jablonka, P., Milvang-Jensen, B., Saglia, R. P., White, S. D. M., Aragón-Salamanca, A., Halliday, C., Poggianti, B., Best, P., Dalcanton, J., Dantel-Fort, M., Fort, B., von der Linden, A., Mellier, Y., Rottgering, H., and Zaritsky, D. (2009). Photometric redshifts and cluster tomography in the ESO Distant Cluster Survey. *A&A*, 508(3):1173–1191.

Peng, C. Y., Ho, L. C., Impey, C. D., and Rix, H.-W. (2002). Detailed Structural Decomposition of Galaxy Images. *AJ*, 124(1):266–293.

Peng, C. Y., Ho, L. C., Impey, C. D., and Rix, H.-W. (2010). Detailed Decomposition of Galaxy Images. II. Beyond Axisymmetric Models. *AJ*, 139(6):2097–2129.

Perez, J., Tissera, P., Padilla, N., Alonso, M. S., and Lambas, D. G. (2009). Global environmental effects versus galaxy interactions. *MNRAS*, 399(3):1157–1166.

Petrosian, V. (1976). Surface Brightness and Evolution of Galaxies. *ApJ*, 210:L53.

Pfeffer, J., Cavanagh, M. K., Bekki, K., Couch, W. J., Drinkwater, M. J., Forbes, D. A., and Koribalski, B. S. (2023). The galaxy morphology-density relation in the EAGLE simulation. *MNRAS*, 518(4):5260–5278.

Pillay, D. S., Turner, D. J., Hilton, M., Knowles, K., Kesebonye, K. C., Moodley, K., Mroczkowski, T., Oozeer, N., Pfrommer, C., Sikhosana, S. P., and Wollack, E. J. (2021). A Multiwavelength Dynamical State Analysis of ACT-CL J0019.6+0336. *Galaxies*, 9(4):97.

Planck Collaboration, Ade, P. A. R., Aghanim, N., Armitage-Caplan, C., Arnaud, M., Ashdown, M., Atrio-Barandela, F., Aumont, J., Baccigalupi, C., Banday, A. J., Barreiro, R. B., Bartlett, J. G., Battaner, E., Benabed, K., Benoît, A., Benoit-Lévy, A., Bernard, J. P., Bersanelli, M., Bielewicz, P., Bobin, J., Bock, J. J., Bonaldi, A., Bond, J. R., Borrill, J., Bouchet, F. R., Bridges, M., Bucher, M., Burigana, C., Butler, R. C., Calabrese, E., Cappellini, B., Cardoso, J. F., Catalano, A., Challinor, A., Chamballu, A., Chary, R. R., Chen, X., Chiang, H. C., Chiang, L. Y., Christensen, P. R., Church, S., Clements, D. L., Colombi, S., Colombo, L. P. L., Couchot, F., Coulais, A., Crill, B. P., Curto, A., Cuttaia, F., Danese, L., Davies, R. D., Davis, R. J., de Bernardis, P., de Rosa, A., de Zotti, G., Delabrouille, J., Delouis, J. M., Désert, F. X., Dickinson, C., Diego, J. M., Dolag, K., Dole, H., Donzelli, S., Doré, O., Douspis, M., Dunkley, J., Dupac, X., Efstathiou, G., Elsner, F., Enßlin, T. A., Eriksen, H. K., Finelli, F., Forni, O., Frailis, M., Fraisse, A. A., Franceschi, E., Gaier, T. C., Galeotta, S., Galli, S., Ganga, K., Giard, M., Giardino, G., Giraud-Héraud, Y., Gjerløw, E., González-Nuevo, J., Górski, K. M., Gratton, S., Gregorio, A., Gruppuso, A., Gudmundsson, J. E., Haissinski, J., Hamann, J., Hansen, F. K., Hanson, D., Harrison, D., Henrot-Versillé, S., Hernández-Monteagudo, C., Herranz, D., Hildebrandt, S. R., Hivon, E., Hobson, M., Holmes, W. A., Hornstrup, A., Hou, Z., Hovest, W., Huffenberger, K. M., Jaffe, A. H., Jaffe, T. R., Jewell, J., Jones, W. C., Juvela, M., Keihänen, E., Keskitalo, R., Kisner, T. S., Kneissl, R., Knoche, J., Knox, L., Kunz, M., Kurki-Suonio, H., Lagache, G., Lähteenmäki, A., Lamarre, J. M., Lasenby, A., Lattanzi, M., Laureijs, R. J., Lawrence, C. R., Leach, S., Leahy, J. P., Leonardi, R., León-Tavares, J., Lesgourgues, J., Lewis, A., Liguori, M., Lilje, P. B., Linden-Vørnle, M., López-Caniego, M., Lubin, P. M., Macías-Pérez, J. F., Maffei, B., Maino, D., Mandolesi, N., Maris, M., Marshall, D. J., Martin, P. G., Martínez-González, E., Masi, S., Massardi, M., Matarrese, S., Matthai, F., Mazzotta, P., Meinhold, P. R., Melchiorri, A., Melin, J. B., Mendes, L., Menegoni, E., Mennella, A., Migliaccio, M., Millea, M., Mitra, S., Miville-Deschênes, M. A., Moneti, A., Montier, L., Morgante, G., Mortlock, D., Moss, A., Munshi, D., Murphy, J. A., Naselsky, P., Nati, F., Natoli, P., Netterfield, C. B., Nørgaard-Nielsen, H. U., Noviello, F., Novikov, D., Novikov, I., O'Dwyer, I. J., Osborne, S., Oxborrow, C. A., Paci, F., Pagano, L., Pajot, F., Paladini, R., Paoletti, D., Partridge, B., Pasian, F., Patanchon, G., Pearson, D., Pearson, T. J., Peiris, H. V., Perdereau, O., Perotto, L., Perrotta, F., Pettorino, V., Piacentini, F., Piat, M., Pierpaoli, E., Pietrobon, D., Plaszczynski, S., Platania, P., Pointecouteau, E., Polenta, G., Ponthieu, N., Popa, L., Poutanen, T., Pratt, G. W., Prézeau, G., Prunet, S., Puget, J. L., Rachen, J. P., Reach, W. T., Rebolo, R., Reinecke, M., Remazeilles, M., Renault, C., Ricciardi, S., Riller, T., Ristorcelli, I., Rocha, G., Rosset, C., Roudier, G., Rowan-Robinson, M., Rubiño-Martín, J. A., Rusholme, B., Sandri, M., Santos, D., Savelainen, M., Savini, G., Scott, D., Seiffert, M. D., Shellard, E. P. S., Spencer, L. D., Starck, J. L., Stolyarov, V., Stompor, R., Sudiwala, R., Sunyaev, R., Sureau, F., Sutton, D., Suur-Uski, A. S., Sygnet, J. F., Tauber, J. A., Tavagnacco, D., Terenzi, L., Toffolatti, L., Tomasi, M., Tristram, M., Tucci, M., Tuovinen, J., Türler, M., Umana, G., Valenziano, L., Valiviita, J., Van Tent, B., Vielva, P., Villa, F., Vittorio, N., Wade, L. A., Wandelt, B. D., Wehus, I. K., White, M., White, S. D. M., Wilkinson, A., Yvon, D., Zacchei, A., and Zonca, A. (2014). Planck 2013 results. XVI. Cosmological parameters. *A&A*, 571:A16.

Planck Collaboration, Ade, P. A. R., Aghanim, N., Arnaud, M., Ashdown, M., Aumont, J., Baccigalupi, C., Banday, A. J., Barreiro, R. B., Barrena, R., Bartlett, J. G., Bartolo, N., Battaner, E., Battye, R., Benabed, K., Benoît, A., Benoit-Lévy, A., Bernard, J. P., Bersanelli, M., Bielewicz, P., Bikmaev, I., Böhringer, H., Bonaldi, A., Bonavera, L., Bond, J. R., Borrill, J., Bouchet, F. R., Bucher, M., Burenin, R., Burigana, C., Butler, R. C., Calabrese, E., Cardoso, J. F., Carvalho, P., Catalano, A., Challinor, A., Chamballu, A., Chary, R. R., Chiang, H. C., Chon, G., Christensen, P. R., Clements, D. L., Colombi, S., Colombo, L. P. L., Combet, C., Comis, B., Couchot, F., Coulais, A., Crill, B. P., Curto, A., Cuttaia, F., Dahle, H., Danese, L., Davies, R. D., Davis, R. J., de Bernardis, P., de Rosa, A., de Zotti, G., Delabrouille, J., Désert, F. X., Dickinson, C., Diego, J. M., Dolag, K., Dole, H., Donzelli, S., Doré, O., Douspis, M., Ducout, A., Dupac, X., Efstathiou, G., Eisenhardt, P. R. M., Elsner, F., Enßlin, T. A., Eriksen, H. K., Falgarone, E., Fergusson, J., Feroz, F., Ferragamo, A., Finelli, F., Forni, O., Frailis, M., Fraisse, A. A., Franceschi, E., Frejsel, A., Galeotta, S., Galli, S., Ganga, K., Génova-Santos, R. T., Giard, M., Giraud-Héraud, Y., Gjerløw, E., González-Nuevo, J., Górski, K. M., Grainge, K. J. B., Gratton, S., Gregorio, A., Gruppuso, A., Gudmundsson, J. E., Hansen, F. K., Hanson, D., Harrison, D. L., Hempel, A., Henrot-Versillé, S., Hernández-Monteagudo, C., Herranz, D., Hildebrandt, S. R., Hivon, E., Hobson, M., Holmes, W. A., Hornstrup, A., Hovest, W., Huffenberger, K. M., Hurier, G., Jaffe, A. H., Jaffe, T. R., Jin, T., Jones, W. C., Juvela, M., Keihänen, E., Keskitalo, R., Khamitov, I., Kisner, T. S., Kneissl, R., Knoche, J., Kunz, M., Kurki-Suonio, H., Lagache, G., Lamarre, J. M., Lasenby, A., Lattanzi, M., Lawrence, C. R., Leonardi, R., Lesgourgues, J., Levrier, F., Liguori, M., Lilje, P. B., Linden-Vørnle, M., López-Caniego, M., Lubin, P. M., Macías-Pérez, J. F., Maggio, G., Maino, D., Mak, D. S. Y., Mandolesi, N., Mangilli, A., Martin, P. G., Martínez-González, E., Masi, S., Matarrese, S., Mazzotta, P., McGehee, P., Mei, S., Melchiorri, A., Melin, J. B., Mendes, L., Mennella, A., Migliaccio, M., Mitra, S., Miville-Deschênes, M. A., Moneti, A., Montier, L., Morgante, G., Mortlock, D., Moss, A., Munshi, D., Murphy, J. A., Naselsky, P., Nastasi, A., Nati, F., Natoli, P., Netterfield, C. B., Nørgaard-Nielsen, H. U., Noviello, F., Novikov, D., Novikov, I., Olamaie, M., Oxborrow, C. A., Paci, F., Pagano, L., Pajot, F., Paoletti, D., Pasian, F., Patanchon, G., Pearson, T. J., Perdereau, O., Perotto, L., Perrott, Y. C., Perrotta, F., Pettorino, V., Piacentini, F., Piat, M., Pierpaoli, E., Pietrobon, D., Plaszczynski, S., Pointecouteau, E., Polenta, G., Pratt, G. W., Prézeau, G., Prunet, S., Puget, J. L., Rachen, J. P., Reach, W. T., Rebolo, R., Reinecke, M., Remazeilles, M., Renault, C., Renzi, A., Ristorcelli, I., Rocha, G., Rosset, C., Rossetti, M., Roudier, G., Rozo, E., Rubiño-Martín, J. A., Rumsey, C., Rusholme, B., Rykoff, E. S., Sandri, M., Santos, D., Saunders, R. D. E., Savelainen, M., Savini, G., Schammel, M. P., Scott, D., Seiffert, M. D., Shellard, E. P. S., Shimwell, T. W., Spencer, L. D., Stanford, S. A., Stern, D., Stolyarov, V., Stompor, R., Streblyanska, A., Sudiwala, R., Sunyaev, R., Sutton, D., Suur-Uski, A. S., Sygnet, J. F., Tauber, J. A., Terenzi, L., Toffolatti, L., Tomasi, M., Tramonte, D., Tristram, M., Tucci, M., Tuovinen, J., Umana, G., Valenziano, L., Valiviita, J., Van Tent, B., Vielva, P., Villa, F., Wade, L. A., Wandelt, B. D., Wehus, I. K., White, S. D. M., Wright, E. L., Yvon, D., Zacchei, A., and Zonca, A. (2016). Planck 2015 results. XXVII. The second Planck catalogue of Sunyaev-Zeldovich sources. *A&A*, 594:A27.

Poggianti, B. M., Calvi, R., Bindoni, D., D'Onofrio, M., Moretti, A., Valentinuzzi, T., Fasano, G., Fritz, J., De Lucia, G., Vulcani, B., Bettoni, D., Gullieuszik, M., and Omizzolo, A. (2013). Superdense Galaxies and the Mass-Size Relation at Low Redshift. *ApJ*, 762(2):77.

Poggianti, B. M., Fasano, G., Omizzolo, A., Gullieuszik, M., Bettoni, D., Moretti, A., Paccagnella, A., Jaffé, Y. L., Vulcani, B., Fritz, J., Couch, W., and D'Onofrio, M. (2016). Jellyfish Galaxy Candidates at Low Redshift. *AJ*, 151(3):78.

Poole, G. B., Fardal, M. A., Babul, A., McCarthy, I. G., Quinn, T., and Wadsley, J. (2006). The impact of mergers on relaxed X-ray clusters - I. Dynamical evolution and emergent transient structures. *MNRAS*, 373(3):881–905.

Postman, M., Franx, M., Cross, N. J. G., Holden, B., Ford, H. C., Illingworth, G. D., Goto, T., Demarco, R., Rosati, P., Blakeslee, J. P., Tran, K. V., Benítez, N., Clampin, M., Hartig, G. F., Homeier, N., Ardila, D. R., Bartko, F., Bouwens, R. J., Bradley, L. D., Broadhurst, T. J., Brown, R. A., Burrows, C. J., Cheng, E. S., Feldman, P. D., Golimowski, D. A., Gronwall, C., Infante, L., Kimble, R. A., Krist, J. E., Lesser, M. P., Martel, A. R., Mei, S., Menanteau, F., Meurer, G. R., Miley, G. K., Motta, V., Sirianni, M., Sparks, W. B., Tran, H. D., Tsvetanov, Z. I., White, R. L., and Zheng, W. (2005). The Morphology-Density Relation in z ~1 Clusters. *ApJ*, 623(2):721–741.

Postman, M. and Geller, M. J. (1984). The morphology-density relation - The group connection. *ApJ*, 281:95–99.

Proust, D., Cuevas, H., Capelato, H. V., Sodré, L., J., Tomé Lehodey, B., Le Fèvre, O., and Mazure, A. (2000). Dynamics of the X-ray clusters Abell 222, Abell 223 and Abell 520. *A&A*, 355:443–453.

Quadri, R. F., Williams, R. J., Franx, M., and Hildebrandt, H. (2012). Tracing the Star-formation-Density Relation to z ~2. *ApJ*, 744(2):88.

Raouf, M., Smith, R., Khosroshahi, H. G., Dariush, A. A., Driver, S., Ko, J., and Hwang, H. S. (2019). The Impact of the Dynamical State of Galaxy Groups on the Stellar Populations of Central Galaxies. *ApJ*, 887(2):264.

Rasia, E., Meneghetti, M., and Ettori, S. (2013). X-ray Morphological Estimators for Galaxy Clusters. *The Astronomical Review*, 8:40–70.

Rawle, T. D., Edge, A. C., Egami, E., Rex, M., Smith, G. P., Altieri, B., Fiedler, A., Haines, C. P., Pereira, M. J., Pérez-González, P. G., Portouw, J., Valtchanov, I., Walth, G., van der Werf, P. P., and Zemcov, M. (2012). The Relation between Cool Cluster Cores and Herschel-detected Star Formation in Brightest Cluster Galaxies. *ApJ*, 747(1):29.

Reiprich, T. H., Basu, K., Ettori, S., Israel, H., Lovisari, L., Molendi, S., Pointecouteau, E., and Roncarelli, M. (2013). Outskirts of Galaxy Clusters. *Space Sci. Rev.*, 177(1-4):195–245.

Reza, M. (2021). Galaxy morphology classification using automated machine learning. *Astronomy and Computing*, 37:100492.

Ribeiro, A. L. B., Lopes, P. A. A., and Rembold, S. B. (2013). NoSOCS in SDSS. III. The interplay between galaxy evolution and the dynamical state of galaxy clusters. *A&A*, 556:A74.

Richard, J., Claeyssens, A., Lagattuta, D., Guaita, L., Bauer, F. E., Pello, R., Carton, D., Bacon, R., Soucail, G., Lyon, G. P., Kneib, J.-P., Mahler, G., Clément, B., Mercier, W., Variu, A., Tamone, A., Ebeling, H., Schmidt, K. B., Nanayakkara, T., Maseda, M., Weilbacher, P. M., Bouché, N., Bouwens, R. J., Wisotzki, L., de la Vieuville, G., Martinez, J., and Patrício, V. (2021). An atlas of MUSE observations towards twelve massive lensing clusters. *A&A*, 646:A83.

Rines, K., Geller, M. J., Diaferio, A., and Kurtz, M. J. (2013). Measuring the Ultimate Halo Mass of Galaxy Clusters: Redshifts and Mass Profiles from the Hectospec Cluster Survey (HeCS). *ApJ*, 767(1):15.

Roberts, M. S. and Haynes, M. P. (1994). Physical Parameters along the Hubble Sequence. *ARA&A*, 32:115–152.

Rodriguez-Gomez, V., Snyder, G. F., Lotz, J. M., Nelson, D., Pillepich, A., Springel, V., Genel, S., Weinberger, R., Tacchella, S., Pakmor, R., Torrey, P., Marinacci, F., Vogelsberger, M., Hernquist, L., and Thilker, D. A. (2019). The optical morphologies of galaxies in the IllustrisTNG simulation: a comparison to Pan-STARRS observations. *MNRAS*, 483(3):4140–4159.

Rodríguez-Muñoz, L., Rodighiero, G., Mancini, C., Pérez-González, P. G., Rawle, T. D., Egami, E., Mercurio, A., Rosati, P., Puglisi, A., Franceschini, A., Balestra, I., Baronchelli, I., Biviano, A., Ebeling, H., Edge, A. C., Enia, A. F. M., Grillo, C., Haines, C. P., Iani, E., Jones, T., Nonino, M., Valtchanov, I., Vulcani, B., and Zemcov, M. (2019). Quantifying the suppression of the (un)-obscured star formation in galaxy cluster cores at 0.2$\lesssim$ z $\lesssim$0.9. *MNRAS*, 485(1):586–619.

Ruel, J., Bazin, G., Bayliss, M., Brodwin, M., Foley, R. J., Stalder, B., Aird, K. A., Armstrong, R., Ashby, M. L. N., Bautz, M., Benson, B. A., Bleem, L. E., Bocquet, S., Carlstrom, J. E., Chang, C. L., Chapman, S. C., Cho, H. M., Clocchiatti, A., Crawford, T. M., Crites, A. T., de Haan, T., Desai, S., Dobbs, M. A., Dudley, J. P., Forman, W. R., George, E. M., Gladders, M. D., Gonzalez, A. H., Halverson, N. W., Harrington, N. L., High, F. W., Holder, G. P., Holzapfel, W. L., Hrubes, J. D., Jones, C., Joy, M., Keisler, R., Knox, L., Lee, A. T., Leitch, E. M., Liu, J., Lueker, M., Luong-Van, D., Mantz, A., Marrone, D. P., McDonald, M., McMahon, J. J., Mehl, J., Meyer, S. S., Mocanu, L., Mohr, J. J., Montroy, T. E., Murray, S. S., Natoli, T., Nurgaliev, D., Padin, S., Plagge, T., Pryke, C., Reichardt, C. L., Rest, A., Ruhl, J. E., Saliwanchik, B. R., Saro, A., Sayre, J. T., Schaffer, K. K., Shaw, L., Shirokoff, E., Song, J., Šuhada, R., Spieler, H. G., Stanford, S. A., Staniszewski, Z., Starsk, A. A., Story, K., Stubbs, C. W., van Engelen, A., Vanderlinde, K., Vieira, J. D., Vikhlinin, A., Williamson, R., Zahn, O., and Zenteno, A. (2014). Optical Spectroscopy and Velocity Dispersions of Galaxy Clusters from the SPT-SZ Survey. *ApJ*, 792(1):45.

Rykoff, E. S., Rozo, E., Busha, M. T., Cunha, C. E., Finoguenov, A., Evrard, A., Hao, J., Koester, B. P., Leauthaud, A., Nord, B., Pierre, M., Reddick, R., Sadibekova, T., Sheldon, E. S., and Wechsler, R. H. (2014). redMaPPer. I. Algorithm and SDSS DR8 Catalog. *ApJ*, 785(2):104.

Santos, J. S., Rosati, P., Tozzi, P., Böhringer, H., Ettori, S., and Bignamini, A. (2008). Searching for cool core clusters at high redshift. *A&A*, 483(1):35–47.

Sarazin, C. L. (2002). The Physics of Cluster Mergers. In Feretti, L., Gioia, I. M., and Giovannini, G., editors, *Merging Processes in Galaxy Clusters*, volume 272 of *Astrophysics and Space Science Library*, pages 1–38.

Sazonova, E., Alatalo, K., Lotz, J., Rowlands, K., Snyder, G. F., Boone, K., Brodwin, M., Hayden, B., Lanz, L., Perlmutter, S., and Rodriguez-Gomez, V. (2020). The Morphology-Density Relationship in 1 ¡ z ¡ 2 Clusters. *ApJ*, 899(1):85.

Schneider, P. (2015). *Extragalactic Astronomy and Cosmology: An Introduction.*

Schuecker, P., Böhringer, H., Reiprich, T. H., and Feretti, L. (2001). A systematic study of X-ray substructure of galaxy clusters detected in the ROSAT All-Sky Survey. *A&A*, 378:408–427.

Sersic, J. L. (1968). *Atlas de Galaxias Australes.*

Shen, S., Mo, H. J., White, S. D. M., Blanton, M. R., Kauffmann, G., Voges, W., Brinkmann, J., and Csabai, I. (2003). The size distribution of galaxies in the Sloan Digital Sky Survey. *MNRAS*, 343(3):978–994.

Sifón, C., Battaglia, N., Hasselfield, M., Menanteau, F., Barrientos, L. F., Bond, J. R., Crichton, D., Devlin, M. J., Dünner, R., Hilton, M., Hincks, A. D., Hlozek, R., Huffenberger, K. M., Hughes, J. P., Infante, L., Kosowsky, A., Marsden, D., Marriage, T. A., Moodley, K., Niemack, M. D., Page, L. A., Spergel, D. N., Staggs, S. T., Trac, H., and Wollack, E. J. (2016). The Atacama Cosmology Telescope: dynamical masses for 44 SZ-selected galaxy clusters over 755 square degrees. *MNRAS*, 461(1):248–270.

Silva, D. R., Blum, R. D., Allen, L., Dey, A., Schlegel, D. J., Lang, D., Moustakas, J., Meisner, A. M., Valdes, F., Patej, A., Myers, A. D., Sprayberry, D., Saha, A., Olsen, K. A., Safonova, S., Yang, Q., Burleigh, K. J., and MzLS Team (2016). The Mayall z-band Legacy Survey. In *American Astronomical Society Meeting Abstracts #228*, volume 228 of *American Astronomical Society Meeting Abstracts*, page 317.02.

Spergel, D. N., Verde, L., Peiris, H. V., Komatsu, E., Nolta, M. R., Bennett, C. L., Halpern, M., Hinshaw, G., Jarosik, N., Kogut, A., Limon, M., Meyer, S. S., Page, L., Tucker, G. S., Weiland, J. L., Wollack, E., and Wright, E. L. (2003). First-Year Wilkinson Microwave Anisotropy Probe (WMAP) Observations: Determination of Cosmological Parameters. *ApJS*, 148(1):175–194.

Strazzullo, V., Pannella, M., Mohr, J. J., Saro, A., Ashby, M. L. N., Bayliss, M. B., Canning, R. E. A., Floyd, B., Gonzalez, A. H., Khullar, G., Kim, K. J., McDonald, M., Reichardt, C. L., Sharon, K., and Somboonpanyakul, T. (2023). Galaxy populations in the most distant SPT-SZ clusters. II. Galaxy structural properties in massive clusters at $1.4 \lesssim z \lesssim 1.7$. *A&A*, 669:A131.

Stroe, A., Sobral, D., Paulino-Afonso, A., Alegre, L., Calhau, J., Santos, S., and van Weeren, R. (2017). A large Hα survey of star formation in relaxed and merging galaxy cluster environments at $z \sim 0.15$-0.3. *MNRAS*, 465(3):2916–2935.

Sunyaev, R. A. and Zeldovich, Y. B. (1972). The Observations of Relic Radiation as a Test of the Nature of X-Ray Radiation from the Clusters of Galaxies. *Comments on Astrophysics and Space Physics*, 4:173.

Teklu, A. F., Remus, R.-S., Dolag, K., and Burkert, A. (2017). The morphology-density relation: impact on the satellite fraction. *MNRAS*, 472(4):4769–4785.

Tempel, E., Tuvikene, T., Kipper, R., and Libeskind, N. I. (2017). Merging groups and clusters of galaxies from the SDSS data. The catalogue of groups and potentially merging systems. *A&A*, 602:A100.

The Dark Energy Survey Collaboration (2005). The Dark Energy Survey. *arXiv e-prints*, pages astro–ph/0510346.

Tremaine, S. (1990). The origin of central cluster galaxies. In Wielen, R., editor, *Dynamics and Interactions of Galaxies*, pages 394–405.

Tucker, E., Walker, M. G., Mateo, M., Olszewski, E. W., Bailey, John I., I., Crane, J. D., and Shectman, S. A. (2017). Magellan/M2FS Spectroscopy of Galaxy Clusters: Stellar Population Model and Application to Abell 267. *AJ*, 154(3):113.

Valluri, M. (1993). Compressive Tidal Heating of a Disk Galaxy in a Rich Cluster. *ApJ*, 408:57.

Van den Bergh, S. (1998). *Galaxy morphology and classification.* Cambridge University Press.

van der Wel, A. (2008). The Dependence of Galaxy Morphology and Structure on Environment and Stellar Mass. *ApJ*, 675(1):L13.

van der Wel, A., Franx, M., van Dokkum, P. G., Skelton, R. E., Momcheva, I. G., Whitaker, K. E., Brammer, G. B., Bell, E. F., Rix, H. W., Wuyts, S., Ferguson, H. C., Holden, B. P., Barro, G., Koekemoer, A. M., Chang, Y.-Y., McGrath, E. J., Häussler, B., Dekel, A., Behroozi, P., Fumagalli, M., Leja, J., Lundgren, B. F., Maseda, M. V., Nelson, E. J., Wake, D. A., Patel, S. G., Labbé, I., Faber, S. M., Grogin, N. A., and Kocevski, D. D. (2014). 3D-HST+CANDELS: The Evolution of the Galaxy Size-Mass Distribution since z = 3. *ApJ*, 788(1):28.

van Zee, L. (2001). The Evolutionary Status of Isolated Dwarf Irregular Galaxies. II. Star Formation Histories and Gas Depletion. *AJ*, 121(4):2003–2019.

Vika, M., Bamford, S. P., Häußler, B., Rojas, A. L., Borch, A., and Nichol, R. C. (2013). MegaMorph - multiwavelength measurement of galaxy structure. Sérsic profile fits to galaxies near and far. *MNRAS*, 435(1):623–649.

Vika, M., Vulcani, B., Bamford, S. P., Häußler, B., and Rojas, A. L. (2015). MegaMorph: classifying galaxy morphology using multi-wavelength Sérsic profile fits. *A&A*, 577:A97.

Vikram, V., Wadadekar, Y., Kembhavi, A. K., and Vijayagovindan, G. V. (2010). PYMORPH: automated galaxy structural parameter estimation using PYTHON. *MNRAS*, 409(4):1379–1392.

Visvanathan, N. and Sandage, A. (1977). The color - absolute magnitude relation for E and S0 galaxies. I. Calibration and tests for universality using Virgo and eight other nearby clusters. *ApJ*, 216:214–226.

Von Der Linden, A., Best, P. N., Kauffmann, G., and White, S. D. M. (2007). How special are brightest group and cluster galaxies? *MNRAS*, 379(3):867–893.

Vulcani, B., Poggianti, B. M., Gullieuszik, M., Moretti, A., Fritz, J., Bettoni, D., Facciolli, B., Fasano, G., and Omizzolo, A. (2023a). Clustercentric Distance or Local Density? It Depends on Galaxy Morphology. *ApJ*, 949(2):73.

Vulcani, B., Treu, T., Calabrò, A., Fritz, J., Poggianti, B. M., Bergamini, P., Bonchi, A., Boyett, K., Caminha, G. B., Castellano, M., Dressler, A., Fontana, A., Glazebrook, K., Grillo, C., Malkan, M. A., Mascia, S., Mercurio, A., Merlin, E., Metha, B., Morishita, T., Nanayakkara, T., Paris, D., Roberts-Borsani, G., Rosati, P., Roy, N., Santini, P., Trenti, M., Vanzella, E., and Wang, X. (2023b). Early Results from GLASS-JWST. XX. Unveiling a Population of “Red Excess” Galaxies in Abell2744 and in the Coeval Field. *ApJ*, 948(2):L15.

Walmsley, M., Lintott, C., Géron, T., Kruk, S., Krawczyk, C., Willett, K. W., Bamford, S., Kelvin, L. S., Fortson, L., Gal, Y., Keel, W., Masters, K. L., Mehta, V., Simmons, B. D., Smethurst, R., Smith, L., Baeten, E. M., and Macmillan, C. (2022). Galaxy Zoo DECaLS: Detailed visual morphology measurements from volunteers and deep learning for 314 000 galaxies. *MNRAS*, 509(3):3966–3988.

Wen, Z. L. and Han, J. L. (2013). Substructure and dynamical state of 2092 rich clusters of galaxies derived from photometric data. *MNRAS*, 436(1):275–293.

Wen, Z. L. and Han, J. L. (2015). Calibration of the Optical Mass Proxy for Clusters of Galaxies and an Update of the WHL12 Cluster Catalog. *ApJ*, 807(2):178.

Wen, Z. L. and Han, J. L. (2021). Photometric redshifts for galaxies in the Subaru Hyper Suprime-Cam and unWISE and a catalogue of identified clusters of galaxies. *MNRAS*, 500(1):1003–1017.

Wen, Z. L. and Han, J. L. (2022). Clusters of galaxies up to z = 1.5 identified from photometric data of the Dark Energy Survey and unWISE. *MNRAS*, 513(3):3946–3959.

Wetzel, A. R., Tinker, J. L., and Conroy, C. (2012). Galaxy evolution in groups and clusters: star formation rates, red sequence fractions and the persistent bimodality. *MNRAS*, 424(1):232–243.

White, S. D. M. and Frenk, C. S. (1991). Galaxy Formation through Hierarchical Clustering. *ApJ*, 379:52.

White, S. D. M. and Rees, M. J. (1978). Core condensation in heavy halos: a two-stage theory for galaxy formation and clustering. *MNRAS*, 183:341–358.

Whitmore, B. C. and Gilmore, D. M. (1991). On the Interpretation of the Morphology-Density Relation for Galaxies in Clusters. *ApJ*, 367:64.

Wijesinghe, D. B., Hopkins, A. M., Kelly, B. C., Welikala, N., and Connolly, A. J. (2010). Morphological classification of galaxies and its relation to physical properties. *MNRAS*, 404(4):2077–2086.

Wright, E. L., Eisenhardt, P. R. M., Mainzer, A. K., Ressler, M. E., Cutri, R. M., Jarrett, T., Kirkpatrick, J. D., Padgett, D., McMillan, R. S., Skrutskie, M., Stanford, S. A., Cohen, M., Walker, R. G., Mather, J. C., Leisawitz, D., Gautier, Thomas N., I., McLean, I., Benford, D., Lonsdale, C. J., Blain, A., Mendez, B., Irace, W. R., Duval, V., Liu, F., Royer, D., Heinrichsen, I., Howard, J., Shannon, M., Kendall, M., Walsh, A. L., Larsen, M., Cardon, J. G., Schick, S., Schwalm, M., Abid, M., Fabinsky, B., Naes, L., and Tsai, C.-W. (2010). The Wide-field Infrared Survey Explorer (WISE): Mission Description and Initial On-orbit Performance. *AJ*, 140(6):1868–1881.

Wu, H., Zou, Z. L., Xia, X. Y., and Deng, Z. G. (1998). A statistical study of the spectra of very luminous IRAS galaxies. II. Spectral and environmental analysis. *A&AS*, 132:181–193.

Yee, H. K. C., Gladders, M. D., and López-Cruz, O. (1999). The Color-Magnitude Relation of Early-Type Galaxies: A Tool for Cluster Finding and Redshift Determination. In Weymann, R., Storrie-Lombardi, L., Sawicki, M., and Brunner, R., editors, *Photometric Redshifts and the Detection of High Redshift Galaxies*, volume 191 of *Astronomical Society of the Pacific Conference Series*, page 166.

Yoon, Y., Im, M., and Kim, J.-W. (2017). Massive Galaxies Are Larger in Dense Environments: Environmental Dependence of Mass-Size Relation of Early-type Galaxies. *ApJ*, 834(1):73.

Yuan, Z. S. and Han, J. L. (2020). Dynamical state for 964 galaxy clusters from Chandra X-ray images. *MNRAS*, 497(4):5485–5497.

Yuan, Z. S., Han, J. L., and Wen, Z. L. (2022). Dynamical state of galaxy clusters evaluated from X-ray images. *MNRAS*, 513(2):3013–3021.

Zabludoff, A. I. and Mulchaey, J. S. (1998). Hierarchical Evolution in Poor Groups of Galaxies. *ApJ*, 498(1):L5–L8.

Zenteno, A., Hernández-Lang, D., Klein, M., Vergara Cervantes, C., Hollowood, D. L., Bhargava, S., Palmese, A., Strazzullo, V., Romer, A. K., Mohr, J. J., Jeltema, T., Saro, A., Lidman, C., Gruen, D., Ojeda, V., Katzenberger, A., Aguena, M., Allam, S., Avila, S., Bayliss, M., Bertin, E., Brooks, D., Buckley-Geer, E., Burke, D. L., Capasso, R., Carnero Rosell, A., Carrasco Kind, M., Carretero, J., Castander, F. J., Costanzi, M., da Costa, L. N., De Vicente, J., Desai, S., Diehl, H. T., Doel, P., Eifler, T. F., Evrard, A. E., Flaugher, B., Floyd, B., Fosalba, P., Frieman, J., García-Bellido, J., Gerdes, D. W., Gonzalez, J. R., Gruendl, R. A., Gschwend, J., Gutierrez, G., Hartley, W. G., Hinton, S. R., Honscheid, K., James, D. J., Kuehn, K., Lahav, O., Lima, M., McDonald, M., Maia, M. A. G., March, M., Melchior, P., Menanteau, F., Miquel, R., Ogando, R. L. C., Paz-Chinchón, F., Plazas, A. A., Roodman, A., Rykoff, E. S., Sanchez, E., Scarpine, V., Schubnell, M., Serrano, S., Sevilla-Noarbe, I., Smith, M., Soares-Santos, M., Suchyta, E., Swanson, M. E. C., Tarle, G., Thomas, D., Varga, T. N., Walker, A. R., Wilkinson, R. D., and DES Collaboration (2020). A joint SZ-X-ray-optical analysis of the dynamical state of 288 massive galaxy clusters. *MNRAS*, 495(1):705–725.

Zenteno, A., Mohr, J. J., Desai, S., Stalder, B., Saro, A., Dietrich, J. P., Bayliss, M., Bocquet, S., Chiu, I., Gonzalez, A. H., Gangkofner, C., Gupta, N., Hlavacek-Larrondo, J., McDonald, M., Reichardt, C., and Rest, A. (2016). Galaxy populations in the 26 most massive galaxy clusters in the South Pole Telescope SPT-SZ survey. *MNRAS*, 462(1):830–843.

Zhang, Y.-Y., Okabe, N., Finoguenov, A., Smith, G. P., Piffaretti, R., Valdarnini, R., Babul, A., Evrard, A. E., Mazzotta, P., Sanderson, A. J. R., and Marrone, D. P. (2010). LoCuSS: A Comparison of Cluster Mass Measurements from XMM-Newton and Subaru—Testing Deviation from Hydrostatic Equilibrium and Non-thermal Pressure Support. *ApJ*, 711(2):1033–1043.

Zhu, X.-P., Dai, J.-M., Bian, C.-J., Chen, Y., Chen, S., and Hu, C. (2019). Galaxy morphology classification with deep convolutional neural networks. *Ap&SS*, 364(4):55.

Zou, H., Zhou, X., Fan, X., Zhang, T., Zhou, Z., Nie, J., Peng, X., McGreer, I., Jiang, L., Dey, A., Fan, D., He, B., Jiang, Z., Lang, D., Lesser, M., Ma, J., Mao, S., Schlegel, D., and Wang, J. (2017). Project Overview of the Beijing-Arizona Sky Survey. *PASP*, 129(976):064101.

Zwicky, F. (1937). On the Masses of Nebulae and of Clusters of Nebulae. *ApJ*, 86:217.

Appendix A

Additional data of galaxy clusters

A.1 Galaxy cluster properties

Table A.1: Full cluster catalog

Name (1)	RA (2)	Dec (3)	z (4)	m_r^* (5)	R_{200} (6)	M_{200} (7)	N (8)	$\log(c)$ (9)	$\log(\omega)$ (10)	$\log(P_3/P_0)$ (11)	δ (12)	D_{BCG-X_P} (13)	D_{BCG-X_C} (14)	Dynamical state (15)
Abell 2715	0.67922	-34.6622	0.116	16.89	1.24	3.08	39	-0.76 ± 0.01	-1.52 ± 0.01	-5.64 ± 0.03	1.51 ± 0.01	24	83	Disturbed
Abell 2697	0.80039	-6.09371	0.2484	18.75	1.56	6.12	154	-0.66 ± 0.02	-2.38 ± 0.02	-6.67 ± 0.13	-0.27 ± 0.01	40	57	Relaxed
Abell 2744	3.5801	-30.39224	0.308	19.31	1.95	11.91	146	-1.01 ± 0.03	-1.54 ± 0.01	-6.19 ± 0.11	0.71 ± 0.01	155	336	Disturbed
CL0019.6+0336	4.91008	3.60216	0.2685	18.95	1.81	9.48	148	-0.70 ± 0.01	-1.78 ± 0.01	-6.26 ± 0.09	0.49 ± 0.01	45	139	Disturbed
Abell S67	10.25233	-44.48705	0.3237	19.44	1.79	9.22	125	-0.71 ± 0.02	-2.75 ± 0.05	-4.66 ± 0.04	1.37 ± 0.01	41	33	Intermediate
Abell 2811	10.53096	-28.53597	0.1079	16.72	1.42	4.59	134	-0.61 ± 0.01	-2.39 ± 0.01	-7.10 ± 0.09	-0.10 ± 0.01	37	40	Relaxed
Abell 2813	10.85321	-20.62456	0.2924	19.17	1.95	11.83	99	-0.67 ± 0.02	-2.26 ± 0.04	-7.32 ± 0.33	0.09 ± 0.01	122	108	Intermediate
Abell S84	12.34609	-29.52026	0.108	16.72	1.53	5.69	107	-0.46 ± 0.01	-3.16 ± 0.05	-9.05 ± 0.51	-0.56 ± 0.01	4	5	Relaxed
Abell 122	14.34501	-26.2826	0.1135	16.84	1.37	4.07	23	-0.66 ± 0.01	-2.40 ± 0.01	-8.54 ± 0.33	0.26 ± 0.01	10	31	Relaxed
WHL J010455.4+000336	16.23031	0.06045	0.2767	19.02	1.76	8.73	172	-0.87 ± 0.01	-1.62 ± 0.01	-6.67 ± 0.04	1.36 ± 0.01	8	121	Disturbed
Abell 141	16.38698	-24.64534	0.23	18.55	1.85	10.12	40	-0.92 ± 0.02	-1.29 ± 0.01	-5.34 ± 0.06	1.53 ± 0.01	517	368	Disturbed
SPT-CLJ0106-5943	16.61843	-59.7206	0.348	19.63	1.49	5.24	186	-0.54 ± 0.01	-2.62 ± 0.01	-7.03 ± 0.03	0.27 ± 0.01	14	35	Relaxed
Z348	16.70622	1.05579	0.2514	18.78	1.27	3.24	72	-0.19 ± 0.01	-3.84 ± 0.01	-7.51 ± 0.02	-0.34 ± 0.01	207	207	Intermediate
RXC J0117.8-5455	19.46415	-54.92244	0.251	18.77	1.16	2.47	119	-0.40 ± 0.01	-4.16 ± 0.01	-5.59 ± 0.02	-0.01 ± 0.01	4	4	Relaxed
Abell 2895	19.54764	-26.96692	0.227	18.52	1.56	6.04	74	-0.87 ± 0.02	-1.68 ± 0.01	-6.42 ± 0.09	0.77 ± 0.01	43	60	Disturbed
PSZ1G295.60-51.95	23.36198	-64.56945	0.333	19.51	1.5	5.41	66	-1.14 ± 0.03	-1.77 ± 0.08	-5.41 ± 0.08	1.69 ± 0.01	864	534	Disturbed
Abell 222	24.392	-12.99177	0.213	18.35	1.73	8.26	111	-0.89 ± 0.02	-1.90 ± 0.02	-6.81 ± 0.24	0.98 ± 0.01	5	110	Disturbed
Abell 223	24.48318	-12.82163	0.207	18.28	1.86	10.33	42	-0.63 ± 0.01	-2.71 ± 0.02	-6.92 ± 0.09	0.30 ± 0.01	25	24	Relaxed
RXC J0138.0-2155	24.51611	-21.926	0.338	19.55	1.65	7.20	182	-0.29 ± 0.01	-3.51 ± 0.01	-7.91 ± 0.15	-0.42 ± 0.01	11	16	Relaxed
Abell 2941	26.236	-53.01854	0.1183	16.93	1.54	5.85	118	-0.89 ± 0.01	-1.61 ± 0.01	-7.05 ± 0.10	1.01 ± 0.01	139	92	Disturbed
ZGX J015223-140420	28.09012	-14.08814	0.3304	19.49	1.27	3.28	133	-0.90 ± 0.02	-1.81 ± 0.04	-6.14 ± 0.16	1.15 ± 0.01	66	75	Disturbed
MACS J0152.5-2852	28.14429	-28.89389	0.341	19.58	1.68	7.63	162	-0.52 ± 0.03	-2.85 ± 0.07	-6.53 ± 0.05	0.52 ± 0.01	322	276	Intermediate
Abell 267	28.17592	1.00993	0.2327	18.58	1.44	4.72	113	-0.58 ± 0.01	-2.17 ± 0.01	-9.28 ± 0.34	-0.04 ± 0.01	40	9	Relaxed
RXC J0153.5-0118	28.39337	-1.30215	0.2438	18.7	1.33	3.72	92	-0.80 ± 0.02	-2.39 ± 0.03	-6.17 ± 0.13	0.57 ± 0.01	6	66	Intermediate
Abell 286	29.61077	-1.77821	0.1603	17.65	1.38	4.21	95	-0.77 ± 0.02	-1.95 ± 0.02	-6.57 ± 0.09	0.71 ± 0.01	28	53	Intermediate
GMBCG J030.1+00.7	30.12775	0.74093	0.3448	19.61	1.07	1.98	49	-0.31 ± 0.01	-3.36 ± 0.01	-4.95 ± 0.03	0.31 ± 0.01	19	18	Intermediate
WHL J020046-064230	30.19207	-6.70814	0.3383	19.55	1.24	3.08	86	-0.71 ± 0.02	-2.85 ± 0.06	-5.98 ± 0.16	1.13 ± 0.01	4	51	Intermediate
Abell 291	30.43004	-2.19734	0.197	18.16	1.32	3.69	97	-0.31 ± 0.01	-3.72 ± 0.26	-9.20 ± 0.56	-0.60 ± 0.01	9	5	Relaxed
ACT-CLJ0217-5245	34.2794	-52.74937	0.3432	19.59	1.45	4.84	58	-1.07 ± 0.01	-0.75 ± 0.05	-6.92 ± 0.41	1.46 ± 0.01	399	190	Disturbed
RXC J0220.9-3829	35.23594	-38.48076	0.2287	18.53	1.34	3.84	67	-0.37 ± 0.01	-3.72 ± 0.01	-7.84 ± 0.06	-0.45 ± 0.01	11	13	Relaxed
PLCKESZG256.4-65	36.35559	-42.01465	0.22	18.44	1.51	5.49	164	-0.58 ± 0.01	-2.99 ± 0.05	-6.97 ± 0.18	0.25 ± 0.01	25	45	Relaxed
WHL J022544-031233	36.42859	-3.20936	0.1412	17.35	1.3	3.52	53	-0.99 ± 0.01	-0.82 ± 0.01	-6.08 ± 0.02	1.09 ± 0.01	77	286	Disturbed
Abell 3017	36.47139	-41.91673	0.2195	18.43	1.66	7.3	73	-0.48 ± 0.02	-3.13 ± 0.08	-5.87 ± 0.10	0.22 ± 0.01	28	56	Intermediate
Abell 362	37.91986	-4.88616	0.1843	17.99	1.75	8.59	54	-0.94 ± 0.01	-1.27 ± 0.01	-6.64 ± 0.14	0.80 ± 0.01	44	79	Disturbed
SPT-CLJ0232-4421	38.07887	-44.34691	0.2836	19.09	1.73	8.30	133	-0.51 ± 0.01	-2.89 ± 0.06	-6.65 ± 0.15	0.55 ± 0.01	119	104	Intermediate
ACT-CLJ0235-5121	38.93774	-51.35299	0.278	19.04	1.56	6.01	137	-0.82 ± 0.01	-1.36 ± 0.01	-6.23 ± 0.10	0.65 ± 0.01	27	115	Disturbed
Abell 368	39.36578	-26.50819	0.22	18.44	1.52	5.64	110	-0.38 ± 0.01	-3.26 ± 0.01	-7.72 ± 0.04	-0.21 ± 0.01	2	14	Relaxed
Abell 3038	39.49933	-52.41362	0.135	17.24	1.29	3.43	138	-0.59 ± 0.01	-2.00 ± 0.01	-6.26 ± 0.02	0.80 ± 0.01	8	56	Intermediate
WHL J023941-012812	39.93056	-1.46822	0.3246	19.44	1.31	3.57	129	-0.95 ± 0.03	-1.62 ± 0.04	-5.20 ± 0.05	1.32 ± 0.01	122	45	Disturbed
Abell 3041	40.3412	-28.65396	0.2352	18.61	1.9	10.93	110	-0.90 ± 0.02	-1.25 ± 0.01	-5.76 ± 0.05	1.31 ± 0.01	107	136	Disturbed
MCXC J0244.1-2611	41.05261	-26.17476	0.1362	17.26	1.57	6.15	81	-0.97 ± 0.01	-1.74 ± 0.02	-6.22 ± 0.08	1.35 ± 0.01	7	79	Disturbed
Abell S295	41.36247	-53.02913	0.3	19.24	1.48	5.19	198	-0.80 ± 0.01	-0.90 ± 0.01	-7.02 ± 0.06	1.12 ± 0.01	88	256	Disturbed

Notes. Columns: (1) galaxy cluster name; (2-3) right ascension and declination in J2000; (4) redshift; (5) characteristic magnitude in the r-band; (6) R_{200} in Mpc; (7) M_{200} in $10^{14} M/M_{\odot}$ units; (8) member galaxies with reliable measurements; (9) concentration; (10) centroid shift; (11) power ratio; (12) morphological parameter; (13) BCG/X-ray peak offset in kpc; (14) BCG/X-ray centroid offset in kpc; (15) Dynamical state.

https://www.youtube.com/watch?v=AIkYhgjpEsglist=PLj-wdMGnooBkZghGvk8QM4yzITfZbagJW

Table A.2: Continuation of Table A.1

Name (1)	RA (2)	Dec (3)	z (4)	m_r^* (5)	R_{200} (6)	M_{200} (7)	N (8)	$\log(c)$ (9)	$\log(\omega)$ (10)	$\log(P_3/P_0)$ (11)	δ (12)	D_{BCG-X_P} (13)	D_{BCG-X_C} (14)	Dynamical state (15)
Abell 3048	41.49346	-20.48822	0.3085	19.31	1.37	4.07	65	-0.64 ± 0.02	-2.57 ± 0.04	-6.25 ± 0.14	0.35 ± 0.01	22	37	Intermediate
PLCKG205.0-63.0	41.60763	-20.5556	0.31	19.32	1.71	7.95	97	-1.03 ± 0.02	-1.60 ± 0.02	-6.28 ± 0.24	1.21 ± 0.01	48	37	Disturbed
Abell 383	42.01462	-3.52909	0.1898	18.07	1.5	5.39	45	-0.27 ± 0.01	-3.68 ± 0.03	-8.18 ± 0.04	-0.59 ± 0.01	4	6	Relaxed
Abell 384	42.04975	-2.2765	0.236	18.61	1.63	6.87	119	-0.73 ± 0.02	-2.13 ± 0.02	-7.10 ± 0.24	0.23 ± 0.01	203	202	Intermediate
Abell 402	44.42285	-22.15555	0.3224	19.43	1.96	11.94	26	-0.47 ± 0.01	-2.56 ± 0.01	-6.39 ± 0.01	0.26 ± 0.01	28	28	Intermediate
WHL J025932+001354	44.88504	0.23107	0.2007	18.21	1.24	3.01	66	-0.69 ± 0.02	-1.75 ± 0.03	-6.43 ± 0.12	0.97 ± 0.01	11	39	Intermediate
Abell 3088	46.759	-28.66657	0.2534	18.8	1.57	6.22	77	-0.46 ± 0.02	-2.71 ± 0.03	-8.22 ± 0.56	-0.70 ± 0.01	10	7	Relaxed
MCXC J0320.6-4311	50.15519	-43.1972	0.149	17.48	1.38	4.2	47	-0.67 ± 0.01	-2.24 ± 0.04	-5.89 ± 0.03	0.79 ± 0.01	13	13	Intermediate
MCXC J0336.8-2804	54.21032	-28.08287	0.105	16.66	1.53	5.69	35	-0.85 ± 0.01	-2.36 ± 0.02	-6.07 ± 0.04	0.98 ± 0.01	27	28	Intermediate
SPT-CLJ0348-4514	57.07059	-45.24917	0.3251	19.45	1.7	7.87	151	-0.68 ± 0.01	-1.94 ± 0.01	-6.38 ± 0.03	0.43 ± 0.01	14	1	Intermediate
Abell 3213	61.0708	-27.09348	0.2502	18.76	1.77	8.84	149	-0.56 ± 0.01	-2.56 ± 0.01	-5.04 ± 0.02	2.19 ± 0.01	2	53	Intermediate
WHY J040650-565840	61.71024	-56.97864	0.2262	18.51	1.18	2.65	149	-0.68 ± 0.02	-2.10 ± 0.07	-6.51 ± 0.12	1.59 ± 0.01	16	42	Intermediate
RXC J0439.2-4600	69.80913	-46.01457	0.34	19.57	1.26	3.18	26	-0.40 ± 0.01	-3.06 ± 0.01	-7.96 ± 0.12	0.06 ± 0.01	21	25	Relaxed
Abell S506	75.28562	-24.42084	0.32	19.41	1.52	5.59	41	-0.93 ± 0.02	-1.58 ± 0.02	-5.98 ± 0.11	0.77 ± 0.01	38	44	Intermediate
Abell 3322	77.56952	-45.31999	0.2	18.2	1.64	7.06	123	-0.65 ± 0.02	-2.60 ± 0.05	-7.02 ± 0.11	0.53 ± 0.01	36	33	Relaxed
Abell S520	79.15079	-54.50209	0.2952	19.19	1.77	8.89	83	-1.03 ± 0.02	-1.37 ± 0.01	-6.73 ± 0.45	1.57 ± 0.01	51	312	Disturbed
SPT-CLJ0522-4818	80.56641	-48.30555	0.296	19.2	1.33	3.75	137	-0.44 ± 0.01	-3.00 ± 0.05	-6.38 ± 0.02	0.03 ± 0.01	20	38	Intermediate
Abell 3343	81.45457	-47.25281	0.1913	18.09	1.52	5.62	47	-0.55 ± 0.01	-3.16 ± 0.01	-6.73 ± 0.01	-0.07 ± 0.01	0	21	Relaxed
RXC J0528.2-2942	82.06221	-29.72152	0.1582	17.62	1.39	4.31	122	-0.62 ± 0.01	-3.17 ± 0.03	-7.35 ± 0.04	0.34 ± 0.01	40	33	Relaxed
MCXC J0528.9-3927	82.22145	-39.47189	0.263	18.89	1.55	5.92	117	-0.62 ± 0.01	-2.28 ± 0.01	-7.36 ± 0.36	0.29 ± 0.01	6	65	Relaxed
RXC J0532.9-3701	83.23233	-37.02731	0.2747	19.01	1.88	10.58	82	-0.53 ± 0.01	-2.56 ± 0.03	-7.02 ± 0.03	-0.28 ± 0.01	10	12	Relaxed
Abell 3364	86.90931	-31.87085	0.1483	17.47	1.61	6.65	50	-0.68 ± 0.01	-2.09 ± 0.02	-7.96 ± 0.28	0.16 ± 0.01	28	38	Relaxed
Abell 3378	91.47533	-35.3029	0.141	17.35	1.33	3.78	76	-0.34 ± 0.01	-3.74 ± 0.01	-6.83 ± 0.01	-0.36 ± 0.01	6	12	Relaxed
Abell S579	94.13566	-39.7998	0.152	17.53	1.3	3.47	210	-0.75 ± 0.01	-2.14 ± 0.03	-6.71 ± 0.12	0.83 ± 0.01	23	69	Intermediate
RXC J2011.3-5725	302.86424	-57.42007	0.2786	19.04	1.15	2.4	33	-0.38 ± 0.01	-2.96 ± 0.11	-7.08 ± 0.12	-0.19 ± 0.01	16	20	Relaxed
RXC J2023.4-5535	305.84066	-55.59667	0.232	18.57	2.01	12.98	130	-0.94 ± 0.01	-1.26 ± 0.01	-6.16 ± 0.06	1.10 ± 0.01	28	160	Disturbed
SPTCL J2031-4037	307.97092	-40.62381	0.3416	19.58	1.5	5.36	84	-0.63 ± 0.01	-1.77 ± 0.01	-6.25 ± 0.01	0.95 ± 0.01	27	95	Intermediate
SPTCL J2032-5627	308.11939	-56.48356	0.284	19.09	1.52	5.62	203	-1.07 ± 0.02	-0.82 ± 0.01	-5.74 ± 0.13	1.27 ± 0.01	896	432	Disturbed
PLCKG334.8-38.0A	313.0701	-61.20882	0.35	19.65	1.12	2.24	85	-0.56 ± 0.01	-3.05 ± 0.04	-7.41 ± 0.44	0.36 ± 0.01	9	31	Relaxed
PLCKG334.8-38.0B	313.27912	-61.18801	0.35	19.65	1.3	3.55	74	-1.00 ± 0.01	-0.93 ± 0.03	-7.24 ± 0.41	1.57 ± 0.01	12	39	Intermediate
Abell 3718	313.98318	-54.92679	0.139	17.31	1.52	5.64	82	-0.31 ± 0.01	-3.01 ± 0.05	-7.53 ± 0.10	0.19 ± 0.01	30	8	Relaxed
Abell 3739	316.07916	-41.34586	0.1651	17.73	1.5	5.44	74	-0.70 ± 0.01	-2.46 ± 0.05	-7.63 ± 0.41	0.22 ± 0.01	10	21	Intermediate
RM J2118.8+0033	319.73815	0.54787	0.27	18.96	1.8	9.24	54	-1.00 ± 0.01	-0.86 ± 0.01	-4.93 ± 0.02	1.50 ± 0.28	526	452	Disturbed
RBS1748	322.41705	0.08834	0.235	18.6	1.51	5.52	141	-0.36 ± 0.01	-2.99 ± 0.03	-7.78 ± 0.19	-0.29 ± 0.01	13	23	Relaxed
WHL J213004-002108	322.51651	-0.35262	0.2431	18.69	1.42	4.59	172	-0.56 ± 0.02	-2.55 ± 0.02	-6.00 ± 0.06	0.32 ± 0.01	6	21	Intermediate
WHL J213027-000024	322.6115	-0.00957	0.1432	17.38	1.28	3.34	42	-0.96 ± 0.02	-1.77 ± 0.02	-5.81 ± 0.05	1.85 ± 0.01	27	20	Intermediate
SPT-CLJ2130-6458	322.73469	-64.97957	0.316	19.37	1.28	3.36	40	-0.63 ± 0.01	-2.50 ± 0.05	-7.00 ± 0.19	0.44 ± 0.01	28	21	Relaxed
Abell 3783	323.50307	-42.64773	0.1955	18.14	1.95	11.85	86	-0.69 ± 0.01	-2.28 ± 0.04	-7.58 ± 0.38	0.12 ± 0.01	5	32	Relaxed
SPT-CLJ2138-6007	324.50529	-60.1328	0.319	19.4	1.8	9.38	40	-0.68 ± 0.02	-2.42 ± 0.04	-6.56 ± 0.20	-0.09 ± 0.01	23	31	Relaxed
Abell 3827	330.47385	-59.94638	0.0984	16.51	1.62	6.77	136	-0.67 ± 0.01	-2.82 ± 0.03	-7.45 ± 0.26	-0.55 ± 0.01	8	9	Relaxed
Abell 3830	330.9509	-61.60083	0.2107	18.33	1.26	3.23	61	-0.47 ± 0.02	-2.81 ± 0.03	-5.59 ± 0.02	0.44 ± 0.01	13	46	Intermediate
Abell S1063	342.18533	-44.53105	0.3475	19.63	1.86	10.25	45	-0.57 ± 0.01	-1.76 ± 0.03	-8.02 ± 0.72	0.04 ± 0.01	27	73	Intermediate
Abell 2537	347.09221	-2.19281	0.2972	19.21	1.98	12.48	69	-0.51 ± 0.01	-2.79 ± 0.03	-7.42 ± 0.05	-0.26 ± 0.01	11	23	Relaxed
Abell 2631	354.40755	0.26709	0.273	18.99	1.6	6.56	90	-0.88 ± 0.03	-1.68 ± 0.02	-6.46 ± 0.17	0.87 ± 0.01	138	34	Disturbed
ZwCl2341.1+0000	355.89806	0.33129	0.27	18.96	1.78	8.94	42	-1.25 ± 0.04	-0.75 ± 0.01	-6.74 ± 0.40	1.50 ± 0.01	9	322	Disturbed

Notes. Columns: (1) galaxy cluster name; (2-3) right ascension and declination in J2000; (4) redshift; (5) characteristic magnitude in the r-band; (6) R_{200} in Mpc; (7) M_{200} in $10^{14} M/M_\odot$ units; (8) member galaxies with reliable measurements; (9) concentration; (10) centroid shift; (11) power ratio; (12) morphological parameter; (13) BCG/X-ray peak offset in kpc; (14) BCG/X-ray centroid offset in kpc; (15) Dynamical state.

A.2 Red galaxies and hot gas distributions

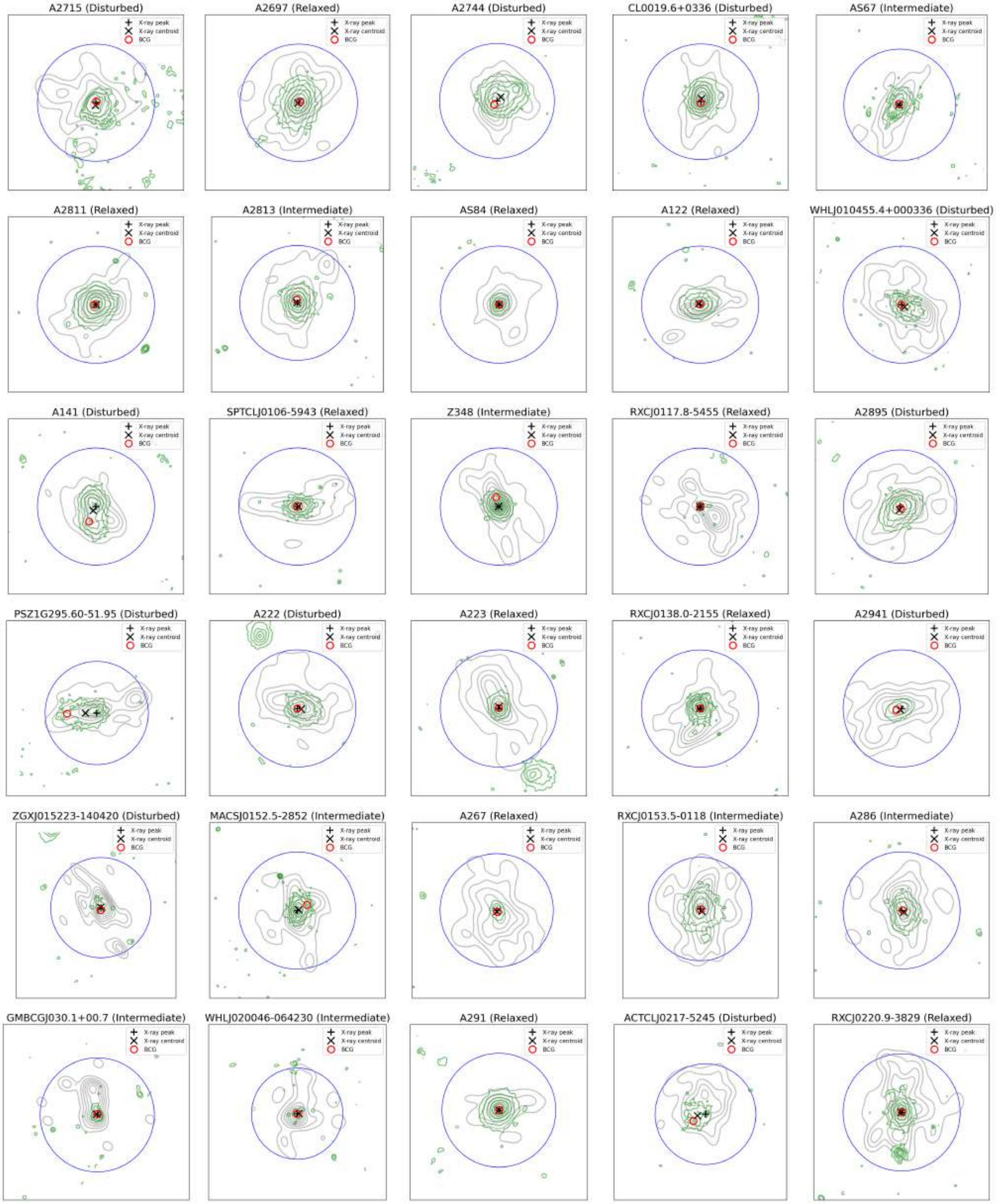
A2715 (Disturbed)
A2697 (Relaxed)
A2744 (Disturbed)
CL0019.6+0336 (Disturbed)
AS67 (Intermediate)
A2811 (Relaxed)
A2813 (Intermediate)
AS84 (Relaxed)
A122 (Relaxed)
WHLJ010455.4+000336 (Disturbed)
A141 (Disturbed)
SPTCLJ0106-5943 (Relaxed)
Z348 (Intermediate)
RXCJ0117.8-5455 (Relaxed)
A2895 (Disturbed)
PSZ1G295.60-51.95 (Disturbed)
A222 (Disturbed)
A223 (Relaxed)
RXCJ0138.0-2155 (Relaxed)
A2941 (Disturbed)
ZGXJ015223-140420 (Disturbed)
MACSJ0152.5-2852 (Intermediate)
A267 (Relaxed)
RXCJ0153.5-0118 (Intermediate)
A286 (Intermediate)
GMBCGJ030.1+00.7 (Intermediate)
WHLJ020046-064230 (Intermediate)
A291 (Relaxed)
ACTCLJ0217-5245 (Disturbed)
RXCJ0220.9-3829 (Relaxed)

Figure A.1: Contours of the X-ray surface brightness distribution (solid green lines) and the distribution of galaxies belonging to the red sequence (solid gray lines). Black crosses symbolize the positions of the X-ray peaks, black “X” marks represent the positions of the X-ray centroids, and open red circles denote the positions of the BCGs. The blue circle corresponds to the R_{200} of each cluster.

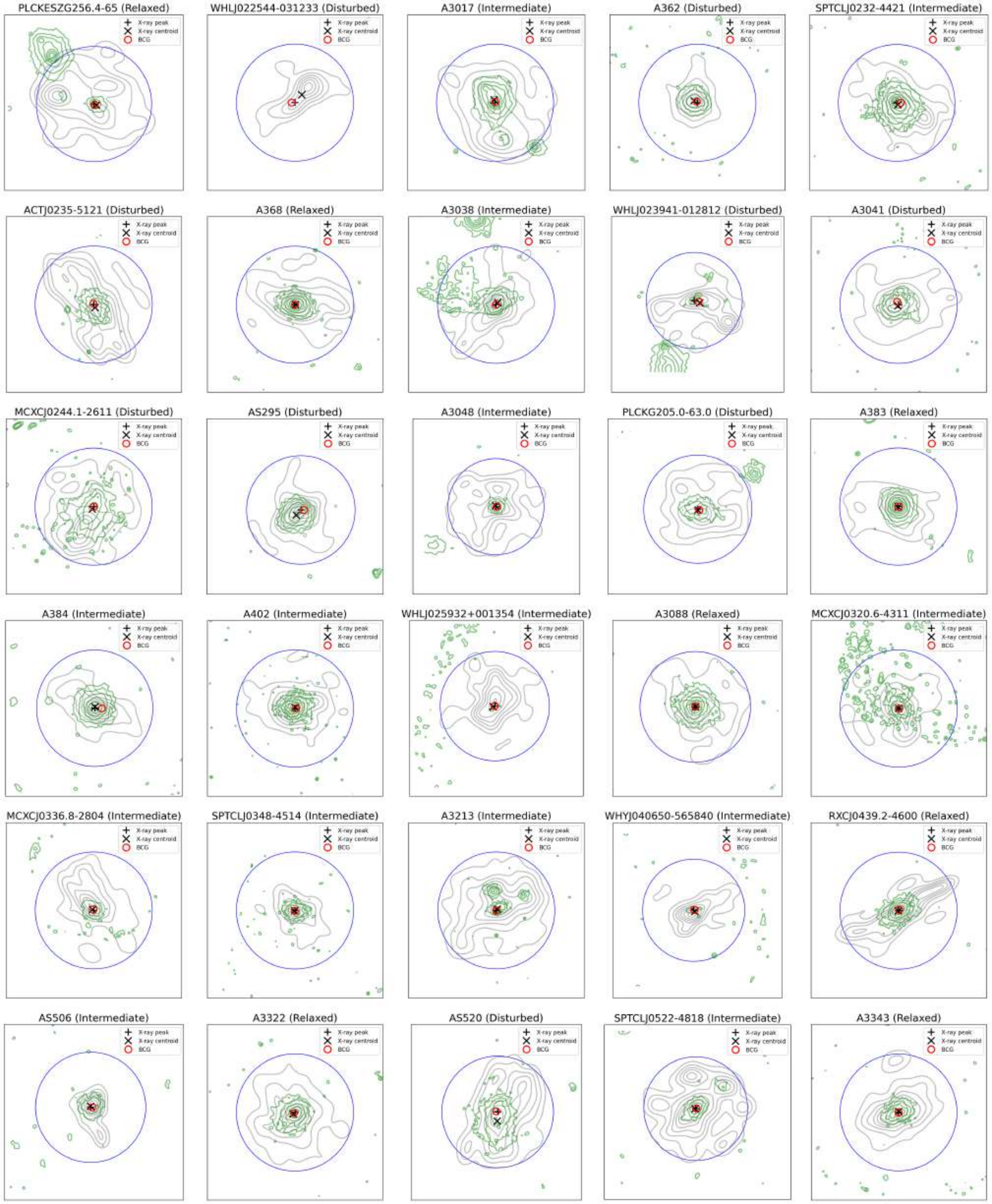

Figure A.2: Continuation of Figure A.1.

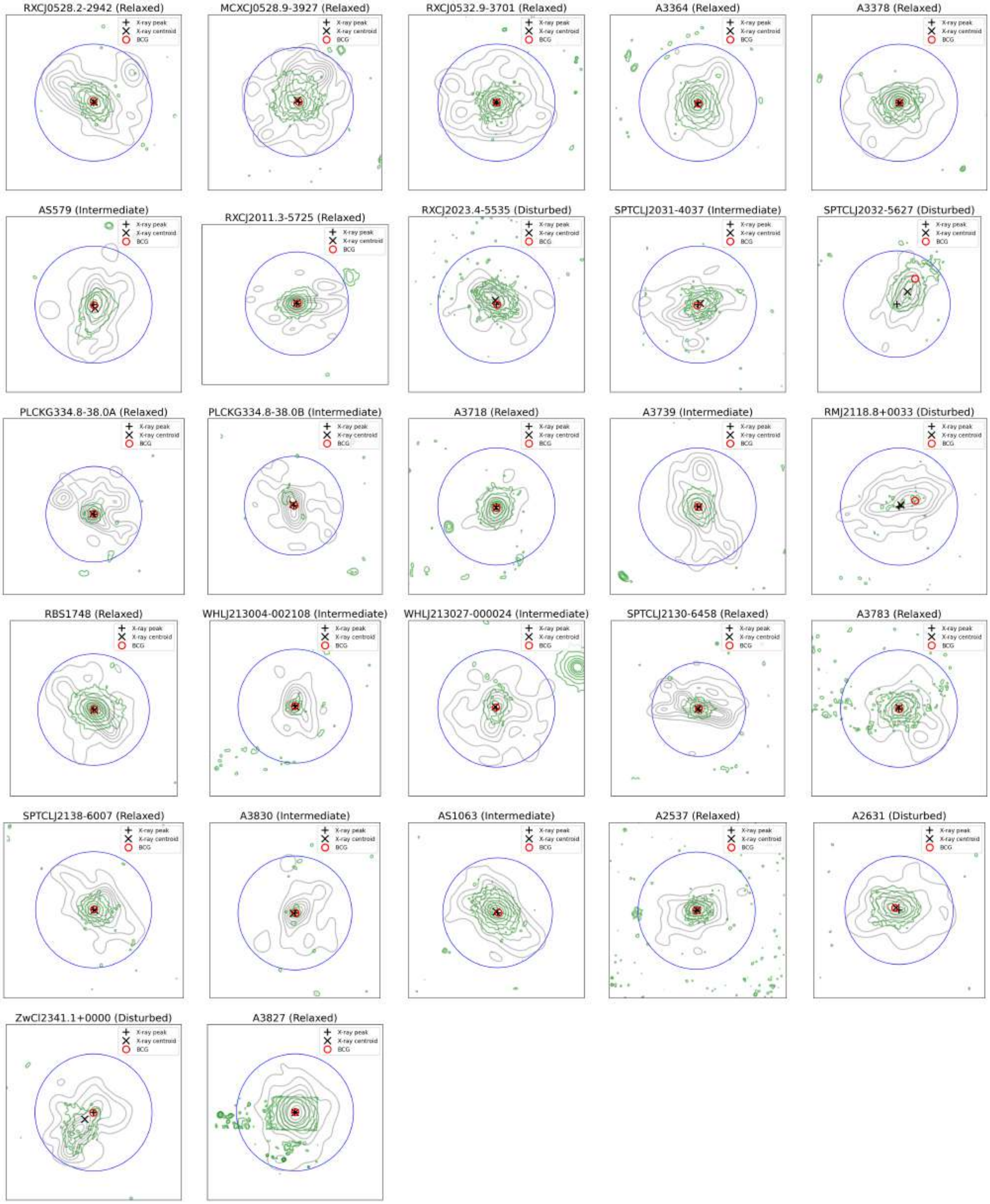
RXCJ0528.2-2942 (Relaxed)
MCXCJ0528.9-3927 (Relaxed)
RXCJ0532.9-3701 (Relaxed)
A3364 (Relaxed)
A3378 (Relaxed)
AS579 (Intermediate)
RXCJ2011.3-5725 (Relaxed)
RXCJ2023.4-5535 (Disturbed)
SPTCLJ2031-4037 (Intermediate)
SPTCLJ2032-5627 (Disturbed)
PLCKG334.8-38.0A (Relaxed)
PLCKG334.8-38.0B (Intermediate)
A3718 (Relaxed)
A3739 (Intermediate)
RMJ2118.8+0033 (Disturbed)
RBS1748 (Relaxed)
WHLJ213004-002108 (Intermediate)
WHLJ213027-000024 (Intermediate)
SPTCLJ2130-6458 (Relaxed)
A3783 (Relaxed)
SPTCLJ2138-6007 (Relaxed)
A3830 (Intermediate)
AS1063 (Intermediate)
A2537 (Relaxed)
A2631 (Disturbed)
ZwCl2341.1+0000 (Disturbed)
A3827 (Relaxed)

Figure A.3: Continuation of Figure A.1.